THESIS
3
(1995)

This is to certify that the

dissertation entitled

ANALYTICAL AND COMPUTATIONAL

APPROACHES

IN MECHANICS OF COMPOSITE MATERIALS

presented by

Peiying Sheng

has been accepted towards fulfillment
of the requirements for

Ph D. degree in Mechanics (Engineering)

Irvona M. Jasnik

Martin Styk-Stavridis

Major professor

Date June 25, 1995

MSU is an Affirmative Action/Equal Opportunity Institution

O-12771

LIBRARY
Michigan State University

PLACE IN RETURN BOX to remove this checkout from your record.
TO AVOID FINES return on or before date due.

DATE DUE	DATE DUE	DATE DUE

MSU Is An Affirmative Action/Equal Opportunity Institution
c:\circ\datedue.pm3-p.1

ANALYTICAL AND COMPUTATIONAL APPROACHES IN MECHANICS OF COMPOSITE MATERIALS

By

Peiying Sheng

A DISSERTATION

Submitted to

Michigan State University

in partial fulfillment of the requirements

for the degree of

DOCTOR OF PHILOSOPHY

Department of Materials Science and Mechanics

1995

ABSTRACT

ANALYTICAL AND COMPUTATIONAL APPROACHES IN MECHANICS OF COMPOSITE MATERIALS

By

Peiying Sheng

This thesis consists of two parts. In the first part, we analyze elastic fields of a half space having a spherical inclusion. The half-space is subjected to either a remote shear stress parallel to its plane boundary or to a uniform shear eigenstrain in the inclusion. The interface between the inclusion and the surrounding matrix is either perfectly bonded or is allowed to slide (slip) without friction. We obtain an analytical solution using displacement potentials in forms of integrals and infinite series.

In the second part, we study the effective moduli and damage formation in out-of-plane elasticity (or, equivalently, two-dimensional conductivity) of matrix-inclusion composite materials with either randomly or periodically distributed inclusions (fibers) by a computational approach based on a finite difference spring-network scheme. Damage evolution is simulated by sequentially removing/breaking springs (bonds) in this lattice in accordance with the evolving state of stress/strain concentrations. The composite systems are characterized by two parameters: stiffness ratio and strength ratio of both phases. In particular we investigate the following aspects: basic classification of effective constitutive responses, geometric patterns of damage, varying degrees of randomness of the inclusions' arrangements, and mesh resolution of continuum phases.

CONTENTS

LIST OF FIGURES

CHAPTER 1

Fig. 7 Stress $\sigma_{\varphi\varphi}(\bar{\sigma}_{\varphi\varphi})$ versus angle φ for different radii a = 0.2 (solid line), 0.5 (dashed line) and 0.8 (dashdot line) when $\Gamma = 2$ and $\theta = 0°$ for sliding and remote shear loading case.

Fig. 8 Stress $\sigma_{\varphi\varphi}(\bar{\sigma}_{\varphi\varphi})$ versus angle φ for different radii a = 0.2 (solid line), 0.5 (dashed line) and 0.8 (dashdot line) when $\Gamma = 0.5$ and $\theta = 0°$ for sliding and remote shear loading case.

Fig. 9 Stress $\sigma_{\varphi\varphi}(\bar{\sigma}_{\varphi\varphi})$ versus angle φ for different radii a = 0.2 (solid line), 0.5 (dashed line) and 0.8 (dashdot line) when $\Gamma = 0.01$ and $\theta = 0°$ for sliding and remote shear loading case.

Fig.10 Stress $\bar{\sigma}_{\varphi\varphi}$ versus angle φ for perfect bonding and sliding cases when $\Gamma = 0.5$, $\theta = 0°$ and different radii a = 0.2 (solid line), 0.5 (dashed line) and 0.8 (dash-dot line) for remote shear loading.

Fig.11 Jump in displacement $[u_\varphi]$ versus angle φ for different radii a = 0.2 (solid line), 0.5 (dashed line) and 0.8 (dashdot line) when $\Gamma = 100$, $\theta = 0°$ for pure sliding case and remote shear loading.

Fig.12 Jump in displacement $[u_\varphi]$ versus angle φ for different radii a = 0.2 (solid line), 0.5 (dashed line) and 0.8 (dashdot line) when $\Gamma = 2$, $\theta = 0°$ for pure sliding case and remote shear loading.

Fig.13 Jump in displacement $[u_\varphi]$ versus angle φ for different radii a = 0.2 (solid line), 0.5 (dashed line) and 0.8 (dashdot line) when $\Gamma = 0.5$, $\theta = 0°$ for pure sliding case and remote shear loading.

Fig.14 Jump in displacement $[u_\varphi]$ versus angle φ for different radii a = 0.2 (solid line), 0.5 (dashed line) and 0.8 (dashdot line) when $\Gamma = 0.01$, $\theta = 0^0$ for pure sliding case and remote shear loading.

Fig.15 Stress $\sigma_{xx}(\bar{\sigma}_{xx})$ along z-axis for different radii a = 0.2 (solid line), 0.5 (dashed line) and 0.8 (dashdot line) when $\Gamma = 100$ for perfect bonding case and remote shear loading.

Fig.16 Stress $\sigma_{xx}(\bar{\sigma}_{xx})$ along z-axis for different radii a = 0.2 (solid line), 0.5 (dashed line) and 0.8 (dashdot line) when $\Gamma = 2$ for perfect bonding case and remote shear loading.

Fig.17 Stress $\sigma_{xx}(\bar{\sigma}_{xx})$ along z-axis for different radii a = 0.2 (solid line), 0.5 (dashed line) and 0.8 (dashdot line) when $\Gamma = 0.5$ for perfect bonding case and remote shear loading.

Fig.18 Stress $\sigma_{xx}(\bar{\sigma}_{xx})$ along z-axis for different radii a = 0.2 (solid line), 0.5 (dashed line) and 0.8 (dashdot line) when $\Gamma = 0.01$ for perfect bonding case and remote shear loading.

Fig.19 Stress $\sigma_{xx}(\bar{\sigma}_{xx})$ at several points along z-axis versus radius of inclusion *a* for both perfect bonding (dashed lines) and pure sliding (solid lines) when $\Gamma = 100$ (remote shear loading).

Fig.20 Stress $\sigma_{xx}(\bar{\sigma}_{xx})$ along z-axis for different radii a = 0.2 (solid line), 0.5 (dashed line) and 0.8 (dashdot line) when $\Gamma = 100$ for perfect bonding and the eigenstrain case.

Fig. 70 Probability distribution function F (ε_{max}) for the case of

$$\varepsilon^i/\varepsilon^m = 0.1, \quad C^i/C^m = 0.1.$$

Fig. 71 Damage map, constitutive curves.

Fig. 72 Damage map, distribution function F (σ_{max}).

Fig. 73 Damage map, distribution function F (ε_{max}).

CHAPTER 1

A SPHERICAL INCLUSION IN AN ELASTIC HALF-SPACE UNDER SHEAR

1. INTRODUCTION

1.1 INTRODUCTION

When an inclusion is present in a matrix and a loading is applied, the elastic fields are disturbed in the vicinity of the inclusion. These stresses depend on a number of factors: the geometry and location of the inclusion, the elastic constants of the inclusion and the matrix, the boundary conditions at the matrix-inclusion interface, the loading, and other.

Inclusion problems have been addressed by many researchers. For a review of literature in this area see Mura (1987). Most of these studies, however, considered the cases when the inclusion is embedded in an infinitely extended material and the matrix-inclusion interface is perfectly bonded.

The elasticity problem of a half-space with a spherical (or spheroidal) inclusion or cavity has been studied by several researchers. Among them, Tsuchida and Nakahara (1970, 1972) solved the problem of a semi-infinite elastic body with a spherical cavity

subjected to a remote all-around tension or a uniform pressure on either the surface of cavity or on the plane boundary. Tsutsui and Saito (1973) solved the problem of a semi-infinite body containing a perfectly bonded spherical inhomogeneity under all around tension, while Tsuchida and Mura (1983) considered a similar problem involving a spheroidal inhomogeneity. Other related papers are due to Atsumi and Itou (1974), Tsuchida *et al.* (1973), Tsuchida *et al.* (1982), and Yu and Sanday (1990). The problem of an ellipsoidal inclusion, having same elastic constants as the matrix and subjected to dilatational strains was solved by Seo and Mura (1979), and the same problem but involving a spherical inclusion was studied by Mindlin and Cheng (1950) and Wachtman and Dundurs (1971). All the above works were restricted to axisymmetric cases. Tsuchida and Nakahara (1974), using a combination of Boussinesq, Neuber and Dougall displacement potentials, solved an asymmetric problem of a spherical cavity in a half space subjected to either a uniaxial tension or a pure shear. Recently, Jasiuk *et al.* (1991) solved the problem of a half space containing a sliding spheroidal inclusion under either an axisymmetric remote tension or an eigenstrain loading.

The corresponding two dimensional problems involving a half-plane include: a hole under a uniaxial tension solved by Jeffery (1920) and Mindlin (1948), an inclusion subjected to an eigenstrain loading considered by Richardson (1969), and a circular perfectly bonded inclusion under a remote uniaxial tension studied by Saleme (1958) and Shioya (1967). Also, Lee *et al.* (1992) addressed the case of a sliding circular inclusion in a half-plane under either a remote uniaxial tension or an eigenstrain loading.

In this thesis, we investigate the joint effect of a traction free-plane boundary and a sliding spherical inclusion embedded in a half-space. The inclusion is subjected to either a remote pure shear stress parallel to the plane boundary or a pure shear eigenstrain in the inclusion. The interface between the inclusion and the matrix is either perfectly bonded or allows slip without friction (shear tractions are zero) while maintaining continuity of normal displacement and tractions. This study is related to earlier works involving a spheroi-

dal sliding inclusion under shear embedded in an infinite matrix (Jasiuk *et al.*, 1987; Sheng, 1992).

1.2 PROBLEM STATEMENT

We consider a semi-infinite elastic material containing a spherical inclusion of radius *a*, having different elastic constants than those of the matrix, as shown in Fig.1. The loading is either a uniform pure shear stress, parallel to the plane boundary, applied at infinity, or an eigenstrain loading of shear type in the inclusion.

These loading conditions can be expressed as

$$\begin{aligned} \sigma_{xx} &= -\sigma_{yy} = p_0 \qquad && (x, y \to \infty) \\ \overset{*}{\varepsilon}_{xx} &= -\overset{*}{\varepsilon}_{yy} = \overset{*}{\varepsilon} && (in \quad \Omega) \end{aligned} \tag{1}$$

where σ_{xx}, σ_{yy} are stresses, $\overset{*}{\varepsilon}_{xx}$, $\overset{*}{\varepsilon}_{yy}$ are eigenstrains, and p_0 and $\overset{*}{\varepsilon}$ are constants. In our notation we use a bar to denote quantities in the inclusion.

In the solution we use all three coordinate systems, Cartesian (x, y, z), cylindrical (r, θ, z) and spherical (R, θ, φ). The relations among these coordinate systems are

$$\begin{aligned} x &= r\cos\theta = R\sin\varphi\cos\theta \\ y &= r\sin\theta = R\sin\varphi\sin\theta \\ z &= R\cos\varphi \end{aligned} \tag{2}$$

We let the origin of coordinates be at the center of the spherical inclusion and the positive direction of the z-axis be downward and, without the loss of generality, we take the perpendicular distance from the origin of the inclusion to the traction-free surface as

unity so that the plane boundary is located at z = -1.

The boundary conditions are as follows:

1. tractions at infinity $(x, y \to \infty)$ are

$$\sigma_{xx}\big|_{x \to \infty} = -\sigma_{yy}\big|_{y \to \infty} = p_0 \tag{3}$$

for a remote shear loading, and vanishing tractions at infinity for an eigenstrain case,

2. the traction-free condition on the plane surface (z = -1)

$$\sigma_{zz}\big|_{z=-1} = 0$$

$$\sigma_{zr}\big|_{z=-1} = 0 \tag{4}$$

$$\sigma_{z\theta}\big|_{z=-1} = 0$$

3. and either perfect bonding boundary conditions at the inclusion-matrix interface $(r = a)$

$$u_R\big|_{R=a} = \bar{u}_R\big|_{R=a}$$

$$u_\theta\big|_{R=a} = \bar{u}_\theta\big|_{R=a}$$

$$u_\varphi\big|_{R=a} = \bar{u}_\varphi\big|_{R=a}$$

$$\sigma_{RR}\big|_{R=a} = \bar{\sigma}_{RR}\big|_{R=a} \tag{5}$$

$$\sigma_{R\theta}\big|_{R=a} = \bar{\sigma}_{R\theta}\big|_{R=a}$$

$$\sigma_{R\varphi}\big|_{R=a} = \bar{\sigma}_{R\varphi}\big|_{R=a}$$

or frictionless sliding at the interface with no separation in the normal direction (pure sliding)

$$u_R\big|_{R=a} = \bar{u}_R\big|_{R=a}$$

$$\sigma_{RR}\big|_{R=a} = \bar{\sigma}_{RR}\big|_{R=a}$$

$$\sigma_{R\theta}\big|_{R=a} = 0 \qquad (6)$$

$$\bar{\sigma}_{R\theta}\big|_{R=a} = 0$$

$$\sigma_{R\varphi}\big|_{R=a} = 0$$

$$\bar{\sigma}_{R\varphi}\big|_{R=a} = 0$$

In the above expressions, u_i and σ_{ij} represent displacements and stresses, respectively.

2. METHOD OF SOLUTION

2.1 ELASTICITY THEORY IN THREE-DIMENSIONS

The problem considered in this thesis is solved by using the displacement potentials approach. If no body forces are accounted for, the displacement equations of equilibrium for elasticity in three-dimensions are

$$\nabla^2 \underset{\sim}{u} + \frac{1}{1-2\nu} \times \nabla e = 0 \tag{7}$$

where $\underset{\sim}{u}$ = displacement vector

ν = Poisson's ratio

e = dilatation, $\nabla \bullet \underset{\sim}{u}$

$\nabla^2 = \frac{\partial^2}{\partial x^2} + \frac{\partial^2}{\partial y^2} + \frac{\partial^2}{\partial z^2}$, Laplacian operator

$\nabla = \frac{\partial}{\partial x}\hat{i} + \frac{\partial}{\partial y}\hat{j} + \frac{\partial}{\partial z}\hat{k}$, where $\hat{i}$, $\hat{j}$, $\hat{k}$ are unit vectors in x, y, z direction respectively.

The general solution of the boundary value problem of the partial differential equations of equilibrium can be given by harmonic displacement potentials.

In order to construct a solution to our problem we use a combination of six harmonic displacement potential functions, namely ϕ_0, ϕ_1, ϕ_2, ϕ_3, ϕ_4 and λ_3. Among them, the set of ϕ_0, ϕ_1, ϕ_2, ϕ_3 is due to Papkovich and Neuber, the set of ϕ_0, ϕ_3 and λ_3 to Boussinesq, and the set of ϕ_0, ϕ_4 and λ_3 to Dougall. For reference, we include the expressions for the stress and displacement fields resulting from these potentials in the Appendix A. It should be pointed out that the combination of the potentials chosen here is not unique. Other combinations, consisting of at least three potentials, may also give

the same solution. We choose our combination for a mathematical convenience.

2.2 UNDISTURBED FIELD

According to a superposition principle in elasticity, for the applied remote loading case the stress and displacement field in the matrix can be considered as a sum of two parts, the undisturbed field in the absence of the inclusion caused only by the applied loading at infinity and the field due to the disturbance by the inclusion. Similarly, for the eigenstrain case, the stress and displacement field in the inclusion can be considered as a sum of two parts, the nonelastic field when the inclusion is allowed to deform freely due to the eigenstrain without any constrain from the matrix and a field resulting from elastic strains caused by the presence of matrix.

For the matrix, the potential function which gives the elastic field due to the remote shear loading (3) in the absence of inclusion is

$$\phi_0 = \frac{1}{2}p_0(x^2-y^2) = p_0\frac{1}{6}R^2P_2^2(\mu)\cos 2\theta \tag{8}$$

where $\mu = \cos\varphi$ and $P_n^m(\mu)$ is the associated Legendre's function of the first kind of order n and degree m. The displacements and stresses corresponding to (8) are

$$2Gu_R = \frac{1}{3}p_0RP_2^2(\mu)\cos 2\theta = p_0R\sin^2\varphi\cos 2\theta$$

$$2Gu_\theta = -\frac{1}{3\sin\varphi}p_0RP_2^2(\mu)\cos 2\theta = -p_0R\sin\varphi\cos 2\theta$$

$$2Gu_\varphi = -\frac{1}{6}p_0RP_2^{2\prime}(\mu)\sin\varphi\cos 2\theta = p_0R\sin\varphi\cos\varphi\cos 2\theta$$

$$\sigma_{RR} = \frac{1}{3}P_0 P_2^2(\mu)\cos 2\theta = P_0 \sin^2\varphi \cos 2\theta$$

$$\sigma_{\theta\theta} = -p_0 \cos 2\theta$$

$$\sigma_{\varphi\varphi} = p_0 \cos^2\varphi \cos 2\theta \tag{9}$$

$$\sigma_{R\theta} = -\frac{1}{3\sin\varphi}p_0 P_2^2(\mu)\sin 2\theta = -p_0 \sin\varphi \sin 2\theta$$

$$\sigma_{\theta\varphi} = -p_0 \cos\varphi \sin 2\theta$$

$$\sigma_{R\varphi} = -\frac{1}{6}p_0 P_2^{2\prime}(\mu)\sin\varphi\cos 2\theta = p_0 \sin\varphi\cos\varphi\cos 2\theta$$

where the prime refers to the derivative with respect to μ and G is the shear modulus of the matrix.

For the eigenstrain loading, the undisturbed stresses in the inclusion are zero and the displacements, derived from displacement-strain relations, are as follows

$$\bar{u}_R^* = \frac{1}{3}\varepsilon^* R P_2^2(\mu)\cos 2\theta$$

$$\bar{u}_\theta^* = -\frac{1}{3\Pi}\varepsilon^* R P_2^2(\mu)\sin 2\theta \tag{10}$$

$$\bar{u}_\varphi^* = -\frac{1}{6}\Pi\varepsilon^* R P_2^{2\prime}(\mu)\cos 2\theta$$

where $\Pi = \sin\varphi$

2.3 HARMONIC POTENTIALS

The main concern in this investigation is to choose the proper harmonic potential functions so that the specified boundary conditions can be satisfied by the corresponding stresses and displacements. Generally, the harmonic potential functions which satisfy the displacement equation of equilibrium in the forms of spherical and cylindrical coordinates are related to Legendre functions and Bessel functions.

For the matrix, the potentials accounting for the disturbance due to the presence of inclusion are

$$\begin{aligned}
\phi_0 &= \sum_{n=2}^{\infty} C_n R^{-(n+1)} P_n^2(\mu)\cos 2\theta \\
\phi_1 &= \sum_{n=1}^{\infty} D_n R^{-(n+1)} P_n^1(\mu)\cos\theta \\
\phi_2 &= -\sum_{n=1}^{\infty} D_n R^{-(n+1)} P_n^1(\mu)\sin\theta \\
\phi_3 &= \sum_{n=2}^{\infty} E_n R^{-(n+1)} P_n^2(\mu)\cos 2\theta \\
\phi_4 &= -\sum_{n=2}^{\infty} \frac{E_n}{n-1} R^{-(n+1)} P_n^2(\mu)\cos 2\theta
\end{aligned} \tag{11}$$

while the following potentials allow to satisfy the traction-free condition (4)

$$\begin{aligned}
\phi_0 &= \int_0^{\infty} \psi_3(\lambda) J_2(\lambda r)\, e^{-\lambda z}\cos 2\theta\, d\lambda \\
\phi_1 &= \int_0^{\infty} \psi_4(\lambda) J_1(\lambda r)\, e^{-\lambda z}\cos\theta\, d\lambda
\end{aligned}$$

$$\phi_2 = -\int_0^\infty \psi_4(\lambda) J_1(\lambda r) e^{-\lambda z} \sin\theta d\lambda \tag{12}$$

$$\phi_3 = \int_0^\infty \lambda\psi_5(\lambda) J_2(\lambda r) e^{-\lambda z} \cos 2\theta d\lambda$$

$$\lambda_3 = \int_0^\infty \psi_6(\lambda) J_2(\lambda r) e^{-\lambda z} \sin 2\theta d\lambda$$

In the above equations C_n, D_n and E_n are the unknown constants, ψ_3, ψ_4, ψ_5 and ψ_6 are the unknown functions which will be determined from the boundary conditions, and $J_n(\lambda r)$ is the Bessel function of the first kind of n order.

For the inclusion region we choose the following displacement potentials

$$\phi_0 = \sum_{n=2}^{\infty} \bar{C}_n R^n P_n^2(\mu) \cos 2\theta$$

$$\phi_1 = \sum_{n=1}^{\infty} \bar{D}_n R^n P_n^1(\mu) \cos\theta$$

$$\phi_2 = -\sum_{n=1}^{\infty} \bar{D}_n R^n P_n^1(\mu) \sin\theta \tag{13}$$

$$\phi_3 = \sum_{n=2}^{\infty} \bar{E}_n R^n P_n^2(\mu) \cos 2\theta$$

The displacements and stresses can be derived from potentials (11)-(13) by using relations given in the Appendix A. We combine these fields with the fields given in (9) and/or (10) and find the total fields.

Note that for the remote shear loading the potential function (8) yields the stresses $\sigma_{xx} = -\sigma_{yy} = p_0$ at infinity, while the other stress components are zero. The stresses derived from the potentials (11) and (12) vanish at infinity. Therefore, the total stresses

satisfy the boundary conditions at infinity (3). For the eigenstrain case for the matrix region we only use the potentials (11) and (12). These satisfy the traction-free boundary conditions at infinity automatically.

2.4 SOLUTION

Potentials (11)-(12) are expressed in spherical and cylindrical coordinates, respectively. In order to satisfy the traction-free boundary condition (4) on the surface z = -1 it is convenient to use cylindrical coordinates. With the aid of the relation,

$$\frac{P_n^m(\mu)}{R^{n+1}} = \frac{(-1)^{n-m}}{(n-m)!}\int_0^\infty \lambda^n J_m(\lambda r)\, e^{\lambda z} d\lambda \qquad (z<0) \tag{14}$$

we can express potentials (11) in terms of cylindrical coordinates as

$$\begin{aligned}
\phi_0 &= \sum_{n=2}^{\infty} \hat{C}_n \int_0^\infty \lambda^n J_2(\lambda r)\, e^{\lambda z}\cos 2\theta\, d\lambda \\
\phi_1 &= \sum_{n=1}^{\infty} \hat{D}_n \int_0^\infty \lambda^n J_1(\lambda r)\, e^{\lambda z}\cos\theta\, d\lambda \\
\phi_2 &= -\sum_{n=2}^{\infty} \hat{D}_n \int_0^\infty \lambda^n J_1(\lambda r)\, e^{\lambda z}\sin\theta\, d\lambda \\
\phi_3 &= \sum_{n=2}^{\infty} \hat{E}_n \int_0^\infty \lambda^n J_2(\lambda r)\, e^{\lambda z}\cos 2\theta\, d\lambda \\
\phi_4 &= -\sum_{n=2}^{\infty} \frac{\hat{E}_n}{n-1} \int_0^\infty \lambda^n J_2(\lambda r)\, e^{\lambda z}\cos 2\theta\, d\lambda
\end{aligned} \tag{15}$$

where

$$\hat{C}_n = C_n \frac{(-1)^n}{(n-2)!}$$

$$\hat{D}_n = D_n \frac{(-1)^n}{(n-1)!}$$

$$\hat{E}_n = E_n \frac{(-1)^n}{(n-2)!} \tag{16}$$

Then, we substitute the potentials ϕ_0, ϕ_1, ϕ_2, ϕ_3, ϕ_4 and λ_3 into the boundary conditions (4) at the plane surface (z = -1) as follows:

$$(\sigma_{zz})_{z=-1} = \frac{\partial^2 \phi_0}{\partial z^2} + \left[r\frac{\partial^2 \phi_1}{\partial z^2} - 2\nu\frac{\partial \phi_1}{\partial r} \right]\cos\theta + 2\nu\frac{1}{r}\frac{\partial \phi_1}{\partial \theta}\sin\theta + \left[r\frac{\partial^2 \phi_2}{\partial z^2} - 2\nu\frac{\partial \phi_2}{\partial r} \right]\sin\theta$$
$$+ 2\nu\frac{1}{r}\frac{\partial \phi_2}{\partial \theta}\cos\theta + z\frac{\partial^2 \phi_3}{\partial z^2} - 2(1-\nu)\frac{\partial \phi_3}{\partial z} - r\frac{\partial^2 \phi_4}{\partial r \partial z} - 2(2-\nu)\frac{\partial \phi_4}{\partial z} = 0$$

$$(\sigma_{z\theta})_{z=-1} = \frac{1}{r}\frac{\partial^2 \phi_0}{\partial \theta \partial z} + \frac{\partial^2 \phi_1}{\partial \theta \partial z}\cos\theta + (1-2\nu)\frac{\partial \phi_1}{\partial z}\sin\theta + \frac{\partial^2 \phi_2}{\partial \theta \partial z}\sin\theta - (1-2\nu)\frac{\partial \phi_2}{\partial z}\cos\theta$$
$$+ \frac{z\partial^2 \phi_3}{r\partial\theta\partial z} - (1-2\nu)\frac{1}{r}\frac{\partial \phi_3}{\partial \theta} - \frac{1}{2}\frac{\partial^2 \phi_4}{\partial r \partial \theta} - 2(1-\nu)\frac{1}{r}\frac{\partial \phi_4}{\partial \theta} - \frac{\partial^2 \lambda_3}{\partial r \partial z} = 0 \tag{17}$$

$$(\sigma_{zr})_{z=-1} = \frac{\partial^2 \phi_0}{\partial r \partial z} + \left[r\frac{\partial^2 \phi_1}{\partial r \partial z} - (1-2\nu)\frac{\partial \phi_1}{\partial z} \right]\cos\theta + \left[r\frac{\partial^2 \phi_2}{\partial r \partial z} - (1-2\nu)\frac{\partial \phi_2}{\partial z} \right]\sin\theta$$
$$+ z\frac{\partial^2 \phi_3}{\partial r \partial z} - (1-2\nu)\frac{\partial \phi_3}{\partial r} + \frac{1}{2r}\frac{\partial^2 \phi_4}{\partial \theta^2} + r\frac{\partial^2 \phi_4}{\partial z^2} - 2(1-\nu)\frac{\partial \phi_4}{\partial r} + \frac{1}{r}\frac{\partial^2 \lambda_3}{\partial \theta \partial z} = 0$$

Note that the potential function (8) gives no tractions on the plane surface z = -1. Next, we substitute the potentials (12) and (15) into the above equations (17) and express boundary conditions on the traction-free plane (4) as

$$\int_0^\infty \Bigg[\Bigg(\sum_{n=2}^{\infty} \{ \hat{C}_n \lambda^n + 2(1-2\nu)\hat{D}_n \lambda^{n-1} - (\lambda + 2 - 2\nu)\hat{E}_n \lambda^{n-1} \} e^{-2\lambda}$$

$$+ \{ \psi_3(\lambda) + \frac{2\nu}{\lambda}\psi_4(\lambda) + (-\lambda + 2 - 2\nu)\psi_5(\lambda) - 2\nu\hat{D}_1 e^{-2\lambda} \} \Bigg) J_2(\lambda r)$$

$$+ \{ -\hat{D}_1 \lambda e^{-2\lambda} + \psi_4(\lambda) \} r J_1(\lambda r) \Bigg] e^{\lambda} \lambda^2 d\lambda = 0$$

$$\int_0^\infty \Bigg[\Bigg(\sum_{n=2}^{\infty} \{ \hat{C}_n \lambda^n + 2(1-2\nu)\hat{D}_n \lambda^{n-1} - (\lambda + 1 - 2\nu)\hat{E}_n \lambda^{n-1} \} e^{-2\lambda}$$

$$- \{ \psi_3(\lambda) + \frac{2\nu}{\lambda}\psi_4(\lambda) + (-\lambda + 1 - 2\nu)\psi_5(\lambda) + 2\nu\hat{D}_1 e^{-2\lambda} \} \Bigg) \lambda^2 J_2'(\lambda r) \qquad (18)$$

$$+ \frac{2\lambda}{r} \Bigg((1-2\nu) \sum_{n=2}^{\infty} \hat{D}_n \lambda^{n-1} e^{-2\lambda} - \psi_6(\lambda) \Bigg) J_2(\lambda r)$$

$$+ \left(-\frac{4\nu}{r} + r\lambda^2 \right) \{ \hat{D}_1 \lambda e^{-2\lambda} + \psi_4(\lambda) \} J_2(\lambda r) \Bigg] e^{\lambda} d\lambda = 0$$

$$\int_0^\infty \Bigg[\Bigg(- \sum_{n=2}^{\infty} \{ \hat{C}_n \lambda^n + 2(1-2\nu)\hat{D}_n \lambda^{n-1} - (\lambda + 1 - 2\nu)\hat{E}_n \lambda^{n-1} \}$$

$$+ \{ \psi_3(\lambda) + \frac{2\nu}{\lambda}\psi_4(\lambda) + (-\lambda + 1 - 2\nu)\psi_5(\lambda) + 2\nu\hat{D}_1 e^{-2\lambda} \} \Bigg) \frac{2\lambda}{r} J_2(\lambda r)$$

$$+ \Bigg(-(1-2\nu) \sum_{n=2}^{\infty} \hat{D}_n \lambda^{n-1} e^{-2\lambda} + 2\nu\hat{D}_1 e^{-2\lambda} + \frac{2\nu}{\lambda}\psi_4(\lambda) + \psi_6(\lambda) \Bigg)$$

$$\times \lambda^2 J_2'(\lambda r) \Bigg] d\lambda = 0$$

Then, we let the coefficients of terms involving $J_1(\lambda r)$, $J_2(\lambda r)$ and $J_2'(\lambda r)$ be zero and use the following relations:

(a) the Fourier-Bessel integral

$$f(x) = \int_0^\infty \int_0^\infty ytf(t) J_s(yt) J_s(yx)\, dydt \qquad (s > -1, x > 0) \tag{19}$$

(b) the transformation from the Legendre function to Bessel function

$$\frac{P_n^m(\mu)}{R^{n+1}} = \frac{(-1)^{n-m}}{(n-m)!} \int_0^\infty \lambda^n J_m(\lambda r)\, e^{\lambda z} d\lambda \qquad (z < 0) \tag{20}$$

(c) the relation between Bessel and modified Bessel function

$$\int_0^\infty \frac{x^{s+1}}{\left(x^2 + y^2\right)^{t+1}} J_s(xb)\, dx = \frac{b^t y^{s-t} K_{s-t}(yb)}{2^t \Gamma(t+1)} \tag{21}$$

where $K_s(z)$ is a modified Bessel function of the second kind and $\Gamma(n)$ is a Gamma function,

(d) the definition of the modified Bessel function

$$K_{1/2}(\lambda) = K_{-1/2}(\lambda) = \sqrt{\frac{\pi}{2\lambda}} e^{-\lambda} \tag{22}$$

(e) the recursion formula for the Gamma function

$$\Gamma(x+1) = x\Gamma(x) \qquad (x > 0) \tag{23}$$

Then, the unknown functions ψ_3, ψ_4, ψ_5 and ψ_6, which satisfy the boundary condition at the plane surface (4), become

$$\psi_3(\lambda) = 2(-\lambda + 1 - 2\nu)^2 \hat{D}_1 e^{-2\lambda} + \sum_{n=2}^{\infty} [(-2\lambda + 3 - 4\nu)\hat{C}_n \lambda$$

$$+ 2(1-2\nu)(-2\lambda+3-4\nu)\hat{D}_n - 2\{2(1-\nu)(1-2\nu) - \lambda^2\}\hat{E}_n]\lambda^{n-1}e^{-2\lambda}$$

$$\psi_4(\lambda) = -\hat{D}_1\lambda e^{-2\lambda} \tag{24}$$

$$\psi_5(\lambda) = -2(-\lambda+1-2\nu)\hat{D}_1 e^{-2\lambda}$$

$$+ \sum_{n=2}^{\infty} [-2\hat{C}_n\lambda - 4(1-2\nu)\hat{D}_n + (2\lambda+3-4\nu)\hat{E}_n]\lambda^{n-1}e^{-2\lambda}$$

$$\psi_6(\lambda) = (1-2\lambda)\sum_{n=2}^{\infty}\hat{D}_n\lambda^{n-1}e^{-2\lambda}$$

Next, we use the relation (16) and express the unknown functions ψ_3, ψ_4, ψ_5, and ψ_6 in terms of unknown constants C_n, D_n and E_n, which are now the only unknowns in the harmonic potential functions (11) and (12) and will be determined from the boundary conditions at the inclusion-matrix interface (5) or (6).

It is convenient to use the spherical coordinate system to satisfy the boundary conditions at the inclusion's interface. We use the following relation to transform potentials from Bessel function to Legendre's function,

$$J_n(\lambda y)e^{-\lambda z} = \sum_{m=n}^{\infty}(-1)^{m+n}\frac{(\lambda R)^m}{(m+n)!}P_m^n(\mu) \tag{25}$$

Then, we rewrite potentials (12) in the spherical coordinates as follows

$$\phi_0 = \sum_{n=2}^{\infty}\xi_n R^n P_n^2(\mu)\cos 2\theta$$

$$\phi_1 = \sum_{n=1}^{\infty}\eta_n R^n P_n^1(\mu)\cos\theta$$

$$\phi_2 = -\sum_{n=1}^{\infty} \eta_n R^n P_n^1(\mu) \sin\theta \tag{26}$$

$$\phi_3 = \sum_{n=2}^{\infty} \zeta_n R^n P_n^2(\mu) \cos 2\theta$$

$$\lambda_3 = \sum_{n=2}^{\infty} \kappa_n R^n P_n^2(\mu) \sin 2\theta$$

where

$$\xi_n = \int_0^{\infty} \psi_3(\lambda) \frac{(-\lambda)^n}{(n+2)!} d\lambda$$

$$\eta_n = -\int_0^{\infty} \psi_4(\lambda) \frac{(-\lambda)^n}{(n+1)!} d\lambda \tag{27}$$

$$\zeta_n = -\int_0^{\infty} \psi_5(\lambda) \frac{(-\lambda)^{n+1}}{(n+2)!} d\lambda$$

$$\kappa_n = -\int_0^{\infty} \psi_6(\lambda) \frac{(-\lambda)^n}{(n+2)!} d\lambda$$

After substituting ψ_3, ψ_4, ψ_5, and ψ_6, given in equations (24), into (27) and using the formula

$$\int_0^{\infty} e^{-xc} x^b dx = \frac{\Gamma(b+1)}{c^{b+1}} \qquad (c>0, b>-1) \tag{28}$$

we have

$$\xi_n = -2\left[\gamma_{0,n+2} + \frac{2(1-2\nu)}{n+2}\gamma_{0,n+1} + \frac{(1-2\nu)^2}{(n+1)(n+2)}\gamma_{0,n}\right] D_1$$

$$+ \sum_{m=2}^{\infty} \left[2(n+3)\gamma_{m-2,n+3} + (3-4\nu)\gamma_{m-2,n+2}\right] C_m$$

$$+\sum_{m=2}^{\infty} 2(1-2\nu)\left[\frac{-2}{n+2}\gamma_{m-1,n+1}-\frac{3-4\nu}{(n+2)(n+1)}\gamma_{m-1,n}\right]D_m$$

$$+\sum_{m=2}^{\infty} 2\left[\frac{2(1-\nu)(1-2\nu)}{n+2}\gamma_{m-2,n+1}-(n+3)\gamma_{m-2,n+3}\right]E_m$$

$$\eta_n = D_1\gamma_{0,n+1}$$

$$\zeta_n = -2\left[\gamma_{0,n+2}+\frac{1-2\nu}{n+2}\gamma_{0,n+1}\right]D_1 \tag{29}$$

$$+\sum_{m=2}^{\infty} 2(n+3)\gamma_{m-2,n+3}C_m-\sum_{m=2}^{\infty}\frac{4(1-2\nu)}{n+2}\gamma_{m-1.,n+1}D_m$$

$$-\sum_{m=2}^{\infty}\left[2(n+3)\gamma_{m-2,n+3}-(3-4\nu)\gamma_{m-2,n+2}\right]E_m$$

$$\kappa_n = -\sum_{m=2}^{\infty}\frac{1-2\nu}{(n+2)(n+1)}\gamma_{m-1,n}D_m$$

where

$$\gamma_{p,q} = \frac{(-1)^{p+q}}{p!q!}\frac{(p+q)!}{2^{p+q+1}} \tag{30}$$

Then, we express displacements and stresses in terms of the potentials (11), (13) and (26) by using the relations given in the Appendix A. Finally we substitute the displacements and stresses, given by the potentials (11)-(13), and the undisturbed ones (9) in the matrix and/or non-elastic ones (10) in the inclusion, into equations (5) and use the recursion formula for Legendre functions given in the Appendix B. Then, the boundary conditions at the interface, for the case of perfect bonding, become:

$$u_R\big|_{R=a} = \bar{u}_R\big|_{R=a}$$

$$-\frac{5-4\nu}{3a^2}D_1P_2^2(\mu)+\sum_{n=2}^{\infty}\Big[\{K^C_{n,n}C_n+K^D_{n,n+1}D_{n+1}+K^E_{n,n-1}E_{n-1}+K^E_{n,n+1}E_{n+1}$$

$$+K^{\xi}_{n,n}\xi_n+K^{\eta}_{n,n-1}\eta_{n-1}+K^{\eta}_{n,n+1}\eta_{n+1}+K^{\zeta}_{n,n-1}\zeta_{n-1}+K^{\zeta}_{n,n+1}\zeta_{n+1}+K^{\kappa}_{n,n}\kappa_{n,n}\}$$

$$-\frac{1}{\Gamma}\{\bar{K}^C_{n,n}\bar{C}_n+\bar{K}^D_{n,n-1}\bar{D}_{n-1}+\bar{K}^D_{n,n+1}\bar{D}_{n+1}+\bar{K}^E_{n,n-1}\bar{E}_{n-1}$$

$$+\bar{K}^E_{n,n+1}\bar{E}_{n,n+1}\}\Big]P_n^2(\mu)=-\frac{1}{3}\Big(p_0-2G\varepsilon^*\Big)aP_2^2(\mu) \tag{31}$$

$$u_{\theta}\big|_{R=a}=\bar{u}_{\theta}\big|_{R=a}$$

$$\sum_{n=2}^{\infty}\Big[\{H^C_{n,n}C_n+H^D_{n,n-1}D_{n-1}+H^D_{n,n+1}D_{n+1}+H^E_{n,n-1}E_{n-1}+H^E_{n,n+1}E_{n+1}+$$

$$+H^{\xi}_{n,n}\xi_n+H^{\eta}_{n,n-1}\eta_{n-1}+H^{\eta}_{n,n+1}\eta_{n+1}+H^{\zeta}_{n,n-1}\zeta_{n-1}+H^{\zeta}_{n,n+1}\zeta_{n+1}+H^{\kappa}_{n,n}\kappa_n$$

$$+H^{\kappa}_{n,n+2}\kappa_{n+2}\}-\frac{1}{\Gamma}\{\bar{H}^C_{n,n}\bar{C}_n+\bar{H}^D_{n,n-1}\bar{D}_{n-1}+\bar{H}^D_{n,n+1}\bar{D}_{n+1}+\bar{H}^E_{n,n-1}\bar{E}_{n-1}$$

$$+\bar{H}^E_{n,n+1}\bar{E}_{n+1}\}\Big]P_n^2(\mu)=\frac{1}{6}(p_0-2G\varepsilon^*)aP_2^2(\mu) \tag{32}$$

$$u_{\varphi}\big|_{R=a}=\bar{u}_{\varphi}\big|_{R=a}$$

$$\sum_{n=2}^{\infty}\Big[\{R^C_{n,n}C_n+R^D_{n,n-1}D_{n-1}+R^D_{n,n+1}D_{n+1}+R^E_{n,n-1}E_{n-1}+R^E_{n,n+1}E_{n+1}$$

$$+R^{\xi}_{n,n}\xi_n+R^{\eta}_{n,n-1}\eta_{n-1}+R^{\eta}_{n,n+1}\eta_{n+1}+R^{\zeta}_{n,n-1}\zeta_{n-1}+R^{\zeta}_{n,n+1}\zeta_{n+1}+R^{\kappa}_{n,n}\kappa_n$$

$$+R^{\kappa}_{n,n+2}\kappa_{n+2}\}-\frac{1}{\Gamma}\{\bar{R}^C_{n,n}\bar{C}_n+\bar{R}^D_{n,n-1}\bar{D}_{n-1}+\bar{R}^D_{n,n+1}\bar{D}_{n+1}+\bar{R}^E_{n,n-1}\bar{E}_{n-1}$$

$$+ \bar{R}^{E}_{n,n+1}\bar{E}_{n+1} \} \Big] P_n^{2\prime}(\mu)$$

$$+ \sum_{n=2}^{\infty} \Big[\{ R^{D}_{n,n} D_n + R^{E}_{n,n} E_n + R^{\eta}_{n,n} \eta_n + R^{\zeta}_{n,n} \zeta_n + R^{\kappa}_{n,n+1} \kappa_{n+1} \}$$

$$- \frac{1}{\Gamma} \{ \bar{R}^{D}_{n,n} \bar{D}_n + \bar{R}^{E}_{n,n} \bar{E}_n \} \Big] P_n^2(\mu) = \frac{1}{6}(p_0 - 2G\varepsilon^*) a P_2^{2\prime}(\mu) \qquad (33)$$

$$\sigma_{RR}\big|_{R=a} = \bar{\sigma}_{RR}\big|_{R=a}$$

$$\frac{2(5-\nu)}{3a^3} D_1 P_2^2(\mu) + \sum_{n=2}^{\infty} \Big[\{ L^{C}_{n,n} C_n + L^{D}_{n,n+1} D_{n+1} + L^{E}_{n,n-1} E_{n-1} + L^{E}_{n,n+1} E_{n+1}$$

$$+ L^{\xi}_{n,n} \xi_n + L^{\eta}_{n,n-1} \eta_{n-1} + L^{\eta}_{n,n+1} \eta_{n+1} + L^{\zeta}_{n,n-1} \zeta_{n-1} + L^{\zeta}_{n,n+1} \zeta_{n+1} + L^{\kappa}_{n,n} \kappa_{n,n} \}$$

$$- \{ L^{C}_{n,n} \bar{C}_n + L^{D}_{n,n-1} \bar{D}_{n-1} + L^{D}_{n,n+1} \bar{D}_{n+1} + L^{E}_{n,n-1} \bar{E}_{n-1} + L^{E}_{n,n+1} \bar{E}_{n+1} \} \Big] P_n^2(\mu)$$

$$= -\frac{p_0}{3} P_2^2(\mu) \qquad (34)$$

$$\sigma_{R\theta}\big|_{R=a} = \bar{\sigma}_{R\theta}\big|_{R=a}$$

$$\frac{5-4\nu}{3a^3} D_1 P_2^2(\mu) + \sum_{n=2}^{\infty} \Big[\{ S^{C}_{n,n} C_n + S^{D}_{n,n-1} D_{n-1} + S^{D}_{n,n+1} D_{n+1} + S^{E}_{n,n-1} E_{n-1}$$

$$+ S^{E}_{n,n+1} E_{n+1} + S^{\xi}_{n,n} \xi_n + S^{\eta}_{n,n-1} \eta_{n-1} + S^{\eta}_{n,n+1} \eta_{n+1} + S^{\zeta}_{n,n-1} \zeta_{n-1} + S^{\zeta}_{n,n+1} \zeta_{n+1}$$

$$+ S^{\kappa}_{n,n} \kappa_n + S^{\kappa}_{n,n+2} \kappa_{n+2} \} - \{ \bar{S}^{C}_{n,n} \bar{C}_n + \bar{S}^{D}_{n,n-1} \bar{D}_{n-1} + \bar{S}^{D}_{n,n+1} \bar{D}_{n+1} + \bar{S}^{E}_{n,n-1} \bar{E}_{n-1}$$

$$+ \bar{S}^{E}_{n,n+1}\bar{E}_{n+1} \} \Big] P_n^2(\mu) = \frac{p_0}{3} P_2^2(\mu) \tag{35}$$

$$\sigma_{R\varphi}\big|_{R=a} = \bar{\sigma}_{R\varphi}\big|_{R=a}$$

$$\frac{5-4\nu}{6a^3} D_1 P_2^2(\mu) + \frac{1}{2}\sum_{n=2}^{\infty} \Big[\{ T^{C}_{n,n} C_n + T^{D}_{n,n-1} D_{n-1} + T^{D}_{n,n+1} D_{n+1} + T^{E}_{n,n-1} E_{n-1}$$

$$+ T^{E}_{n,n+1} E_{n+1} + T^{\xi}_{n,n} \xi_n + T^{\eta}_{n,n-1} \eta_{n-1} + T^{\eta}_{n,n+1} \eta_{n+1} + T^{\zeta}_{n,n-1} \zeta_{n-1} + T^{\zeta}_{n,n+1} \zeta_{n+1}$$

$$+ T^{\kappa}_{n,n} \kappa_n + T^{\kappa}_{n,n+2} \kappa_{n+2} \} - \{ \bar{T}^{C}_{n,n} \bar{C}_n + \bar{T}^{D}_{n,n-1} \bar{D}_{n-1} + \bar{T}^{D}_{n,n+1} \bar{D}_{n+1} + \bar{T}^{E}_{n,n-1} \bar{E}_{n-1}$$

$$+ \bar{T}\bar{S}^{E}_{n,n+1} \bar{E}_{n+1} \} \Big] P_n^{2\prime}(\mu) + \frac{1}{2}\sum_{n=2}^{\infty} \Big[\{ T^{D}_{n,n} D_n + T^{E}_{n,n} E_n + T^{\eta}_{n,n} \eta_n + T^{\zeta}_{n,n} \zeta_n +$$

$$T^{\kappa}_{n,n+1} \kappa_{n+1} \} - \{ \bar{T}^{D}_{n,n} \bar{D}_n + \bar{T}^{E}_{n,n} \bar{E}_n \} \Big] P_n^2(\mu) = \frac{p_0}{6} P_2^{2\prime}(\mu) \tag{36}$$

where the primed quantities are the first derivatives with respect to μ and $\Gamma = \bar{G}/G$. The coefficients are defined as

$$K^{C}_{n,n} = -\frac{n+1}{a^{n+2}}$$

$$K^{D}_{n,n+1} = \frac{2(1-2\nu)}{n a^{n+2}}$$

$$K^{E}_{n,n-1} = -\frac{(n+3-4\nu)(n-2)}{(2n-1)a^n}$$

$$K^{E}_{n,n+1} = -\frac{(n+5-4\nu)(n+3)}{(2n+3)a^{n+2}}$$

$$K^{\xi}_{n,n} = na^{n-1} \tag{37}$$

$$K^{\eta}_{n,n-1} = \frac{n-4+4\nu}{2n-1}a^{n-1}$$

$$K^{\eta}_{n,n+1} = -\frac{n-2+4\nu}{2n+3}a^{n+1}$$

$$K^{\zeta}_{n,n-1} = \frac{(n-4+4\nu)\ (n-2)}{2n-1}a^{n-1}$$

$$K^{\zeta}_{n,n+1} = \frac{(n-2+4\nu)\ (n+3)}{2n+3}a^{n+1}$$

$$K^{\kappa}_{n,n} = 4a^{n-1}$$

$$H^{C}_{n,n} = -\frac{1}{a^{n+2}} = R^{C}_{n,n}$$

$$H^{D}_{n,n-1} = \frac{1-2\nu}{(2n-1)\,a^{n}} = R^{D}_{n,n-1}$$

$$H^{D}_{n,n+1} = -\frac{1-2\nu}{(2n+3)\,a^{n+2}} = R^{D}_{n,n+1}$$

$$H^{E}_{n,n-1} = -\frac{n-2}{(2n-1)\,a^{n}} = R^{E}_{n,n-1}$$

$$H^{E}_{n,n+1} = -\frac{n+3}{(2n+3)\,a^{n+2}} = R^{E}_{n,n+1}$$

$$H^{\xi}_{n,n} = -a^{n-1} = R^{\xi}_{n,n} \tag{38}$$

$$H^{\eta}_{n,n-1} = \frac{1-2\nu}{2n-1}a^{n-1} = R^{\eta}_{n,n-1}$$

$$H^{\eta}_{n,n+1} = -\frac{1-2\nu}{2n+3}a^{n+1} = R^{\eta}_{n,n+1}$$

$$H^{\zeta}_{n,n-1} = -\frac{(n-2)}{2n-1}a^{n-1} = R^{\zeta}_{n,n-1}$$

$$H^{\zeta}_{n,n+1} = -\frac{n+3}{2n+3}a^{n+1} = R^{\zeta}_{n,n+1}$$

$$H^{\kappa}_{n,n} = \frac{-n^2+n-4}{2n-1}a^{n-1} = R^{\kappa}_{n,n}$$

$$H^{\kappa}_{n,n+2} = \frac{(n+3)\,(n+4)}{2n+3}a^{n+1} = R^{\kappa}_{n,n+2}$$

$$R^{D}_{n,n} = -\frac{(n+1)\,(1-2\nu)}{(n-1)\,a^{n+1}}$$

$$R^{E}_{n,n+1} = \frac{4\,(1-\nu)}{a^{n+1}}$$

$$R^{\eta}_{n,n-1} = -2\,(1-\nu)\,a^{n} \qquad (39)$$

$$R^{\zeta}_{n,n-1} = 4\,(1-\nu)\,a^{n}$$

$$R^{\kappa}_{n,n-1} = n\,(n+3)\,a^{n}$$

$$L^{C}_{n,n} = \frac{(n+1)\,(n+2)}{a^{n+3}}$$

$$L^{D}_{n,n+1} = -\frac{2\,(1-2\nu)\,(n+2)}{na^{n+3}}$$

$$L^{E}_{n,n-1} = \frac{(n-2)\,(n\,(n+3)-2\nu)}{(2n-1)\,a^{n+1}}$$

$$L^{E}_{n,n+1} = \frac{(n+2)\,(n+3)\,(n+5-4\nu)}{(2n+3)\,a^{n+3}}$$

$$L^{\xi}_{n,n} = n\,(n-1)\,a^{n-2} \qquad (40)$$

$$L^{\eta}_{n,n-1} = \frac{(n-1)\,(n-4+4\nu)}{2n-1}a^{n-2}$$

$$L^{\eta}_{n,n+1} = -\frac{(n+1)\,(n-2)-2\nu}{2n+3}a^{n}$$

$$L^{\zeta}_{n,n-1} = \frac{(n-1)\,(n-2)\,(n-4+4\nu)}{2n-1}a^{n-2}$$

$$L^{\zeta}_{n,n+1} = \frac{(n+3)\,(\,(n-2)\,(n+1)-2\nu)}{2n+3}a^{n}$$

$$L^{\kappa}_{n,n} = 4\,(n-1)\,a^{n-2}$$

$$S^{C}_{n,n} = \frac{2\,(n+2)}{a^{n+3}} = T^{C}_{n,n}$$

$$S^{D}_{n,n-1} = -\frac{(1-2\nu)\,(n+1)}{(2\,n-1\,)\,a^{n+1}} = T^{D}_{n,n-1}$$

$$S^{D}_{n,n+1} = \frac{(1-2\nu)\,(n-3)\,(n+2)}{n\,(2n+3)\,a^{n+3}} = T^{D}_{n,n+1}$$

$$S^{E}_{n,n-1} = \frac{2\,(n-2)\,(n+2-2\nu)}{(2n-1)\,a^{n+1}} = T^{E}_{n,n-1}$$

$$S^{E}_{n,n+1} = \frac{2(n+3)(n+4-2\nu)}{(2n+3)a^{n+3}} = T^{E}_{n,n+1}$$

$$S^{\xi}_{n,n} = -2(n-1)a^{n-2} = T^{\xi}_{n,n}$$

$$S^{\eta}_{n,n-1} = \frac{2(1-\nu n)}{2n-1}a^{n-2} = T^{\eta}_{n,n-1} \qquad (41)$$

$$S^{\eta}_{n,n+1} = -\frac{2(1-\nu(n+2))}{2n+3}a^{n} = T^{\eta}_{n,n+1}$$

$$S^{\zeta}_{n,n-1} = -\frac{2(n-2)(n-3+2\nu)}{2n-1}a^{n-2} = T^{\zeta}_{n,n-1}$$

$$S^{\zeta}_{n,n+1} = -\frac{2(n+3)(n-1+2\nu)}{2n+3}a^{n} = T^{\zeta}_{n,n+1}$$

$$S^{\kappa}_{n,n} = -\left(n(n+2)+4-\frac{(n-2)^2(n+2)}{2n-1}\right)a^{n-2} = T^{\kappa}_{n,n}$$

$$S^{\kappa}_{n,n+2} = \frac{n(n+3)(n+4)}{2n+3}a^{n} = T^{\kappa}_{n,n+2}$$

$$T^{D}_{n,n} = -\frac{(1-2\nu)(n+1)(n+2)}{2(n-1)a^{n+2}}$$

$$T^{E}_{n,n} = -\frac{2(1-\nu)(n+2)}{a^{n+2}}$$

$$T^{\eta}_{n,n} = -(1-\nu)(n-1)a^{n-1} \qquad (42)$$

$$T^{\zeta}_{n,n} = 2(1-\nu)(n-1)a^{n-1}$$

$$T^{\kappa}_{n,n+1} = \frac{n(n-1)(n+3)}{2}a^{n-1}$$

All terms with a bar in equations (31)-(36) can be obtained from the corresponding terms without a bar, given in eqns. (37)-(42), by replacing ξ, η, ζ and ν with C, D, E and ∇. For example, $\bar{K}^{C}_{n,n}$, $\bar{K}^{D}_{n,n-1}$, $\bar{K}^{D}_{n,n+1}$, $\bar{K}^{E}_{n,n-1}$ and $\bar{K}^{E}_{n,n+1}$ can be obtained from $K^{\xi}_{n,n}$, $K^{\eta}_{n,n-1}$, $K^{\eta}_{n,n+1}$ $K^{\zeta}_{n,n-1}$ and $K^{\zeta}_{n,n+1}$, respectively, by replacing ν with ∇.

Using eqns. (29), we reduce the unknown constants in equations (31)-(36), representing the boundary conditions on the interface, to only $C_n, D_n, E_n, \bar{C}_n, \bar{D}_n$ and $\bar{E}_n$. Finally, we equate the coefficients of $P_n^2(\mu)$ and $P_n^{2\prime}(\mu)$ on both sides of eqns. (31)-(36) for each n from $n=2$ to $n \to \infty$, and obtain an infinite set of algebraic equations. Each of these sets contains six equations and six unknowns. For the numerical solution we truncate this infinite set of equations at $n = N$. Therefore, there are $6N$ equations and $6N$ unknowns to be solved. We truncate the series such that the boundary conditions (5) or (6) are satisfied to at least three significant figures. After these constants are evaluated, the stresses and displacements are known everywhere in the matrix and in the inclusion.

We follow the same procedure for the sliding interface case, but use the sliding boundary conditions (6) instead of (5). The sliding boundary conditions at the interface include eqns. (31) and (34)-(36) and

$$\bar{\sigma}_{R\theta}\big|_{R=a} = 0$$

$$\sum_{n=2}^{\infty} \left[\bar{S}^{C}_{n,n}\bar{C}_n + \bar{S}^{D}_{n,n-1}\bar{D}_{n-1} + \bar{S}^{D}_{n,n+1}\bar{D}_{n+1} + \bar{S}^{E}_{n,n-1}\bar{E}_{n-1} + \bar{S}^{E}_{n,n+1}\bar{E}_{n+1} \right] P_n^2(\mu) = 0 \tag{43}$$

$$\bar{\sigma}_{R\varphi}\big|_{R=a} = 0$$

$$\frac{1}{2}\sum_{n=2}^{\infty} \left[\bar{T}^{C}_{n,n}\bar{C}_n + \bar{T}^{D}_{n,n-1}\bar{D}_{n-1} + \bar{T}^{D}_{n,n+1}\bar{D}_{n+1} + \bar{T}^{E}_{n,n-1}\bar{E}_{n-1} + \bar{T}\bar{S}^{E}_{n,n+1}\bar{E}_{n+1} \right] P_n^{2\prime}(\mu)$$

$$+\frac{1}{2}\sum_{n=2}^{\infty} \left[\bar{T}^{D}_{n,n}\bar{D}_n + \bar{T}^{E}_{n,n}\bar{E}_n \right] P_n^2(\mu) = 0 \tag{44}$$

In the calculations, for the case of a perfectly bonded inclusion, we set the constant $\bar{D}_1$ to zero since $\bar{D}_1$ and $\bar{C}_2$ play the same role in the potentials and only one needs to be kept. Furthermore, we take one of the constants $\bar{D}_2$ and $\bar{E}_2$ as zero for the case of the perfectly bonded inclusion, and set both constants to zero for the sliding inclusion case.

In particular, when the matrix is infinite, the analytical solution involves only a finite number of terms in potential functions. For the case of an infinite body containing a spherical cavity and subjected to uniform shear stresses $\sigma_{xx} = -\sigma_{yy} = p_0$ at infinity, the constants become

$$C_2 = \frac{1}{2(7-5\nu)}a^5$$

$$D_2 = -\frac{5}{2(7-5\nu)}a^3 \tag{45}$$

while the other terms vanish.

For the case of an infinite body containing a spherical inhomogeneity subjected to uniform shear stresses $\sigma_{xx} = -\sigma_{yy} = p_0$ at infinity with the pure sliding interface, the solution is

$$E_3 = -\frac{70\Gamma(1-\nu)}{(17-19\nu)(7+5\nu)+4(7-5\nu)(7-4\nu)}\frac{1}{a^2}$$

$$\bar{D}_1 = 2E_3$$

$$\bar{C}_2 = -\left(1+\frac{2\nu}{7}\right)a^2E_3$$

$$\bar{C}_4 = -\frac{4\nu}{7}E_3 \tag{46}$$

$$D_1 = -\frac{3a^3}{7-5\nu}\left(\frac{5}{6}+\frac{2(7+5\nu)}{7}a^2E_3\right)$$

$$C_2 = \frac{a^2}{24}\left(a^3-2(1+\nu)D_1\right)$$

with the other terms vanishing. This solution in a form of finite series is expected from the work of Ghahremani (1980). The solution for perfectly bonded spherical inclusion in an infinite space is also expressed in terms of finite series as shown by Goodier (1933).

Similarly, the solution for the spherical inclusion in an infinite space with an eigen-strain loading case involves finite series for both perfect bonding and sliding cases.

3. RESULTS AND DISCUSSION

We carry out the numerical computations for various radii of inclusion a ranging from 0.2 to 0.99 and for the different ratios of shear modulus of the inclusion to the matrix $\Gamma = \bar{G}/G$. We take the Poisson's ratio as 0.3 for both the inclusion and the matrix, for simplicity. We give the numerical results for the case of the uniform shear loading in Figs. 2-19 and for the uniform shear eigenstrain in Fig. 20.

Fig. 2 shows stresses $\sigma_{\varphi\varphi}$ and $\bar{\sigma}_{\varphi\varphi}$ along the surface of the perfectly bonded inclusion when the radius of inclusion a = 0.2, 0.5 and 0.8 (plotted in solid, dashed and dashdot lines respectively), $\theta = 0^o$, and $\Gamma = 100$. Recall that the inclusion is located a unit distance from the free surface so the larger the radius a the closer is the inclusion to the free surface. As expected, the radius of the inclusion has a small influence on the stresses $\sigma_{\varphi\varphi}$ and $\bar{\sigma}_{\varphi\varphi}$ when the angle φ is less than 90^o, and the larger effect when φ is greater than 90^o which corresponds to the region near the free surface. Note that the stress $\bar{\sigma}_{\varphi\varphi}$ in the inclusion is more influenced by the free surface than the corresponding stress component $\sigma_{\varphi\varphi}$ in the matrix.

Figs. 3 - 5 show stresses $\sigma_{\varphi\varphi}$ and $\bar{\sigma}_{\varphi\varphi}$ in the same cases as in Fig. 2, but the ratio of shear moduli is 2, 0.5, 0.01 respectively. Once again, the radius of the inclusion has a small influence on the stresses $\sigma_{\varphi\varphi}$ and $\bar{\sigma}_{\varphi\varphi}$ when the angle φ is less than 90^o, and the larger effect when φ is greater than 90^o. Further more, the following can be observed as the ratio of shear moduli decreases. The influence of the free surface on stress $\sigma_{\varphi\varphi}$ in the matrix becomes larger and larger and on stress $\bar{\sigma}_{\varphi\varphi}$ smaller and smaller. The stress $\bar{\sigma}_{\varphi\varphi}$ almost vanishes as $\Gamma = 0.01$ which is close to the case of a cavity so that the obtained

result is reasonable. The stress $\sigma_{\varphi\varphi}$ in the matrix increases around the points $\varphi = 0^o$ and 180^o while decreases around point $\varphi = 90^o$, and it will be compressive when the ratio Γ is less then 1, or say, the inclusion is weaker than the matrix.

Figs. 6 - 9 show stresses $\sigma_{\varphi\varphi}$ and $\bar{\sigma}_{\varphi\varphi}$ along the surface of the sliding inclusion when the radius of inclusion $a = 0.2$, 0.5 and 0.8 (plotted in solid, dashed and dashdot lines respectively), $\theta = 0^o$. The corresponding ratios of shear moduli Γ are 100, 2, 0.5, 0.01. As expected, similar to the case of perfectly bonded inclusion, the radius of the inclusion has a small influence on the stresses $\sigma_{\varphi\varphi}$ and $\bar{\sigma}_{\varphi\varphi}$ when the angle φ is less than 90^o, and the larger effect when φ is greater than 90^o which corresponds to the region near the free surface. Note that the stress $\bar{\sigma}_{\varphi\varphi}$ in the inclusion is more influenced by the free surface than the corresponding stress component $\sigma_{\varphi\varphi}$ in the matrix when Γ takes big values, while the stress $\bar{\sigma}_{\varphi\varphi}$ in the inclusion is less influenced by the free surface than the corresponding stress component $\sigma_{\varphi\varphi}$ in the matrix when Γ takes small values. As $\Gamma = 0.01$ which is close to the case of a cavity, the stress $\bar{\sigma}_{\varphi\varphi}$ in the inclusion goes towards zero. The stress $\sigma_{\varphi\varphi}$ in the matrix increases around the points $\varphi = 0^o$ and 180^o as the ratios of shear modulus Γ decrease, however, it decreases around point $\varphi = 90^o$, and is always compressive there regardless of value of ratio, Γ .

Fig. 10 compares the stress $\bar{\sigma}_{\varphi\varphi}$ versus the angle φ for the cases of perfectly bonded and sliding interfaces when $\Gamma = 2$. We observe that the stress increases for the sliding case and decreases for the perfect case as φ increases from 0^o to 90^o, and vice versa from 90^o to 180^o, so that $\bar{\sigma}_{\varphi\varphi}$ reaches its maximum value at $\varphi = 0^o$ and the minimum value at $\varphi = 90^o$ for the case of perfectly bonded interface, while the minimum at $\varphi = 0^o$ and the maximum at $\varphi = 90^o$ for the case of sliding interface. The maximum value of $\bar{\sigma}_{\varphi\varphi}$ in the inclusion for the sliding case is about 2.7 p_0 for $\Gamma = 2$ and increases as Γ goes up. The similar situation occurs for $\sigma_{\varphi\varphi}$ for the case of perfectly bonded interface when Γ increases. For example, when $\Gamma = 100$ the maximum of stress $\sigma_{\varphi\varphi}$ in the matrix occurs at $\varphi = 90^o$ but when $\Gamma = 2$ at $\varphi = 0^o$. In this case the stress $\sigma_{\varphi\varphi}$ is much

lower than that of the sliding case and has a value of 0.8 to $0.9p_0$ depending on the radius of the inclusion (i.e. the distance from the free surface). Note that the traction-free surface has a higher influence on $\bar{\sigma}_{\varphi\varphi}$ for the sliding case. As the ratio Γ becomes small, say 0.01, which is close to the case of a cavity, the stresses $\sigma_{\varphi\varphi}$ and $\bar{\sigma}_{\varphi\varphi}$ coincide in cases of both perfectly bonded and sliding inclusion.

Figs. 11 - 14 illustrate the jump of the tangential displacement $[u_\varphi]$ along the interface for various radii of the inclusion a = 0.2, 0.5 and 0.8 (plotted in solid, dashed and dashdot lines respectively) and $\theta = 0^o$ for the sliding case. The same as before, the corresponding ratios of shear modulus Γ are 100, 2, 0.5, 0.01. Note that the jump of the displacement is higher for $\varphi \geq 90^0$ (i.e. near the traction-free surface) and increases when the inclusion is closer to the free surface. This is true for all ratios of shear modulus Γ, according to the results from our sample computations. This is expected since the inclusion can deform more freely near the free surface.

Figs. 15 - 18 illustrates the stresses σ_{xx} and $\bar{\sigma}_{xx}$ along the z-axis from z = -1 to z = 1 when the inclusion is perfectly bonded. The radius of the inclusion takes on the values a = 0.2, 0.5 and 0.8 (plotted in solid, dashed and dashdot lines respectively). The corresponding ratios of shear modulus Γ are 100, 2, 0.5, 0.01. First, we consider the case in which the ratio Γ is larger than 1, i.e., the case of stiffer inclusion. The stress $\bar{\sigma}_{xx}$ in the inclusion decreases from z = a to z = -a when the inclusion is close to the free surface ($a \geq 0.5$). The slope of $\bar{\sigma}_{xx}$ goes to zero when the radius is small, which implies that for the situation of $a << 1$, equivalent to that of an infinite body containing the inclusion, the stress $\bar{\sigma}_{xx}$ is uniform which is expected from Eshelby's (1957) solution. The curves have similar forms for other $\Gamma > 1$, but have bottom up image for $\Gamma < 1$. Note from Fig. 18 that when Γ is very small (close to the case of a cavity), there is large stress concentration at the interface near the free surface. When $\Gamma = 1$ the curve is a straight line, as expected, since this is the case of a homogeneous material.

Fig. 19 shows the stresses σ_{xx} and $\bar{\sigma}_{xx}$ at selected points P, M1, I1, I2, and M2 along

the z-axis (see Fig.1) when the radius a of the inclusion varies continuously from 0.2 to 0.99 for both the perfectly bonded (dashed curves) and sliding (solid curves) cases and $\Gamma = 100$. The point P is on the free plane surface, M1 and M2 on the side of the matrix at the interface, I1 and I2 on the side of the inclusion at the interface. It can be seen that the free plane surface will contribute significantly to the stresses σ_{xx} and $\bar{\sigma}_{xx}$ at the points P, M1 and I1, but will have a very small effect at points I2 and M2, which are away from the plane boundary.

For the case of the perfectly bonded interface, σ_{xx} at M1 and M2 in the matrix is very small (almost zero for $\Gamma = 100$), but $\bar{\sigma}_{xx}$ at I1 and I2 in the inclusion is high (larger than $2p_0$ for $\Gamma = 100$). This is expected because when the inclusion is much stiffer than the matrix it carries most of the loading. The stress σ_{xx} at the point P decreases when the radius a increases. The inverse situation occurs when the inclusion is softer than the matrix.

For the case of the sliding inclusion, when the inclusion is not close to the free plane surface, the stresses σ_{xx} and $\bar{\sigma}_{xx}$ at these five points are not greater than the applied stress. But if the radius of the inclusion is close to unity, there is a high stress concentration in σ_{xx} at the points P and M1 and it increases as the radius a increases. Also, the stresses are very high in the extreme situation of a cavity addressed by Tsuchida and Nakahara (1974).

Fig. 20 illustrates the variation of stress σ_{xx} and $\bar{\sigma}_{xx}$ along z axis from z = -1 to z = 1 when the inclusion is perfectly bonded at the interface for the shear eigenstrain loading case. The radius of the inclusion has the value of 0.2, 0.5 and 0.8, and $\Gamma = 2$. It is interesting to note that comparing the results to a similar case for the shear stress loading problem with the same Γ, Fig. 7 has an inverse image. However it is similar to one for the case of a uniform shear loading when $\Gamma = 0.5$.

In conclusion, in this paper we solve the problem of an inclusion in a half-space under an asymmetric loading, either remote or eigenstrain loading of shear type. We study the joint effect of traction-free surface and the boundary conditions at the matrix-inclusion

interface, which is either perfectly bonded or allows slip. We show that both the free surface and sliding may alter significantly the stress fields and may cause high stress concentrations.

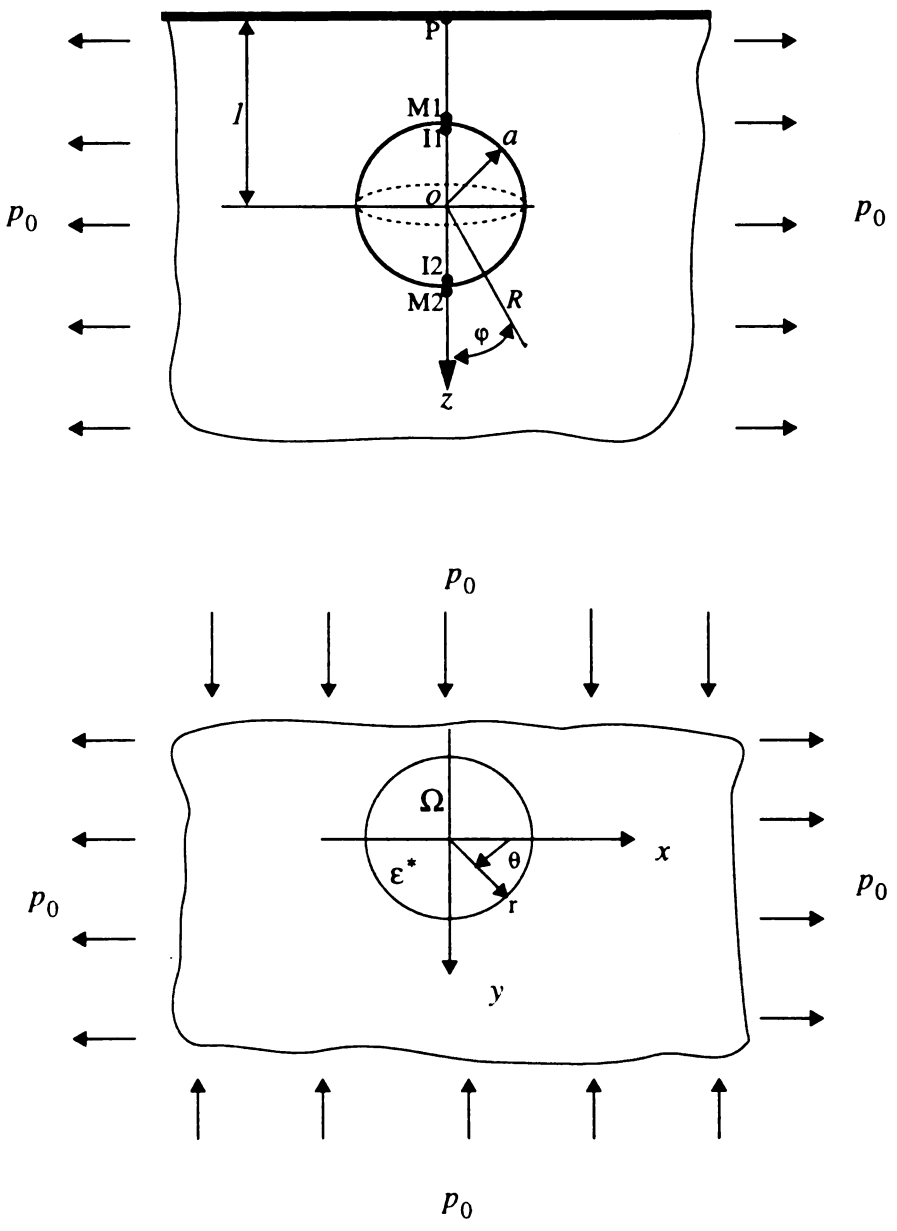

Fig. 1 Spherical inhomogeneity in a half-space.

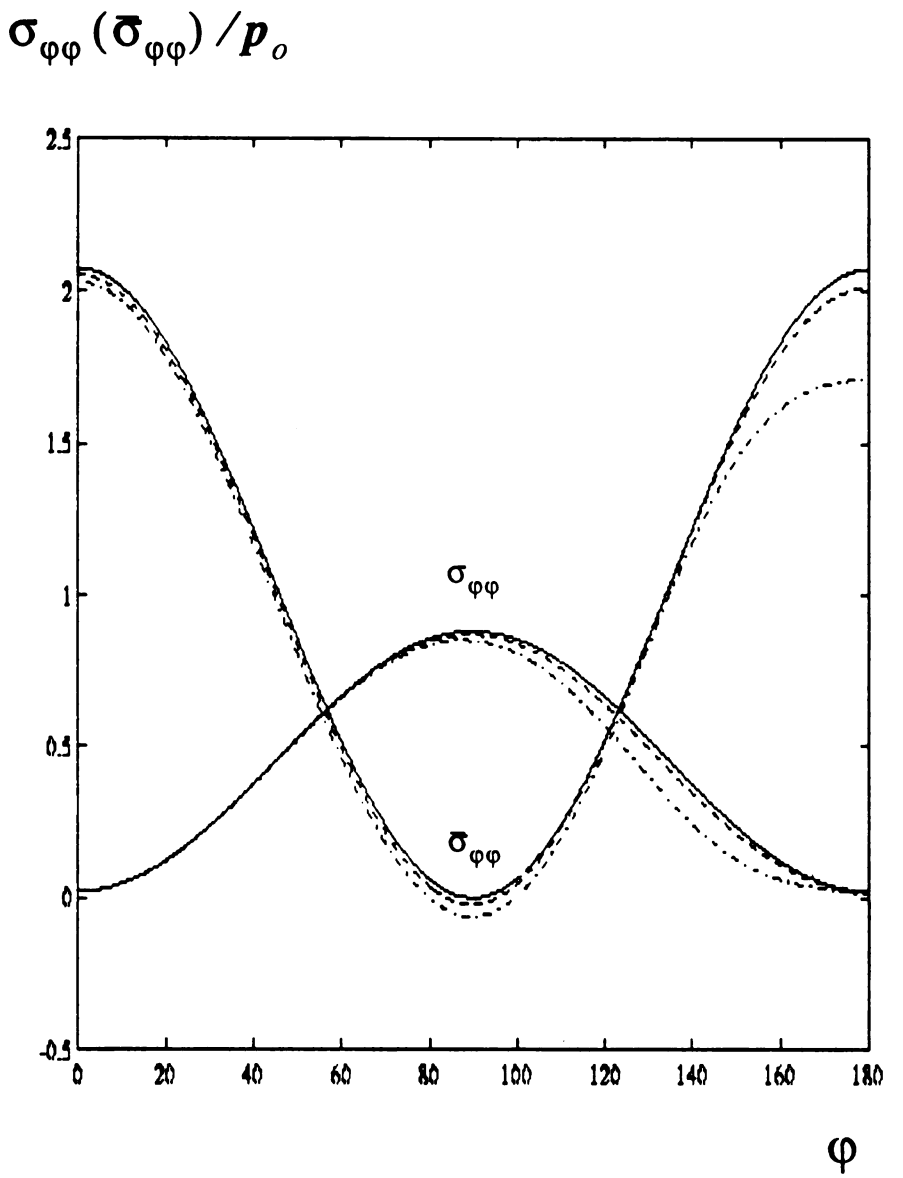

Fig. 2 Stress $\sigma_{\varphi\varphi}(\bar{\sigma}_{\varphi\varphi})$ versus angle φ for different radii $a = 0.2$ (solid line), 0.5 (dashed line) and 0.8 (dashdot line) when $\Gamma = 100$ and $\theta = 0^0$ for perfect bonding and remote shear loading case.

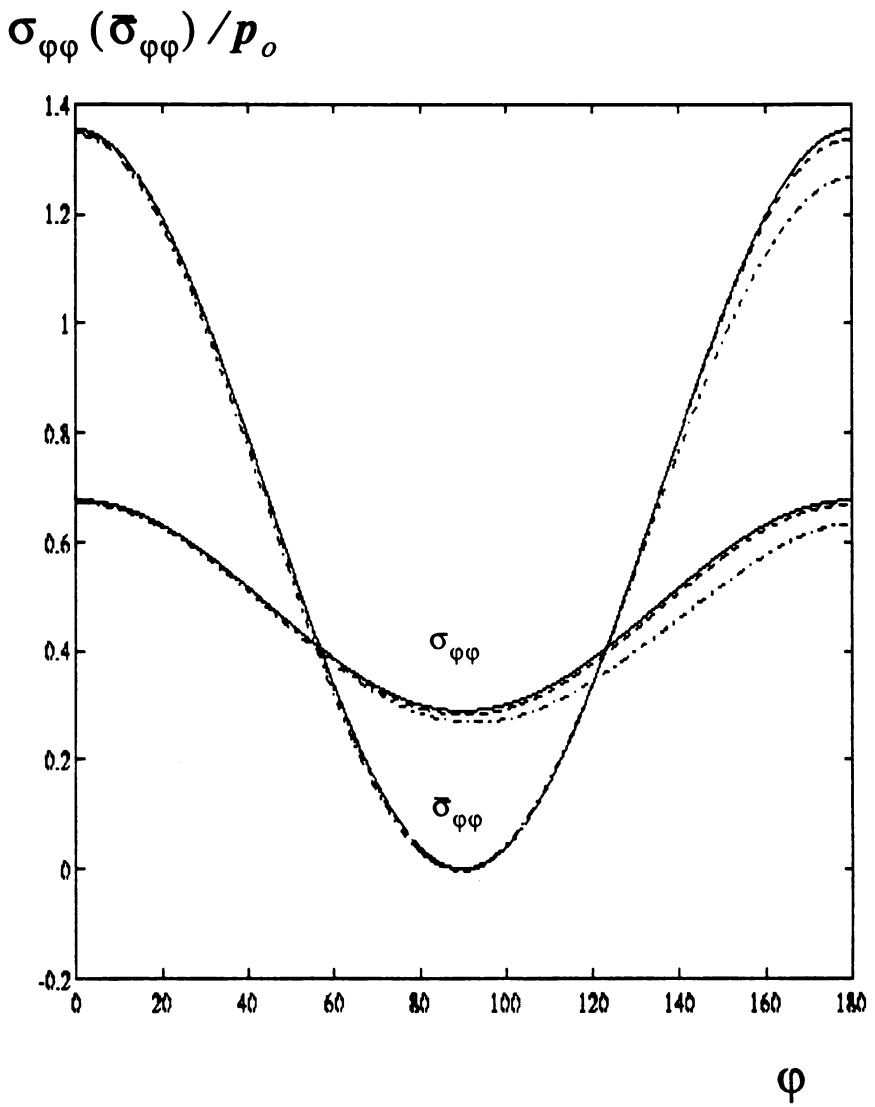

Fig. 3 Stress $\sigma_{\varphi\varphi}(\bar{\sigma}_{\varphi\varphi})$ versus angle φ for different radii $a = 0.2$ (solid line), 0.5 (dashed line) and 0.8 (dashdot line) when $\Gamma = 2$ and $\theta = 0^0$ for perfect bonding and remote shear loading case.

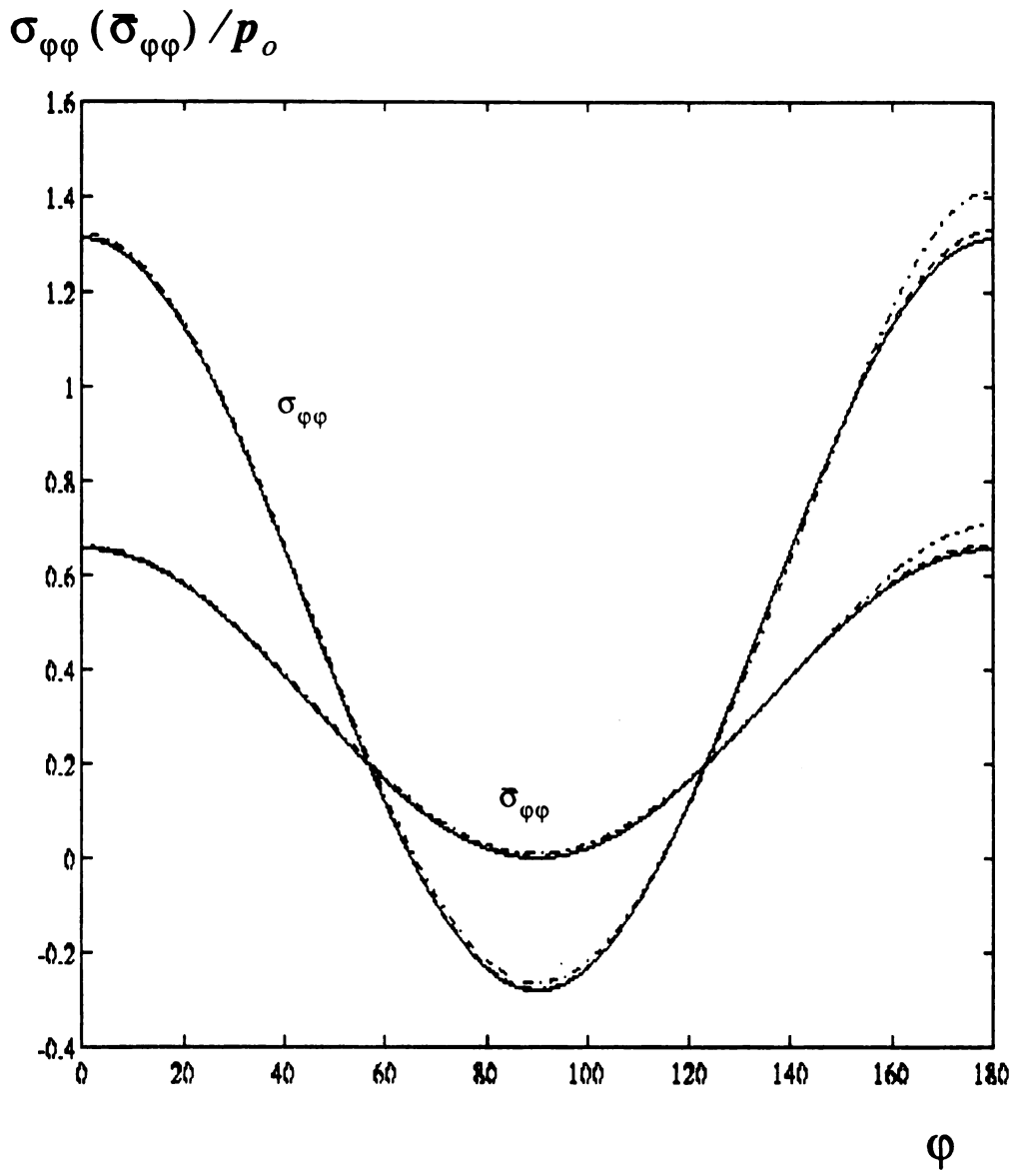

Fig. 4 Stress $\sigma_{\varphi\varphi}(\bar{\sigma}_{\varphi\varphi})$ versus angle φ for different radii a = 0.2 (solid line), 0.5 (dashed line) and 0.8 (dashdot line) when Γ = 0.5 and $\theta = 0^0$ for perfect bonding and remote shear loading case.

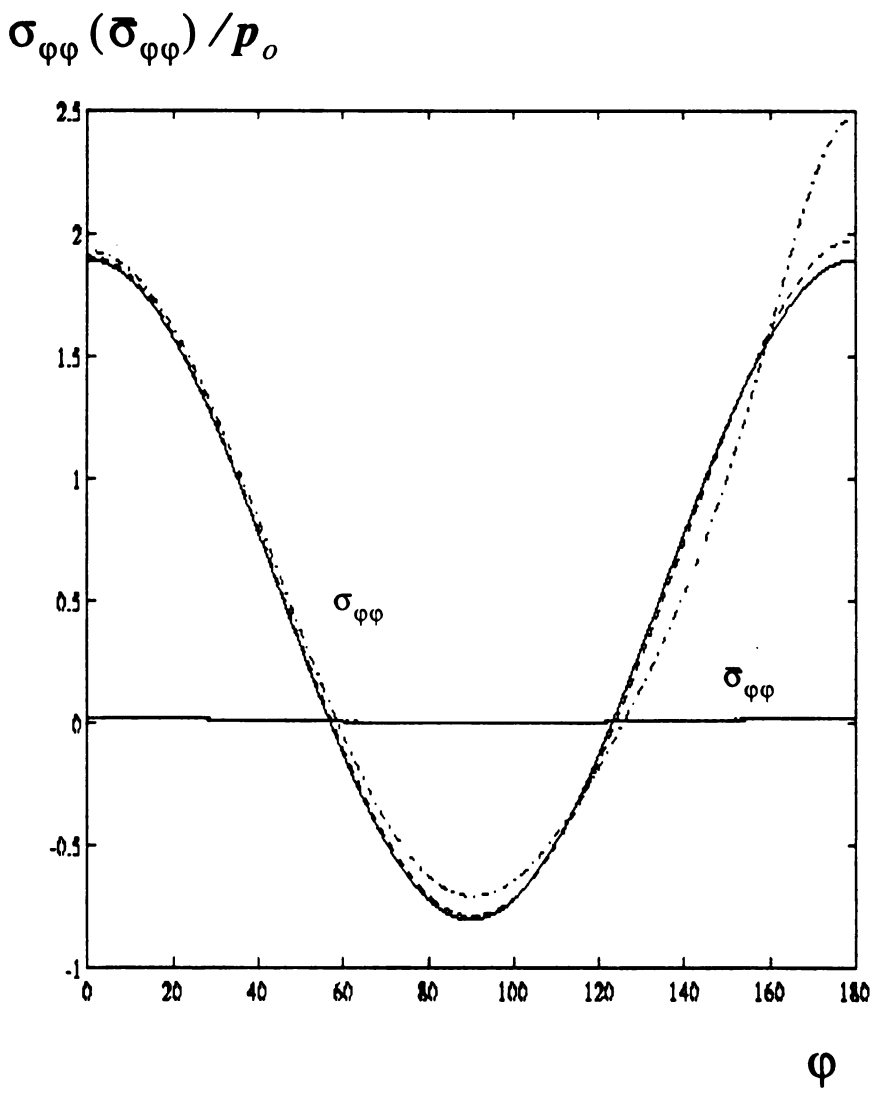

Fig. 5 Stress $\sigma_{\varphi\varphi}(\bar{\sigma}_{\varphi\varphi})$ versus angle φ for different radii $a = 0.2$ (solid line), 0.5 (dashed line) and 0.8 (dashdot line) when $\Gamma = 0.01$ and $\theta = 0^0$ for perfect bonding and remote shear loading case.

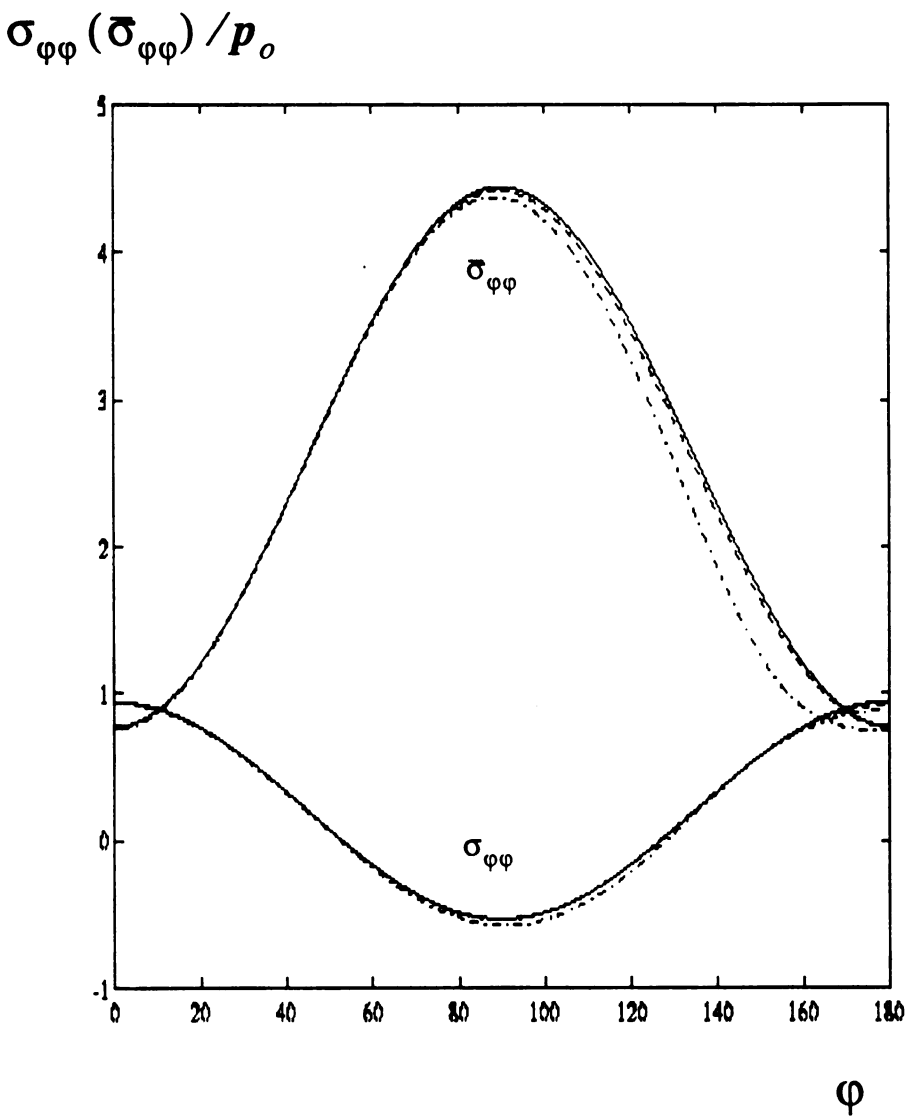

Fig. 6 Stress $\sigma_{\varphi\varphi}(\bar{\sigma}_{\varphi\varphi})$ versus angle φ for different radii a = 0.2 (solid line), 0.5 (dashed line) and 0.8 (dashdot line) when Γ = 100 and $\theta = 0^0$ for sliding and remote shear loading case.

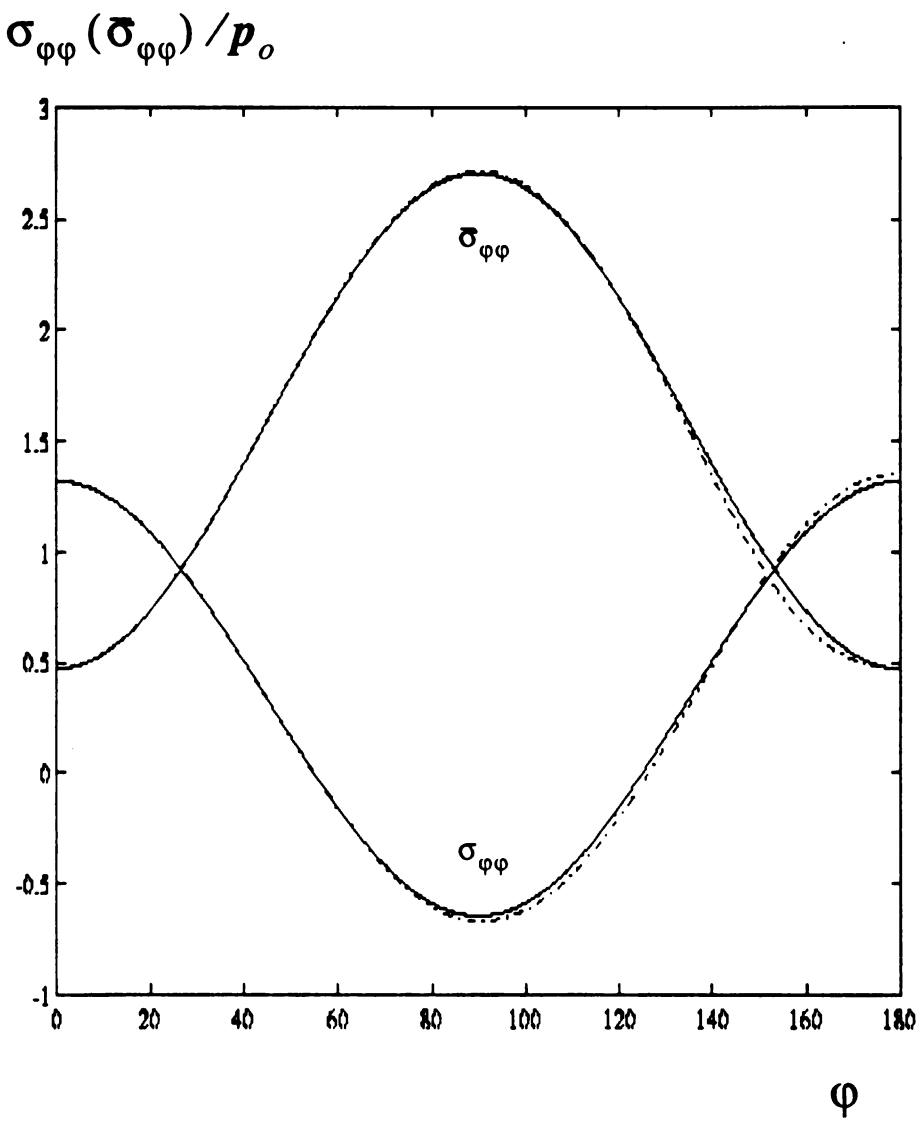

Fig. 7 Stress $\sigma_{\varphi\varphi}(\bar{\sigma}_{\varphi\varphi})$ versus angle φ for different radii $a = 0.2$ (solid line), 0.5 (dashed line) and 0.8 (dashdot line) when $\Gamma = 2$ and $\theta = 0^0$ for sliding and remote shear loading case.

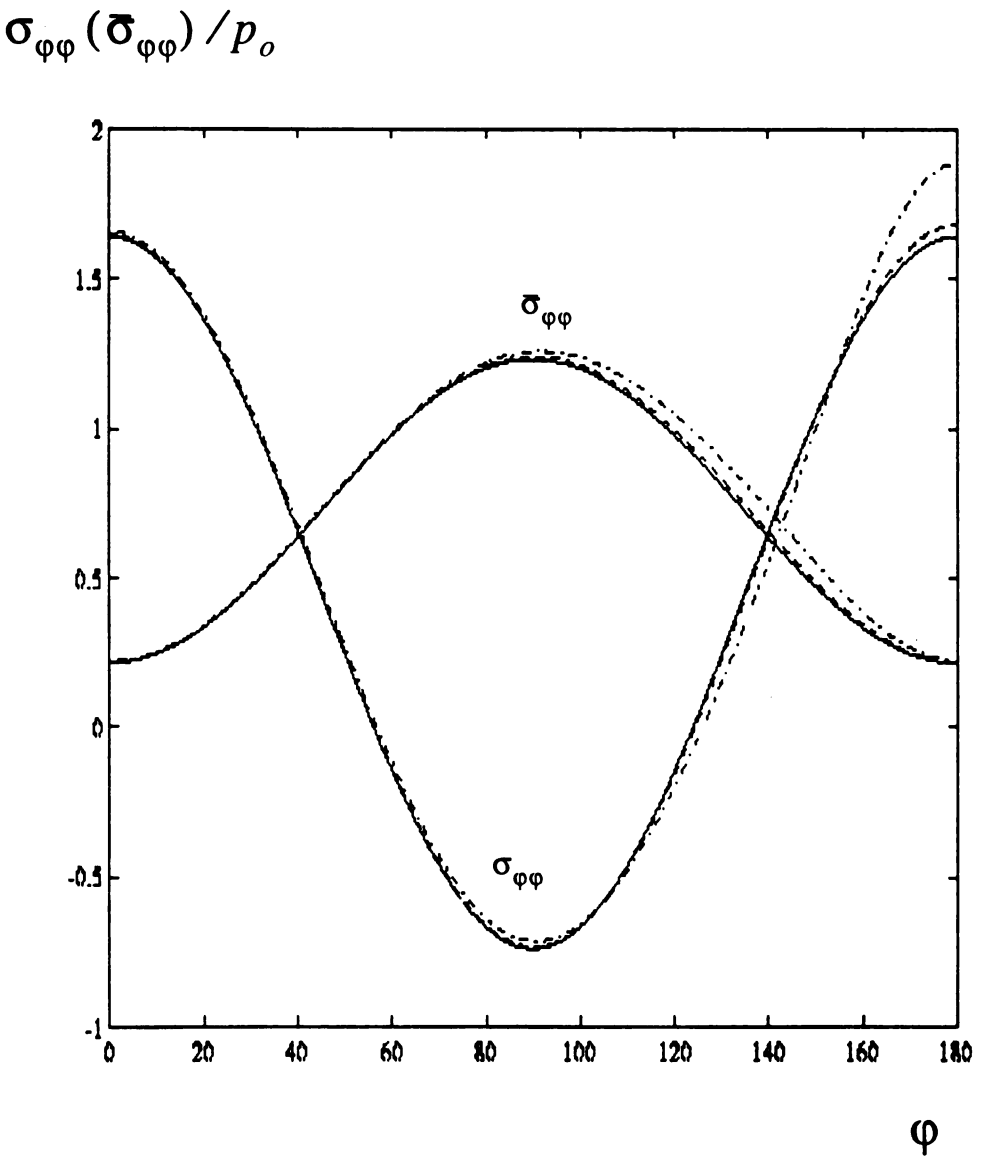

Fig. 8 Stress $\sigma_{\varphi\varphi}(\bar{\sigma}_{\varphi\varphi})$ versus angle φ for different radii a = 0.2 (solid line), 0.5 (dashed line) and 0.8 (dashdot line) when Γ = 0.5 and $\theta = 0^0$ for sliding and remote shear loading case.

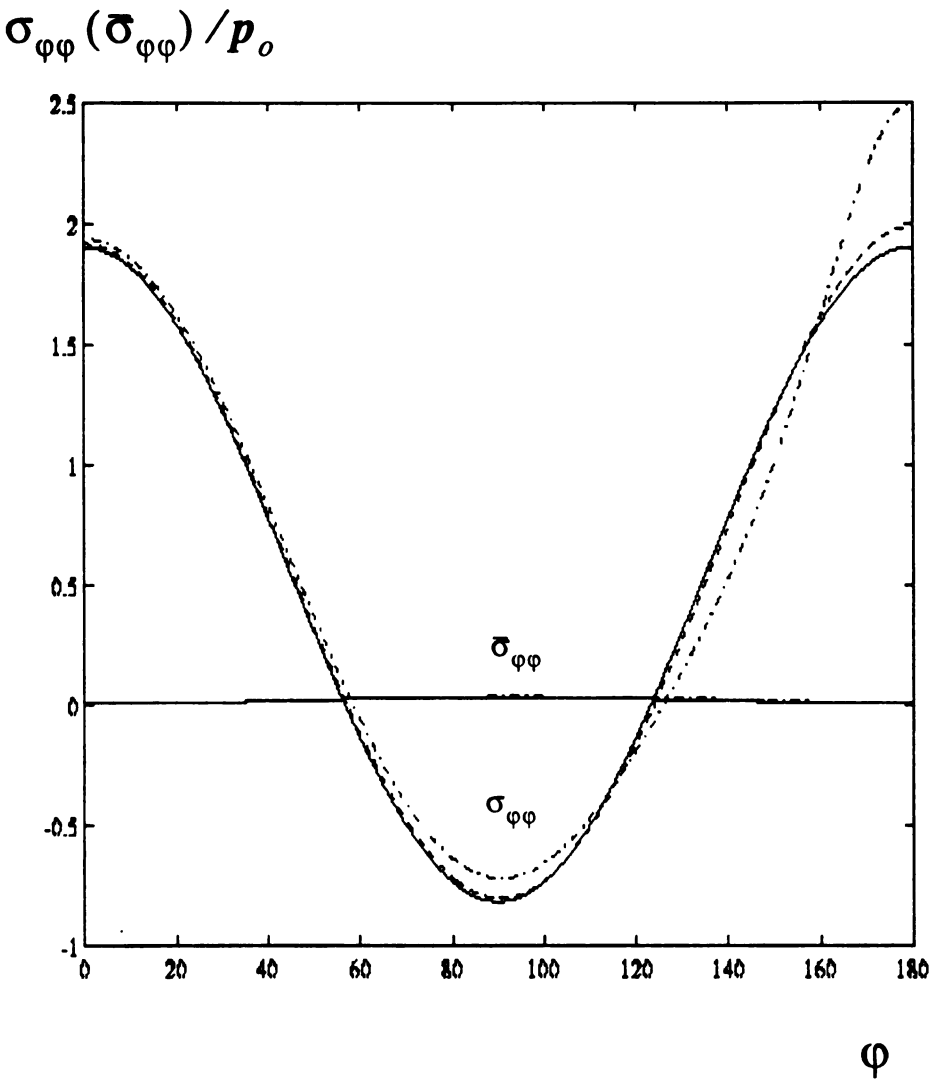

Fig. 9 Stress $\sigma_{\varphi\varphi}(\bar{\sigma}_{\varphi\varphi})$ versus angle φ for different radii a = 0.2 (solid line), 0.5 (dashed line) and 0.8 (dashdot line) when Γ = 0.01 and $\theta = 0^0$ for sliding and remote shear loading case.

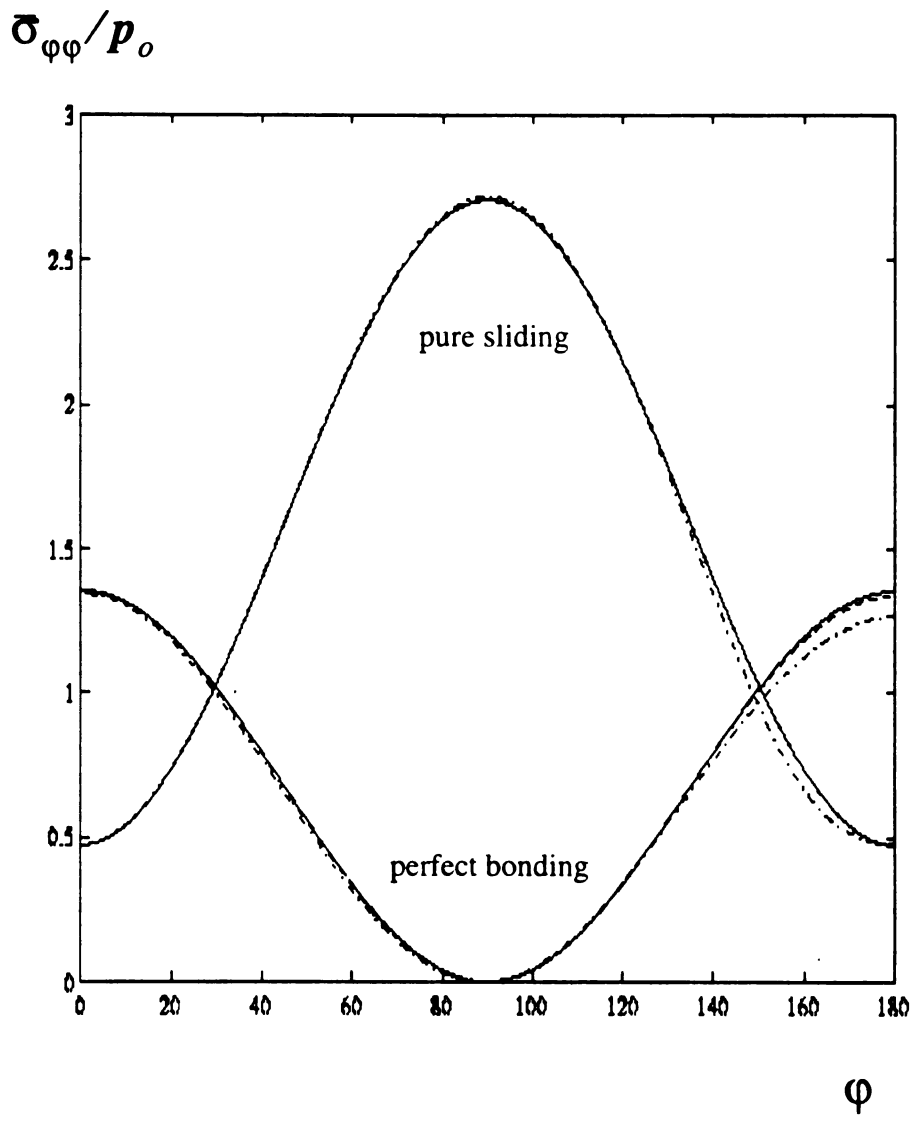

Fig.10 Stress $\bar{\sigma}_{\varphi\varphi}$ versus angle φ for perfect bonding and sliding cases when $\Gamma = 0.5$, $\theta = 0^0$ and different radii $a = 0.2$ (solid line), 0.5 (dashed line) and 0.8 (dashdot line) for remote shear loading

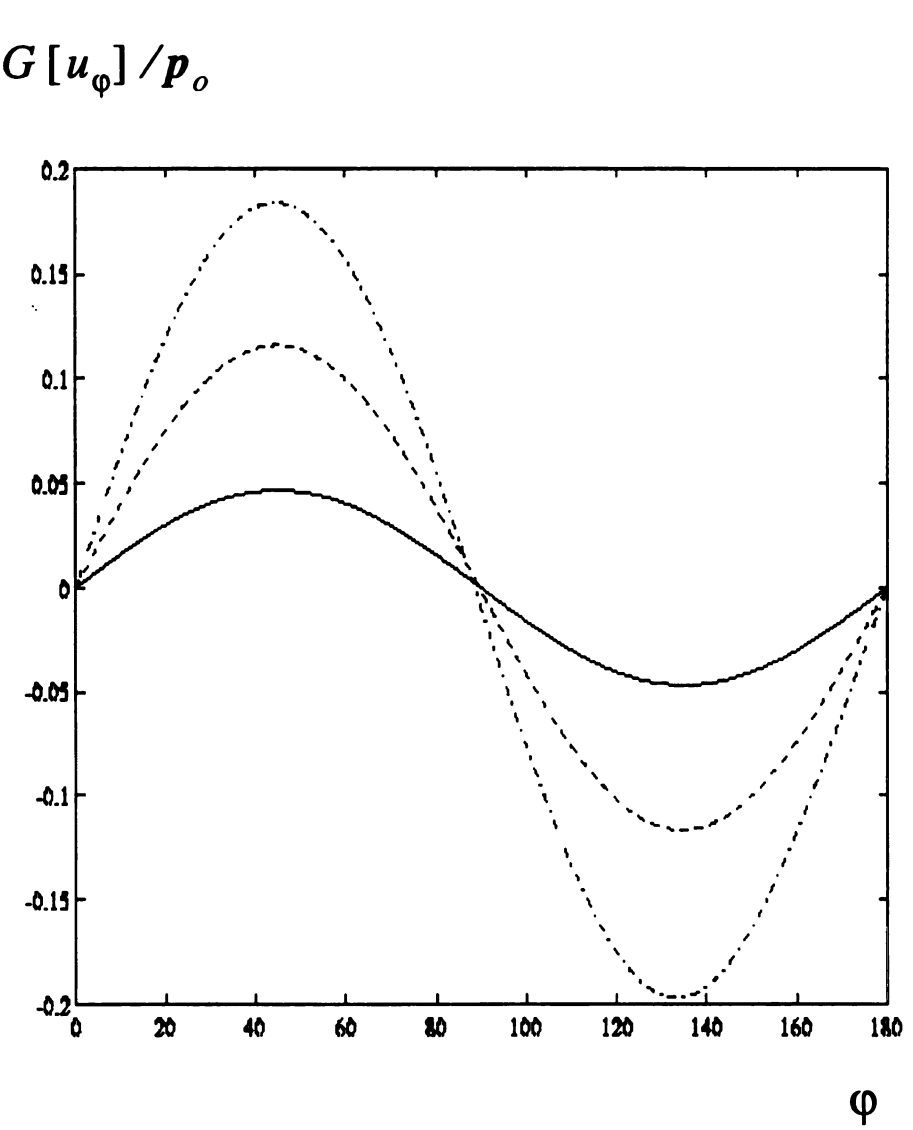

Fig.11 Jump in displacement $[u_\varphi]$ versus angle φ for different radii a = 0.2 (solid line), 0.5 (dashed line) and 0.8 (dashdot line) when Γ = 100 , $\theta = 0^0$ for pure sliding case and remote shear loading.

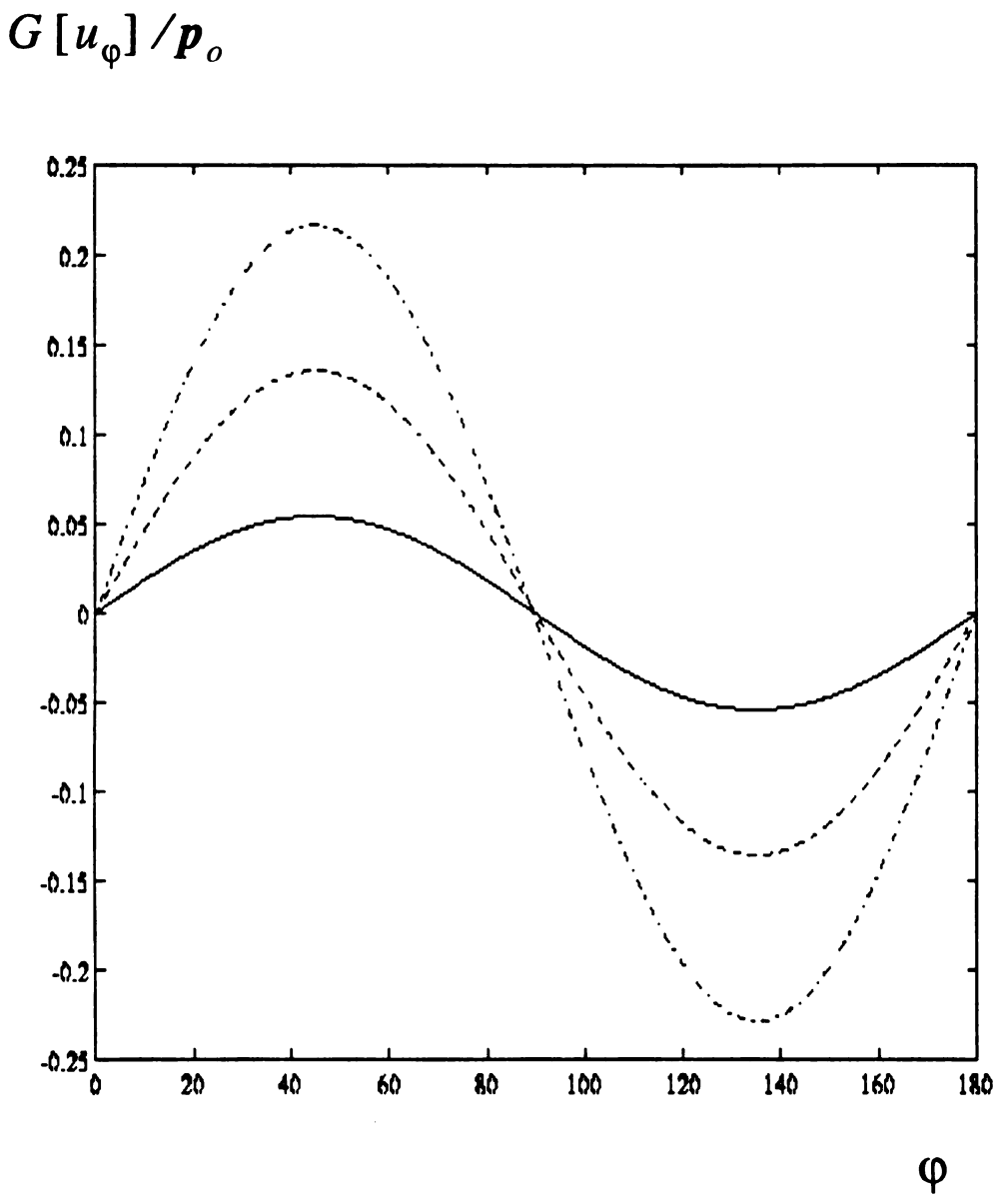

Fig.12 Jump in displacement $[u_\varphi]$ versus angle φ for different radii a = 0.2 (solid line), 0.5 (dashed line) and 0.8 (dashdot line) when $\Gamma = 2$, $\theta = 0^0$ for pure sliding case and remote shear loading.

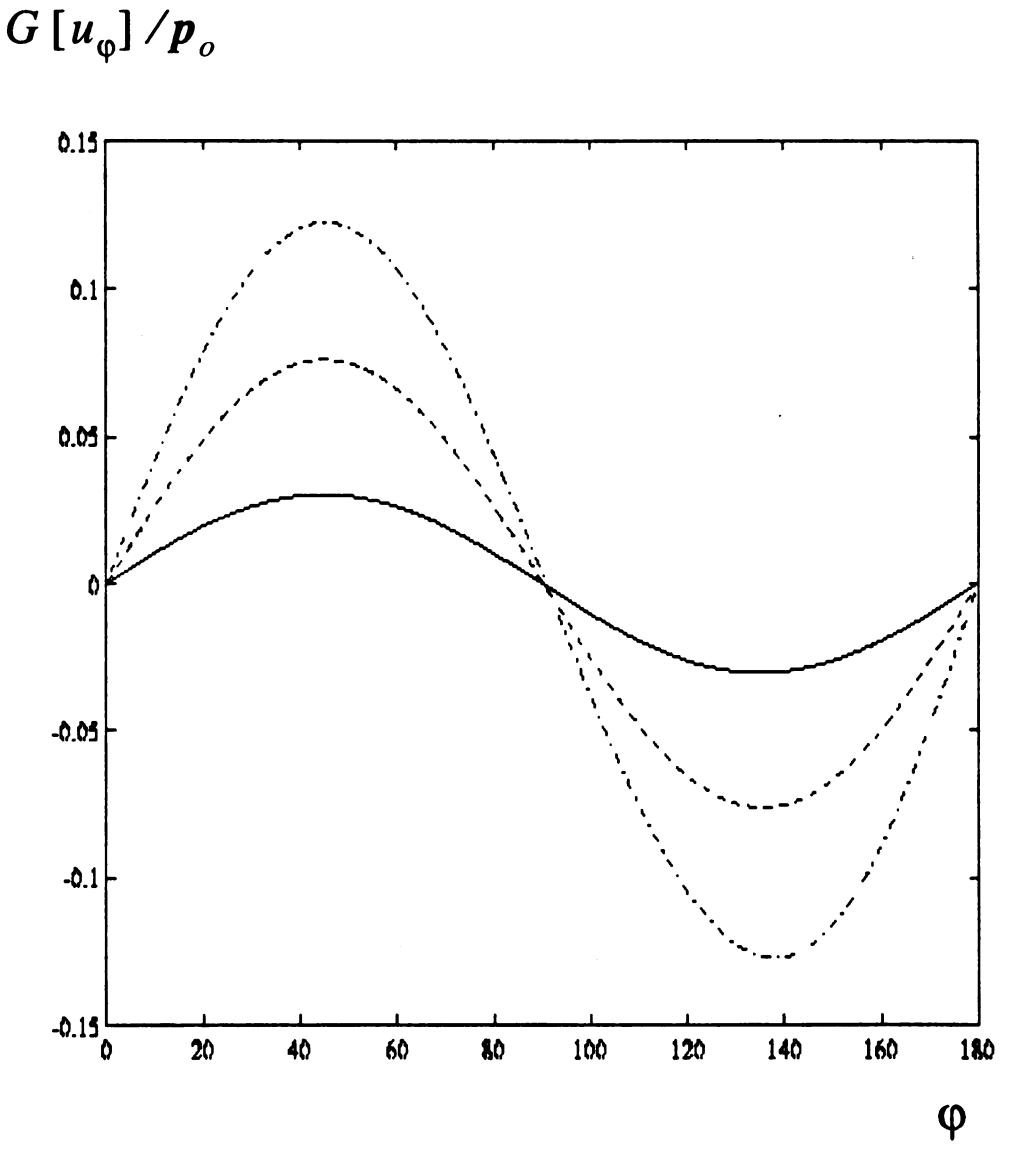

Fig.13 Jump in displacement $[u_\varphi]$ versus angle φ for different radii a = 0.2 (solid line), 0.5 (dashed line) and 0.8 (dashdot line) when Γ = 0.5 , $\theta = 0^0$ for pure sliding case and remote shear loading.

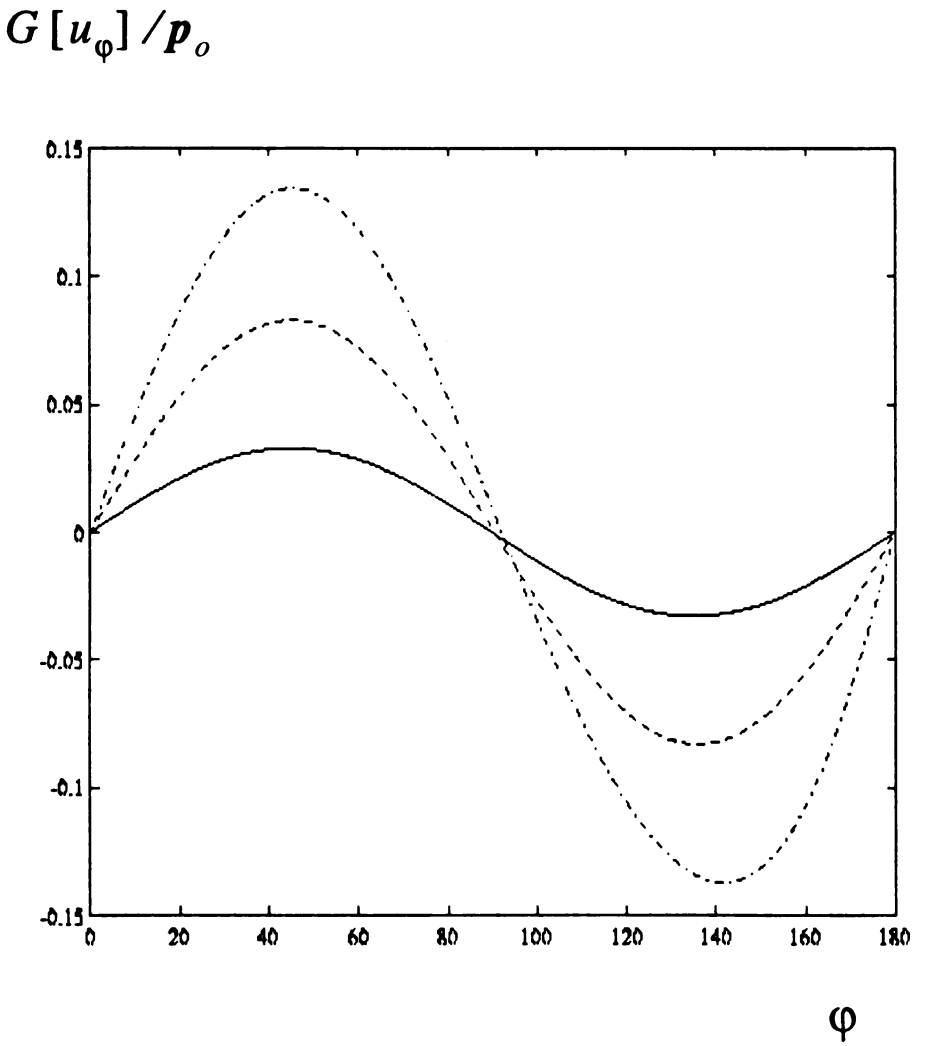

Fig.14 Jump in displacement $[u_\varphi]$ versus angle φ for different radii a = 0.2 (solid line), 0.5 (dashed line) and 0.8 (dashdot line) when Γ = 0.01 , $\theta = 0^0$ for pure sliding case and remote shear loading.

$\sigma_{xx}(\bar{\sigma}_{xx})/p_o$

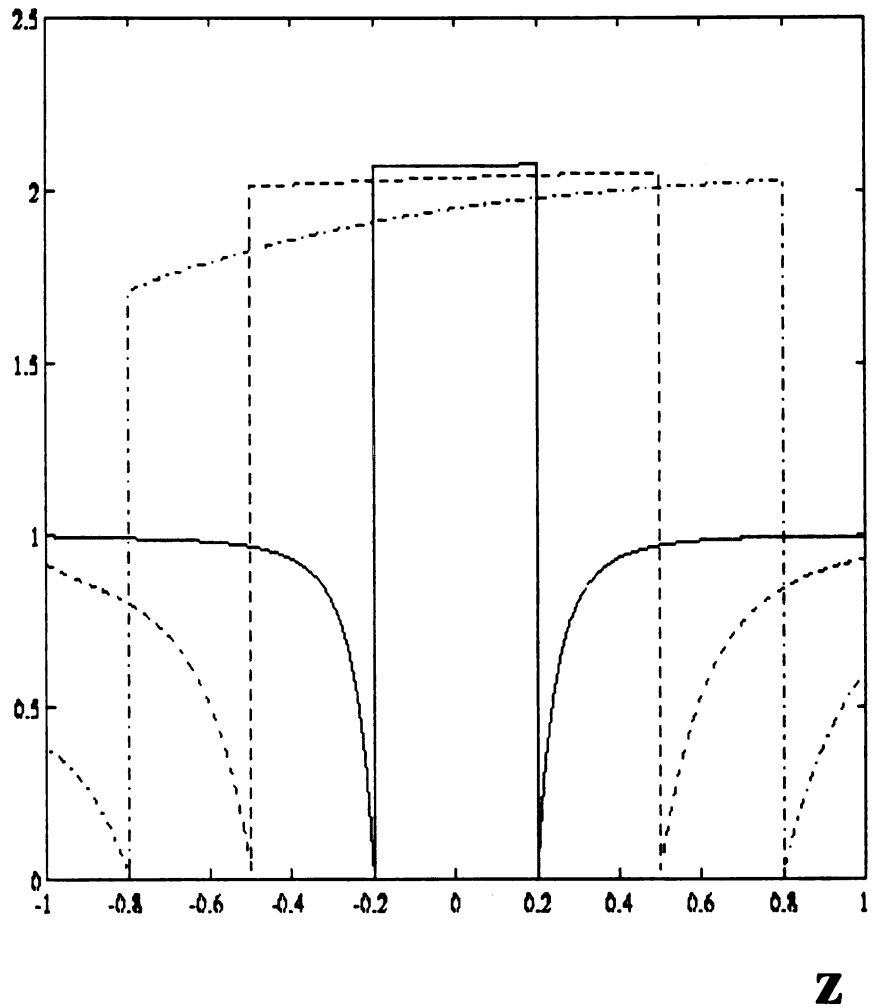

Fig.15 Stress $\sigma_{xx}(\bar{\sigma}_{xx})$ along z-axis for different radii a = 0.2 (solid line), 0.5 (dashed line) and 0.8 (dashdot line) when Γ = 100 for perfect bonding case and remote shear loading.

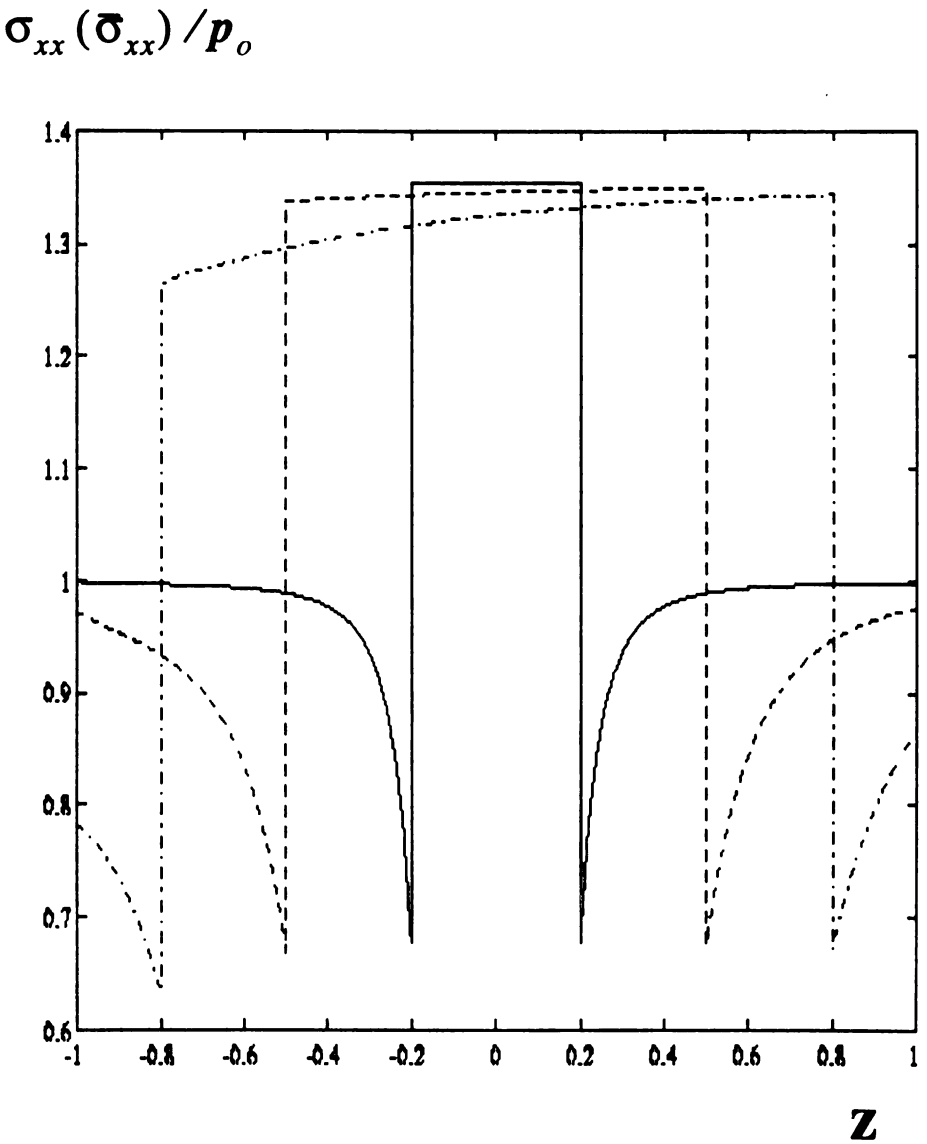

Fig.16 Stress $\sigma_{xx}(\bar{\sigma}_{xx})$ along z-axis for different radii a = 0.2 (solid line), 0.5 (dashed line) and 0.8 (dashdot line) when Γ = 2 for perfect bonding case and remote shear loading.

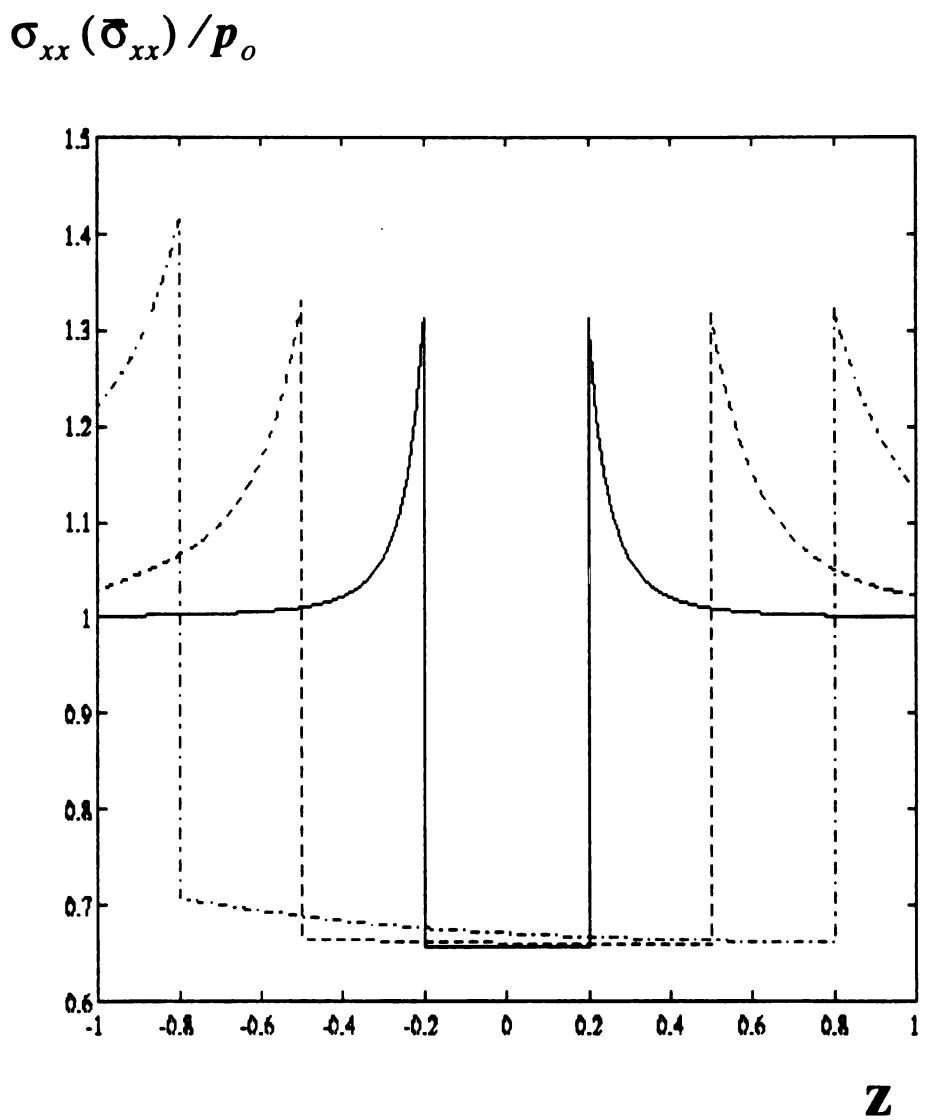

Fig.17 Stress $\sigma_{xx}(\bar{\sigma}_{xx})$ along z-axis for different radii a = 0.2 (solid line), 0.5 (dashed line) and 0.8 (dashdot line) when Γ = 0.5 for perfect bonding case and remote shear loading.

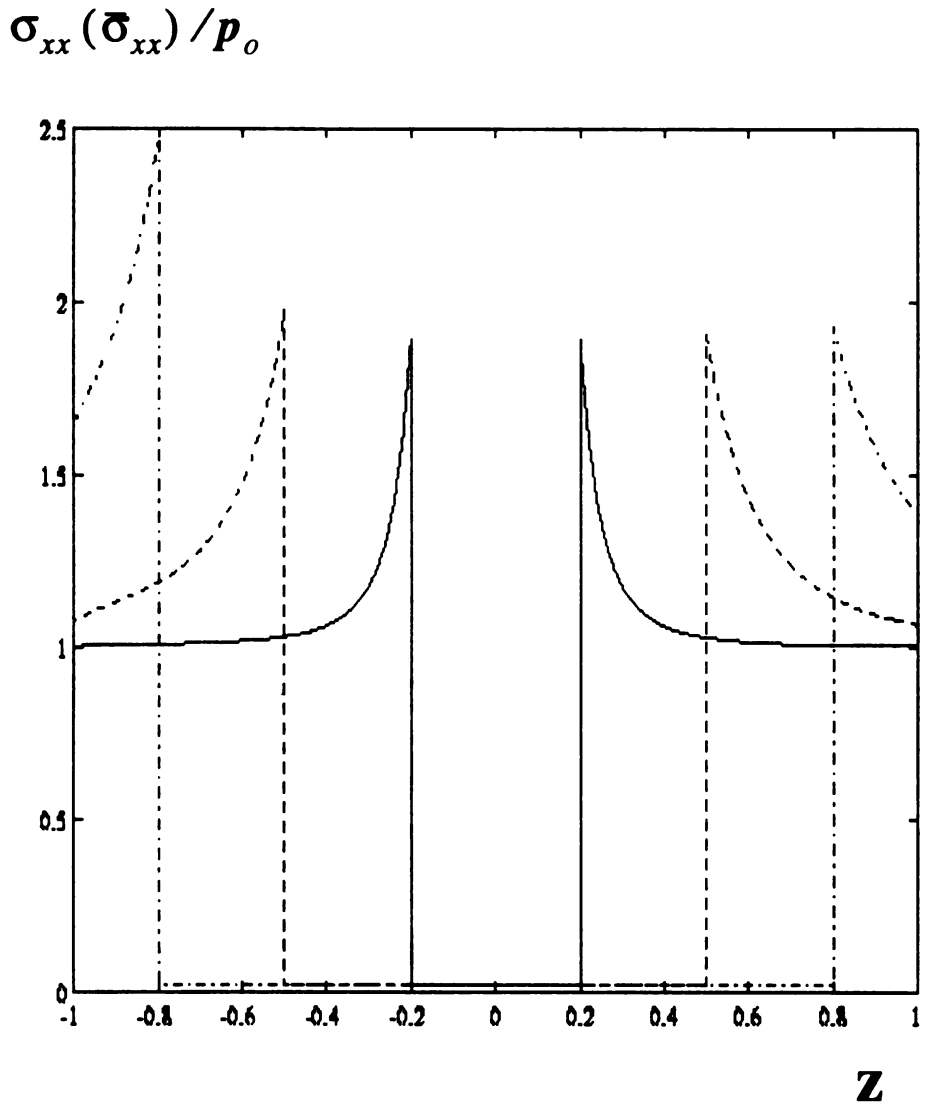

Fig.18 Stress $\sigma_{xx}(\bar{\sigma}_{xx})$ along z-axis for different radii a = 0.2 (solid line), 0.5 (dashed line) and 0.8 (dashdot line) when Γ = 0.01 for perfect bonding case and remote shear loading.

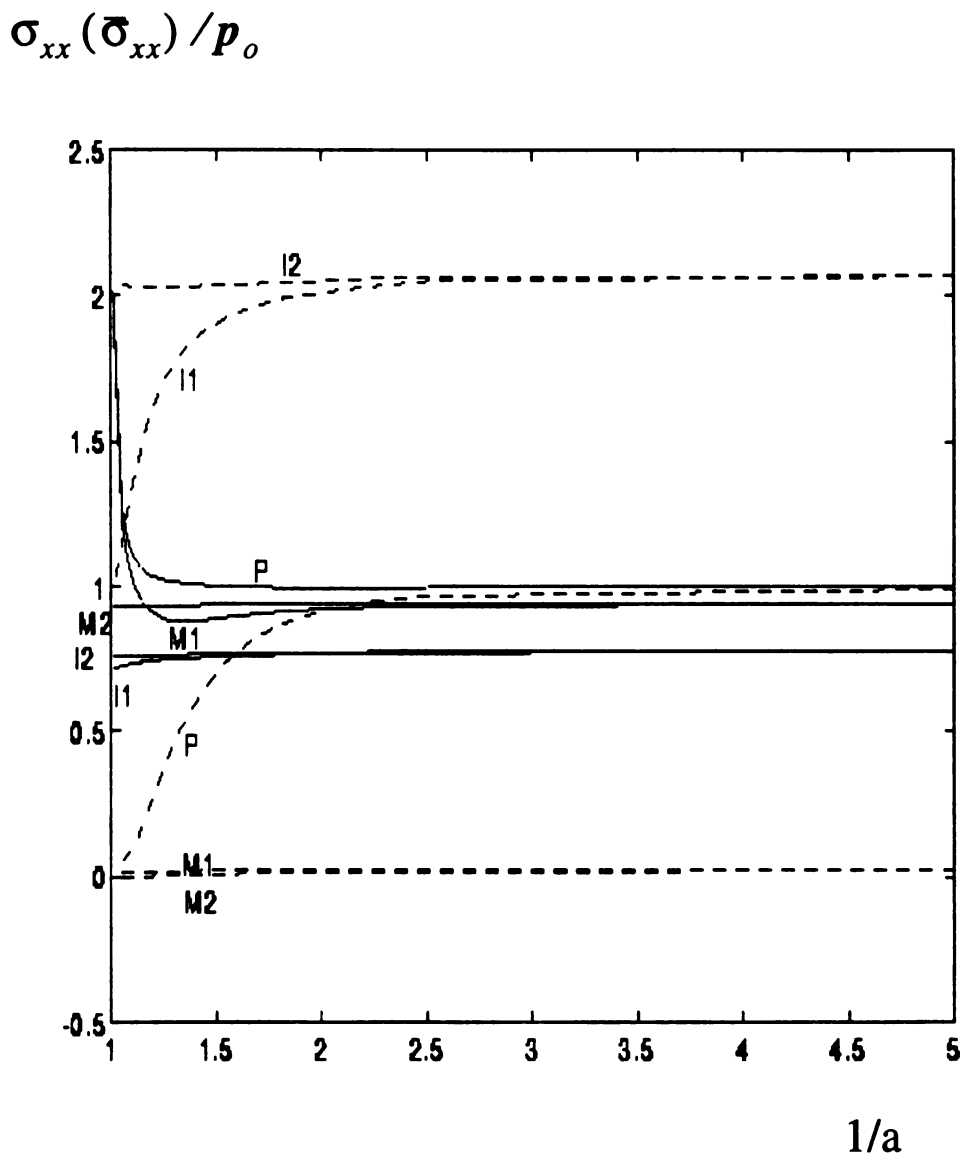

Fig.19 Stress $\sigma_{xx}(\bar{\sigma}_{xx})$ at several points along z-axis versus radius of inclusion a for both perfect bonding (dashed lines) and pure sliding (solid lines) when $\Gamma = 100$ (remote shear loading).

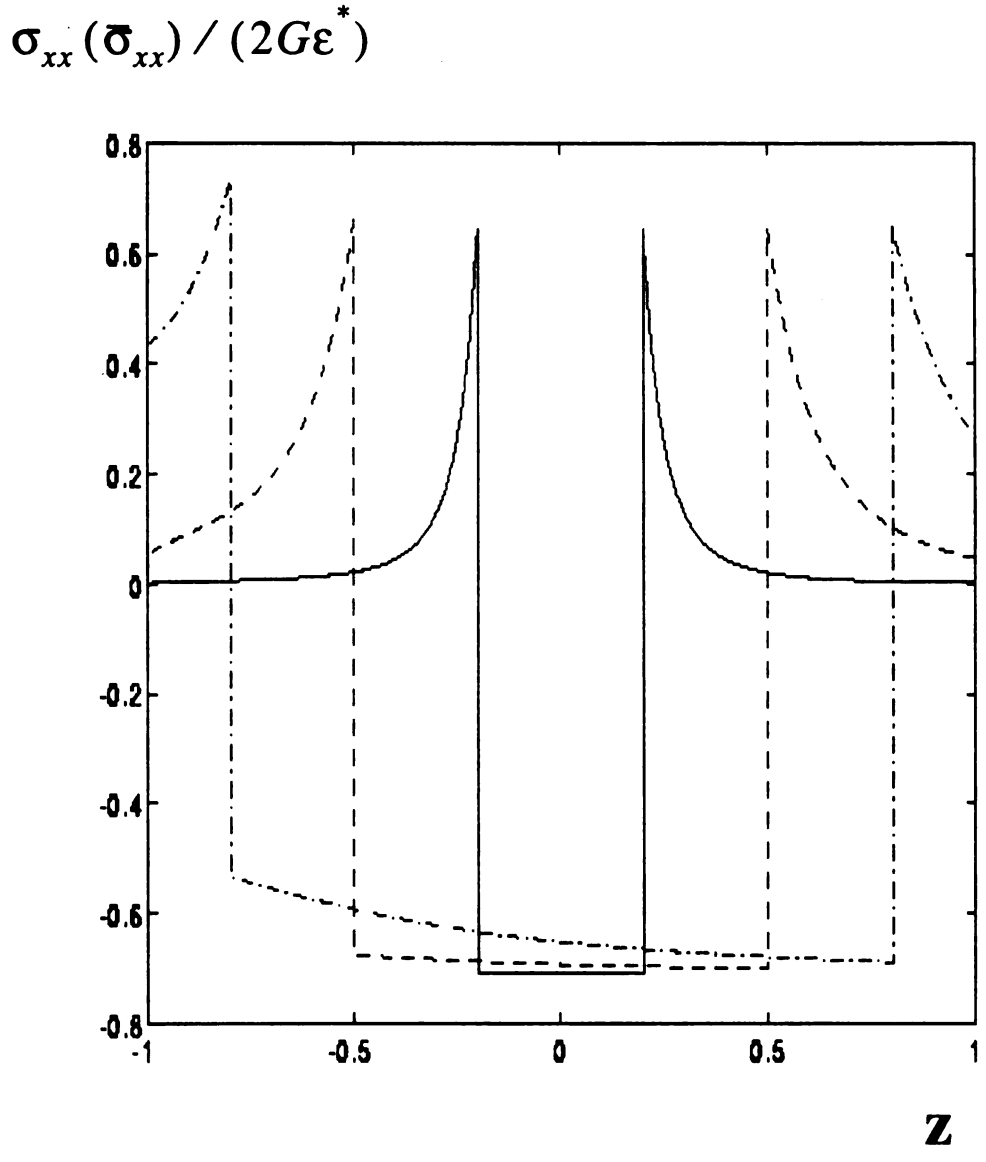

Fig.20 Stress $\sigma_{xx}(\bar{\sigma}_{xx})$ along z-axis for different radii a = 0.2 (solid line), 0.5 (dashed line) and 0.8 (dashdot line) when Γ = 100 for perfect bonding and the eigenstrain case.

REFERENCES

Atsumi, A. and Itou, S., 1974, "Stresses in a transversely isotropic half space having a spherical cavity," *ASME Journal of Applied Mechanics,* Vol. 41, pp. 708-712.

Eshelby, J.D., 1957, "The determination of the elastic field of an ellipoidal inclusion, and related problems," *Proceedings of Royal Society, London,* Series A, Vol. 241, pp. 376-396.

Ghahremani, F., 1980, "Effect of grain boundary sliding on anelasticity of polycrystals," *International Journal of Solids and Structures,* Vol. 16, pp. 825-845.

Goodier, J.N., 1933, "Concentration of stress around spherical and cylindrical inclusions and flaws," *ASME Transactions*, Vol. 55, pp. A-39-44.

Jasiuk, I., Tsuchida, E. and Mura, T., 1991, "Spheroidal sliding inclusion in an elastic half-space," *Applied Mechanics Reviews,* Vol. 44, No. 11, pp. 143-149.

Jasiuk, I., Tsuchida, E. and Mura, T., 1987, "The sliding inclusion under shear," *International Journal of Solids and Structures,* Vol. 23, No. 10, pp. 1373-1385.

Jeffery, G.B., 1920, "Plane stress and plane strain in bipolar coordinates,' *Transactions of Royal Society,* Series A, Vol. 221, pp. 265-293.

Lee, M., Jasiuk, I. and Tsuchida,E., 1992, "The sliding circular inclusion in an elastic half-plane," *ASME Journal of Applied Mechanics,*" Vol. 59, pp. S57-S64.

Mindlin, R.D., 1948, "Stress distribution around a hole near the edge of a plate under tension," *Proceedings of the Society for Experimental Stress Analysis,* Vol. 5, pp. 56-68.

Mindlin, R.D. and Cheng, D.H., 1950, "Thermoelastic stress in the semi-infinite solid, *Journal of Applied Physics*, Vol. 21, pp. 931-933.

Mura, T., 1987, *Micromechanics of Defects in Solids*, 2nd. ed. Martinus Nijhoff Publishers, Dordrecht.

Richardson, M.K., 1969, "Interference stresses in a half plane containing an elastic disk of the same material," *ASME Journal of Applied Mechanics,* Vol. 36, pp. 128-130.

Saleme, E.M., 1958, "Stress distribution around a circular inclusion in a semi-infinite elastic plate," *ASME Journal of Applied Mechanics,* Vol. 25, pp. 129-135.

Seo, K. and Mura, T., 1979, "The elastic field in a half-space due to ellipsoidal inclusions with uniform dilatational eigenstrains," *ASME Journal of Applied Mechanics*, Vol. 46, pp. 568-572.

Sheng, P.Y., 1992, *The Stress Field of a Spheroidal Sliding Inclusion under Shear*, M.S. Dissertation, Michigan State University.

Shioya, S., 1967, "On a semi-infinite thin plate with a circular inclusion under uniform

tension," *Bulletin of the JSME,* Vol. 10, pp. 1-9.

Tsuchida, E. and Mura, T., 1983, "The stress field in an elastic half space having a spheroidal inhomogeneity under all-around tension parallel to the plane boundary," *ASME Journal of Applied Mechanics*, Vol. 50, pp. 807-816.

Tsuchida, E. and I. Nakahara, I. 1970, "Three-dimensional stress concentration around a spherical cavity in a semi-infinite elastic body," *Bulletin of the JSME*, Vol.13, No.58, pp. 499-508.

Tsuchida, E. and Nakahara, I., 1972, "Stresses in a semi-infinite body subjected to uniform pressure on the surface of a cavity and the plane boundary," *Bulletin of the JSME,* Vol.15, No.79, pp. 1-10.

Tsuchida, E. and Nakahara, I., 1974, "Stress concentration around a spherical cavity in a semi-infinite body under uniaxial tension," *Bulletin of the JSME,* Vol. 17, No.112, pp.1207-1217.

Tsuchida, E, I. Nakahara, I., and M.Kodama, M., 1973, "Stresses in a semi-infinite body having a spherical cavity compressed by rigid body, " *Proceedings of the 23rd Japan National Congress for Applied Mechanics*, Vol. 23, pp. 531-546.

Tsuchida, E., Saito, Y., Nakahara, I., and Kodama, M., 1982, "Stress concentration around a prolate spheroidal cavity in a semi-infinite elastic body under all-around tension," *Bulletin of the JSME,* Vol. 25, No. 202, pp. 493-500.

Tsutsui, S. and Saito, K., 1973, "On the effect of a free surface and a spherical inhomoge-

neity on stress fields of a semi-infinite medium under axisymmetric tension," *Proceedings of the 23rd Japan National Congress for Applied Mechanics,* Vol. 23, pp. 547-560.

Wachtman, J.B. and Dundurs, J., 1971, "Large localized surface stresses caused by thermal expansion anisotropy," *Journal of the American Ceramic Society,* Vol. 54, pp. 525-526.

Yu, H.Y. and Sanday, S.C., 1990, "Axisymmetric inclusion in a half space", *ASME Journal of Applied Mechanics,* Vol. 57, pp. 74-77.

APPENDIX A

displacement and stress fields in spherical coordinates

for ϕ_0

$$2Gu_R = \frac{\partial \phi_0}{\partial R}$$

$$2Gu_\theta = \frac{1}{R\sin\varphi}\frac{\partial \phi_0}{\partial \theta}$$

$$2Gu_\varphi = \frac{1}{R}\frac{\partial \phi_0}{\partial \varphi}$$

$$\sigma_{RR} = \frac{\partial^2 \phi_0}{\partial R^2}$$

$$\sigma_{\theta\theta} = \frac{1}{R^2\sin^2\varphi}\frac{\partial^2 \phi_0}{\partial \theta^2} + \frac{1}{R}\frac{\partial \phi_0}{\partial R} + \frac{\cot\varphi}{R^2}\frac{\partial \phi_0}{\partial \varphi}$$

$$\sigma_{\varphi\varphi} = \frac{1}{R^2}\frac{\partial^2 \phi_0}{\partial \varphi^2} + \frac{1}{R}\frac{\partial \phi_0}{\partial R}$$

$$\sigma_{R\theta} = \left[\frac{1}{R}\frac{\partial^2 \phi_0}{\partial R \partial \theta} - \frac{1}{R^2}\frac{\partial \phi_0}{\partial \theta}\right]\frac{1}{\sin\varphi}$$

$$\sigma_{\theta\varphi} = \left[\frac{\partial^2 \phi_0}{\partial \theta \partial \varphi} - \cot\varphi\frac{\partial \phi_0}{\partial \theta}\right]\frac{1}{R^2\sin\varphi}$$

$$\sigma_{\varphi R} = \frac{1}{R}\frac{\partial^2 \phi_0}{\partial R \partial \varphi} - \frac{1}{R^2}\frac{\partial \phi_0}{\partial \varphi}$$

for ϕ_1

$$2Gu_R = \left[R\sin\varphi\frac{\partial\phi_1}{\partial R} - (3-4\nu)\sin\varphi\phi_1\right]\cos\theta$$

$$2Gu_\theta = \frac{\partial\phi_1}{\partial\theta}\cos\theta + (3-4\nu)\phi_1\sin\theta$$

$$2Gu_\varphi = \left[\sin\varphi\frac{\partial\phi_1}{\partial\varphi} - (3-4\nu)\cos\varphi\phi_1\right]\cos\theta$$

$$\sigma_{RR} = \frac{2\nu}{R\sin\varphi}\frac{\partial\phi_1}{\partial\theta}\sin\theta + \left[R\sin\varphi\frac{\partial^2\phi_1}{\partial R^2} - 2(1-\nu)\sin\varphi\frac{\partial\phi_1}{\partial R} - 2\nu\frac{\cos\varphi}{R}\frac{\partial\phi_1}{\partial\varphi}\right]\cos\theta$$

$$\sigma_{\theta\theta} = \frac{2(1-\nu)}{R\sin\varphi}\frac{\partial\phi_1}{\partial\theta}\sin\theta + \left[\frac{1}{R\sin\varphi}\frac{\partial^2\phi_1}{\partial\theta^2} + (1-2\nu)\sin\varphi\frac{\partial\phi_1}{\partial R} + (1-2\nu)\frac{\cos\varphi}{R}\frac{\partial\phi_1}{\partial\varphi}\right]\cos\theta$$

$$\sigma_{\varphi\varphi} = \frac{2\nu}{R\sin\varphi}\frac{\partial\phi_1}{\partial\theta}\sin\theta - \left[R\sin\varphi\frac{\partial^2\phi_1}{\partial R^2} + \frac{1}{R\sin\varphi}\frac{\partial^2\phi_1}{\partial\theta^2} + (3-2\nu)\frac{\cos\varphi}{R}\frac{\partial\phi_1}{\partial\varphi}\right.$$

$$\left. + (1+2\nu)\sin\varphi\frac{\partial\phi_1}{\partial R}\right]\cos\theta$$

$$\sigma_{R\theta} = (1-2\nu)\frac{\partial\phi_1}{\partial R}\sin\theta + \left[\frac{\partial^2\phi_1}{\partial R\partial\theta} - 2(1-\nu)\frac{1}{R}\frac{\partial\phi_1}{\partial\theta}\right]\cos\theta$$

$$\sigma_{\theta\varphi} = (1-2\nu)\frac{1}{R}\frac{\partial\phi_1}{\partial\varphi}\sin\theta + \frac{1}{R}\left[\frac{\partial^2\phi_1}{\partial\theta\partial\varphi} - 2(1-\nu)\cot\varphi\frac{\partial\phi_1}{\partial\theta}\right]\cos\theta$$

$$\sigma_{\varphi R} = \left[\sin\varphi\frac{\partial^2\phi_1}{\partial R\partial\varphi}(1-2\nu)\cos\varphi\frac{\partial\phi_1}{\partial R} - 2(1-\nu)\frac{\sin\varphi}{R}\frac{\partial\phi_1}{\partial\varphi}\right]\cos\theta$$

for ϕ_2

$$2Gu_R = \left[R\sin\varphi\frac{\partial\phi_2}{\partial R} - (3-4\nu)\sin\varphi\phi_2\right]\sin\theta$$

$$2Gu_\theta = \frac{\partial\phi_2}{\partial\theta}\sin\theta - (3-4\nu)\,\phi_2\cos\theta$$

$$2Gu_\varphi = \left[\sin\varphi\frac{\partial\phi_2}{\partial\varphi} - (3-4\nu)\cos\varphi\phi_2\right]\sin\theta$$

$$\sigma_{RR} = -\frac{2\nu}{R\sin\varphi}\frac{\partial\phi_2}{\partial\theta}\cos\theta + \left[R\sin\varphi\frac{\partial^2\phi_2}{\partial R^2} - 2(1-\nu)\sin\varphi\frac{\partial\phi_2}{\partial R} - 2\nu\frac{\cos\varphi}{R}\frac{\partial\phi_2}{\partial\varphi}\right]\sin\theta$$

$$\sigma_{\theta\theta} = -\frac{2(1-\nu)}{R\sin\varphi}\frac{\partial\phi_2}{\partial\theta}\cos\theta + \left[\frac{1}{R\sin\varphi}\frac{\partial^2\phi_2}{\partial\theta^2} + (1-2\nu)\sin\varphi\frac{\partial\phi_2}{\partial R} + (1-2\nu)\frac{\cos\varphi}{R}\frac{\partial\phi_2}{\partial\varphi}\right]\sin\theta$$

$$\sigma_{\varphi\varphi} = -\frac{2\nu}{R\sin\varphi}\frac{\partial\phi_2}{\partial\theta}\cos\theta - \left[R\sin\varphi\frac{\partial^2\phi_2}{\partial R^2} + \frac{1}{R\sin\varphi}\frac{\partial^2\phi_2}{\partial\theta^2} + (3-2\nu)\frac{\cos\varphi}{R}\frac{\partial\phi_2}{\partial\varphi}\right.$$

$$\left. + (1+2\nu)\sin\varphi\frac{\partial\phi_2}{\partial R}\right]\sin\theta$$

$$\sigma_{R\theta} = -(1-2\nu)\frac{\partial\phi_2}{\partial R}\sin\theta + \left[\frac{\partial^2\phi_2}{\partial R\partial\theta} - 2(1-\nu)\frac{1}{R}\frac{\partial\phi_2}{\partial\theta}\right]\sin\theta$$

$$\sigma_{\theta\varphi} = -(1-2\nu)\frac{1}{R}\frac{\partial\phi_2}{\partial\varphi}\sin\theta + \frac{1}{R}\left[\frac{\partial^2\phi_2}{\partial\theta\partial\varphi} - 2(1-\nu)\cot\varphi\frac{\partial\phi_2}{\partial\theta}\right]\sin\theta$$

$$\sigma_{\varphi R} = \left[\sin\varphi\frac{\partial^2\phi_2}{\partial R\partial\varphi}(1-2\nu)\cos\varphi\frac{\partial\phi_2}{\partial R} - 2(1-\nu)\frac{\sin\varphi}{R}\frac{\partial\phi_2}{\partial\varphi}\right]\sin\theta$$

for ϕ_3

$$2Gu_R = R\cos\varphi\frac{\partial\phi_3}{\partial R} - (3-4\nu)\cos\varphi\phi_3$$

$$2Gu_\theta = \cot\varphi\frac{\partial\phi_3}{\partial\theta}$$

$$2Gu_\varphi = \cos\varphi\frac{\partial\phi_3}{\partial\varphi} + (3-4\nu)\sin\varphi\phi_3$$

$$\sigma_{RR} = R\cos\varphi\frac{\partial^2\phi_3}{\partial R^2} - 2(1-\nu)\cos\varphi\frac{\partial\phi_3}{\partial R} + 2\nu\frac{\sin\varphi}{R}\frac{\partial\phi_3}{\partial\varphi}$$

$$\sigma_{\theta\theta} = (1-2\nu)\cos\varphi\frac{\partial\phi_3}{\partial R} + \frac{1}{R}\left[\frac{1}{\sin\varphi} - (1-2\nu)\sin\varphi\right]\frac{\partial\phi_3}{\partial\varphi} + \frac{1}{R}\frac{\cot\varphi}{\sin\varphi}\frac{\partial^2\phi_3}{\partial\theta^2}$$

$$\sigma_{\varphi\varphi} = (1-2\nu)\cos\varphi\frac{\partial\phi_3}{\partial R} + \frac{\cos\varphi}{R}\frac{\partial^2\phi_3}{\partial\varphi^2} + 2(1-\nu)\frac{\sin\varphi}{R}\frac{\partial\phi_3}{\partial\varphi}$$

$$\sigma_{R\theta} = \cot\varphi\frac{\partial^2\phi_3}{\partial R\partial\theta} - 2(1-\nu)\frac{\cot\varphi}{R}\frac{\partial\phi_3}{\partial\theta}$$

$$\sigma_{\theta\varphi} = \frac{\cot\varphi}{R}\frac{\partial^2\phi_3}{\partial\theta\partial\varphi} + \frac{1}{R}\left[(1-2\nu) - \cot^2\varphi\right]\frac{\partial\phi_3}{\partial\theta}$$

$$\sigma_{\varphi R} = (1-2\nu)\sin\varphi\frac{\partial\phi_3}{\partial R} + \cos\varphi\frac{\partial^2\phi_3}{\partial R\partial\varphi} - 2(1-\nu)\frac{\cos\varphi}{R}\frac{\partial\phi_3}{\partial\varphi}$$

for ϕ_4

$$2Gu_R = -\sin\varphi\frac{\partial\phi_4}{\partial\varphi} - 4(1-\nu)\cos\varphi\phi_4$$

$$2Gu_\theta = 0$$

$$2Gu_\varphi = R\sin\varphi\frac{\partial\phi_4}{\partial R} + 4(1-\nu)\sin\varphi\phi_4$$

$$\sigma_{RR} = -2(2-\nu)\cos\varphi\frac{\partial\phi_4}{\partial R} - \sin\varphi\frac{\partial^2\phi_4}{\partial R\partial\varphi} + 2\nu\frac{\sin\varphi}{R}\frac{\partial\phi_4}{\partial\varphi}$$

$$\sigma_{\theta\theta} = (1-2\nu)\left[\cos\varphi\frac{\partial\phi_4}{\partial R} - \frac{\sin\varphi}{R}\frac{\partial\phi_4}{\partial\varphi}\right]$$

$$\sigma_{\varphi\varphi} = (1-2\nu)\cos\varphi\frac{\partial\phi_4}{\partial R} + \sin\varphi\frac{\partial^2\phi_4}{\partial R\partial\varphi} + (3-2\nu)\frac{\sin\varphi}{R}\frac{\partial\phi_4}{\partial\varphi}$$

$$\sigma_{R\theta} = -\frac{1}{2}\left[\frac{1}{R}\frac{\partial^2\phi_4}{\partial\theta\partial\varphi} + 4(1-\nu)\frac{\cot\varphi}{R}\frac{\partial\phi_4}{\partial\theta}\right]$$

$$\sigma_{\theta\varphi} = \frac{1}{2}\left[\frac{\partial^2\phi_4}{\partial R\partial\theta} + 4(1-\nu)\frac{1}{R}\frac{\partial\phi_4}{\partial\theta}\right]$$

$$\sigma_{\varphi R} = \frac{1}{2}\left[R\sin\varphi\frac{\partial^2\phi_4}{\partial R^2} + 4(1-\nu)\sin\varphi\frac{\partial\phi_4}{\partial R} - \frac{\sin\varphi}{R}\frac{\partial^2\phi_4}{\partial\varphi^2} - (5-4\nu)\frac{\cos\varphi}{R}\frac{\partial\phi_4}{\partial\varphi}\right]$$

for λ_3

$$2Gu_R = \frac{2}{R}\frac{\partial \lambda_3}{\partial \theta}$$

$$2Gu_\theta = -2\left[\sin\varphi\frac{\partial \lambda_3}{\partial R} + \frac{\cos\varphi}{R}\frac{\partial \lambda_3}{\partial \varphi}\right]$$

$$2Gu_\varphi = \frac{2}{R}\cot\varphi\frac{\partial \lambda_3}{\partial \theta}$$

$$\sigma_{RR} = 2\left[\frac{1}{R}\frac{\partial^2 \lambda_3}{\partial R\partial\theta} - \frac{1}{R^2}\frac{\partial \lambda_3}{\partial \theta}\right]$$

$$\sigma_{\theta\theta} = -2\left[\frac{1}{R}\frac{\partial^2 \lambda_3}{\partial R\partial\theta} + \frac{\cot\varphi}{R^2}\frac{\partial^2 \lambda_3}{\partial\theta\partial\varphi} - \frac{1}{R^2\sin^2\varphi}\frac{\partial \lambda_3}{\partial \theta}\right]$$

$$\sigma_{\varphi\varphi} = 2\left[\frac{\cot\varphi}{R^2}\frac{\partial^2 \lambda_3}{\partial\theta\partial\varphi} - \frac{\cot^2\varphi}{R^2}\frac{\partial \lambda_3}{\partial \theta}\right]$$

$$\sigma_{R\theta} = \sin\varphi\left[-\frac{\partial^2 \lambda_3}{\partial R^2} + \frac{1}{R}\frac{\partial \lambda_3}{\partial R} - \frac{\cot\varphi}{R}\frac{\partial^2 \lambda_3}{\partial R\partial\varphi} + \frac{2\cot\varphi}{R^2}\frac{\partial \lambda_3}{\partial \varphi} + \frac{1}{R^2\sin^2\varphi}\frac{\partial^2 \lambda_3}{\partial\theta^2}\right]$$

$$\sigma_{\theta\varphi} = \cos\varphi\frac{\partial^2 \lambda_3}{\partial R^2} + \frac{2\cot\varphi}{R}\frac{\partial \lambda_3}{\partial \varphi} - \frac{\sin\varphi}{R}\frac{\partial^2 \lambda_3}{\partial R\partial\varphi} + \frac{(2-\sin^2\varphi)}{R^2\sin\varphi}\frac{\partial \lambda_3}{\partial \varphi} + \frac{2\cot\varphi}{R^2\sin^2\varphi}\frac{\partial^2 \lambda_3}{\partial\theta^2}$$

$$\sigma_{\varphi R} = \frac{\cot\varphi}{R}\frac{\partial^2 \lambda_3}{\partial R\partial\theta} + \frac{1}{R^2}\frac{\partial^2 \lambda_3}{\partial\theta\partial\varphi} - \frac{2\cot\varphi}{R^2}\frac{\partial \lambda_3}{\partial \theta}$$

APPENDIX B

displacement and stress fields in cylindrical coordinates

for ϕ_0

$$2Gu_r = \frac{\partial \phi_0}{\partial r}$$

$$2Gu_\theta = \frac{1}{r}\frac{\partial \phi_0}{\partial \theta}$$

$$2Gu_z = \frac{\partial \phi_0}{\partial z}$$

$$\sigma_{rr} = \frac{\partial^2 \phi_0}{\partial r^2}$$

$$\sigma_{\theta\theta} = \frac{1}{r}\frac{\partial \phi_0}{\partial r} + \frac{1}{r^2}\frac{\partial^2 \phi}{\partial \theta^2}$$

$$\sigma_{zz} = \frac{\partial^2 \phi_0}{\partial z^2}$$

$$\sigma_{r\theta} = \frac{1}{r}\frac{\partial^2 \phi_0}{\partial r \partial \theta} - \frac{1}{r^2}\frac{\partial \phi_0}{\partial \theta}$$

$$\sigma_{\theta z} = \frac{1}{r}\frac{\partial^2 \phi}{\partial \theta \partial z}$$

$$\sigma_{zr} = \frac{\partial^2 \phi_0}{\partial r \partial z}$$

for ϕ_1

$$2Gu_r = \left[r\frac{\partial \phi_1}{\partial r} - (3-4\nu)\,\phi_1 \right] \cos\theta$$

$$2Gu_\theta = \frac{\partial \phi_1}{\partial \theta} \cos\theta + (3-4\nu)\,\phi_1 \sin\theta$$

$$2Gu_z = \left[r\frac{\partial \phi_1}{\partial z} \right] \cos\theta$$

$$\sigma_{zz} = \frac{2\nu}{r}\frac{\partial \phi_1}{\partial \theta} \sin\theta + \left[r\frac{\partial^2 \phi_1}{\partial z^2} - 2\nu\frac{\partial \phi_1}{\partial r} \right] \cos\theta$$

$$\sigma_{\theta\theta} = \frac{2(1-\nu)}{r}\frac{\partial \phi_1}{\partial \theta} \sin\theta + \left[\frac{1}{r}\frac{\partial^2 \phi_1}{\partial \theta^2} + (1-2\nu)\frac{\partial \phi_1}{\partial r} \right] \cos\theta$$

$$\sigma_{rr} = \frac{2\nu}{r}\frac{\partial \phi_1}{\partial \theta} \sin\theta - \left[r\frac{\partial^2 \phi_1}{\partial z^2} + \frac{1}{r}\frac{\partial^2 \phi_1}{\partial \theta^2} + (3-2\nu)\frac{\partial \phi_1}{\partial r} \right] \cos\theta$$

$$\sigma_{r\theta} = (1-2\nu)\frac{\partial \phi_1}{\partial r} \sin\theta + \left[\frac{\partial^2 \phi_1}{\partial r \partial \theta} - 2(1-\nu)\frac{1}{r}\frac{\partial \phi_1}{\partial \theta} \right] \cos\theta$$

$$\sigma_{\theta z} = (1-2\nu)\frac{\partial \phi_1}{\partial z} \sin\theta + \frac{\partial^2 \phi_1}{\partial \theta \partial z} \cos\theta$$

$$\sigma_{zr} = \left[r\frac{\partial^2 \phi_1}{\partial r \partial z} - (1-2\nu)\frac{\partial \phi_1}{\partial z} \right] \cos\theta$$

for ϕ_2

$$2Gu_r = \left[r\frac{\partial \phi_2}{\partial r} - (3-4\nu)\,\phi_2 \right] \sin\theta$$

$$2Gu_\theta = \frac{\partial \phi_2}{\partial \theta} \sin\theta - (3-4\nu)\,\phi_2 \cos\theta$$

$$2Gu_z = r\frac{\partial \phi_2}{\partial z} \sin\theta$$

$$\sigma_{zz} = -\frac{2\nu}{r}\frac{\partial \phi_2}{\partial \theta}\cos\theta + \left[r\frac{\partial^2 \phi_2}{\partial z^2} - 2\nu\frac{\partial \phi_2}{\partial r} \right] \sin\theta$$

$$\sigma_{\theta\theta} = -\frac{2(1-\nu)}{r}\frac{\partial \phi_2}{\partial \theta}\cos\theta + \left[\frac{1}{r}\frac{\partial^2 \phi_2}{\partial \theta^2} + (1-2\nu)\frac{\partial \phi_2}{\partial r} \right] \sin\theta$$

$$\sigma_{rr} = -\frac{2\nu}{r}\frac{\partial \phi_2}{\partial \theta}\cos\theta - \left[r\frac{\partial^2 \phi_2}{\partial z^2} + \frac{1}{r}\frac{\partial^2 \phi_2}{\partial \theta^2} + (3-2\nu)\frac{\partial \phi_2}{\partial r} \right] \cos\theta$$

$$\sigma_{r\theta} = -(1-2\nu)\frac{\partial \phi_2}{\partial r}\cos\theta + \left[\frac{\partial^2 \phi_2}{\partial r \partial \theta} - 2(1-\nu)\frac{1}{r}\frac{\partial \phi_2}{\partial \theta} \right] \sin\theta$$

$$\sigma_{\theta z} = -(1-2\nu)\frac{\partial \phi_2}{\partial z}\cos\theta + \frac{\partial^2 \phi_2}{\partial \theta \partial z}\sin\theta$$

$$\sigma_{zr} = \left[\frac{\partial^2 \phi_2}{\partial r \partial z} - (1-2\nu)\frac{\partial \phi_2}{\partial z} \right] \sin\theta$$

for ϕ_3

$$2Gu_r = z\frac{\partial \phi_3}{\partial r}$$

$$2Gu_\theta = \frac{z}{r}\frac{\partial \phi_3}{\partial \theta}$$

$$2Gu_z = z\frac{\partial \phi_3}{\partial z} - (3-4\nu)\,\phi_3$$

$$\sigma_{rr} = z\frac{\partial^2 \phi_3}{\partial r^2} - 2\nu\frac{\partial \phi_3}{\partial z}$$

$$\sigma_{\theta\theta} = -2\nu\cos\varphi\frac{\partial \phi_3}{\partial z} + \frac{z}{r}\frac{\partial \phi_3}{\partial r} + \frac{z}{r^2}\frac{\partial^2 \phi_3}{\partial \theta^2}$$

$$\sigma_{zz} = z\frac{\partial^2 \phi_3}{\partial z^2} - 2(1-\nu)\frac{\partial \phi_3}{\partial z}$$

$$\sigma_{r\theta} = \frac{z}{r}\frac{\partial^2 \phi_3}{\partial r \partial \theta} - \frac{z}{r^2}\frac{\partial \phi_3}{\partial \theta}$$

$$\sigma_{\theta z} = \frac{z}{r}\frac{\partial^2 \phi_3}{\partial \theta \partial z} - (1-2\nu)\frac{1}{r}\frac{\partial \phi_3}{\partial \theta}$$

$$\sigma_{zr} = z\frac{\partial^2 \phi_3}{\partial r \partial z} - (1-2\nu)\frac{\partial \phi_3}{\partial r}$$

for ϕ_4

$$2Gu_r = r\frac{\partial \phi_4}{\partial z}$$

$$2Gu_\theta = 0$$

$$2Gu_\varphi = -r\frac{\partial \phi_4}{\partial r} - 4(1-\nu)\phi_4$$

$$\sigma_{rr} = r\frac{\partial^2 \phi_4}{\partial r \partial z} + (1-2\nu)\frac{\partial \phi_4}{\partial z}$$

$$\sigma_{\theta\theta} = (1-2\nu)\frac{\partial \phi_4}{\partial z}$$

$$\sigma_{zz} = -r\frac{\partial^2 \phi_4}{\partial r \partial z} - 2(2-\nu)\frac{\partial \phi_4}{\partial z}$$

$$\sigma_{r\theta} = \frac{1}{2}\frac{\partial^2 \phi_4}{\partial \theta \partial z}$$

$$\sigma_{\theta z} = -\frac{1}{2}\left[\frac{\partial^2 \phi_4}{\partial r \partial \theta} - 2(1-\nu)\frac{1}{r}\frac{\partial \phi_4}{\partial \theta}\right]$$

$$\sigma_{zr} = \frac{1}{2r}\frac{\partial^2 \phi_4}{\partial \theta^2} + r\frac{\partial^2 \phi_4}{\partial z^2} - 2(1-\nu)\frac{\partial \phi_4}{\partial r}$$

for λ_3

$$2Gu_r = \frac{2}{r}\frac{\partial \lambda_3}{\partial \theta}$$

$$2Gu_\theta = -2\frac{\partial \lambda_3}{\partial r}$$

$$2Gu_z = 0$$

$$\sigma_{rr} = 2\left[\frac{1}{r}\frac{\partial^2 \lambda_3}{\partial r \partial \theta} - \frac{1}{r^2}\frac{\partial \lambda_3}{\partial \theta}\right]$$

$$\sigma_{\theta\theta} = -2\left[\frac{1}{r}\frac{\partial^2 \lambda_3}{\partial r \partial \theta} - \frac{1}{r^2}\frac{\partial \lambda_3}{\partial \theta}\right]$$

$$\sigma_{zz} = 0$$

$$\sigma_{r\theta} = \frac{\partial^2 \lambda_3}{\partial z^2} + \frac{2}{r}\frac{\partial \lambda_3}{\partial r} + \frac{2}{r^2}\frac{\partial^2 \lambda_3}{\partial \theta^2}$$

$$\sigma_{\theta z} = \frac{\partial^2 \lambda_3}{\partial r \partial z}$$

$$\sigma_{zr} = \frac{1}{r}\frac{\partial^2 \lambda_3}{\partial \theta \partial z}$$

APPENDIX C

definitions of Legendre's function and recursion formulas

$$P_n(x) = \frac{1}{2^n n! dx^n}\left(x^2 - 1\right)^n$$

$$P_n^m(x) = (1-x^2)^{m/2}\frac{d^m}{dx^m}P_n(x)$$

$$P_n^m(x) = \frac{1}{(2n+1)x}\left[(n-m+1)P_{n+1}^m(x) + (n+m)P_{n-1}^m(x)\right]$$

$$P_{n+1}^m(x) = \frac{1}{n-m+1}\left[(2n+1)xP_n^m(x) - (n+m)P_{n-1}^m(x)\right]$$

$$\frac{d}{dx}P_n^m(x) = \frac{1}{\left(1-x^2\right)}\left[(n+1)xP_n^m(x) - (n-m+1)P_{n+1}^m(x)\right]$$

$$\frac{d^2}{dx^2}P_n^m(x) = \frac{1}{\left(1-x^2\right)}\left[\left(2x\frac{d}{dx}\right)P_n^m(x) - \left\{n(n+1) - \frac{m^2}{1-x^2}\right\}P_n^m(x)\right]$$

$$\left(1-x^2\right)^{1/2}P_n^{m-1}(x) = \frac{1}{2n+1}\left[P_{n+1}^m(x) - P_{n-1}^m(x)\right]$$

$$\left(1-x^2\right)^{1/2}P_n^{m-1}(x) = \frac{1}{n-m+1}\left[xP_n^m(x) - P_{n-1}^m(x)\right]$$

$$\left(1-x^2\right)^{1/2}P_n^{m-1}(x) = \frac{1}{n+m}\left[P_{n+1}^m(x) - xP_n^m(x)\right]$$

$$\left(1-x^2\right)\frac{d}{dx}P_n^m(x) = (1-x^2)^{1/2}P_n^{m+1}(x) - mxP_n^m(x)$$

CHAPTER 2

EFFECTIVE PROPERTIES AND DAMAGE FORMATION IN RANDOM COMPOSITE MATERIALS: A COMPUTATIONAL APPROACH

1. INTRODUCTION

Industrial applications of composite materials are constantly growing, necessitating an improved understanding of their thermomechanical response. The heterogeneous nature of composites indicates that their mechanical properties have to be understood basically at the microscopic level - this is the task of micromechanics.

Most research conducted in micromechanics concerns the local fields and effective properties of composites and is based on the simplest case: a single inclusion problem. Some analytical solutions were obtained. The early research involving heterogeneous materials can be found from the classical textbooks of elasticity where some simple inclusion problems, especially the hole problem are mentioned. For example, one of them written by Muskhelishvili (1953) shows the solution of the plane problem containing a circular inclusion under several loadings. A famous paper dealing with a single inclusion is due to Eshelby (1957), who found that the stresses in an ellipsoidal and perfectly bonded inclusion are uniform under a constant loading.

It is obvious that even for a single inclusion case, the micromechanics problem is very complex. There is a large number of factors which influence the local and global fields. These include the material constants of the constituents, the shape and relative size of reinforcement (inclusion), the geometric arrangement, the boundary condition at the inclusion-matrix interfaces, and others. As a result, only a few analytical solutions have been obtained for some simpler cases.

Composites containing many inclusions, usually distributed in an irregular fashion, pose great challenges making those analytical solutions practically impossible. For this case, many theories or methods, such as generalized self-consistent scheme, self-consistent scheme, differential scheme and Mori-Tanaka method are presented to predict approximate effective elastic properties of composites, based on the fundamental solution of a single inclusion. Generally, these methods give effective properties as a function of the properties of each phase and the volume fractions of phases, and are applicable to relatively simple condition, such as two phases and perfectly bonded interfaces, although some solutions dealing with more than two phases have been reported. Comprehensive reviews of literature in micromechanics are given by Christensen (1979), Hashin (1983), Mura (1982).

Although the above mentioned methods show quite good approximation of effective elastic moduli of composites, solving for the local fields, and hence, the strength and damage characteristics still poses a challenge. Here, we take note of two approximation concepts - the periodic assumption of structure in composite materials and the numerical solution for a discrete model of composites. First, geometric distribution of fibers (inclusions) in the composites is often approximated by assuming a periodic arrangement. This simplifies significantly the complicated problem and enables one to solve for the local and effective fields by considering a unit cell. Regarding the numerical calculation, one choice, of course, would be the finite element method which is powerful and can handle arbitrary geometry and properties of constituents. However there is another algorithm,

involving a so-called spring network, which is simpler and more efficient with regard to time and expense in calculation.

The lattice algorithm is based on the idea introduced by Kirkwood (1939) and Keating (1966) for the long wave method whereby the force on an atom is calculated in terms of two nearest neighbor force constants α and β (central and noncentral, or stretching and bending force, respectively) and atomic displacements. The relation between the force constants and the elastic coefficients is obtained by comparing the potential energy at macroscopic level and microscopic level. When the method is translated from physics to micromechanics, the force constants in the former become stiffnesses of springs in a spring-network, which is a discrete representation of the original continuum model. The spring network model of composites can have a topology of triangle, square, honeycomb, and other lattices. The algorithm is actually equivalent to a finite difference method.

More and more, the lattice algorithm has been used for composite mechanics because of the advancing computer technology. In most cases the triangular lattice was used; Snyder, Garboczi and Day (1992), and Day et al. (1992) worked on effective elastic response; Chen and Thorpe (1992) compared the elastic moduli of glass/epoxy fiber reinforced composites with the second and third order bonds; Sahimi and Goddard (1986), and Beale and Srolovitz (1988) investigated elastic fracture in randomly inhomogeneous materials; Chan et al. (1992), using honeycomb lattice, gave the elastic moduli and tensile fracture stress as a function of the number of removed bonds in the network (randomly distributed defects in materials).

It is interesting to note that Holnicki-Szulc and Rogula (1979) used this idea inversely, i.e., to simulate a discrete engineering structure with a continuum model. In this way, they simplified the analysis of mechanics of a truss structure.

There are many other references in the literature taking advantage of the lattice network. However, to our knowledge, no study has been conducted on the local fields and

the damage initiation and propagation in composites with randomly distributed inclusions.

In this second part of the thesis, we study the effect of random geometry in composites on their effective properties and damage by using the above mentioned lattice algorithm. The relation between elastic moduli of continuous material model and stiffness of springs in the corresponding discrete model is derived in details in terms of tensors. This is done for both two-dimensional elasticity and conductivity. Then, problems involving effective two-dimensional conductivity (equivalent to the out-of-plane elasticity) of composite materials with either randomly or periodically distributed inclusion are solved and the results compared with Hashin's bounds on these properties. Finally, we study the initiation and propagation of microdamage, which are simulated by breaking springs (bonds) according to local stress concentrations in the spring network modelling the composite material. The main focus is on the effects of random geometry on damage formation in composite materials; this will be studied for various parameters of constituents, such as elastic moduli and fracture criteria, different system size and different random configurations of composites.

2. COMPOSITE MICROSTRUCTURE AND THE MESO-CONTINUUM MODELS

2.1 THE RANDOM COMPOSITE MODEL

By a random composite we understand a set $\boldsymbol{B} = \{\mathbf{B}(\omega);\ \omega \in \Omega\}$ of deterministic media $\mathbf{B}(\omega)$, where ω indicates one specimen (realization), and Ω is an underlying sample (probability) space (Ostoja-Starzewski 1993a). All specimens $\mathbf{B}(\omega)$ occupy the same domain in x_1,x_2-plane, whereby we employ a two-dimensional (2-D) setting for the clarity of presentation. Formally speaking, Ω is equipped with a σ-algebra F and a probability distribution P. We specify P as a Poisson process with inhibition, which ensures that there is no overlap of inclusions shaped as round disks. In particular, we use a sequential Poisson process and assume the disks to be occupied by a homogeneous isotropic continuum of one kind, while the matrix by a continuum of another kind.

In setting up of the model we assume both phases to satisfy the so-called ellipticity conditions: $\exists \zeta, \eta > 0$ such that for any $\underset{\sim}{\varepsilon}$ the following inequalities hold for all the phases

$$\zeta \underset{\sim}{\varepsilon}\underset{\sim}{\varepsilon} \le \underset{\sim}{\varepsilon}\underset{\sim}{C}\underset{\sim}{\varepsilon} \le \eta \underset{\sim}{\varepsilon}\underset{\sim}{\varepsilon} \tag{1}$$

As a result, we have a realistic ergodic medium model without holes and rigid inclusions described by a random field $\underset{\sim}{C} = \{\, \underset{\sim}{C}(\underset{\sim}{x}, \omega)\ ;\underset{\sim}{x} \in \boldsymbol{B};\omega \in \Omega \,\}$ with piecewise-constant realizations. It is clear that this piecewise-constant nature of stiffness fields is an obstacle with employing the governing equations of continuum elasticity, which require that the stiffness fields be once differentiable. Thus, there is a need for another, so-called, *meso-continuum* model - one that possibly loses some information due to a "smearing - out"

procedure, but is sufficiently differentiable.

2.2 TWO SCALE-DEPENDENT RANDOM MESO-CONTINUUM FIELDS

First, with the help of Fig. 1, we introduce a square-shaped window of scale

$$\delta = \frac{L}{d} \tag{2}$$

Equation (2) defines a nondimensional parameter $\delta \geq 1$ specifying the scale L of observation (and/or measurement) relative to a typical microscale d (i.e. grain size) of the material structure. $\delta = 1$ is the smallest scale we consider: scale of a fiber. In view of the fact that the composite is a random medium, the window bounds a random microstructure $B_\delta = \{B_\delta(\omega); \omega \in \Omega\}$, where $B_\delta(\omega)$ is a single realization from a given specimen $\mathbf{B}(\omega)$.

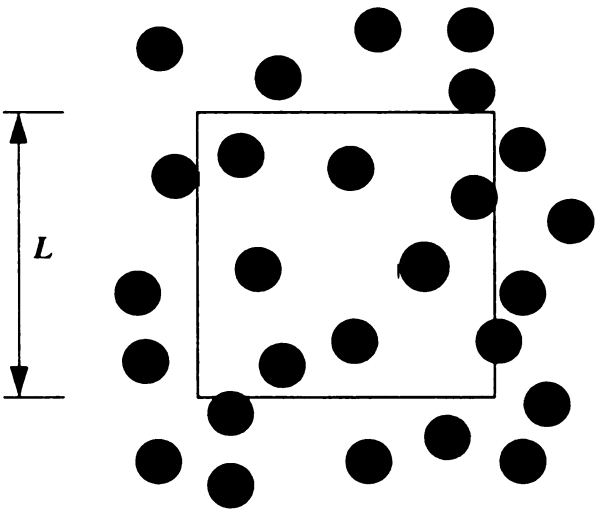

Fig.1 Square - shaped window

A continuum-type constitutive law is obtained by postulating the existence of an effective homogeneous continuum $B_\delta^{cont}(\omega)$ of the same volume V_δ (i.e. area in 2-D), whose

potential energy E, or complementary energy E*, under given uniform boundary conditions equals that of a microstructure $B_\delta(\omega)$ under the same boundary conditions. These are of two basic types:

i) displacement-controlled (*essential*)

$$u(\underline{x}) = \varepsilon_j^0 x_j \qquad on \qquad \partial B_\delta \tag{3}$$

where $\underline{\varepsilon}^0$ is a given constant tensor and ∂B_δ is the boundary of B_δ,

ii) stress-controlled (*natural*)

$$t = \sigma_j^0 n_j \qquad on \qquad \partial B_\delta \tag{4}$$

where $\underline{\sigma}^0$ is a given constant tensor.

Boundary condition (3) results in an effective random stiffness tensor $\underline{C}_\delta^e(\omega)$, with the constitutive law being stated as

$$\underline{\sigma}(\omega) = \underline{C}_\delta^e(\omega)\,\underline{\varepsilon}^0 \tag{5}$$

ω-dependence in (5) points to a random nature of the resulting stress field and of the effective stiffness tensor, with the fluctuations disappearing in the limit $\delta \to \infty$.

Condition (4) results in a following random operator form, involving a random compliance tensor, of constitutive law

$$\underline{\varepsilon}(\omega) = \underline{S}_\delta^n(\omega)\,\underline{\sigma}^0 \tag{6}$$

Hereinafter, superscripts ^{e} and ^{n} stand for essential and natural conditions, respectively. Also, we use here the same type of notation for out-of-plane elasticity and conductivity, whereby $\underline{\varepsilon}$ and $\underline{\sigma}$ are vectors, C_{ij} is an elastic stiffness (conductivity), and S_{ij} is an elastic compliance (resistivity).

Following (Ostoja-Starzewski, 1992, 1993a) we list here these principal observations:

1. Due to the heterogeneity of the microstructure $B_\delta(\omega)$, the inverse

$$\underline{C}^n_\delta(\omega) = \left[\underline{S}^n_\delta(\omega)\right]^{-1} \tag{7}$$

is for any finite δ, in general, different from $\underline{C}^e_\delta$ obtained under essential conditions.

2. $\underline{C}^e_\delta(\omega)$ and $\underline{C}^n_\delta(\omega)$ satisfy an inequality

$$\underline{C}^n_\delta(\omega) \leq \underline{C}^e_\delta(\omega) \tag{8}$$

Hereinafter, for two second-rank tensors A and B, an order relation $B \leq A$ means

$$t_i B_{ij} t_j \leq t_i A_{ij} t_j \qquad \forall \underline{t} \neq 0 \tag{9}$$

3. In view of the spatial homogeneity of microstructure's statistics, $\underline{C}^n_\delta(\omega)$ and $\underline{C}^e_\delta(\omega)$ converge as δ tends to infinity; this defines a deterministic continuum $\mathbf{B}_{\text{det}}$ for a single specimen $\mathbf{B}(\omega)$

$$\underline{C}^{det}(\omega) = \underline{C}^n_\infty(\omega) = \underline{C}^e_\infty(\omega) \tag{10}$$

whereby the window of infinite extent plays the role of an RVE of deterministic elasticity (conductivity) theory; in other words, it is at $\delta \to \infty$ that the invertibility of the constitutive law is obtained.

4. Ergodicity of the microstructure implies that

$$\underline{C}^{det}(\omega) = \underline{C}^{eff} \qquad \forall \omega \in \Omega \tag{11}$$

where $\underline{C}^{\text{eff}}$ is the effective response tensor (independent of ω) of a homogeneous medium.

5. At any finite δ both response tensors are, in general, anisotropic, with the nature of

anisotropy dependent on any specific $B_\delta(\omega)$.

6. Since the window may be placed arbitrarily in the domain of $\mathbf{B}(\omega)$, the essential and natural boundary conditions define two different inhomogeneous tensor fields at the scale δ with continuous realizations, which lead to two basic *random continuum approximations*: $\boldsymbol{B}^e_\delta = \{\boldsymbol{B}^e_\delta(\omega)\ ;\ \omega \in \Omega\}$ and $\boldsymbol{B}^n_\delta = \{\boldsymbol{B}^n_\delta(\omega)\ ,\ \omega \in \Omega\}$, respectively. Accordingly, a window of size δ may be considered as an RVE of these two random continuum models.

7. Our definition of two inhomogeneous tensor fields is conceptually similar - but not the same - to the procedure of local averaging (Vanmarcke, 1983) in the theory of random fields applied to a single realization $\underline{C}(\omega)$; $\omega \in \Omega$; it becomes the same in case of a 1-D model only when applied to compliance. In two and three dimensions computational mechanics methods have to be implemented - in a Monte Carlo sense - to find the energies and, hence, the effective constants of finite windows and their probability distributions $P\left(\underline{C}^e_\delta\right)$ and $P\left(\underline{C}^n_\delta\right)$. Similarly, the autocorrelation (autocovariance) functions may be determined (see also Ostoja-Starzewski and Wang, 1989 and 1990).

8. Principles of minimum potential and complementary energies can be used to obtain a hierarchy of scale-dependent bounds on the effective stiffness tensor $\underline{C}^{\text{eff}}$

$$C^R \equiv \left(S^R\right)^{-1} \equiv \langle S^n_1\rangle^{-1} \le \langle S^n_{\delta'}\rangle^{-1} \le \langle S^n_\delta\rangle^{-1} \le C^{eff} \le \langle C^e_\delta\rangle \le \langle C^e_{\delta'}\rangle \le \langle C^e_1\rangle \equiv C^V \qquad (12)$$
$$\delta' < \delta$$

9. Since two different random anisotropic continua result, a given boundary value problem must then be solved to find the upper and lower bounds on response of composites.

3. THE FINITE-DIFFERENCE MODEL

3.1 LAYOUT

The nature of a composite microstructure - i.e. presence of many inclusions distributed at random in the specimen - precludes any simple analytical solution of the local fields for this problem and of the crack propagation study in such a system. Therefore we adopt a method analogous to those used in modelling of stiffness and/or failure of atomic lattices (see Day et al., 1992; Beale and Srolovitz, 1988) and conduct the simulations in two dimensions. Such investigations are based, in the simplest setup, on simulations of breakdown of a lattice with central-force interactions, in which some bonds are initially taken out to represent the disorder, and from which cracks then develop in the course of simulation (see Section 4 below).

To use the discrete model, a two-dimensional triangle lattice (Fig.2) is arranged to cover the area occupied by the material. Suppose the material consists of cells of hexagon shaded in Fig.1. All the cells have the same size, shape and orientation, and are centered at vertices of the lattice. However, the material for each cell maybe different.

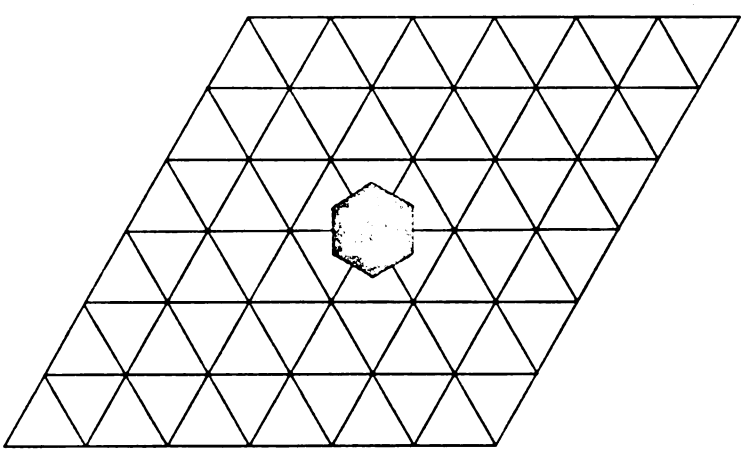

Fig.2 Two - dimensional discrete triangle lattice configuration

We consider a single cell (Fig.3), as a discrete model and describe the original continuum with six normal springs α^n and six angular springs (or watch spring) β^n. To answer what material problems this kind of model can describe, we need to find the relation between the stiffness of springs and the elastic moduli of the represented continuum.

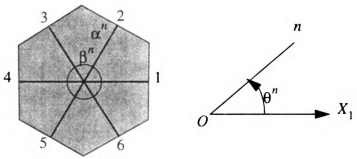

Fig.3 A discrete spring model of a single hexagon cell

3.2 MODEL FOR PLANE ELASTICITY

3.2.1 Alpha Model

As mentioned above, the model consists of straight and angular springs, but we prefer to discuss them separately for the sake of clarity and simplicity. Consider a cell of isotropic material as shown in Fig.3. A discretized model consisting of six straight springs which connect at the center of hexagon will be used to simulate the original material of continuous model. All springs are linear elastic and can rotate around the center freely. The nth spring has an angle θ^n with the coordinate axis X_1 and stiffness α^n, so the model is called an α - model.

The relation of elastic properties between the continuum and the discrete model can be derived from the equivalence of energy of both models. For the continuum model, the elastic energy E of the hexagon is expressed as

$$E = \frac{1}{2} C^{\alpha}_{ijkl} \varepsilon_{ij} \varepsilon_{kl} A \qquad i,j,k=1,2 \tag{13}$$

where, C is the fourth order tensor of elastic moduli, the stiffness tensor. A is the area of the hexagon cell. ε_{ij} is the linear strain tensor of the second order.

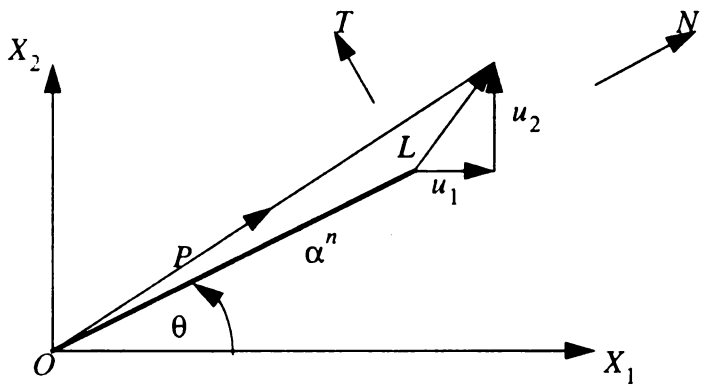

Fig.4 Normal spring

To get the energy expression for the discrete model, we note that OL represents nth spring of stiffness α^n and length l (Fig. 4). X_1 and X_2 are the rectangular Cartesian coordinates. N is directed along the axis of the spring. We assume that point O is fixed and the displacements of point L are u^n_1 and u^n_2.

The force P in the spring is

$$P^n = \alpha^n u^n_N \ , \tag{14}$$

and

$$u^n_N = l^n_j u^n_j \tag{15}$$

where $l_1 = \cos\theta$, $l_2 = \sin\theta$ are the directions of the spring.

Using (14) and (15), the strain energy in the spring can be written as

$$
\begin{aligned}
E^n &= \frac{1}{2} P_i^n u_i^n \\
&= \frac{1}{2} \alpha^n l_i^n l_j^n u_j^n u_i^n \\
&= \frac{l^2}{2} \alpha^n l_i^n l_j^n \varepsilon_{jk} l_k^n \varepsilon_{il} l_l^n \\
&= \frac{l^2}{2} \alpha^n l_i^n l_j^n l_k^n l_l^n \varepsilon_{ij} \varepsilon_{kl}
\end{aligned}
\tag{16}
$$

The total energy of all six springs with the same length l is

$$
E = \sum_{n=1}^{6} E^n = \frac{l^2}{2} \sum_{n=1}^{6} \alpha^n l_i^n l_j^n l_k^n l_l^n \varepsilon_{ij} \varepsilon_{kl} \tag{17}
$$

Comparing expressions (17) and (13) , the elastic moduli of a material represented by the discrete spring model are found as

$$
C^{\alpha}_{ijkl} = \frac{l^2}{A} \sum_{n=1}^{6} \alpha^n l_i^n l_j^n l_k^n l_l^n \tag{18}
$$

The area of the hexagon is

$$
A = 2\sqrt{3} l^2 \tag{19}
$$

Substituting the expression (19) into (18), we get

$$
C^{\alpha}_{ijkl} = \frac{1}{2\sqrt{3}} \sum_{n=1}^{6} \alpha^n l_i^n l_j^n l_k^n l_l^n \tag{20}
$$

It is obvious that this expression for elastic moduli satisfies the requirements of the symmetry of stress and strain tensors which is necessary. The result obtained here is exactly the same as given by Holnicki - Szulc and Rogula (1979).

3.2.2 Beta Model

Again consider the single cell given in Fig.3, but only with six linear elastic angular springs used to constrain the free-rotation of the α springs. The stiffness of the nth angular spring is denoted by β^n, so the model is called a β - model.

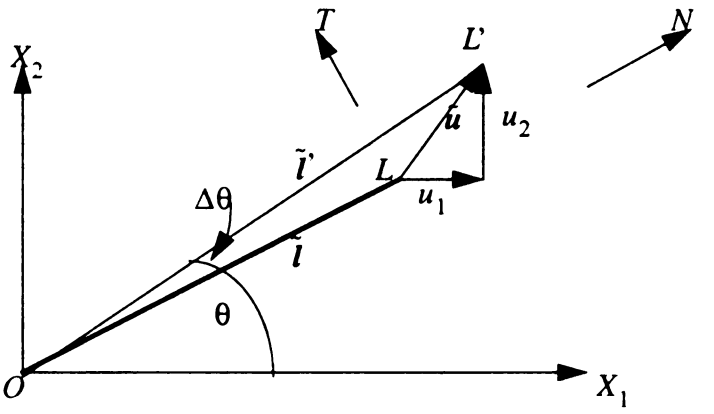

Fig.5 Angle change, $\Delta\tilde{\theta}$

Using Fig. 5, we want to find what is the angle change $\Delta\tilde{\theta}$ when the point L moves to the point L' through an infinitesimal displacement. Let $\hat{l}$ be the unit vector along OL and l be the length of OL. It is seen that

$$\hat{l}\times\tilde{u} = \hat{l}\times\tilde{l}' = l\cdot\Delta\tilde{\theta} \tag{21}$$

Equation (21) leads to

$$\Delta\tilde{\theta} = \frac{1}{l}\cdot\hat{l}\times\tilde{u} = \frac{1}{l}\varepsilon_{kij}l_i u_j = \varepsilon_{kij}\varepsilon_{jp}l_i l_p \tag{22}$$

where, ε_{kij} is the permutation tensor and ε_{jp} is a strain tensor, $i, j, p = 1, 2$, $l_1 = \cos\theta$

and $l_2 = \sin\theta$.

The angle change between two segments is measured by (Fig. 6)

$$\Delta\tilde{\phi} = \Delta\tilde{\theta}^{n+1} - \Delta\tilde{\theta}^{n} \tag{23}$$

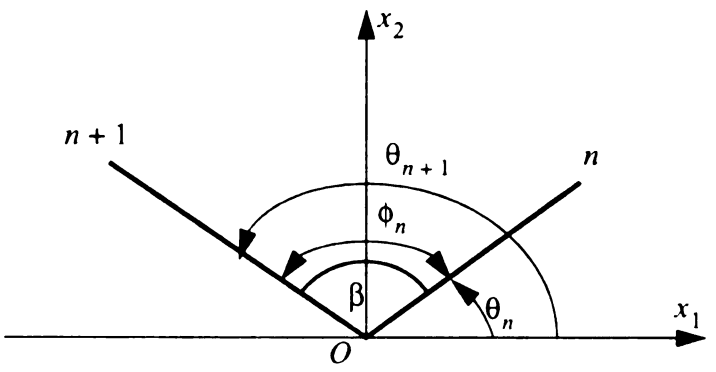

Fig.6 Angular spring

Substituting equation (22) into (23), we get,

$$\Delta\tilde{\phi} = \varepsilon_{kij}\varepsilon_{jp}\left(l_i^{n+1} l_p^{n+1} - l_i^n l_p^n \right) \tag{24}$$

For a single angle spring β^n, the strain energy due to $\Delta\tilde{\phi}$ is

$$E^n = \frac{1}{2}\beta^n |\Delta\phi|^2 \tag{25}$$

Substituting equation (24) into (25), we get

$$E^n = \frac{1}{2}\beta^n \left\{ \varepsilon_{kij}\varepsilon_{jp}\left(l_i^{n+1} l_p^{n+1} - l_i^n l_p^n \right) \right\}^2 \tag{26}$$

Expanding expression (26) and using the identity

$$\varepsilon_{kij}\varepsilon_{kpq} = \delta_{ip}\delta_{jq} - \delta_{iq}\delta_{jp} \tag{27}$$

where δ_{ij} is Kronecker delta, and taking advantage of permutation function of δ_{ij}, we finally get,

$$\begin{aligned} E^n = \frac{\beta^n}{2} \{ & \delta_{ik} l_p^n l^n{}_j l_p^n l_l^n - l_i^n l_j^n l_k^n l_l^n \\ & + \delta_{ik} l_p^{n+1} l_j^{n+1} l_p^{n+1} l_l^{n+1} - l_i^{n+1} l_j^{n+1} l_k^{n+1} l_l^{n+1} \\ & -2\delta_{ik} l_p^n l_j^{n+1} l_p^{n+1} l_l^n + 2 l_i^n l_j^{n+1} l_k^{n+1} l_l^n \} \varepsilon_{ij}\varepsilon_{kl} \end{aligned} \tag{28}$$

The total energy in a cell with six angular springs is

$$\begin{aligned} E = \sum_{n=1} \frac{\beta^n}{2} \{ & \delta_{ik} l_p^n l^n{}_j l_p^n l_l^n - l_i^n l_j^n l_k^n l_l^n \\ & + \delta_{ik} l_p^{n+1} l_j^{n+1} l_p^{n+1} l_l^{n+1} - l_i^{n+1} l_j^{n+1} l_k^{n+1} l_l^{n+1} \\ & -2\delta_{ik} l_p^n l_j^{n+1} l_p^{n+1} l_l^n + 2 l_i^n l_j^{n+1} l_k^{n+1} l_l^n \} \varepsilon_{ij}\varepsilon_{kl} \end{aligned} \tag{29}$$

where superscript (n+1) takes the value of 1 when n=6.

Equation (29) is really an expression of the strain energy of the unit cell of discrete model. But to get the expression for elastic moduli, the symmetry with respect to *i* and *j*, *k* and *l*, and *ij* and *kl* should be satisfied. That means some subscripts in equation (29) should be permuted and the expression of the energy needs to be reconstructed so that it can be symmetric. There is no difficulty to work it out, but the desired expression will be tedious for the general case.

For the cases we consider, i.e., the cases of two-dimensional isotropy and orthot-

ropy, only a few permutations are needed. In this case, equation (29) can be rewritten as follows

$$
\begin{aligned}
E = \frac{1}{2}\sum_{n=1} \{ & \left(\beta^n + \beta^{n-1}\right)\delta_{ik} l_p^n l^n{}_j l_p^n l_l^n - \left(\beta^n + \beta^{n-1}\right) l_i^n l_j^n l_k^n l_l^n \\
& -\beta^n \delta_{ik} l_p^n l_j^{n+1} l_p^{n+1} l_l^n + \beta^n l_i^n l_j^{n+1} l_k^{n+1} l_l^n \\
& -\beta^n \delta_{ik} l_p^n l_j^n l_p^{n+1} l_l^{n+1} + \beta^n l_i^{n+1} l_j^n l_k^n l_l^{n+1} \} \varepsilon_{ij} \varepsilon_{kl}
\end{aligned} \tag{30}
$$

The elastic energy of a continuous cell should be

$$
E = \frac{1}{2} C_{ijkl}^{\beta} \varepsilon_{ij} \varepsilon_{kl} A \tag{31}
$$

Comparing equation (31) and (30), the elastic constants of the equivalent continuum model can be simulated by the discrete lattice model according to

$$
\begin{aligned}
C_{ijkl}^{\beta} = \frac{1}{A}\sum_{n=1}^{6} \{ & \left(\beta^n + \beta^{n-1}\right)\delta_{ik} l_p^n l^n{}_j l_p^n l_l^n - \left(\beta^n + \beta^{n-1}\right) l_i^n l_j^n l_k^n l_l^n \\
& -\beta^n \delta_{ik} l_p^n l_j^{n+1} l_p^{n+1} l_l^n + \beta^n l_i^n l_j^{n+1} l_k^{n+1} l_l^n \\
& -\beta^n \delta_{ik} l_p^n l_j^n l_p^{n+1} l_l^{n+1} + \beta^n l_i^{n+1} l_j^n l_k^n l_l^{n+1} \}
\end{aligned} \tag{32}
$$

where superscript (n-1) takes the value of 1 when n=1.

3.2.3 The General Model

By superposition of equation (20) and (32), the elastic moduli of a cell of continuum are expressed in terms of stiffness of general discrete $\alpha - \beta$ model as follows

$$
\begin{aligned}
C_{ijkl} = {} & \frac{l^2}{A}\sum_{n=1}^{6}\alpha^n l_i^n l_j^n l_k^n l_l^n \\
& + \frac{1}{A}\sum_{n=1}^{6}\{\left(\beta^n+\beta^{n-1}\right)\delta_{ik}l_p^n l_j^n l_p^n l_l^n - \left(\beta^n+\beta^{n-1}\right)l_i^n l_j^n l_k^n l_l^n \\
& \quad -\beta^n\delta_{ik}l_p^n l_j^{n+1} l_p^{n+1} l_l^n + \beta^n l_i^n l_j^{n+1} l_k^{n+1} l_l^n \\
& \quad -\beta^n\delta_{ik}l_p^n l_j^n l_p^{n+1} l_l^{n+1} + \beta^n l_i^{n+1} l_j^n l_k^n l_l^{n+1}\}
\end{aligned}
\tag{33}
$$

where $A = 2\sqrt{3}l^2$

3.3 APPLICATION OF THE MODEL FOR PLANE ELASTICITY

3.3.1 Application to orthotropic material

For a two dimensional orthotropic material, there should be two axes about which the material is symmetric. To satisfy this condition, we take the coordinate axes as the symmetric ones, and choose (Fig.7)

$$\alpha^1 = \alpha^4 \tag{34}$$

$$\alpha^2 = \alpha^3 = \alpha^5 = \alpha^6 \tag{35}$$

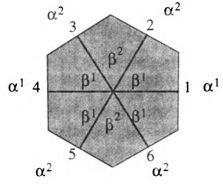

Fig.7 Discrete model of a two dimensional orthotropic cell

$$\beta^1 = \beta^3 = \beta^4 = \beta^6 \tag{36}$$

$$\beta^2 = \beta^5 \tag{37}$$

Using directly expression (33) with the conditions (34)-(37), the elastic moduli corresponding to the orthotropic discrete model are evaluated as

$$C_{1112} = C_{2212} = 0 \tag{38}$$

$$C_{1111} = \frac{1}{2\sqrt{3}}\left[\left(2\alpha^1 + \frac{1}{4}\alpha^2\right) + \frac{1}{l^2}\left(\frac{3}{4}\beta^1 + \frac{3}{2}\beta^2\right)\right] \tag{39}$$

$$C_{1122} = \frac{1}{2\sqrt{3}}\left[\frac{3}{4}\alpha^2 - \frac{1}{l^2}\left(\frac{3}{4}\beta^1 + \frac{3}{2}\beta^2\right)\right] \tag{40}$$

$$C_{2222} = \frac{1}{2\sqrt{3}}\left[\frac{9}{4}\alpha^2 + \frac{1}{l^2}\left(\frac{3}{4}\beta^1 + \frac{3}{2}\beta^2\right)\right] \tag{41}$$

$$C_{1212} = \frac{1}{2\sqrt{3}}\left[\frac{3}{4}\alpha^2 + \frac{1}{l^2}\frac{9}{4}\beta^1\right] \tag{42}$$

where subscripts in the tensor are simplified notation as general convention. The obtained tensor of elastic moduli is symmetric.

3.3.2 Application to isotropy

3.3.2.1 Using both α and β model

For isotropic material, we assign all straight and angular springs the same values of stiffness, respectively. In this case, the elastic moduli of a cell in (33) degenerate as follows

$$\begin{aligned} C_{ijkl} = & \frac{\alpha}{2\sqrt{3}} \sum_{n=1}^{6} l_i^n l_j^n l_k^n l_l^n \\ & + \frac{\beta}{A} \sum_{n=1}^{6} \{ 2\delta_{ik} l_p^n l^n{}_j l_p^n l_l^n - 2 l_i^n l_j^n l_k^n l_l^n \\ & - \delta_{ik} l_p^n l_j^{n+1} l_p^{n+1} l_l^n + l_i^n l_j^{n+1} l_k^{n+1} l_l^n \\ & - \delta_{ik} l_p^n l_j^n l_p^{n+1} l_l^{n+1} + l_i^{n+1} l_j^n l_k^n l_l^{n+1} \} \end{aligned} \tag{43}$$

Assume that the straight and angular springs are distributed uniformly, the length of l is taken as a unit, the corresponding relation between the elastic moduli of the continuum model and the stiffnesses of the discrete model is determined as

$$C_{1112} = C_{1211} = C_{2212} = C_{1222} = 0 \tag{44}$$

$$C_{1111} = C_{2222} = \frac{1}{2\sqrt{3}} \left(\frac{9}{4}\alpha + \frac{1}{l^2}\frac{9}{4}\beta \right) \tag{45}$$

$$C_{1122} = C_{2211} = \frac{1}{2\sqrt{3}} \left(\frac{3}{4}\alpha - \frac{1}{l^2}\frac{9}{4}\beta \right) \tag{46}$$

$$C_{1212} = \frac{1}{2\sqrt{3}} \left(\frac{3}{4}\alpha + \frac{1}{l^2}\frac{9}{4}\beta \right) \tag{47}$$

In view of the listed results, it is obvious that the obtained elastic moduli in terms

of stiffness of the discrete model satisfy the requirements of symmetry due to stress and strain tensors and strain energy. It is also observed that the condition

$$C_{1212} = \frac{1}{2}(C_{1111} - C_{1122}) \tag{48}$$

is satisfied, so that there are only two independent constants and the proposed model can really represent an isotropic continuum of isotropy.

Using the relation,

$$\kappa + \mu = C_{11} \tag{49}$$

$$\mu = C_{66} \tag{50}$$

a pair of independent elastic constants in the other form are obtained

$$\kappa = \frac{1}{2\sqrt{3}}\left(\frac{3}{2}\alpha\right) \tag{51}$$

$$\mu = \frac{1}{2\sqrt{3}}\left(\frac{3}{4}\alpha + \frac{19}{l^2 4}\beta\right) \tag{52}$$

where μ is the shear modulus and κ is the two-dimensional bulk modulus. It may be noted that the bulk modulus due to the angular springs is identically zero, i. e.,

$$\kappa^{\beta} = 0 \tag{53}$$

That implies the presence of angular springs never change the area of material.

The formula for a two-dimensional Poisson's ratio is as follows,

$$\nu = \frac{\kappa - \mu}{\kappa + \mu} = \frac{C_{12}}{C_{11}} \tag{54}$$

Substituting equations (51) and (52) into (54), we get

$$\nu = \frac{\alpha l^2 - 3\beta}{3\alpha l^2 + 3\beta} \tag{55}$$

From equation (55), we find the range of Poisson's ratio which can be covered with this model, i.e.,

$$\begin{aligned} \nu &= -1 \qquad && if \quad \frac{\beta}{\alpha} \to \infty \\ \nu &= \frac{1}{3} \qquad && if \quad \frac{\alpha}{\beta} \to \infty \end{aligned} \tag{56}$$

Note that this is a two dimensional Poisson's ratio.

3.3.2.2. Using only the α - model

In this modeling without angular spring, the straight springs are chosen such that all the six have the same length and stiffness, and all the angles between any adjacent ones are equal to each other. In this case, equation (8) can be rewritten as

$$C_{ijkl} = \frac{\alpha}{2\sqrt{3}} \sum_{n=1}^{6} l_i^n l_j^n l_k^n l_l^n \tag{57}$$

From equation (57), the elastic moduli are evaluated. The results show all the conditions of isotropic elastic properties are satisfied, such as

$$C_{1111} = C_{2222} \tag{58}$$

$$C_{1112} = C_{2212} = 0. \tag{59}$$

$$C_{1212} = \frac{1}{2}(C_{1111} - C_{1122}) \tag{60}$$

The elastic constants are listed as

$$C_{1111} = C_{11} = \frac{3\sqrt{3}}{8}\alpha \tag{61}$$

$$C_{1122} = C_{12} = \frac{\sqrt{3}}{8}\alpha \tag{62}$$

$$C_{1212} = C_{66} = \frac{\sqrt{3}}{8}\alpha \tag{63}$$

Using the relation (49) and (50), a pair of independent elastic constants is obtained

$$\kappa = \frac{\sqrt{3}}{4}\alpha \tag{64}$$

$$\mu = \frac{\sqrt{3}}{8}\alpha \tag{65}$$

where μ is the shear modulus and κ is two-dimensional bulk modulus.

The same expression as in equation (57) was mentioned by Holnicki-Szulc (1979). The results equivalent to equations (64) and (65) were given by Keating (1966) and Kirkwood (1939), but the stiffness of springs which they took is half of what we take here so that the coefficients in their expression would be twice the ones in equations (64) and (65).

As we did above, if we substitute equations (64) and (65) into (54), we get $\nu = 1/3$, which means the above-mentioned model can be used only for the case of two-dimensional Poisson's ratio being 1/3.

To get Poisson's ratio different from 1/3, the parameters, such as stiffness of springs or angles between springs may be changed instead of adding angular springs. Chen and Thorpe (1992) employed the equilateral triangular lattice without angle springs, but assigned three different stiffnesses to the straight springs. the range of Poisson ratio is from 1/3 to 1. Thus, by combination of Thorpe's model and ours, Poisson's ratio in the full range for 2-dimensions, from -1 to 1, can be obtained.

3.4 APPLICATION TO CONDUCTIVITY

We now consider the two-dimensional conductivity problem governed by Laplace's equation. The model can also be used for several other problems, such as out - of - plane elasticity, membrane problem, etc., which have the same governing equation.

3.4.1 Triangle lattice model

Again we refer to Fig.2 , to the model with the normal springs. Following the same procedure we used for the two-dimensional elastic problem but at lower level of tensor, we get

$$\begin{aligned} E^n &= \frac{1}{2} P^n u^n \\ &= \frac{1}{2} \alpha^n \left(\varepsilon_i l_i^n \right)^2 \\ &= \frac{1}{2} \alpha^n l_i^n l_j^n \varepsilon_i \varepsilon_j \end{aligned} \tag{66}$$

where u is out of plane displacement (temperature), ε is gradient of displacement (gradient of temperature). The total energy of all six springs is

$$E = \sum_{n=1}^{6} E^n = \frac{1}{2} \sum_{n=1}^{6} \alpha^n l_i^n l_j^n \varepsilon_i \varepsilon_j \tag{67}$$

For the continuous model, the elastic energy E of the hexagon is expressed as

$$E = \frac{1}{2} C_{ij}^{\alpha} \varepsilon_i \varepsilon_j A \tag{68}$$

where C_{ij} is the tensor of elastic moduli (conductivity). Comparing expressions (67) and (68) and substituting the area of the hexagon (19), the elastic moduli represented by the discrete spring model are found as

$$C_{ij}^{\alpha} = \frac{1}{2\sqrt{3}} \sum_{n=1}^{6} \alpha^n l_i^n l_j^n \tag{69}$$

Assume the straight springs are chosen such that all six have the same length and stiffness, and all the angles between any adjacent ones are equal to each other. In this case, equation (69) can be evaluated as

$$C_{11} = C_{22} = \frac{\sqrt{3}}{2}\alpha \tag{70}$$

$$C_{12} = C_{21} = 0 \tag{71}$$

It is obvious that obtained conductivity tensor satisfies the requirements of symmetry and indicates the isotropy of the model.

3.4.2 Square Lattice Model

Fig. 8 shows the two-dimensional square lattice which is to cover the area which materials occupy. Suppose the material consists of cells of square shaded in the figure. All the cells have the same size, shape and orientation, and are centered at vertices of the lattice and fill the lattice. However, the material for each cell maybe different.

We consider a single cell (Fig.9), as a discrete model, and describe the original continuum with four straight springs α^n of the same length. Following the same procedure as for the triangular lattice, we get the conductivity of the original continuum in terms of the stiffness of the discrete model as

$$C_{ij} = \frac{1}{4} \sum_{n=1}^{4} \alpha^n l_i^n l_j^n \tag{72}$$

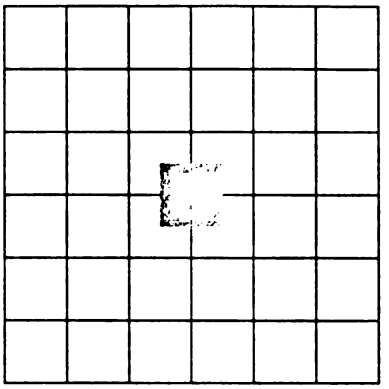

Fig.8 Square lattice

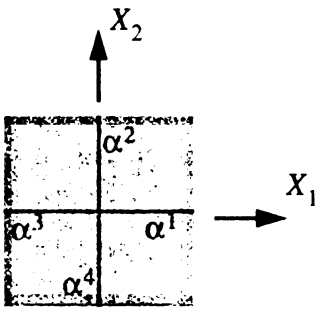

Fig.9 Discrete square cell

Let all four stiffnesses α be equal to each other. The expression (72) is evaluated as

$$C_{11} = C_{22} = \frac{1}{2}\alpha \tag{73}$$

$$C_{12} = C_{21} = 0 \tag{74}$$

An orthotropic model can also be established by using square lattice if we set α^1, α^2 equal to α^3, α^4 respectively. As a result, the model will be represented by

$$C_{11} = \frac{1}{2}\alpha^1 \tag{75}$$

$$C_{22} = \frac{1}{2}\alpha^2 \tag{76}$$

$$C_{12} = C_{21} = 0 \tag{77}$$

4. EFFECTIVE CONDUCTIVITY

4.1 METHOD OF SOLUTION

To study the effective conductivity of a composite material, the above-mentioned square and triangular lattices are used to discretize its domain. We consider two - phase materials, i.e., composites containing inclusions, which are arranged either periodically or randomly in the matrix. Regarding the latter, the structure of composite material is created by generating, in a Monte Carlo sense, pseudo-random numbers for coordinates of the centers of inclusions. A rounding off of these numbers is done to set the center of inclusion exactly on the grid points. Then the stiffness of all springs (or, say, bonds) are assigned according to whether they fall in the matrix or in the inclusion. Any spring straddling the circular boundaries of inclusions has its stiffness (α) assigned according to a series spring system weighted by the partial lengths (l_I, l_{II}) of the springs that belong to the respective domains, i.e., by the harmonic average:

$$\alpha = \left(\frac{l_I}{l\alpha_I} + \frac{l_{II}}{l\alpha_{II}} \right)^{-1} \tag{78}$$

where l = total spring length

α_I, α_{II} = stiffness of partial spring.

The two-dimensional conductivity and the out - of - plane elasticity problems that we are concerned with in this investigation have the same governing equations mathematically. For the two problems, the constitutive equation is

$$\sigma_i(\underset{\sim}{x}) = C_{ij}(\underset{\sim}{x})\,\varepsilon_j(\underset{\sim}{x}) \tag{79}$$

where σ_j is either heat flux for the conductivity case or stress for the out - of - plane elasticity case. ε_j is temperature gradient for the conductivity and strain for the out-of-plane elasticity. C_{ij} is the conductivity or, out-of-plane shear modulus for the two cases, respectively. All of these are random variables depending on their local position.

In order to solve problems related to inhomogeneity, 'effective modulus' should be defined. The formula used here can be found from a general textbook so that it is shown here without more details. Based on the stochastic concept of random field theory, there are two kinds of 'average', volume average and ensemble average. Using the concept of volume average, we take a special specimen subject to a displacement boundary (essential) condition as follows

$$u = \bar{\varepsilon}_j x_j \tag{80}$$

where u is the displacement and temperature for out - of - plane elasticity and conductivity cases, respectively. x_j is the position vector, $\bar{\varepsilon}_j$ is the average strain or intensity which is defined by

$$\bar{\varepsilon}_i = \frac{1}{A}\int_A \varepsilon_i dA \tag{81}$$

Furthermore, the effective modulus can be defined as

$$\bar{\sigma}_i = C_{ij}^{eff}\bar{\varepsilon}_j \tag{82}$$

In this case, the potential energy is

$$E = \frac{1}{2}\underline{\bar{\varepsilon}}\,\underline{\underline{C}}^{eff}\underline{\bar{\varepsilon}} \tag{83}$$

On the other hand, using the discrete model in section 2, the same potential energy can be obtained by simply summing the energy in each spring as

$$E = \sum_{i=1}^{n} \frac{1}{2}\alpha_i (\Delta u_i)^2 \tag{84}$$

where α_i is the stiffness of the *ith* spring in the model, and Δu_i is its deformation. n is the number of springs in the model.

Equating the energy in (82) and (83), the effective modulus can be found. The following three tests are carried out to evaluate C_{11}, C_{22} and C_{12} respectively.

i) taking $\varepsilon_1 = 1$, $\varepsilon_2 = 0$ leads to (85)

$$C_{11} = 2E_1 \tag{86}$$

ii) taking $\varepsilon_1 = 0, \varepsilon_2 = 1$ leads to (87)

$$C_{22} = 2E_2 \tag{88}$$

iii) taking $\varepsilon_1 = 1, \varepsilon_2 = 1$ leads (89)

$$C_{12} = E_3 - E_2 - E_1 \tag{90}$$

where E_1, E_2 and E_3 are the energies in the three tests, respectively.

4.2 RESULTS

We examine the effects of several factors on the conductivity. These include the arrangement of inclusions, the type and size of lattice, the ratio of conductivity of inclusion to matrix, the volume fraction of inclusions and randomness, and compare the obtained results with their Hashin second - order bounds.

Specimens have inclusions arranged either periodically or randomly. In both two

cases, all the boundaries are periodic. The samples of composite configuration are shown in Fig.10. Only essential (displacement) boundary problems are solved. Following issues are discussed,

(i) Since we represent a continuum system by a discrete lattice, the first important question is how large should the diameter of the inclusion relative to the mesh spacing be in order to adequately approximate the continuous material. We explore this issue by considering a classical case of effective conductivity of a material with a dilute concentration of circular hole for which an exact solution is known to have the form

$$C^{eff} = (1 - \Re f)\, C^{m} \tag{91}$$

where C^{eff} is the effective conductivity of a composite, C^{m} is the conductivity of a matrix, f is the volume fraction of the inclusion to the composite and $\Re$ is a constant which equals to 2 for a hole in dilute case.

A specimen of size 114x114 with square lattices is used to test the effect of the size of an inclusion on accuracy of solution. The diameter of the single cavity in the matrix changes from 2 to 20 spacings, the corresponding conductivities are obtained and the constant $\Re$ is calculated from equation (78). All the related data are given in Table 1 below. It is seen that the inclusion having a very small diameter d = 2 or 4 does not represent the continuum system well. As we increase the diameter, the accuracy improves and $\Re$ converges to the analytical solution, although there is a fluctuation. However, for large diameters we have two competing effects - the larger the diameter the better the approximation, but, at the same time, the dilute assumption ceases to hold. Note that we have computer limitations on the lattice size. Finally we compromise by choosing d=14 where the volume fraction, close to 1 percent, corresponds to a dilute system. The effect of the hole size on the effective conductivity is also shown in Fig. 11. In Fig. 11 and the following Figs. 12 - 15 and 20 - 21, the calculation points are connected simply by the straight lines for clarity.

No regression has been made.

Table 1:

diameter	volume fraction	$\Re$	percent error
2	.00024	0.9997	
4	.00097	1.7373	
6	.00218	2.0356	+1.5
8	.00387	1.9783	-1.5
10	.00604	1.9078	-5.0
12	.00870	2.0541	+2.5
14	.01185	1.9848	-1.0
16	.01547	2.0032	+0.1
18	.01958	2.0193	+1.0
20	.02417	1.9914	-0.5

(ii) In addition to (i), the mesh dependence is examined as follows. We vary the size of specimens and inclusions simultaneously, but keep the volume fraction of the inclusions unchanged. A volume fraction of 0.349 is used here. The sizes of the window are L = 64, 127, 253 and 379, and the corresponding diameters of the inclusions are d = 14, 28, 56 and 84, respectively. δ is fixed. In other words, we consider the dependence of effective conductivities on the mesh. The investigation is conducted for various ratios, 0.0, 0.01, 0.1, 0.2, 0.5, 1, 2, 5 and 10, of the conductivity of inclusions to those of matrices. Fig.12 shows the relation between the ratio and the effective conductivity which is also normalized by the conductivity of matrix. The results indicate that the effective conductivities from the window size 64 and 127 coincide well, and the effective conductivi-

ties go up when the window size increases after that. The bigger is the contrast C^i/C^m in conductivities, the stronger is the scale dependence.

(iii) As mentioned in section 2, the conductivity is scale-dependent. To understand this effect, we vary the size of window with L = 64, 127, 253 and 379. The diameter of inclusion is still taken as 14 in order to ensure the accuracy of solution. The corresponding values of scale δ are 4.5, 9, 18 and 27, respectively. No bigger specimen can be taken because of the computer limitation.

Fig. 13 shows the relation between the ratio of the conductivity of inclusions to those of matrices and the effective conductivity which is also normalized by the conductivity of matrix. The results show that the effective conductivities coincide well for the case of C^i/C^m<10. The effective conductivities go down when the ratio L/d increases.

Figs. 14 - 15 and Figs. 20 - 21 show the conductivity for the cases of L=64 and 128, respectively. Fig. 14 and Fig. 20 give the dimensionless effective conductivity (normalized by the conductivity of matrix), C^{eff}/C^m, versus the ratio of the conductivity of the inclusion to the matrix, C^i/C^m and the volume fraction of the inclusion to the composite, f, in two - dimensions. The volume fractions are taken as 0.03879, 0.1939, 0.3491, 0.4266, 0.5042 and 0.5818, respectively. The upper figure is the shaded effective conductivity surface and the lower one is the intersection of the above surface with the planes where the volume fraction is fixed. To see more details, Fig. 15 and Fig. 21 give the curves of the effective conductivity versus the volume fraction with ratio of the conductivity of the inclusion to the matrix being 100, 50, 10, 5, 2, 1, 0.5, 0.2, 0.1, 0.02 and 0.01, respectively. In the figures, the curves for 11 cases are plotted in various forms of solid, dashed or dashdot lines for the sake of clarity. The difference of conductivities obtained in these cases is very small, for most cases, in a range of 1 percent relatively, so that they appear to be weakly scale-dependent for the range of the ratio of the conductivity of the inclusion to one of the matrix, 0.1 - 10, which is more practically applicable to composites. In other words, the effective conductivity obtained from different δ scale but contain-

ing inclusions of diameter 14 are comparable to each other.

(iv) Regarding the stochastic aspects, 10 samples are randomly chosen for each case. The mean value and variance of the results obtained are calculated. The results from two loading conditions, $\bar{\varepsilon}_1 = 1, \bar{\varepsilon}_2 = 0$ and $\bar{\varepsilon}_1 = 0, \bar{\varepsilon}_2 = 1$ are also averaged to eliminate the macroscopic anisotropy because of the limited window size. The distribution of the conductivity with different random arrangements of inclusions can be found in Figs. 16 - 19 which show the effective conductivities corresponding to various volume (area, here) fractions for a certain conductivity ratio, C^i/C^m. In the figures, the dot marker stands for the case of L=64 and the circular marker for L=127. The scatter of the results is obvious but not significant, and the relative variance, for most cases, does not exceed 0.06. It is noted that randomness plays a more important role when the ratio of conductivity of the inclusion to the matrix is far from a unity, such as the case $C^i/C^m = 0.02$ in Fig. 16.

(v) As a special case, comparing to random ones, the effective conductivity of composites with periodically arranged inclusions are evaluated for the same volume fraction and stiffness ratio. Fig. 24 and 32 display for two different stiffness ratios the stress-strain curves of a periodic composite and of several random composites. It is seen that the effective conductivity for the periodic composite is within the range of scatter of the effective conductivities for the random composites, i.e., although the stress-strain curves appear different, the initial slopes, i.e. conductivities, are almost the same. It should be noted, however, that this result has been obtained for a rather restrictive model: a periodic window with the dimension only about 3.5 times larger than the diameter of the inclusion. This is not the case with C^{eff} calculated via C_δ^n and C_δ^e (see Section 2.2).

(vi) The range of volume fraction of inclusions is from zero to about 0.6, the maximum value that can be obtained in the case of non-overlapping inclusions. For the above test, the volume fractions are taken as 0.03879, 0.1939, 0.3491, 0.4266, 0.5042 and 0.5818, respectively. Figs. 16-19, where the solid lines are the Hashin second upper and lower bounds for the effective conductivity of composite in two-dimensions, show that the

effective conductivities for various volume fractions are consistent with the Hashin second - order bounds.

(vii) A sample is also made of for the ratio of conductivities of the inclusion to the matrix from 0.01 to 100 which covers a range wide enough to be applicable to most practical composite materials. The results show that all the values of the effective conductivity fall within their feasible range enclosed by Hashin second-order bounds in Figs. 16-19. Furthermore, the values approach the lower bounds as the ratio is larger than 1, and the upper bounds for the ratio less than 1. This implies the model lattice has a little lower stiffness, since according to the theory in (12), all conductivity should be near the upper bounds.

(viii) In order to understand the sensitivity of conductivities to the type of lattice, both triangle and square lattice are used. The results from the two different types of discrete models are quite consistent for the same composite material. No more comparison of lattice types will be mentioned, it is not the main concern in our study.

In this section, the effect on the conductivity of many facts, such as the size of mesh, the ratio of the window dimension to the diameter of inclusions, the composite configurations (randomly and periodically arranged inclusions), the ratio of the conductivity of inclusion to the conductivity of matrix, the volume fraction of inclusions and the lattice shapes are examined. The inclusion of diameter 14 and the window of 64x64 are used to get reasonable conductivities with feasible expenses on HP or SUN work station. The calculated conductivities fall within Hashin second order bounds.

5. DAMAGE AND FRACTURE SIMULATION OF COMPOSITES

5.1 METHOD OF SOLUTION

The investigation of damage and fracture in composite material is based on a simple and straight - forward idea, i.e., simulation of breakdown of a spring lattice model, in which heterogeneity is introduced by, for example, taking out some springs to represent the disorder and from which cracks then develop in the course of simulation.

In this part of thesis, we assume that the microstructural response of composites is elastic-brittle. In other words, the springs in the lattice will have linear elastic property until they break according to the established criterion. For the two phase material, there are two kinds of springs representing matrix and inclusion, respectively. Therefore, the composite material can be characterized by four parameters. Of them, C^m and C^i are stiffnesses of springs for inclusions and matrices, and ε_{cr}^m and ε_{cr}^i are critical strains at which springs will break. In this notation, the superscripts *m* and *i* stand for the matrix and inclusion, respectively, and *cr* for 'critical'. The global response of a composite is, however, a result of cooperative spatio-temporal phenomena of breaking along with the stress and strain redistribution in the microstructure - a process which is simulated as described below.

The fine mesh model of the matrix-inclusion composite forms the basis of computational simulation of damage formation. These are conducted in the following steps.

(i) We subject the boundary of a square-shaped lattice to kinematic boundary con-

ditions

$$u = \varepsilon_j x_j \qquad j = 1, 2 \tag{92}$$

where $\underset{\sim}{\varepsilon} = (\varepsilon_1, \varepsilon_2)$ is the macroscopic (applied) strain (for out of plane elasticity case where $\varepsilon_1 \equiv \varepsilon_{31}$ and $\varepsilon_2 \equiv \varepsilon_{32}$) or intensity (for conductivity case). In the numerical examples in this paper we take $\varepsilon_1 = \varepsilon$ and $\varepsilon_2 = 0$.

(ii) We simulate the increasing loading conditions through raising ε by small increment $\Delta\varepsilon$ in every next run of the simulation.

(iii) In every run we use a relaxation algorithm for the square lattice (conjugate gradient algorithm for the triangle lattice) to solve for the equilibrium of the lattice, and next, we search for all springs, in either matrix or inclusions, whose strains exceed the local fracture criterion

$$\varepsilon^m > \varepsilon^m_{cr} \qquad \text{and} \qquad \varepsilon^i > \varepsilon^i_{cr} \tag{93}$$

For any spring straddling the circular boundaries of inclusions having a weighted stiffness assigned, a harmonic averaged fracture criterion is set up also and a criterion similar to (93) is used. If the above criterion is met, given springs will be removed from the lattice - thus representing a crack - and the microscopic strain ε is increased according to step ii).

(iv) The increase of ε by $\Delta\varepsilon$ is conducted by first unloading the entire lattice, and then reloading it by strain $\varepsilon + \Delta\varepsilon$.

(v) We repeat the above steps until a continuous crack is formed through the whole specimen (state of crack percolation).

the terminology of Section 2, a single specimen $B_\delta(\omega)$ at $\delta \cong 4.5$ and $\omega = \omega_1$, whose overall stress-strain response is given in Fig. 24. Thus, a question arises as to how strong is the scatter among specimens of the same type. To that end we present damage evolution patterns (Figs. 25 and 26) and corresponding stress-strain curves (Fig. 24) for two other configurations indexed by ω_2 and ω_3, respectively. These three stress-strain curves are marked with a, b and c in the figure, respectively. Fig. 24 shows also the response curves of the inclusion material and matrix material *per se*.

Following observations are now in order:

- Scatter in effective moduli in the pre-damage region, as shown in the last chapter, is much smaller than that which sets in after damage starts taking place.
- As expected, qualitatively same damage phenomena occur. A big space of 20 samples will be presented later for statistical study.
- The stress-strain curves are all of the same type - i.e. pre-peak - albeit the scatter in their shapes and the strain - to - failure is significant.
- Presence of inclusions - both random and periodic - has a strongly weakening effect on the overall strength of a composite as compared with the strength of the inclusion material or matrix material; this is due to the strain/stress concentrations.
- Spatial randomness in the distribution of inclusions has a strongly weakening effect on the overall strength of a composite as compared with the strength of an idealized periodic composite, Fig. 24; note that this observation is highly dependent on the particular material parameters - for example, the case $C^i/C^m = 5$ and $\varepsilon^i_{cr}/\varepsilon^m_{cr} = 5$ exhibited a much smaller effect.

Up until now the randomness was due to nonuniform geometric arrangements, while the properties of matrix and inclusions were taken as homogeneous - in reality each material possesses some spatial random inhomogeneity in elastic moduli and strength, and thus the damage patterns and the effective response of an actual periodic system would differ from the one in Fig. 24 because of damage localization; those effects are examined

later.

(iii) The issue of material microstructure randomness effects on the overall composite properties can further be clarified by a comparison with a composite of exactly same volume fraction (i.e. 0.349) but a perfectly periodic distribution of inclusions, the results from which configuration are shown in Fig. 24 and Fig. 27. The former contains the entire stress-strain response of such a composite, and the latter illustrates the evolution of damage.

Once again, in view of Fig. 24, it is seen that the effective conductivities in both random and periodic cases are almost identical. However, the stress-strain curve for the periodic case extends much longer than for the random cases, and there are some differences between the random cases themselves. The smaller strength in the random case is caused by the stress concentration due to the nonuniform distribution of inclusions. This can also be observed from Fig. 27 where the deformation appears uniform, and the damage happens periodically in the configuration at same time so that the composite can undertake higher loading than in the random case. Also, the fact that the breaks occur uniformly in Fig. 27 for the case of a composite with the periodic arrangement of inclusions shows our algorithm and program work well.

(iv) In order to better understand the effect of randomness of special arrangements of inclusions on the overall mechanical properties, the other case with the different stiffness ratio and strength ratio, $C^i/C^m = 2$ and $\varepsilon^i_{cr}/\varepsilon^m_{cr} = 0.2$, is illustrated here. Figs. 28 - 30 and Fig. 31 are the damage evolution graphs for three random samples and the periodic one. The corresponding stress-strain curves are shown in Fig. 32. From these graphs the following conclusions are drawn.

The stress-strain curves are all of the same type, although the scatter between them in their strain-failure is noticeable. But different from the case in the last section, the effective response of the composite, both random and periodic, is of the elastic-brittle type with feature of one peak only in the curve.

As expected, qualitatively same damage phenomena occur, but the idealized periodic composite leads to an overestimate of the effective strength: geometric randomness has a weakening effect. However, different from the last case, here the damage forms initially in the denser region due to stress concentrations in their vicinity, stiff inclusions tend to form links carrying relatively more load. Microcracking then spreads across the specimen whereby the random character of the damage pattern reflects the heterogeneity of the microstructure.

Presence of inclusion, both random and periodic, has a weakening effect on the overall strength of a composite as compared with the strength of the inclusion material or matrix material, due to the stress and strain concentration.

(v) Comparing to the case in section (ii), the effect of changing $\varepsilon_{cr}^{i}/\varepsilon_{cr}^{m}$ while keeping the stiffness ratio C^i/C^m fixed is shown in Figs. 33 and 34; the first one gives the damage evolution pattern, while the second presents the stress-strain curve; note that the same geometry as in Fig. 23 is being used. We see that:

- Although the inclusions are softer than the matrix, just as in the previously studied case, their now higher strength causes damage to initiate in the matrix.
- Cracking occurs within the inclusions at a later stage, and is seen to be needed for a total breakdown of a composite. Comparing with the case in the last section, the different strength ratio leads to the different damage processes.
- The stress-strain response is of the pre-peak type.

(vi) A question may be raised at this point as to the effect of a small change in composite's geometry on both the damage pattern and the overall stress-strain response. Such a change is present in the composite of Fig. 35 as compared to the original one of Fig. 33. It is seen from the ensuing damage evolution that such small microstructural variations can lead to some differences in crack patterns and thus to nonnegligible changes in stress-strain curves as shown in Fig. 34 in which the curves for the two different configuration are marked by d and e, respectively.

(vii) At this stage we return to the aspect of mesh dependence in our simulation method. Some light on this very broad and important issue is shed by simulations of

exactly same composite as the one of Fig. 35 at double the mesh spacing per inclusion as presented in Fig. 36. The corresponding stress-strain curve is marked by f. A comparison of these two figures indicates that cracks form and evolve in almost same locations at two different mesh resolutions. However, this is a delicate issue which requires a further study; see also (de Borst et al, 1993). The stress-strain response curves given in Fig.34 show that the qualitative features are preserved under a change of mesh.

(viii) Furthermore, we are concerned with the effects of intrinsic randomness of geometric arrangements of inclusions on the overall stress-strain response of composite in the entire parameter space which is specified by two parameters, as used previously: the stiffness ratio C^i/C^m and strain-to-failure (strength) ratio $\varepsilon_{cr}^i/\varepsilon_{cr}^m$. In the following we call the plane defined by these two parameters a 'damage plane', and a representation of a given property, such as effective stress-strain curves, a 'damage map'.

Fig. 37 shows the damage map of stress-strain curves of composites and the related matrix and inclusion materials for the all nine combination of the two parameters which are valued as 0.1, 1 or 10. Fig.38 shows the same damage map without the curves for matrix and inclusion materials so that a bigger scale can be used to get more details. It is observed that from the left of the map to the right, from the bottom to the top, i.e., as the strength ratio and stiffness ratio increase, the type stress-strain curve changes from the pre-peak to the elastic-brittle one. Correspondingly, the break initiates from inside the inclusion to inside the matrix. In the former case, cracks initiate in the weak inclusion, then stop growing until a high level of load is reached due to the difference between the properties of matrix and inclusion materials. The cracking procedure is discontinuous so that the stress-strain curves are of the pre-peak type. In the latter case, cracks develop through the matrix material continuously and the stress- strain curve is of the post-peak (or elastic-brittle) type.

Fig. 39 is the corresponding damage pattern map. It is clear that from the left side, fluctuation of location of the figure to the right side, from the bottom to the top, the crack initiates from inside the inclusion to inside the matrix.

(ix) As stated earlier, models of uniform materials are usually used for analysis, however, real materials are always heterogeneous due to fluctuation of geometry or prop-

erties of material's constituents. The influence of geometry is considered here.

Figs. 40 - 41 illustrate the effect of fluctuation of inclusion location on the damage pattern map and the stress-strain curve for the parameters $\varepsilon_{cr}^{i}/\varepsilon_{cr}^{m} = 2$ and $C^i/C^m = 0.2$, respectively. In Fig. 40, the left column represents the evolution of the idealized periodic arrangement of inclusions, while the right column the case of that the inclusion at the third column and the third row is moved up one unit. Although the cracks initiate in the matrix in both cases, only one crack, instead of many in the idealized case, forms in the vicinity of the inclusion which is moved. It indicates the damage pattern is quite different due to the stress concentration.

Fig. 41 shows the stress-strain curve also fluctuates due to the concentration and the composite is weakened.

Figs. 42 - 43 illustrate the cases with two different sets of parameters: $\varepsilon_{cr}^{i}/\varepsilon_{cr}^{m} = 2$, $C^i/C^m = 5$ and $\varepsilon_{cr}^{i}/\varepsilon_{cr}^{m} = 0.5$, $C^i/C^m = 0.1$. Similarly as before, the cracks are not uniformly distributed any more. It should be noted that for the first two case is cracks always occur in the matrix no matter if the location of the inclusion moved, but for the last case the crack which initiates in the inclusion for the idealized composite, will start in the matrix responding to the small change of the inclusion location.

(x) In addition to geometry, we examine the effect of fluctuation of matrix materials on the damage pattern and stress-strain curves which are shown in Figs. 44 - 49. At this point, we assume that the strength of matrix deviates a little from the uniform status as following

$$\begin{aligned} \hat{\varepsilon}_{cr} &= \varepsilon_{cr} + \Delta\varepsilon_{cr} \\ &= \varepsilon_{cr}\left(1 + \frac{r}{N}\right) \end{aligned} \tag{94}$$

where, ε_{cr} = strength of uniform material

$\Delta\varepsilon_{cr}$ = strength fluctuation

r = uniform distribution random number, [-0.5, 0.5]

N = weight factor, 100 in this case.

The parameter pairs chosen for the material fluctuation are: $\varepsilon_{cr}^{i}/\varepsilon_{cr}^{m} = 2$, $C^i/C^m = 0.2$; $\varepsilon_{cr}^{i}/\varepsilon_{cr}^{m} = 2$, $C^i/C^m = 5$ and $\varepsilon_{cr}^{i}/\varepsilon_{cr}^{m} = 0.5$, $C^i/C^m = 0.1$ for three different cases. Comparing with the uniform materials, the figures show that the damage of composites is not uniform any more due to the stress concentration caused by the existing fluctuation. The appearance and location of cracks are very much similar to those without material fluctuation, but the number of them reduce to one. Figs. 45, 47 and 49 indicate the stress-strain responses with or without material fluctuation are quite similar to each other, the stiffness is unchanged and only the strength of composites is reduced.

(xi) All previous studies are conducted by using one or a few samples for each case of randomly arranged inclusions. The problem to be deal with is: what is the response of stress-strain relation to the random configuration of inclusions? For this purpose, the Ω space containing 20 samples is employed for statistical study. The numerical characteristics are also included. Figs. 50, 53, 56, 59, 62, 65 and 68 are assembly of effective constitutive responses. Figs. 51, 54, 57, 60, 63, 66, 69 and 52, 55, 58, 61, 64, 67, 70 give the distribution function of maximum stresses and strain which are normalized by the corresponding matrix properties, respectively.

Fig. 71 gives the damage map of constitutive curves. The pair of parameters, $\varepsilon_{cr}^{i}/\varepsilon_{cr}^{m}$ and C^i/C^m are used. The results from the 20 samples for each different pair of parameter show the type of constitutive curves may change by chance. Fig. 72 and 73 give the damage map of maximum stress distribution function and maximum strain distribution function, respectively.

5.3 CLOSURE

As expected, the statistical analysis reported here shows that the conductivities of composites are less dependent on the randomness of configuration. In contrast to this, big deviations of maximum stress or strain are found, which suggests that the stochastic study is necessary and important to determine properties of heterogeneous materials.

We would like to conclude with the following statement. The discrete lattice and continuum models have quite different - if not opposing, and hence mutually complementing - features. Thus, for example, the discrete lattice approach as presented here enables one to capture the global aspects of randomness, while the continuum based approach is suited to conduct a detailed study of interaction of a crack with a single inclusion, see e.g. Li and Chudnovsky (1993). The damage initiation and propagation in composite materials cannot be adequately addressed without the incorporation of geometric and material randomness, and thus the present study illustrates a need as well as a possible basis for a stochastic continuum damage mechanics of such systems. The damage information obtained in this study needs to be compared with experiments and results of other numerical methods.

REFERENCES

Beale, P.D. and Srolovits, D.J., 1988, "Elastic fracture in random materials," *Phys. Rev.*, Vol. B37, pp. 5500-5507.

Brockenbrough, J.R., Suresh, S. and Wienecke, H.A., 1991, "Deformation of metal-matrix composites with continuous fibers: geometrical effects of fiber distribution and shape," *Acta Metall. Mater.*, Vol. 39 (5), pp. 735-752.

Carmeliet, J. and De Borst, R., 1994, "Stochastic approaches for damage evolution in quasi-brittle materials," *Probabilities and Materials - Tests, Models and Applications,* NATO ASI Series E - Vol.269, pp. 491-503, Kluwer, Dordrecht.

Chan, S., Kim, S.G. and Duxbury, P.M., 1992, "Elasticity and fracture of tubular honeycombs containing random vacancies," Unpublished work.

Chen, J. and Thorpe, M.F., 1992, "Fiber aligned glass/epoxy composites with second and third order bounds," Unpublished work.

Christensen, R.M., 1979, *Mechanics of Composite Materials*, J. Wiley & Sons, New York.

de Borst, R., Pamin, J., Schellekens, J.C.J. and Sluys, L.J., 1993, "Continuum models for localized failure," *Proc. IUTAM Symp. on Fracture of Brittle Disordered Materials.*

Day, A.R., Snyder, K.A., Garboczi, E.J. and Thorpe, M.F., 1992, "The elastic moduli of a sheet containing circular holes," *J. Mech. Phys. Solids*, Vol. 40 (5), pp. 1031-1051.

Duxbury, P.M., Kim, S.G., and Leath, P.L., 1994, "Size effect and statistics of fracture in random materials," *Mat. Sci. and Eng. A*, A176, pp. 25-31.

Duxbury, P.M., 1990, "Breakdown of diluted and hierarchical systems," in *statistical Models for the Fracture of Disordered Media,* Herrmann, H.J. and Roux, S., eds., Elsevier/North-Holland, pp. 189-228

Eshelby, J.D., 1957, "The determination of the field of an ellipsoidal inclusion and related problems," *Proc. Royal Soc. Lond. A*, Vol. 241, pp. 376-396.

Hashin, Z., 1983, "Analysis of composite materials - A survey," *J. Appl. Mech.*, Vol. 50, pp. 481-505.

Herrmann, H.J. and S. Roux, S., eds., 1990, *Statistical Models for Fracture of Disordered Media*, Elsevier.

Holnicki-Szulc, J. and Rogula, D., 1979, "Nonlocal, continuum models of large engineering structures," *Arch. Mech.*, Vol. 31 (6), pp. 793-802.

Huet, C., 1990, "Application of variational concepts to size effects in elastic heteroge-

neous bodies," *J. Mech. Phys Solids.*, 38 (6), pp. 813-841.

Jagota, A. and Bennison, S.J., 1993, "Spring-network and finite-element models for elasticity and fracture," in *Breakdown and Non-Linearity in Soft Condensed Matter,* Bardhan, K.K., Chakrabarti, B.K. and Hansen, A.,eds., Springer-Verlag, in print.

Keating, P.N., 1966, "Effect of invariance requirements on the elastic strain energy of crystals with application to the diamond structure," *Phys. Rev.*, Vol. 145, pp. 637-645.

Khang, B., Batrouni, G.G., Redner, S., de Arcangelis, L. and Herrmann, H.J., 1988, "Electrical breakdown in a fuse network with random, continuously distributed breaking strengths," *Phys. Rev.*, Vol. B37, pp. 7625-7637.

Kirkwood, J.G., 1939, "The skeletal modes of vibration of long chain molecules," *J. Chem. Phys.*, Vol. 7, pp. 506-509.

Krajcinovic, D. and Lemaitre, J., 1987, *Continuum Damage Mechanics - Theory and Applications*, CISM Lectures, Springer-Verlag.

Lemaitre, J., 1992, *A Course on Damage Mechanics*, Springer-Verlag, Berlin.

Li, R. and Chudnovsky, A., 1993, "Variation of the energy release rate as a crack approaches and passes through an elastic inclusion," *Intl. J. Fracture*, Vol. 59, pp. R69-R74.

Maugin, G.A., 1992, *The Thermomechanics of Plasticity and Fracture*, Cambridge Uni-

versity Press.

Mura, T., 1987, *Micromechanics of Defects in Solids,* Martinus Nijhoff Publishers, Hague.

Murzewski, J., 1957, "A statistical theorey of brittle quasi-homogeneous solids," *Proc. 9th IUTAM Congress,* Vol. 5, pp. 313-320.

Muskhelishrili, N.I., 1953, *Some Basic Problems of the Mathematical Theory of Elasticity,* Noordhoff.

Ostoja-Starzewski, M. and Wang, C., 1989, "Linear elasticity of planar Delaunay networks: random field characterization of effective moduli," *Acta Mech,* Vol. 80, pp.61-80.

Ostoja-Starzewski, M. and Wang, C., 1990, "Linear elasticity of planar Delaunay networks - II: Voigt and Reuss bounds, and modification for centroids," *Acta Mech,* Vol. 84, pp.47-61.

Ostoja-Starzewski, M., 1992, "Random fields and processes in mechanics of granular materials," in *Advances in Micromechanics of Granular Materials* (Proc. 2nd US-Japan Seminar on Micromechanics of Granular Materials; H. Shen et al, Eds.); *Stud. Appl. Mech.*, Vol. 31, pp. 71-80, Elsevier; extended version in *Mech. Mater.*, Vol. 16 (1-2), pp. 55-64, 1993.

Ostoja-Starzewski, M., 1993a, "Micromechanics as a basis of random elastic continuum approximations," *Probabilistic Engng Mech.*, Vol. 31 (2), pp. 107-114.

Ostoja-Starzewski, M., 1993b, "Micromechanics as a basis of stochastic finite elements and differences - an overview," *Appl. Mech. Rev.* (Special Issue: *Mechanics Pan-America 1993*, M.R.M. Crespo da Silva and C.E.N. Mazzilli, eds.), Vol. 46 (11, Part 2), pp. S136-S147.

Ostoja-Starzewski, M., Alzebdeh, K. and Jasiuk, I., 1994, "Linear elasticity of planar Delaunay networks - III: Self-consistent approximations," *Acta Mech.*, in press.

Ostoja-Starzewski, M. and Jasiuk, I. eds., 1994, *Appl. Mech. Rev.* (Special Issue: *Micromechanics of Random Media*), Vol. 47 (1, Part 2).

Ostoja-Starzewski, P.Y. Sheng and I. Jasiuk, 1994, "Influence of random geometry on effective properties and damage formation in composite materials," *ASME Journal of Engineering Materials and Technology*, Vol. 116, pp. 384-391.

Ostoja-Starzewski, P.Y. Sheng and I. Jasiuk, 1994, "Micromechanics as a basis of stochastic continuum damage mechanics," *in Material Instabilities: Theory and Application (R.C. Batra and H.M. Zbib, Eds)*, AMD-Vol.183, MD-Vol.50, ASME-Press, pp.131-141.

Ostoja-Starzewski, P.Y. Sheng and I. Jasiuk, 1994, "Influence of random fiber arrangement on crack propagation in brittle-matrix composites," *Proc. 4th Conference on Brittle-Matrix Composites (A.M. Brandt, ED.), Warsaw, Poland.*, pp. 200-207.

Sahimi, M. and Goddard, J.D., 1986, "Elastic percolation models for cohesive mechanical failure in heterogeneous systems," *Phys. Rev.*, Vol. B33, pp. 7848-7851.

Schlangen, E., 1993, "Experimental and numerical analysis of fracture processes in concrete," *Ph.D. Dissertation*, Technological University of Delft.

Snyder, K.A., Garboczi, E.J., and Day, A.R., 1992, "The elastic moduli of simple two-dimensional isotropic composites: Computer simulation and effective medium theory," *J. Appl. Phys.*, Vol. 72 (12), pp. 5948-5955.

Vanmarcke, E.H., 1983, *Random Fields: Analysis and Synthesis*, MIT Press, Cambridge, MA.

Volkov, S.D., 1960, *Statistical Theory of Strenth of Materials*, Mashgiz, Moscow.

Weibull, W., 1938, A statistical theory of the strenth of materials, *Ingen. Vetenskap. Akad. Handl.*, Vol. 15, pp. 1-45.

Ziegler, H. and Wehrli, Ch., 1987, "The derivation of constitutive relations from the free energy and the disspation functions," in *Adv. Appl. Mech.* 25, pp. 182-238, Academic Press.

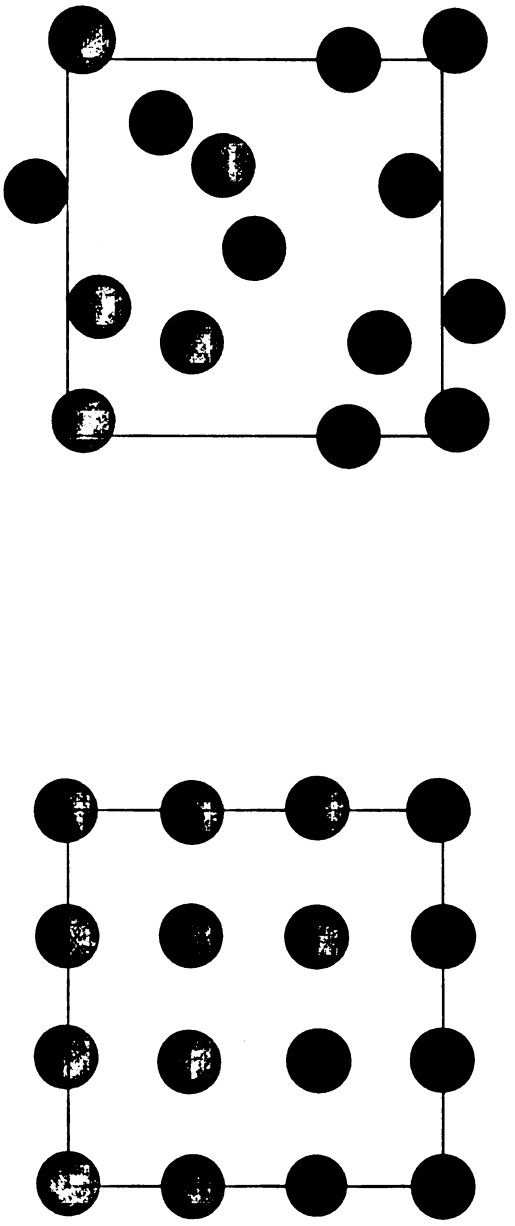

Fig. 10 Composite configuration: periodic and random arragement of inclusions

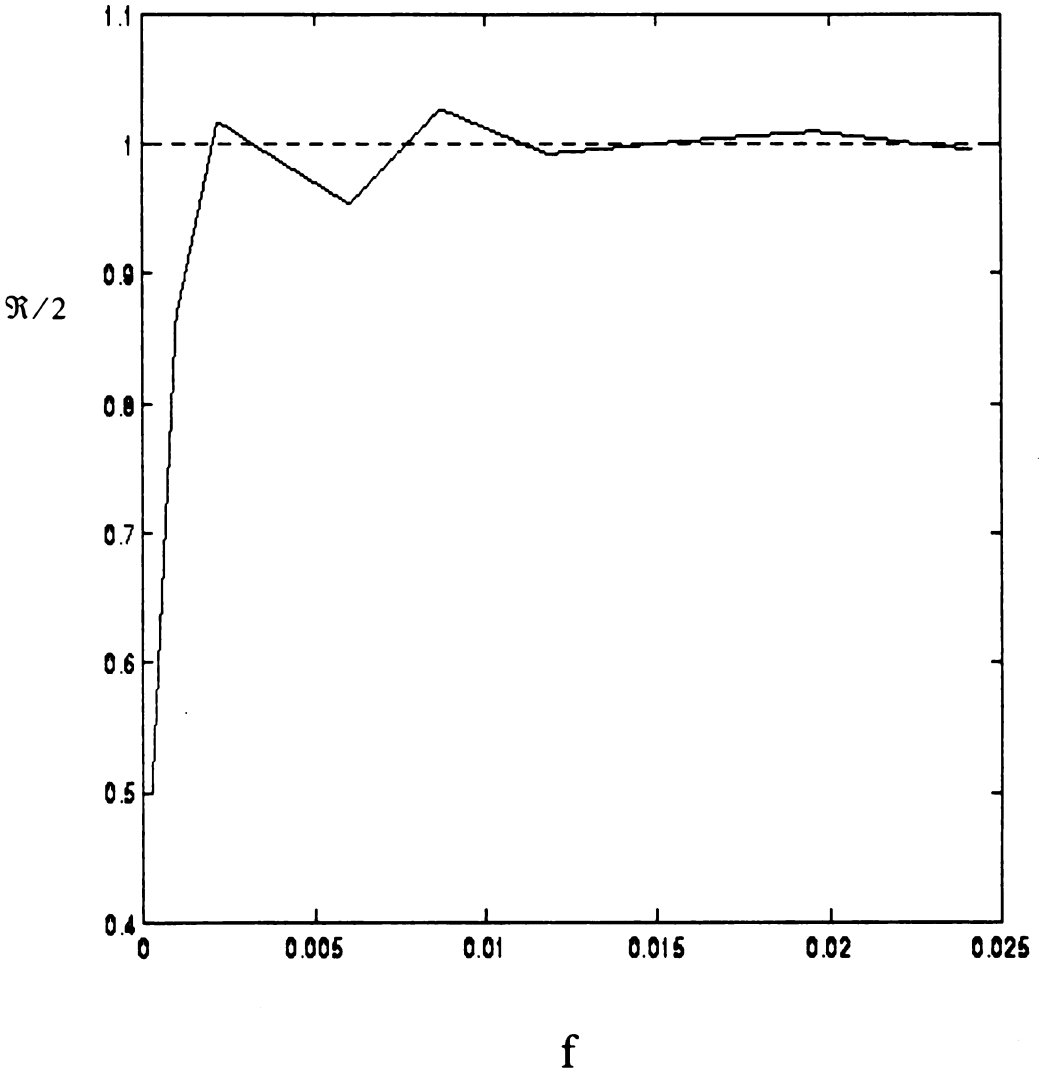

Fig. 11 Influence of hole size on effective conductivity

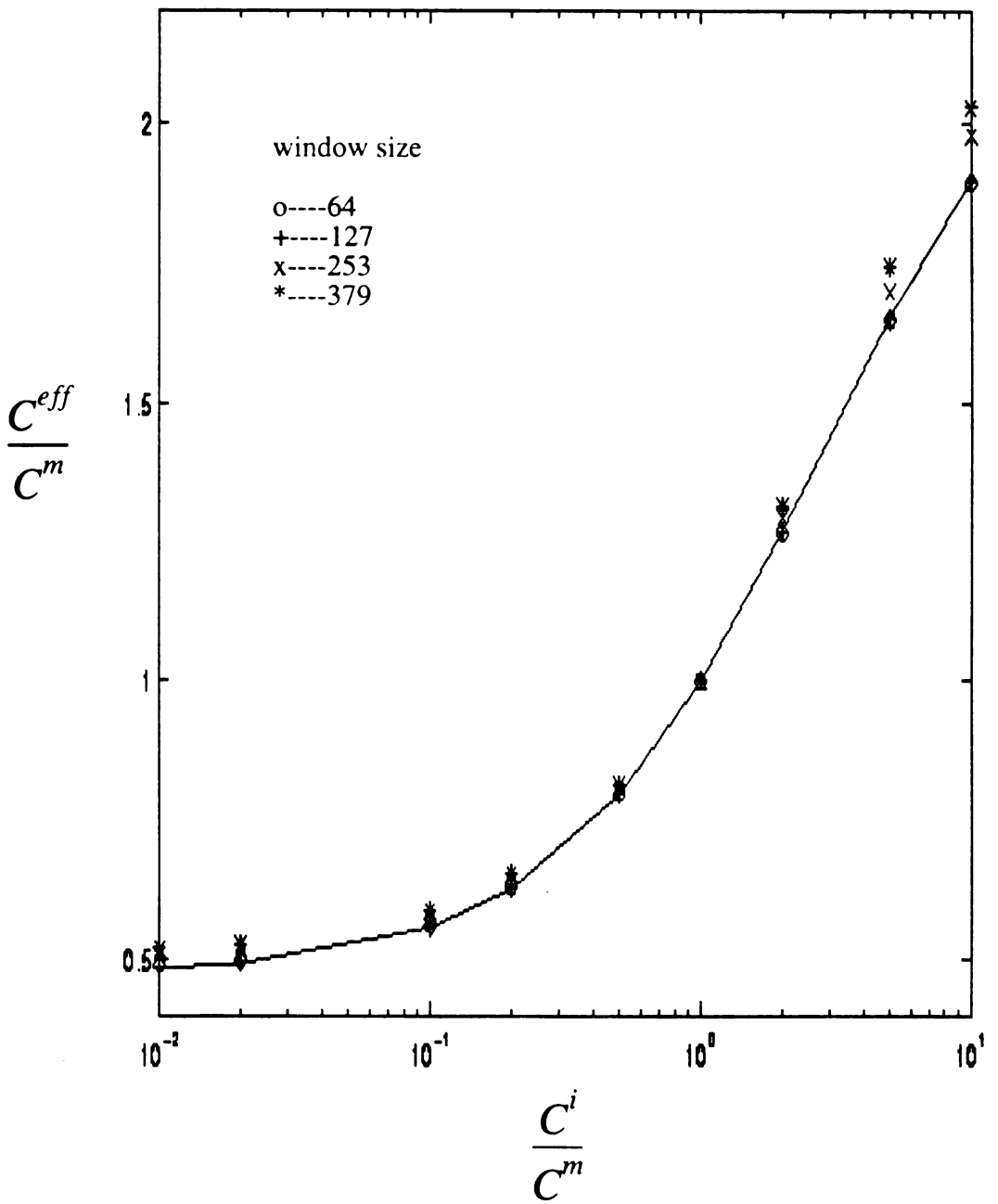

Fig.12 Mesh dependence of effective conductivity

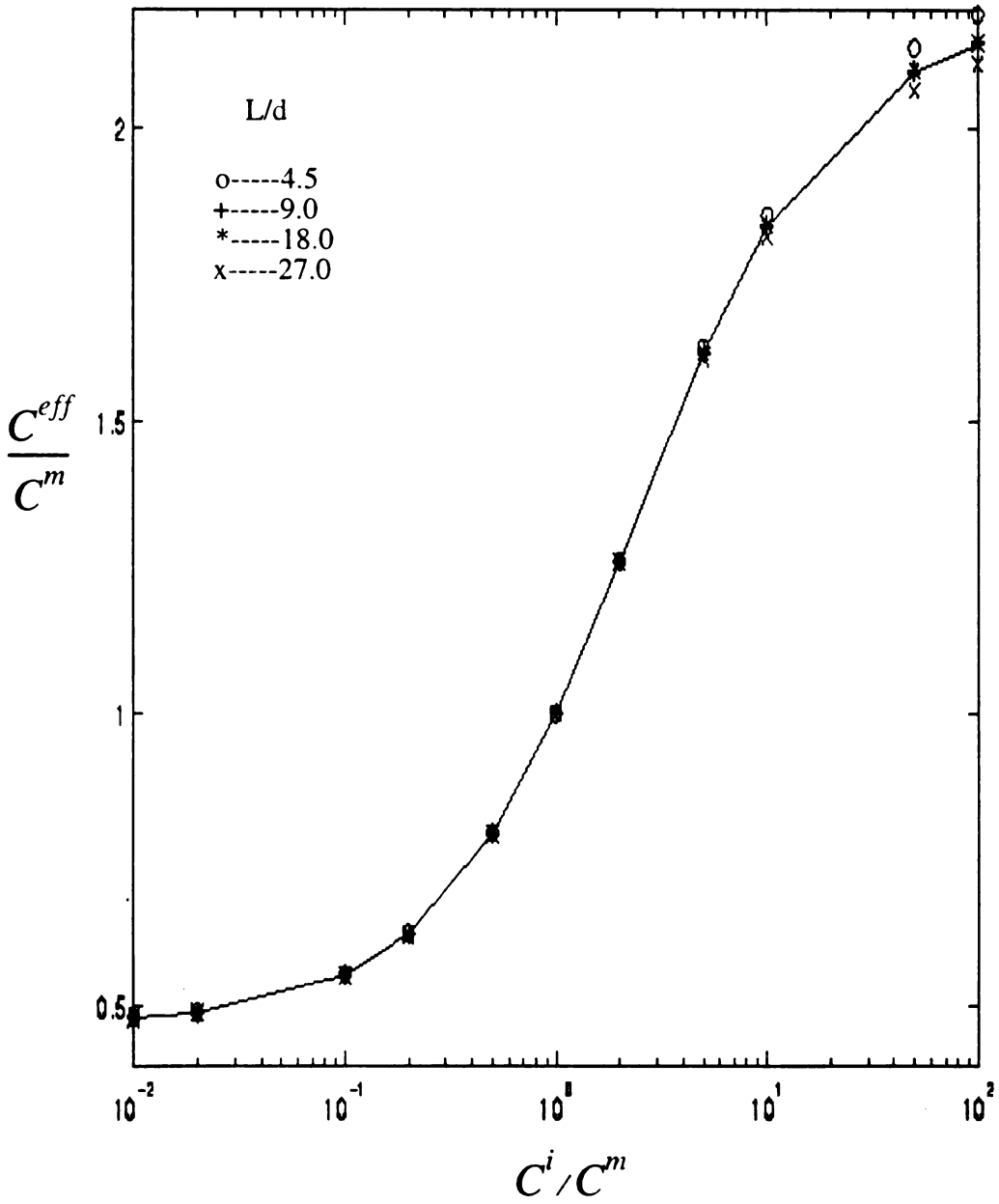

Fig. 13 Delta dependence of effective conductivity

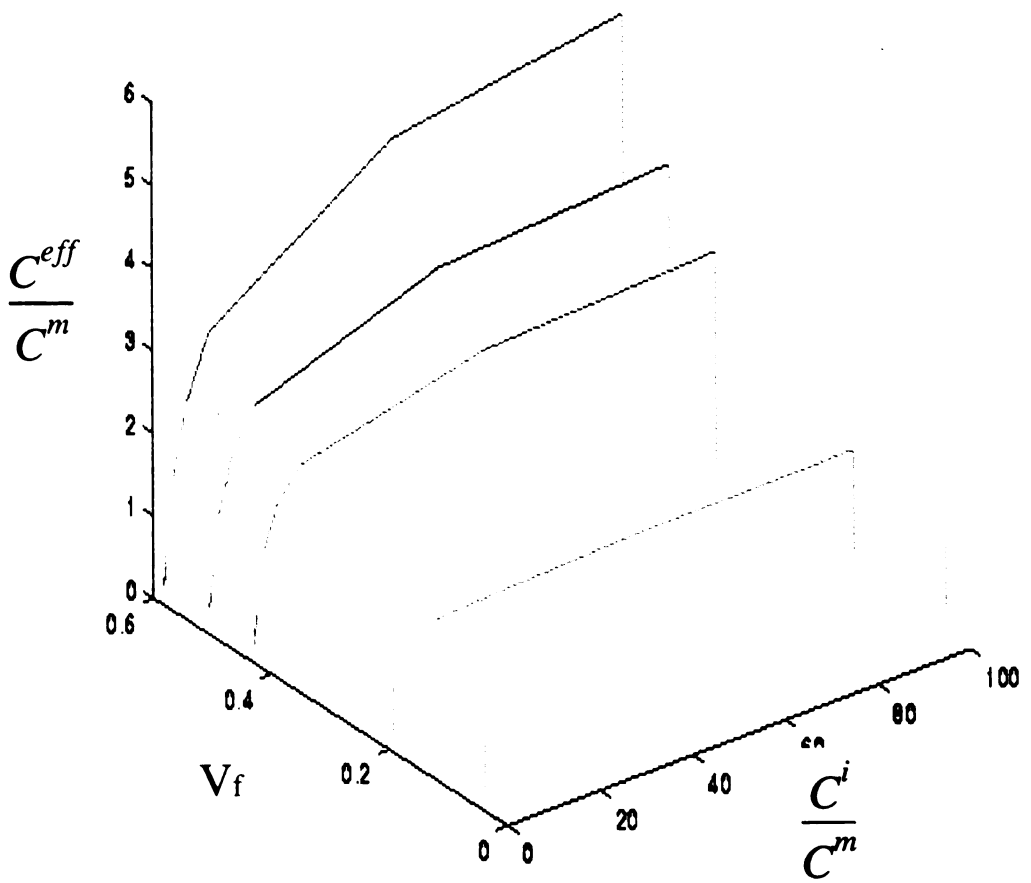

Fig. 14 Effective conductivity, at window size L=64

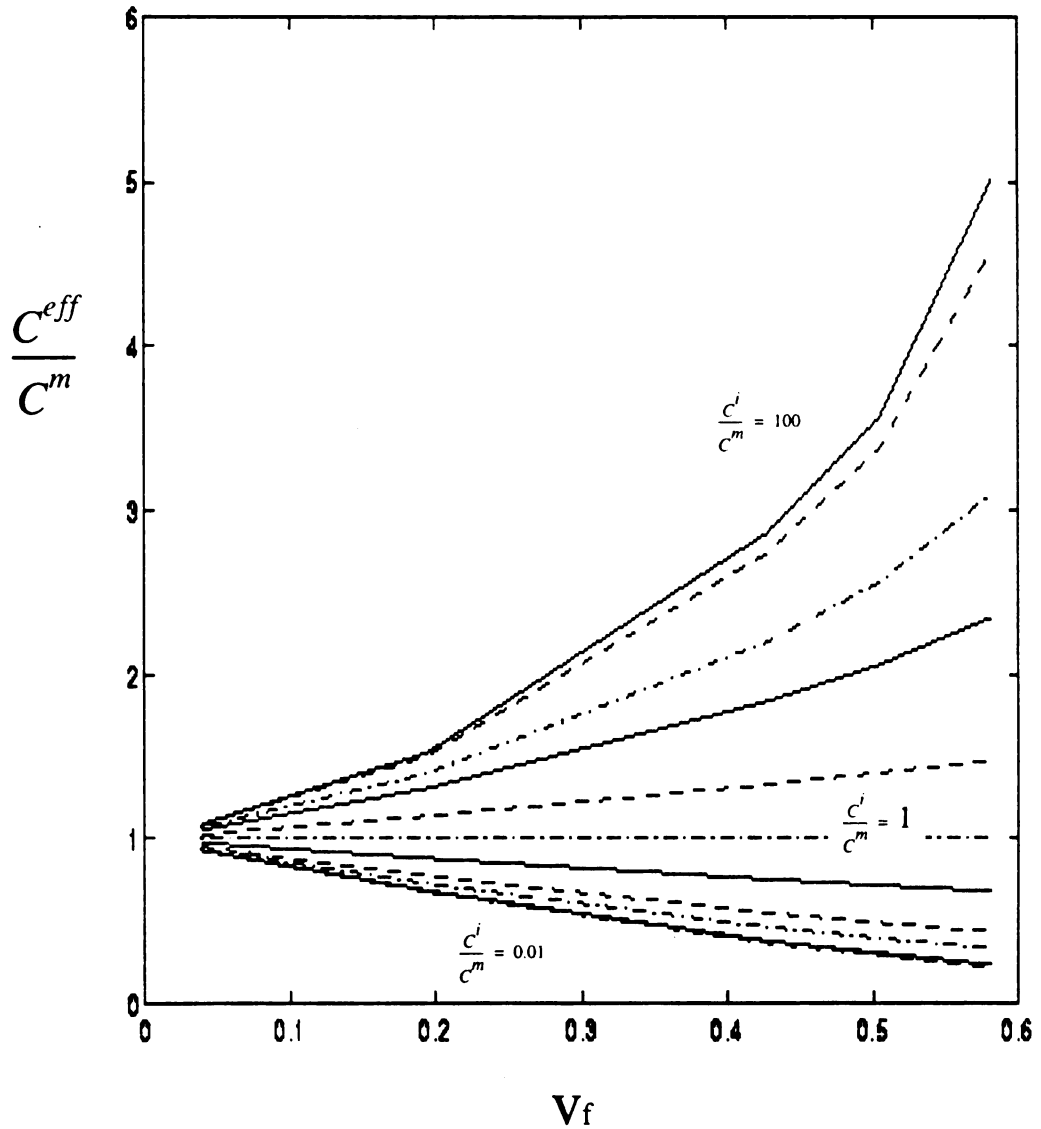

Fig. 15 Effective conductivity versus volume fraction, at window size L=64

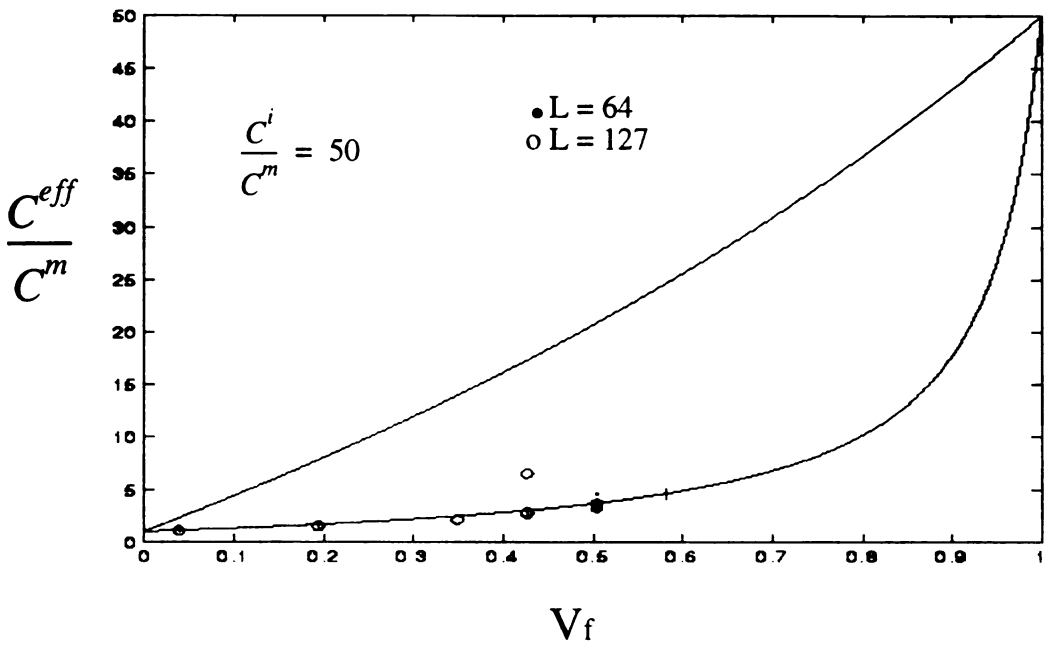

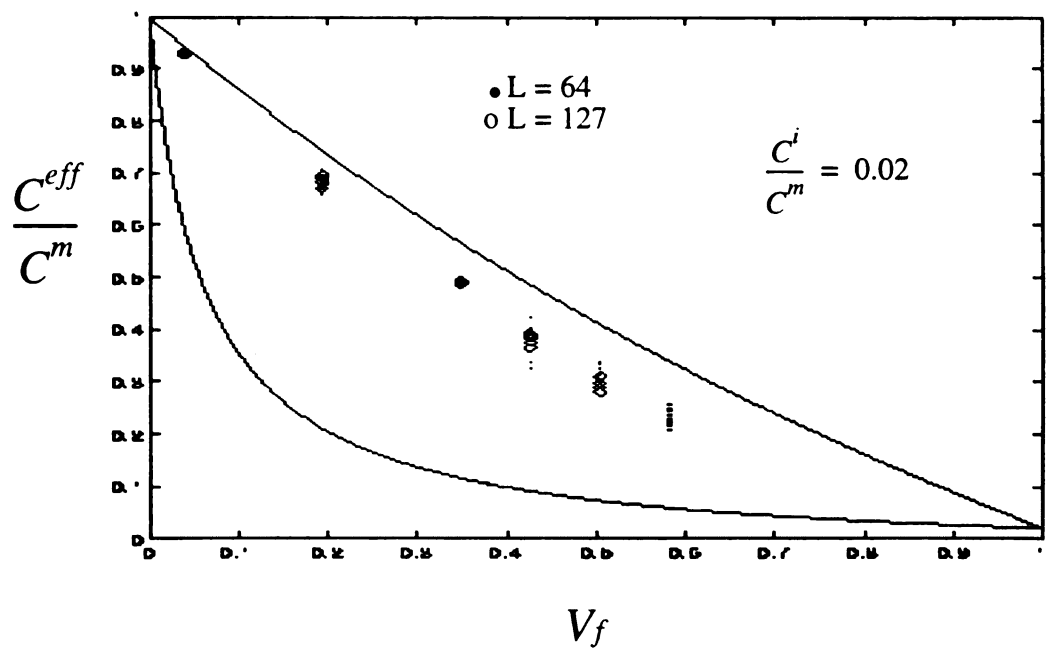

Fig. 16 Effective conductivity and Hashin second order bounds versus volume fraction, C^i/C^m = 0.02 and 50

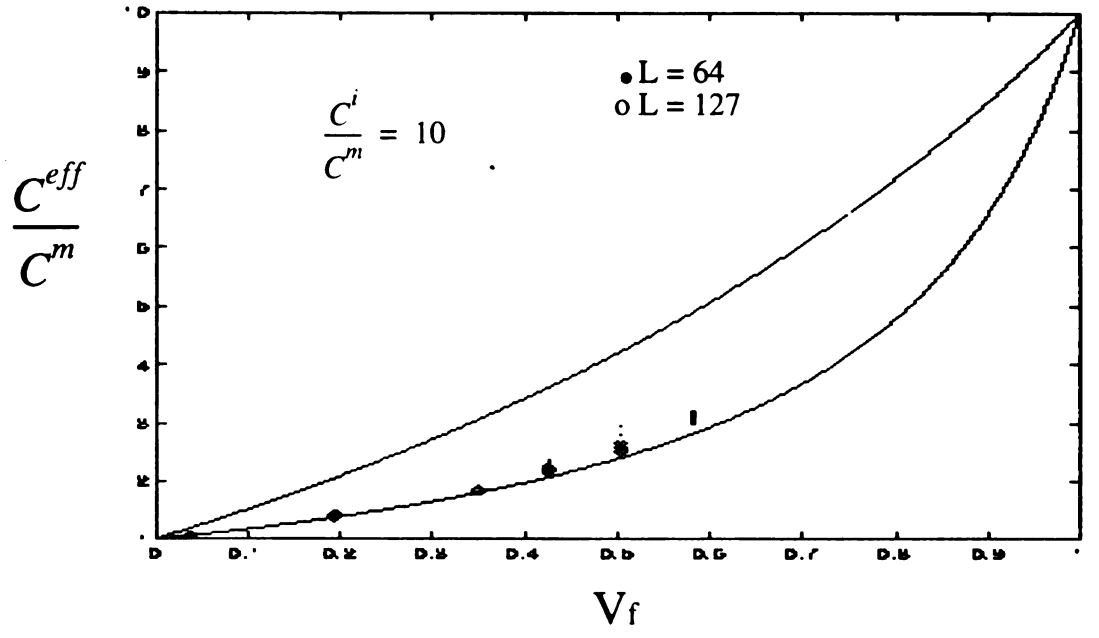

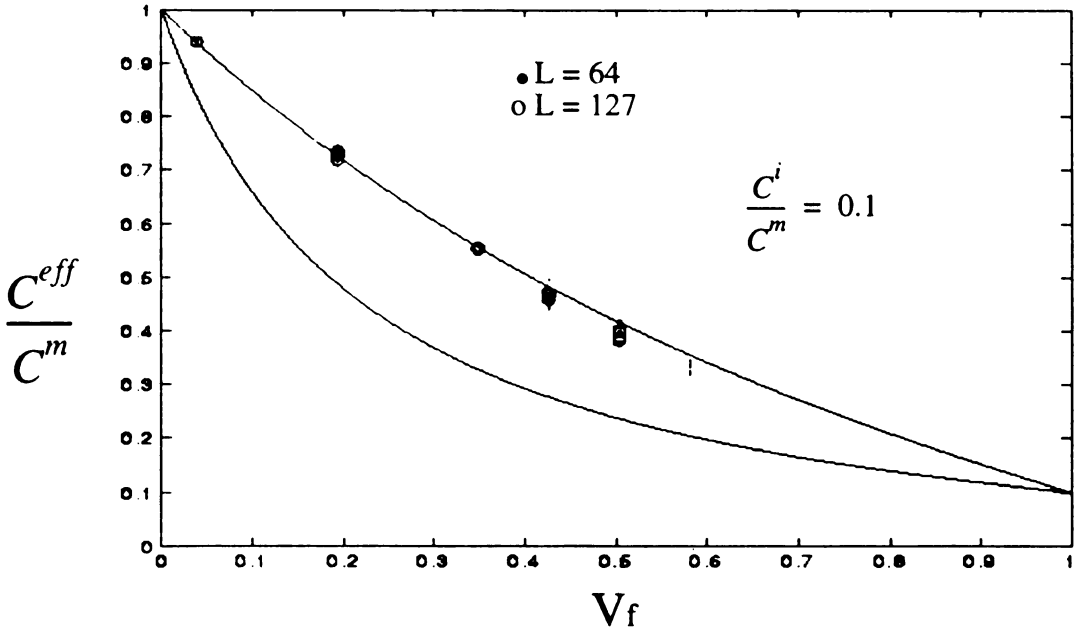

Fig. 17 Effective conductivity and Hashin second order bounds versus volume fraction, C^i/C^m = 0.1 and 10

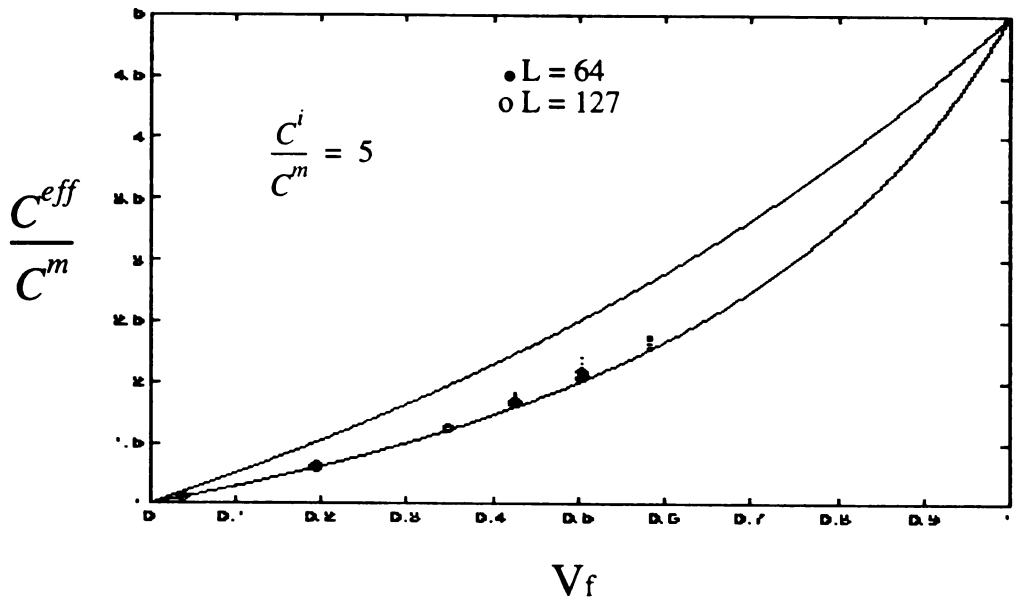

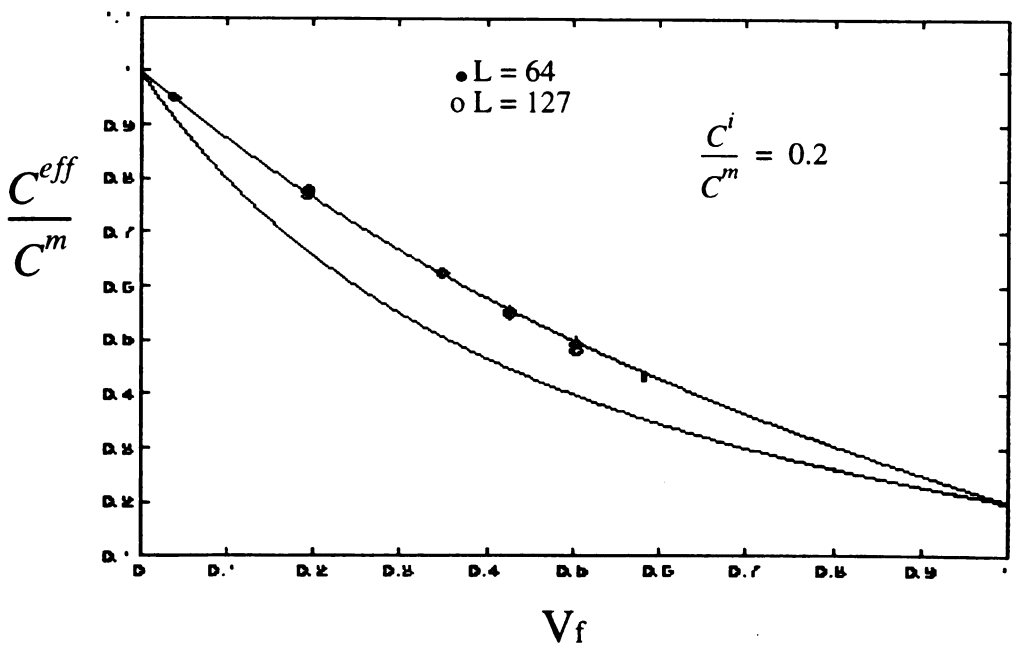

Fig. 18 Effective conductivity and Hashin second order bounds versus volume fraction, C^i/C^m = 0.2 and 5

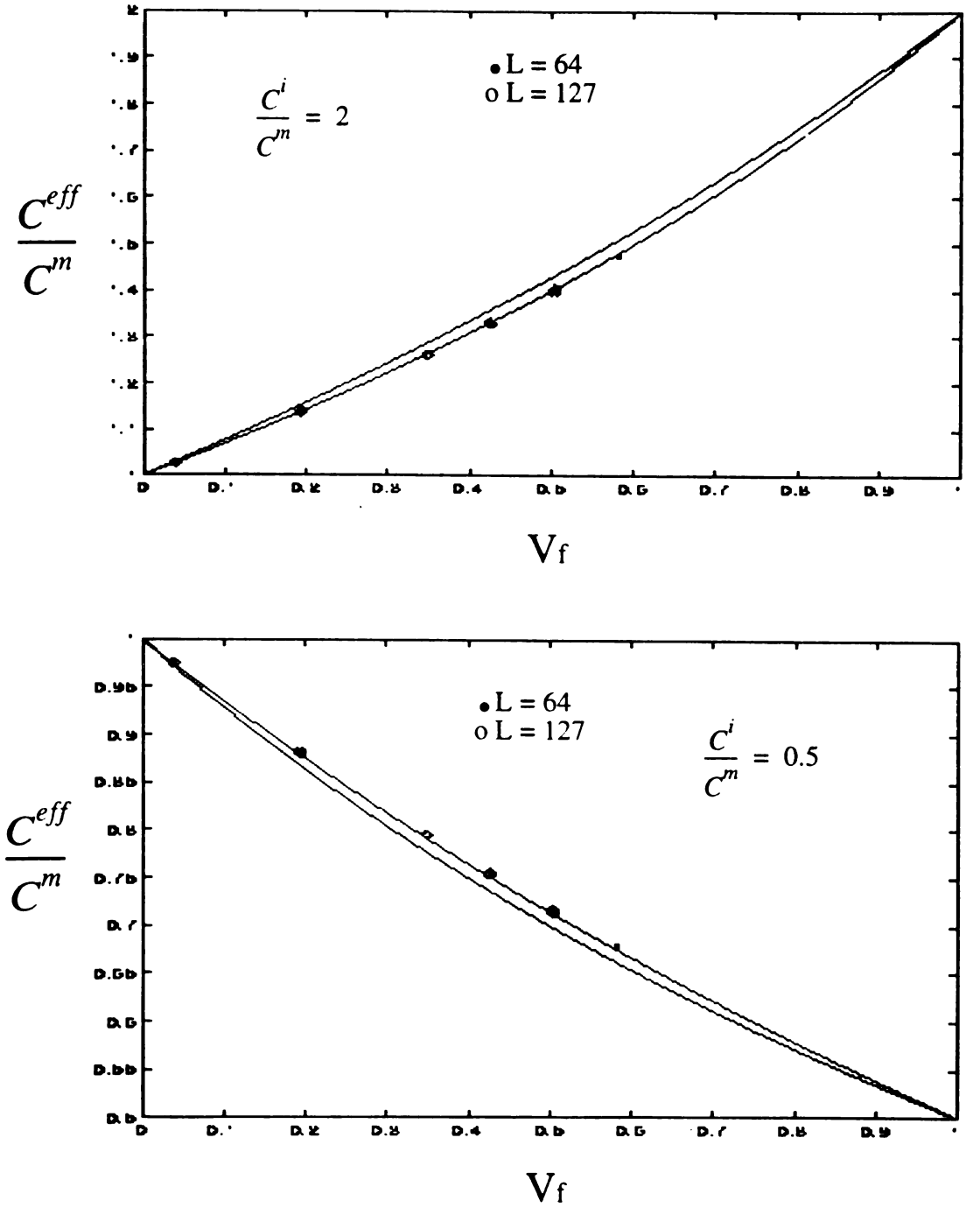

Fig. 19 Effective conductivity and Hashin second order bounds versus volume fraction, C^i/C^m = 0.5 and 2

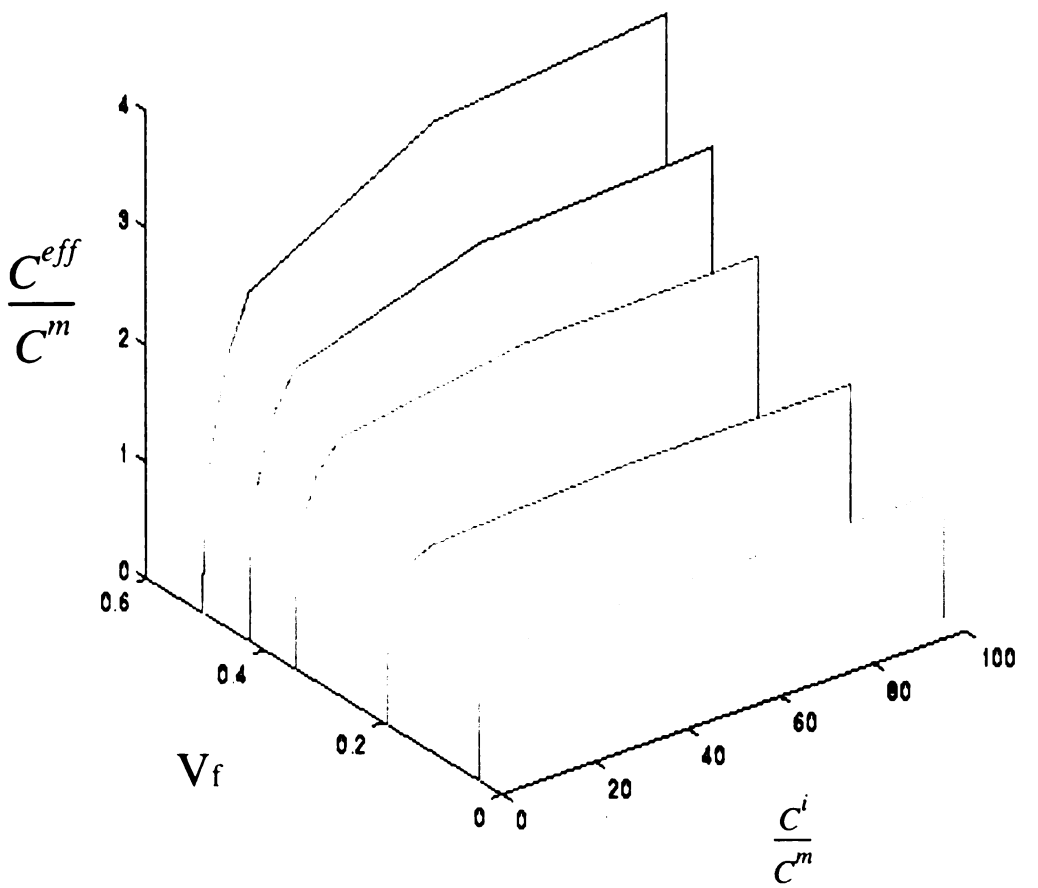

Fig. 20 Effective conductivity, at window size L = 128

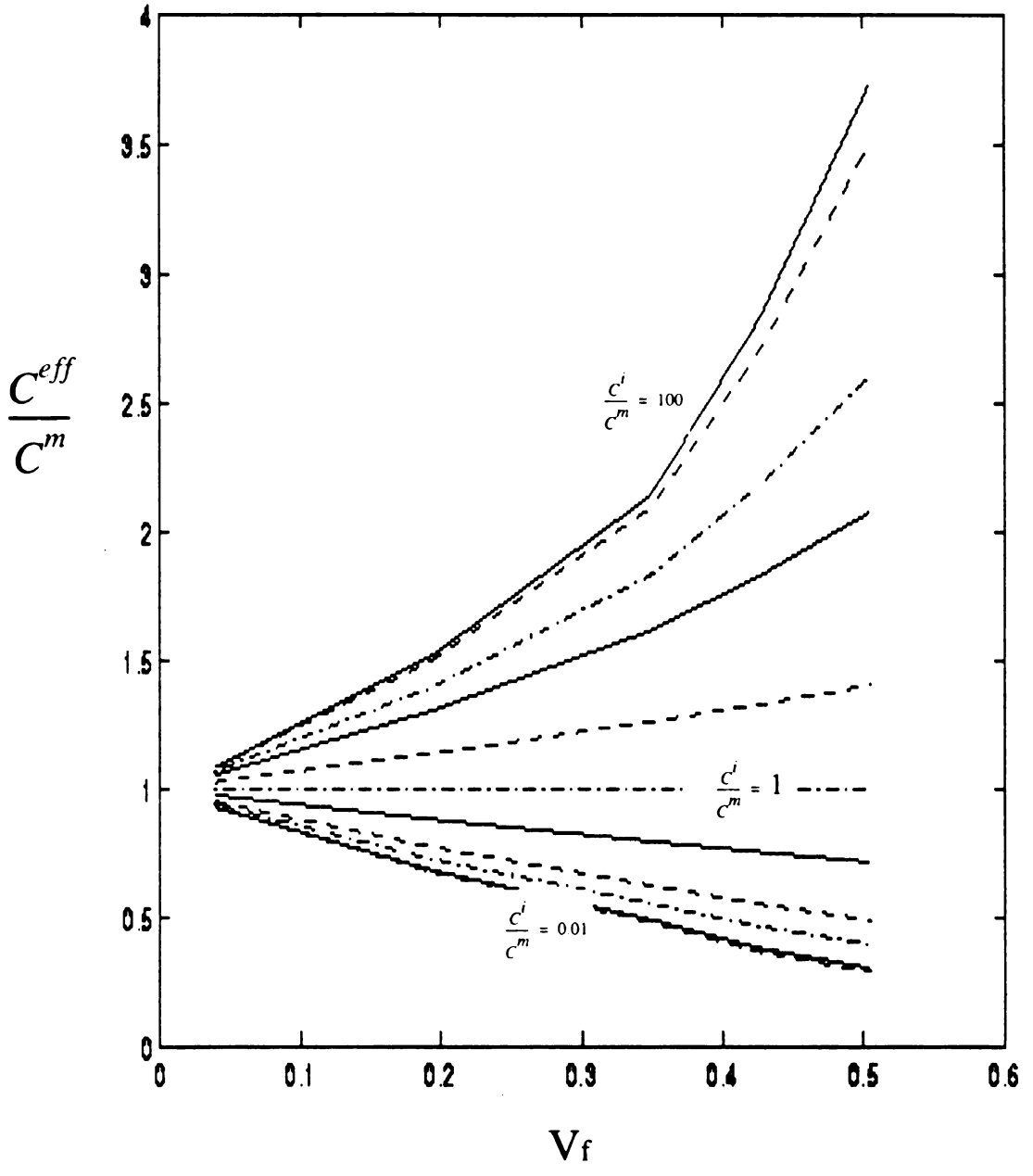

Fig. 21 Effective conductivity versus volume fraction, at window size L = 128

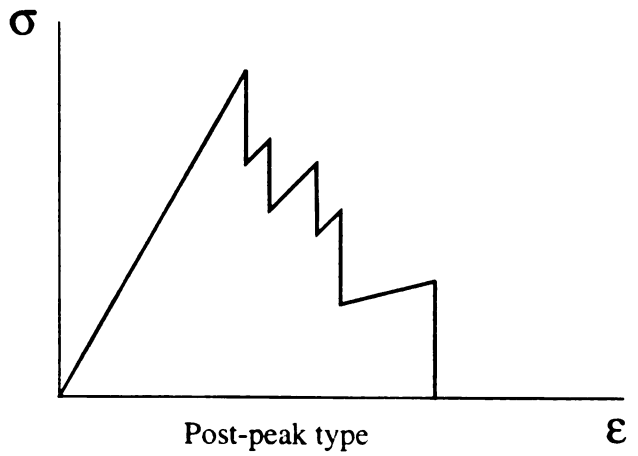

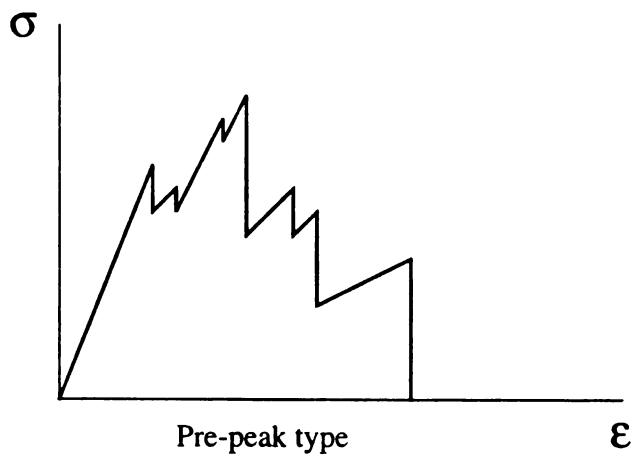

Fig. 22 Two kinds of constitutive responses

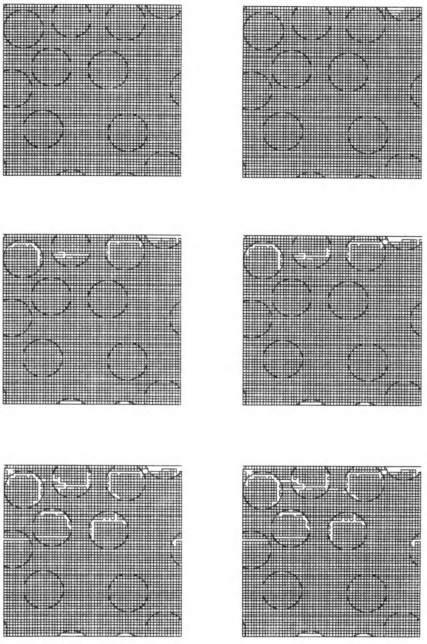

Fig. 23 Damage pattern for random arrangement of inclusion,

$\varepsilon^i/\varepsilon^m = 0.5, \quad C^i/C^m = 0.1$

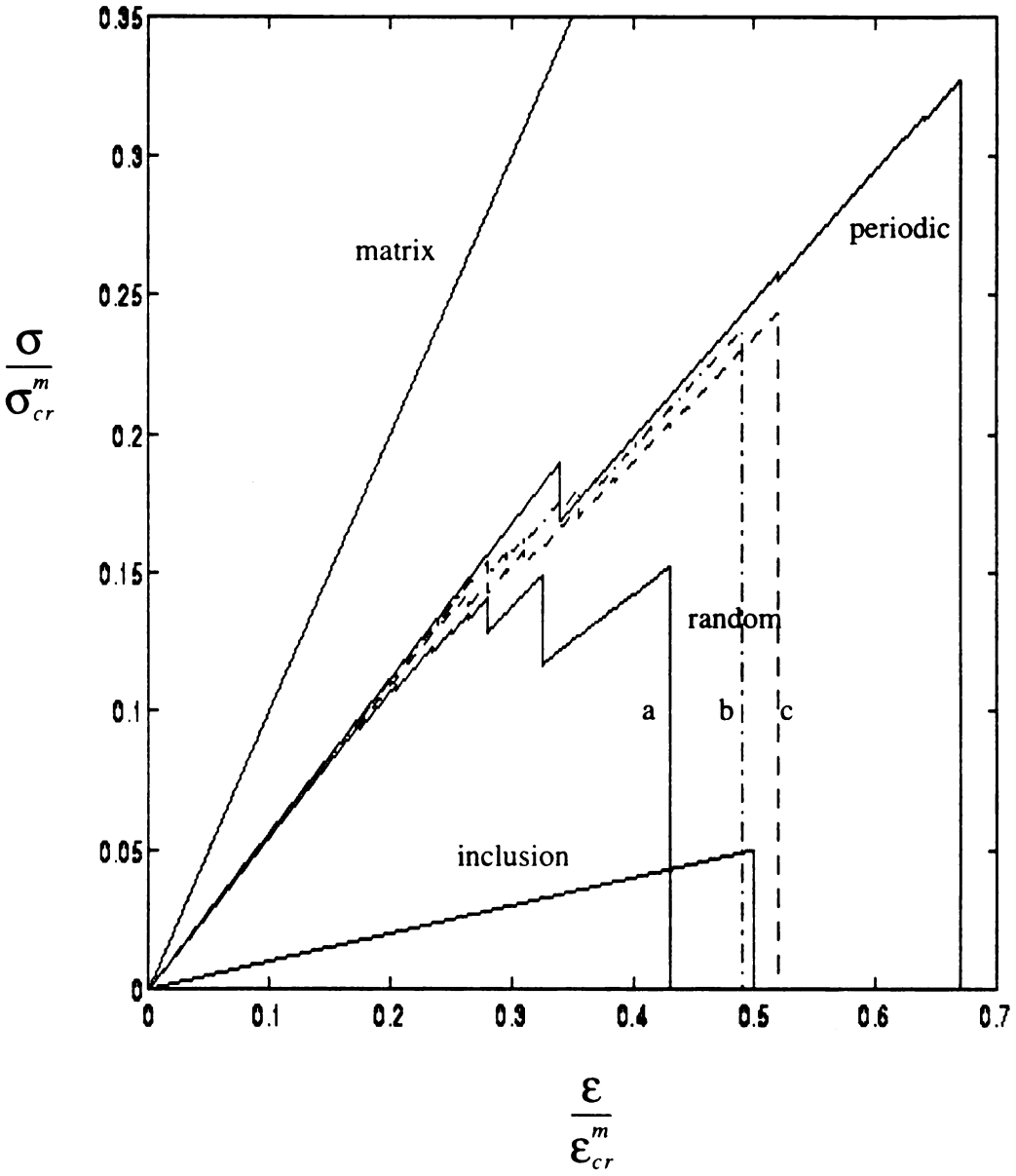

Fig. 24 Effective constitutive laws for the case of $\varepsilon^i/\varepsilon^m = 0.5$, $C^i/C^m = 0.1$

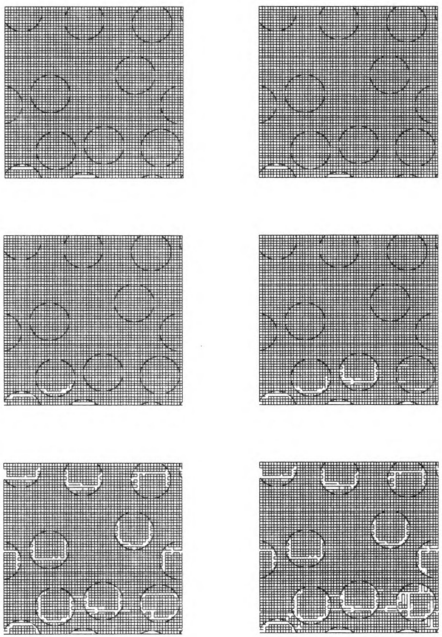

Fig. 25 Damage pattern for random arrangement of inclusion,
$\varepsilon^i/\varepsilon^m = 0.5, \quad C^i/C^m = 0.1$

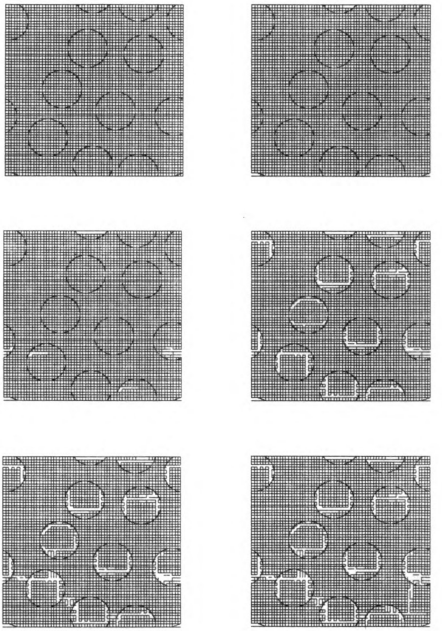

Fig. 26 Damage pattern for random arrangement of inclusion,
$\varepsilon^i/\varepsilon^m = 0.5, \quad C^i/C^m = 0.1$

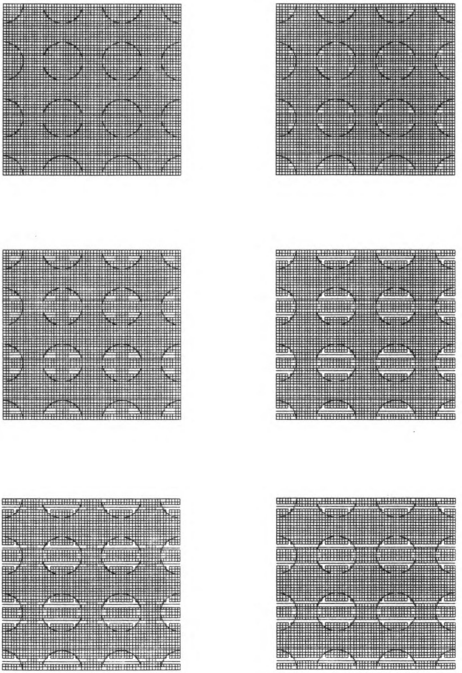

Fig. 27 Damage pattern for random arrangement of inclusion,
$\varepsilon^i/\varepsilon^m = 0.5, \quad C^i/C^m = 0.1$

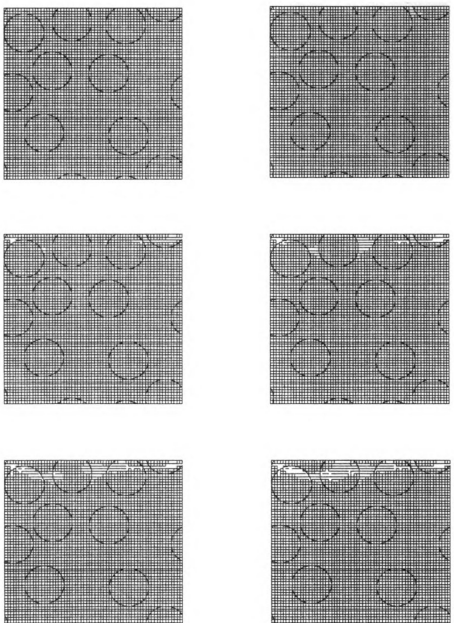

Fig. 28 Damage pattern for random arrangement of inclusion,
$\varepsilon^i/\varepsilon^m = 2, \quad C^i/C^m = 0.2$

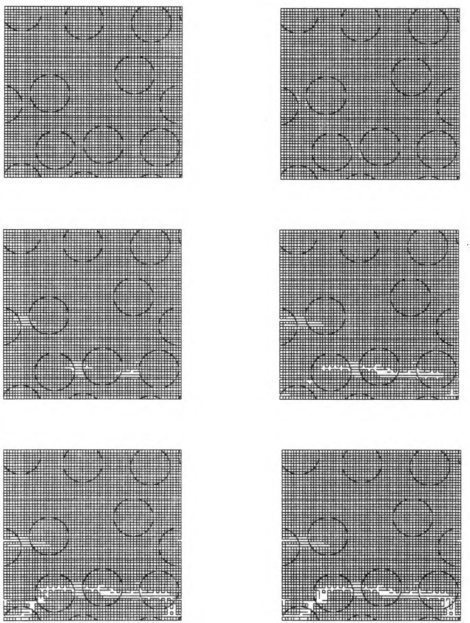

Fig. 29 Damage pattern for random arrangement of inclusion,
$\varepsilon^i/\varepsilon^m = 2, \quad C^i/C^m = 0.2$

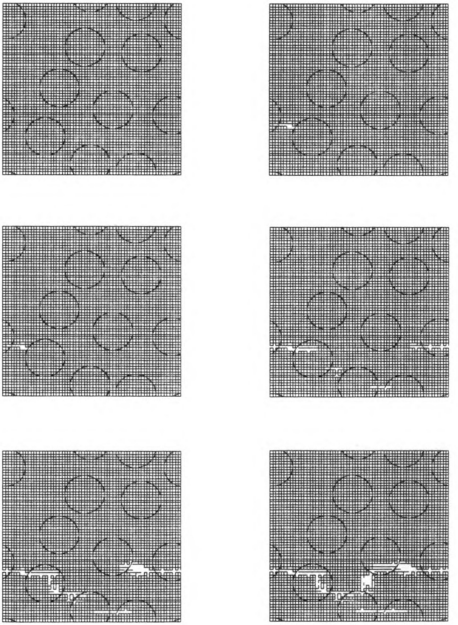

Fig. 30 Damage pattern for random arrangement of inclusion,

$\varepsilon^i/\varepsilon^m = 2, \quad C^i/C^m = 0.2$

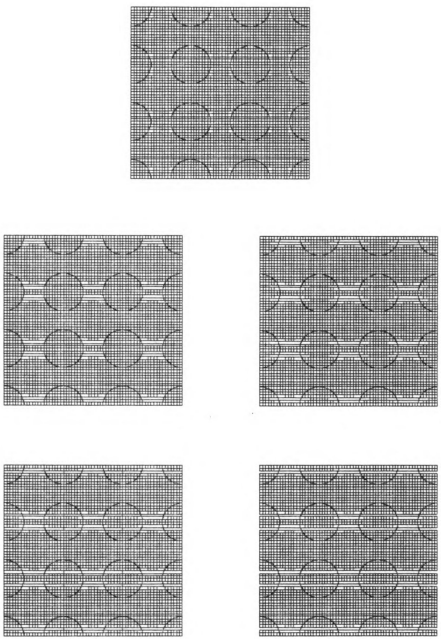

Fig. 31 Damage pattern for random arrangement of inclusion,
$\varepsilon^i/\varepsilon^m = 2, \quad C^i/C^m = 0.2$

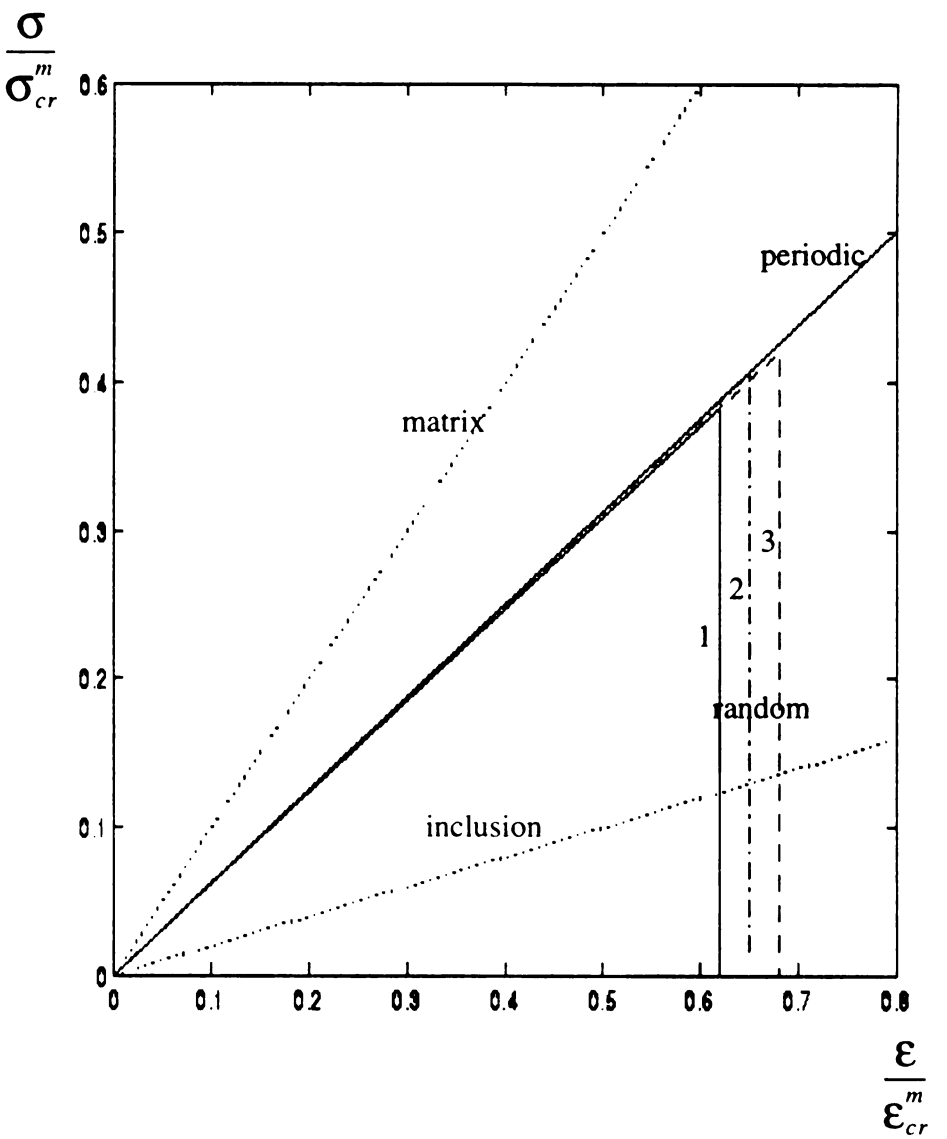

Fig. 32 Effective constitutive laws for the case of

$\varepsilon^i/\varepsilon^m = 2, \quad C^i/C^m = 0.2$

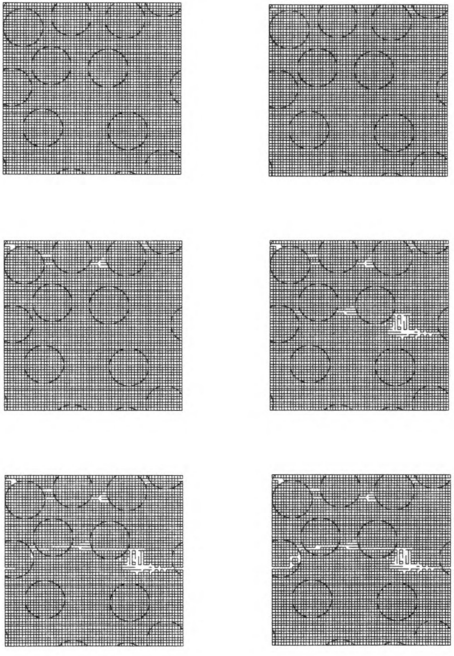

Fig. 33 Damage pattern for random arrangement of inclusion,

$\varepsilon^i/\varepsilon^m = 10, \quad C^i/C^m = 0.1$

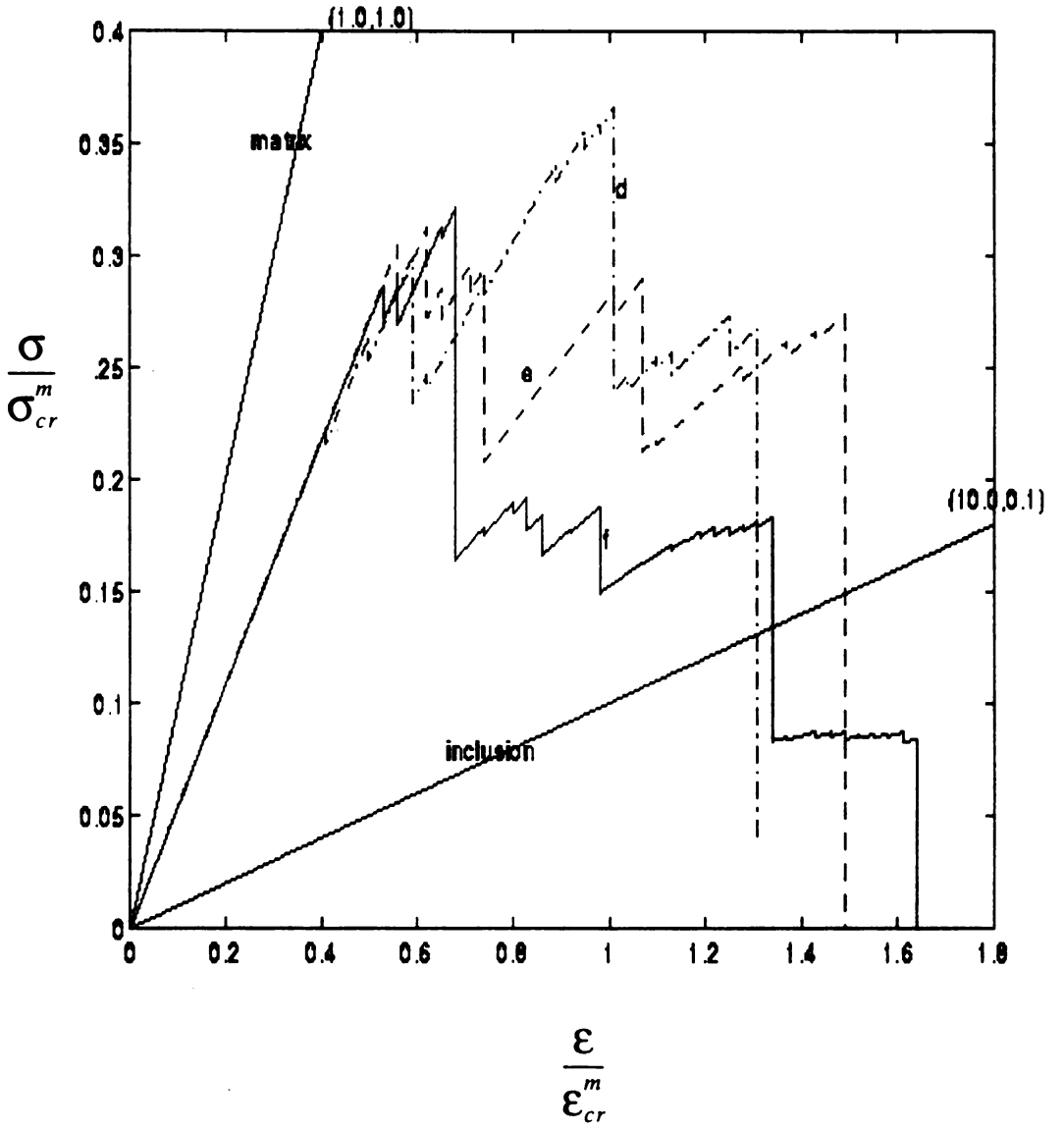

Fig. 34 Effective constitutive laws for the case of $\varepsilon^{i}/\varepsilon^{m} = 10$, $C^{i}/C^{m} = 0.1$

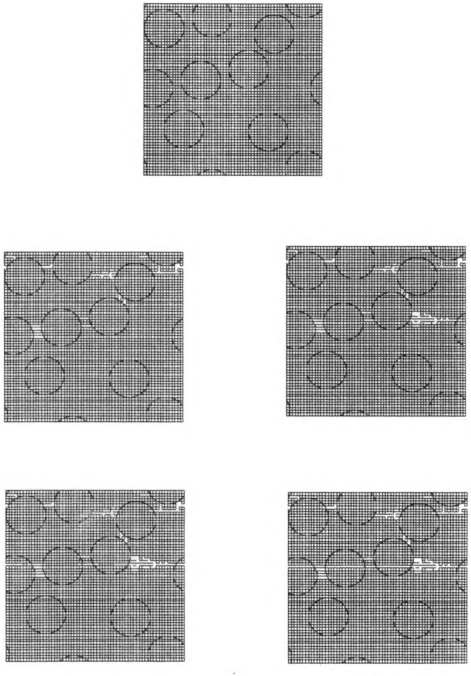

Fig. 35 Damage pattern for random arrangement of inclusion,
$\varepsilon^i/\varepsilon^m = 10, \quad C^i/C^m = 0.1$

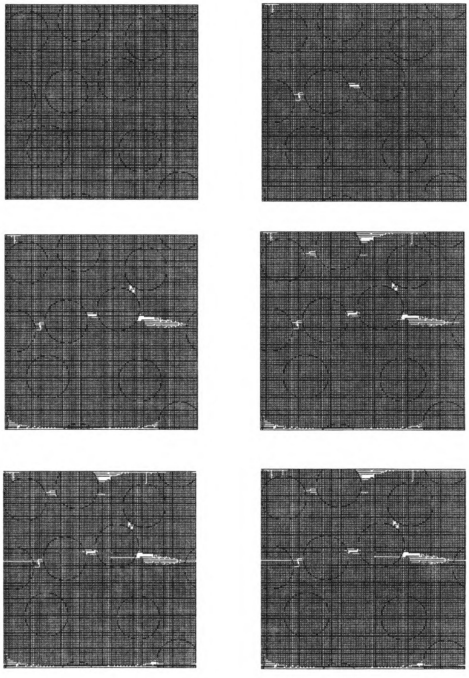

Fig. 36 Damage pattern for random arrangement of inclusion

$\varepsilon^i/\varepsilon^m = 10, \quad C^i/C^m = 0.1$, L = 127

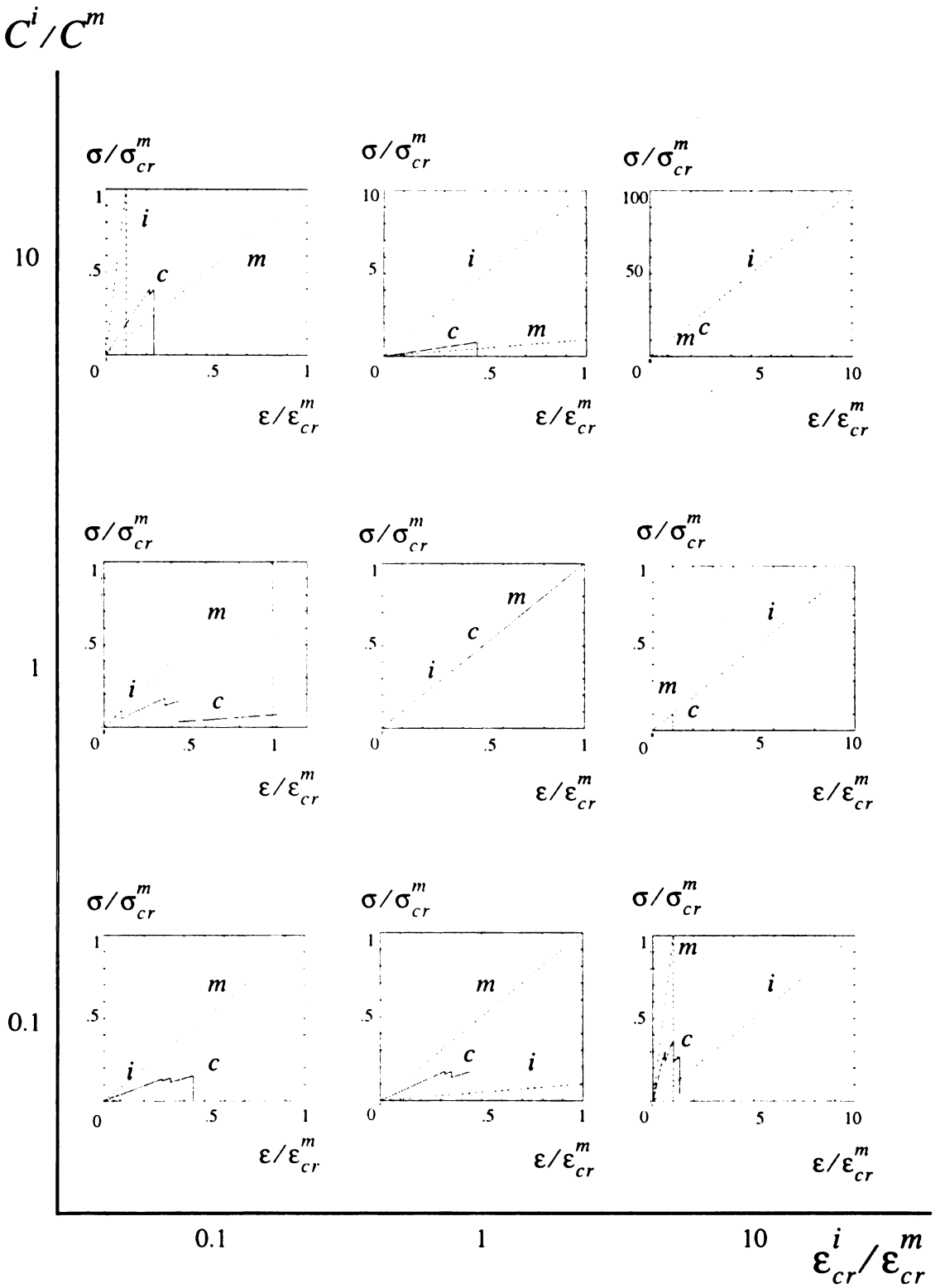

Fig 37 Damage map of effective constitutive laws, also showing response of inclusions and matrix

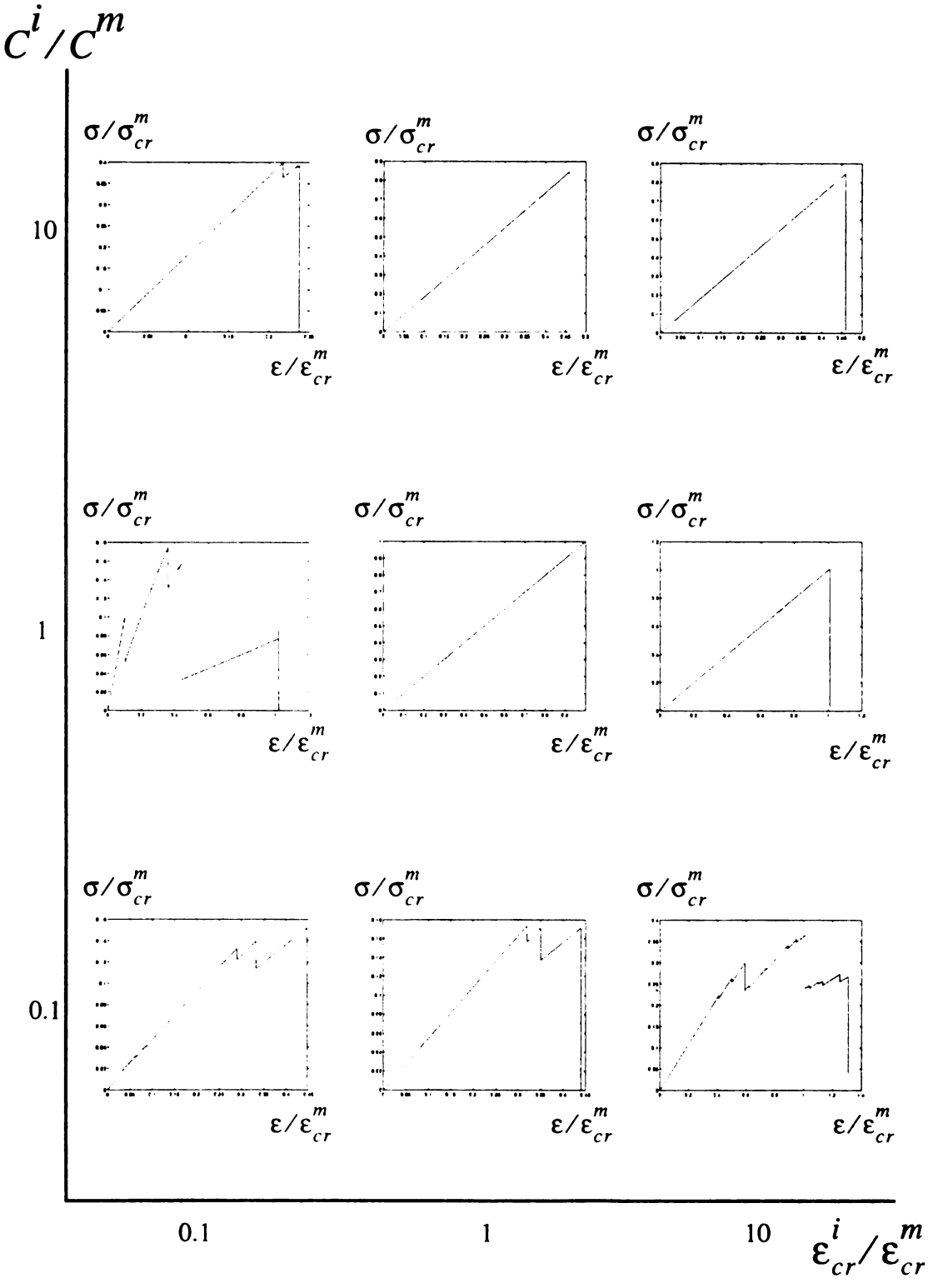

Fig. 38 Damage map of effective constitutive laws

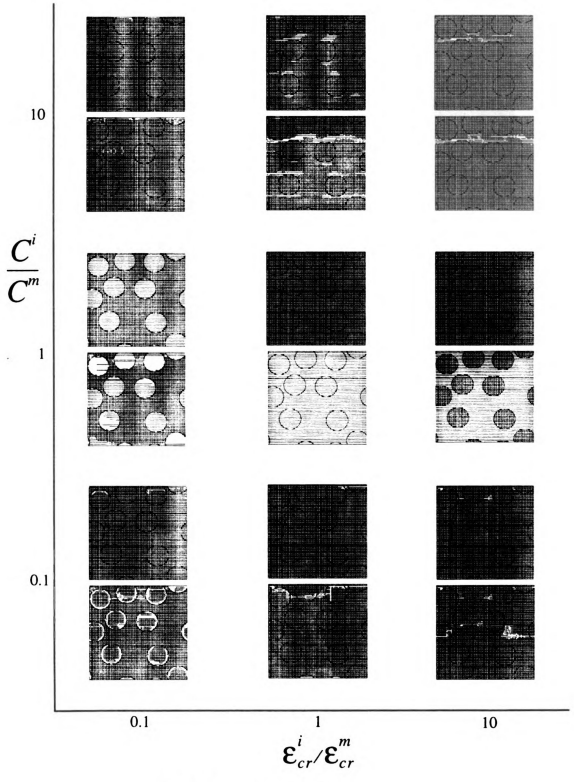

Fig. 39 Damage map of damage patterns

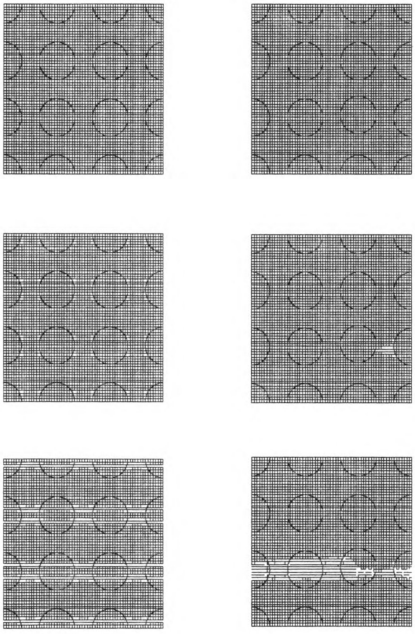

Fig. 40 Effect of fluctuation of inclusion arrangement on damage pattern,

$\varepsilon^i/\varepsilon^m = 2.0, \quad C^i/C^m = 0.2$

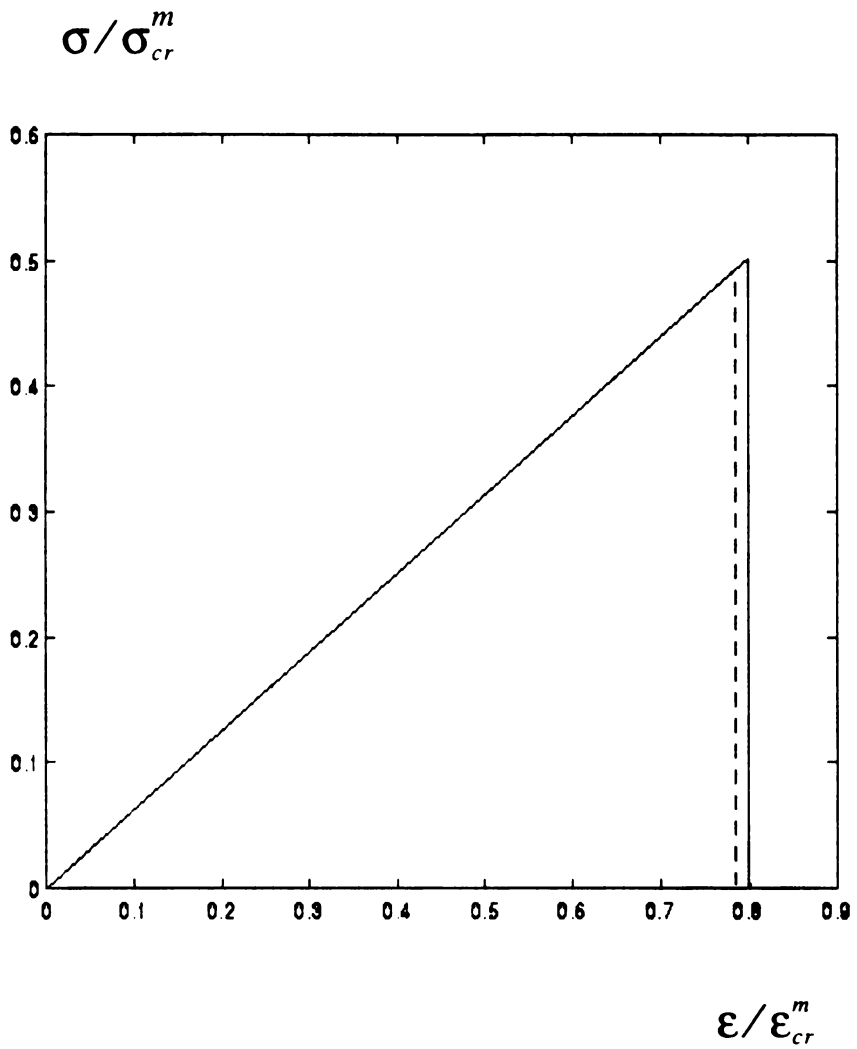

Fig. 41 Effect of fluctuation of inclusion arrangement on stress-strain laws,
$\varepsilon^i/\varepsilon^m = 2.0 \quad C^i/C^m = 0.2$

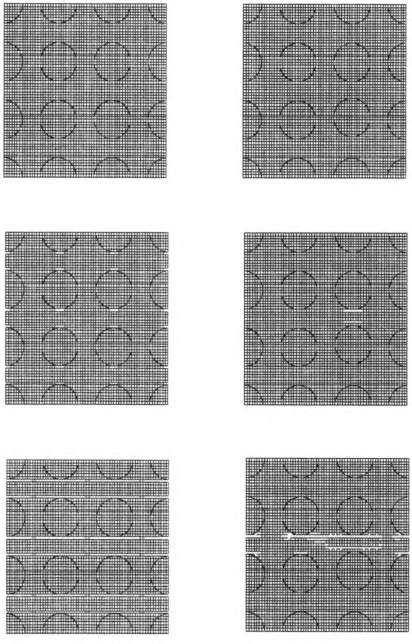

Fig. 42 Effect of fluctuation of inclusion arrangement on damage pattern,

$\varepsilon^i/\varepsilon^m = 2, \quad C^i/C^m = 5$

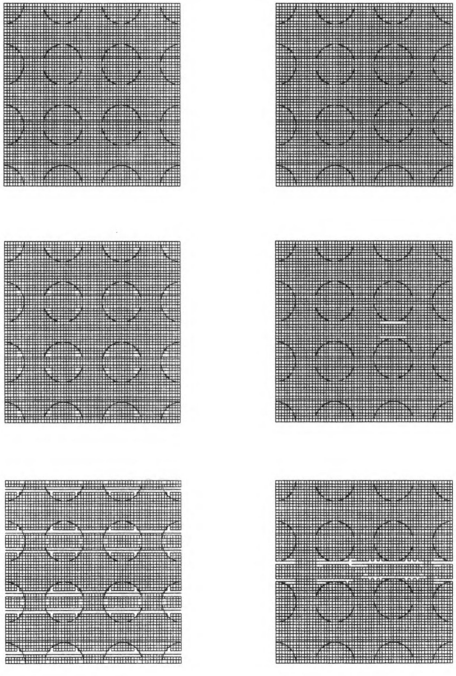

Fig. 43 Effect of fluctuation of inclusion arrangement on damage pattern,

$\varepsilon^i/\varepsilon^m = 0.5, \quad C^i/C^m = 0.1$

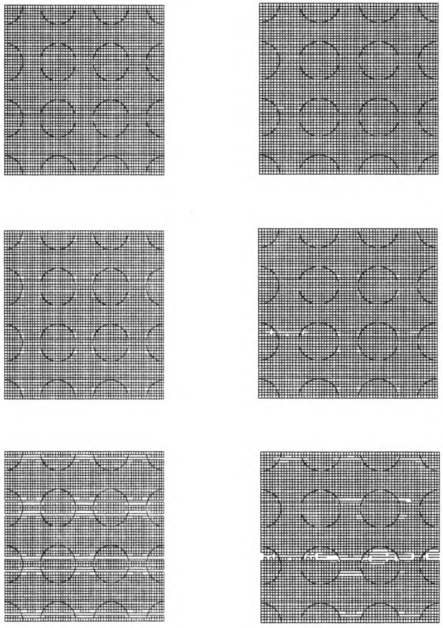

Fig. 44 Effect of fluctuation of matrix material on damage pattern,

$\varepsilon^i / \varepsilon^m = 2, \quad C^i / C^m = 0.2$

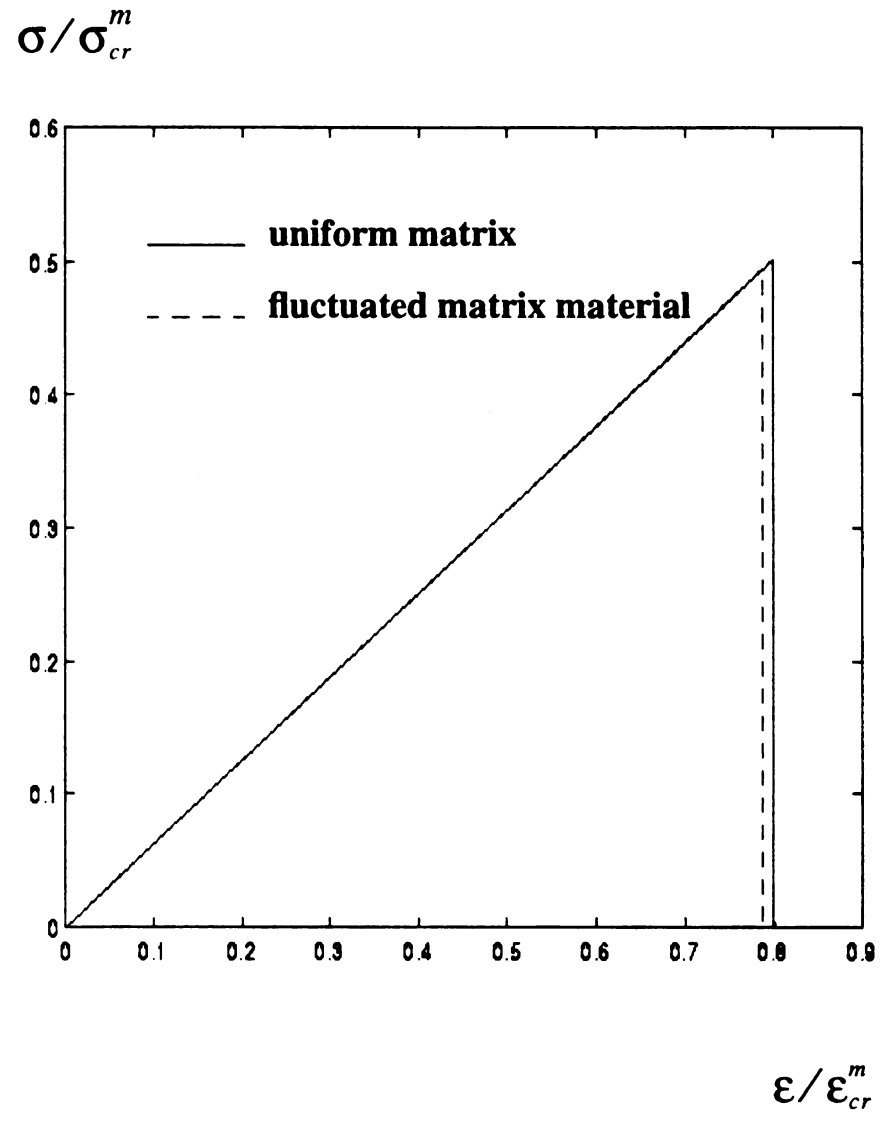

Fig. 45 Effect of fluctuation of matrix material on constitutive law,

$\varepsilon^{i}/\varepsilon^{m} = 2, \quad C^{i}/C^{m} = 0.2$

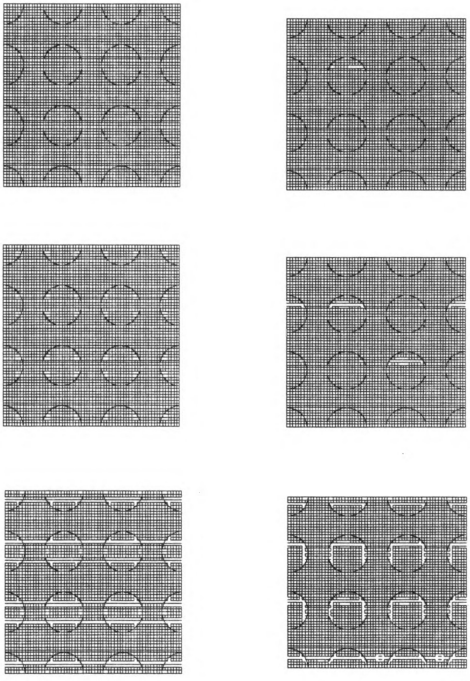

Fig. 46 Effect of fluctuation of matrix material on damage pattern,

$\varepsilon^i/\varepsilon^m = 0.5, \quad C^i/C^m = 0.1$

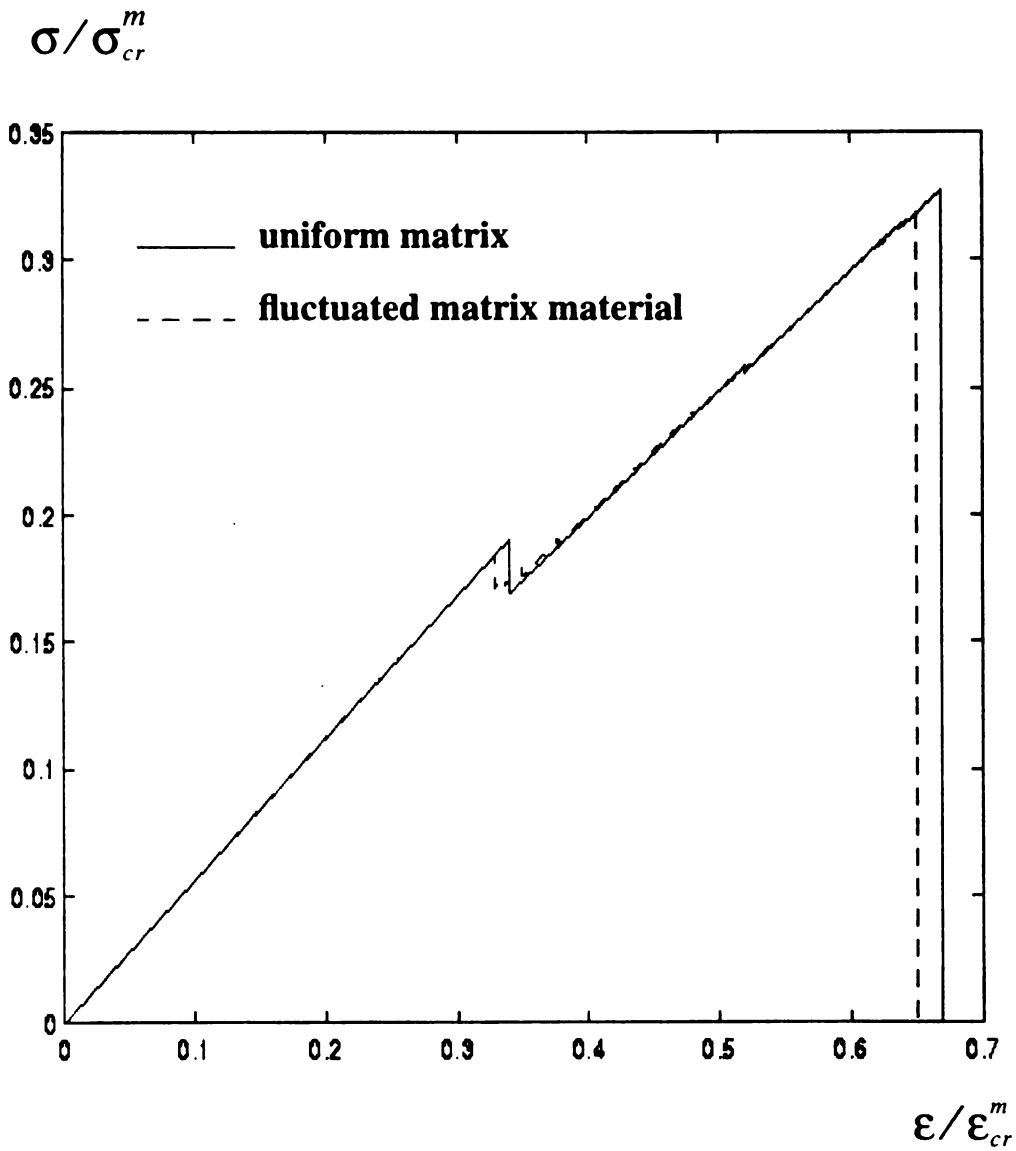

Fig. 47 Effect of fluctuation of matrix material on constitutive law,

$\varepsilon^{i}/\varepsilon^{m} = 0.5, \quad C^{i}/C^{m} = 0.1$

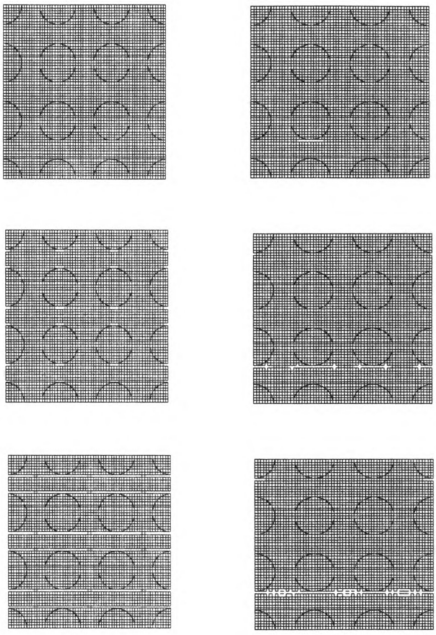

Fig. 48 Effect of fluctuation of matrix material on damage pattern,

$\varepsilon^i/\varepsilon^m = 2, \quad C^i/C^m = 5$

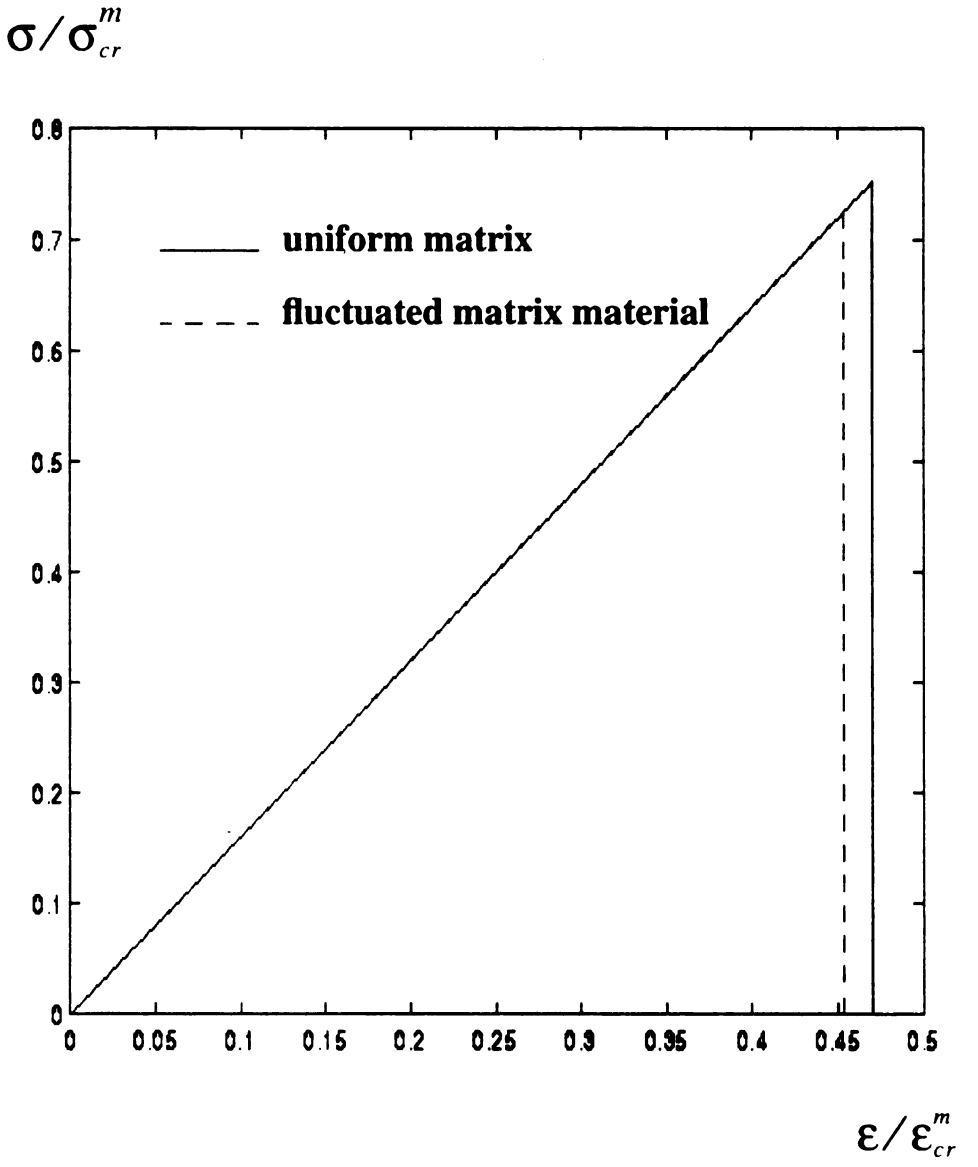

Fig. 49 Effect of fluctuation of matrix material on constitutive law,

$\varepsilon^{i}/\varepsilon^{m} = 2, \quad C^{i}/C^{m} = 5$

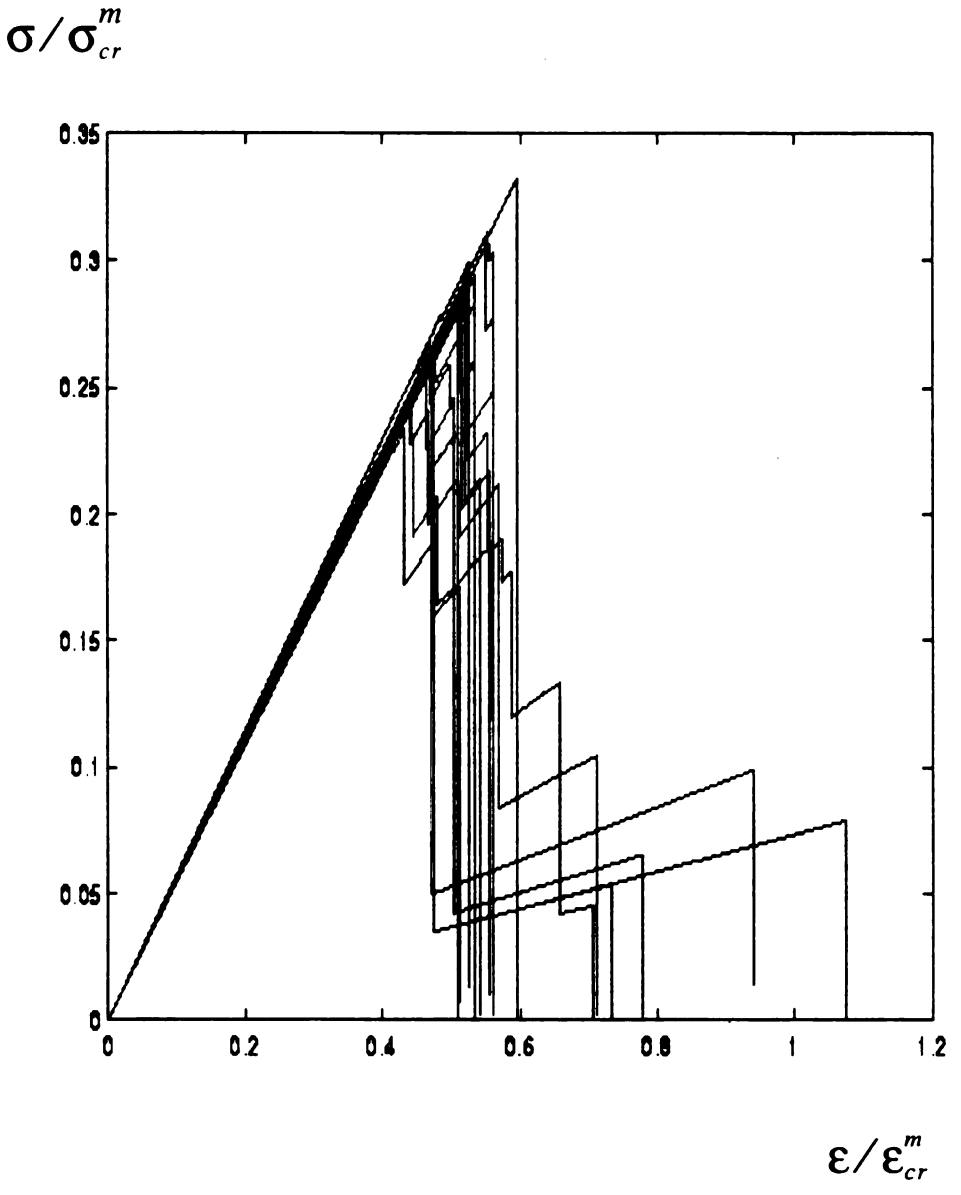

Fig. 50 Effective constitutive curve, $\varepsilon^{i}/\varepsilon^{m} = 1$, $C^{i}/C^{m} = 0.1$ and 20 samples

$F\left(\sigma_{max}/\sigma_{cr}^{m}\right)$

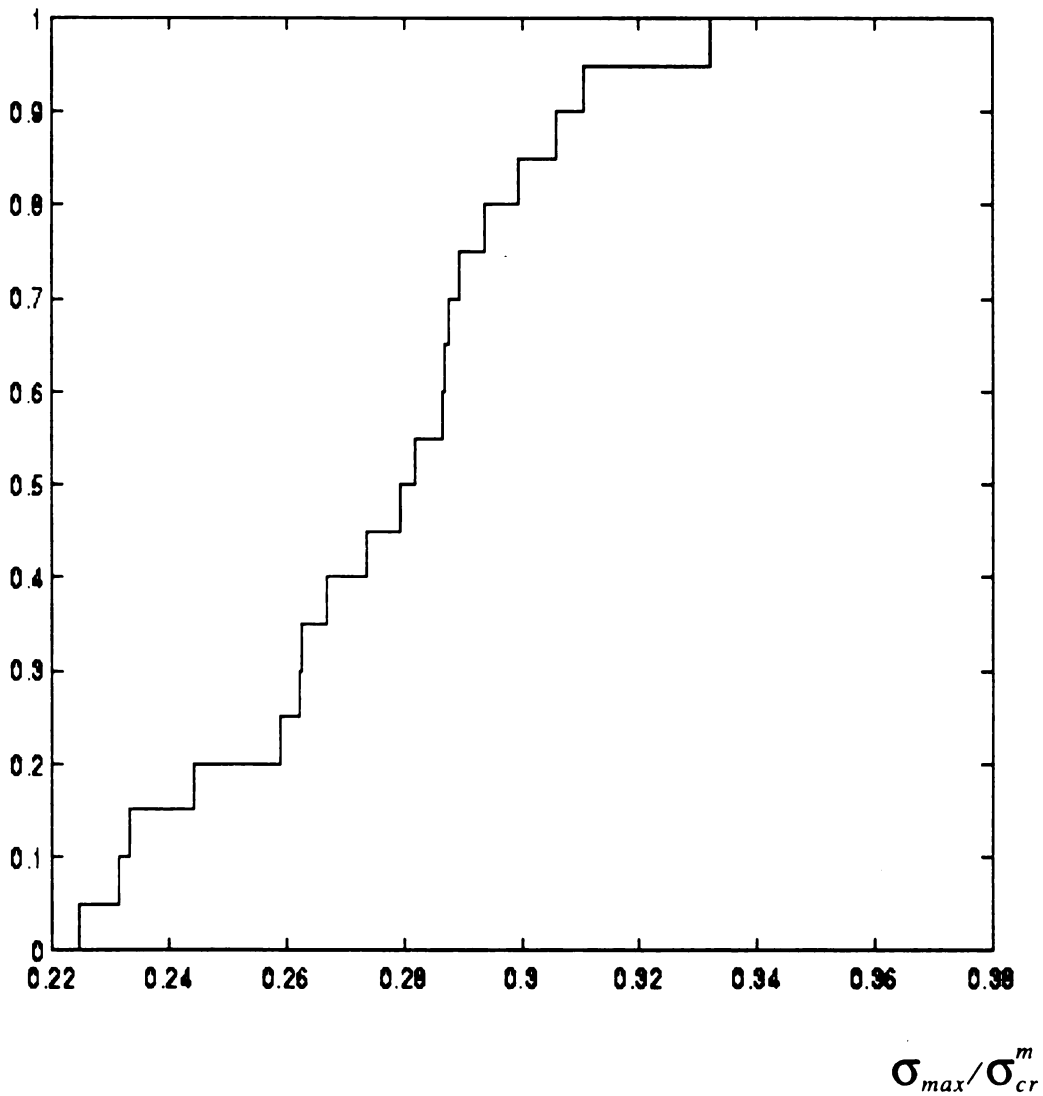

Fig. 51 Probability distribution function F (σ_{max}) for the case of

$\varepsilon^{i}/\varepsilon^{m} = 1, \quad C^{i}/C^{m} = 0.1$

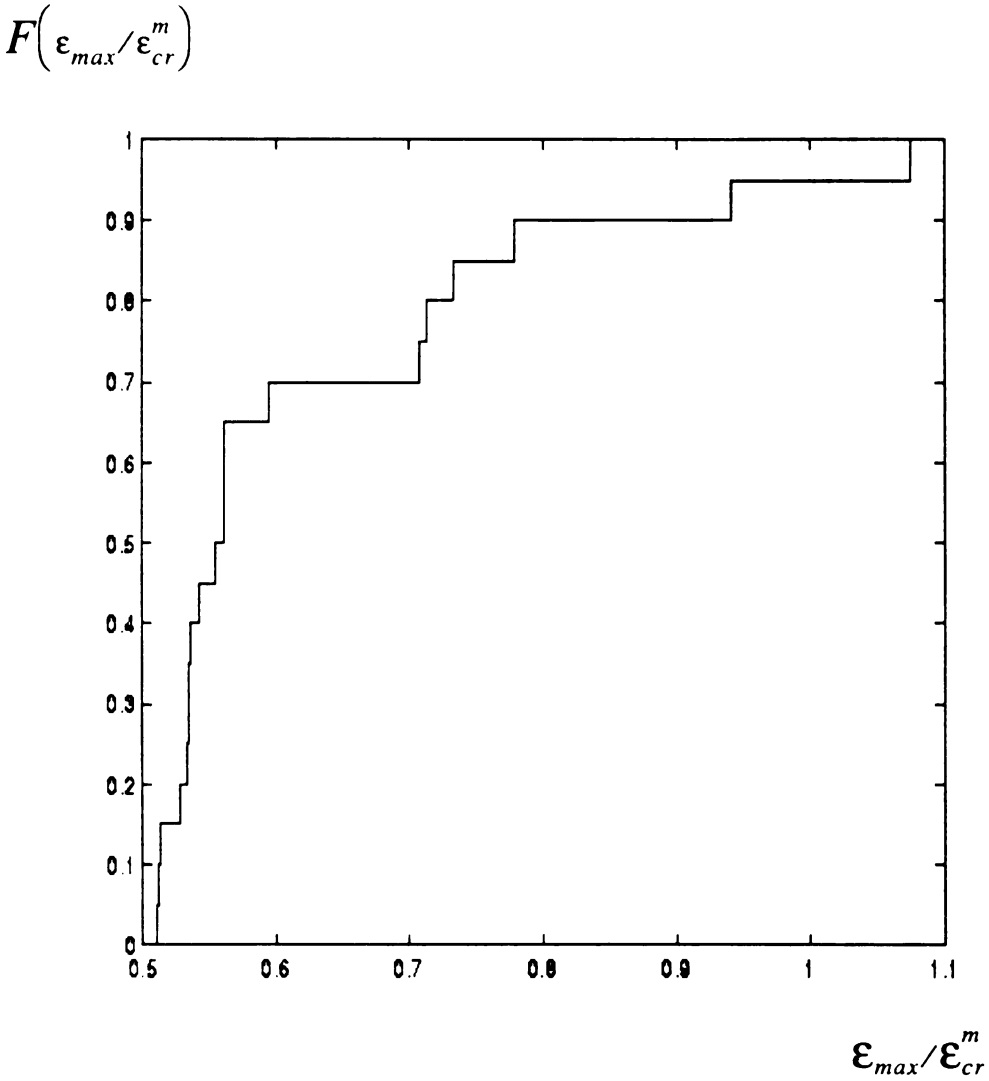

Fig. 52 Probability distribution function F (ε_{max}) for the case of

$\varepsilon^{i}/\varepsilon^{m} = 1, \quad C^{i}/C^{m} = 0.1$

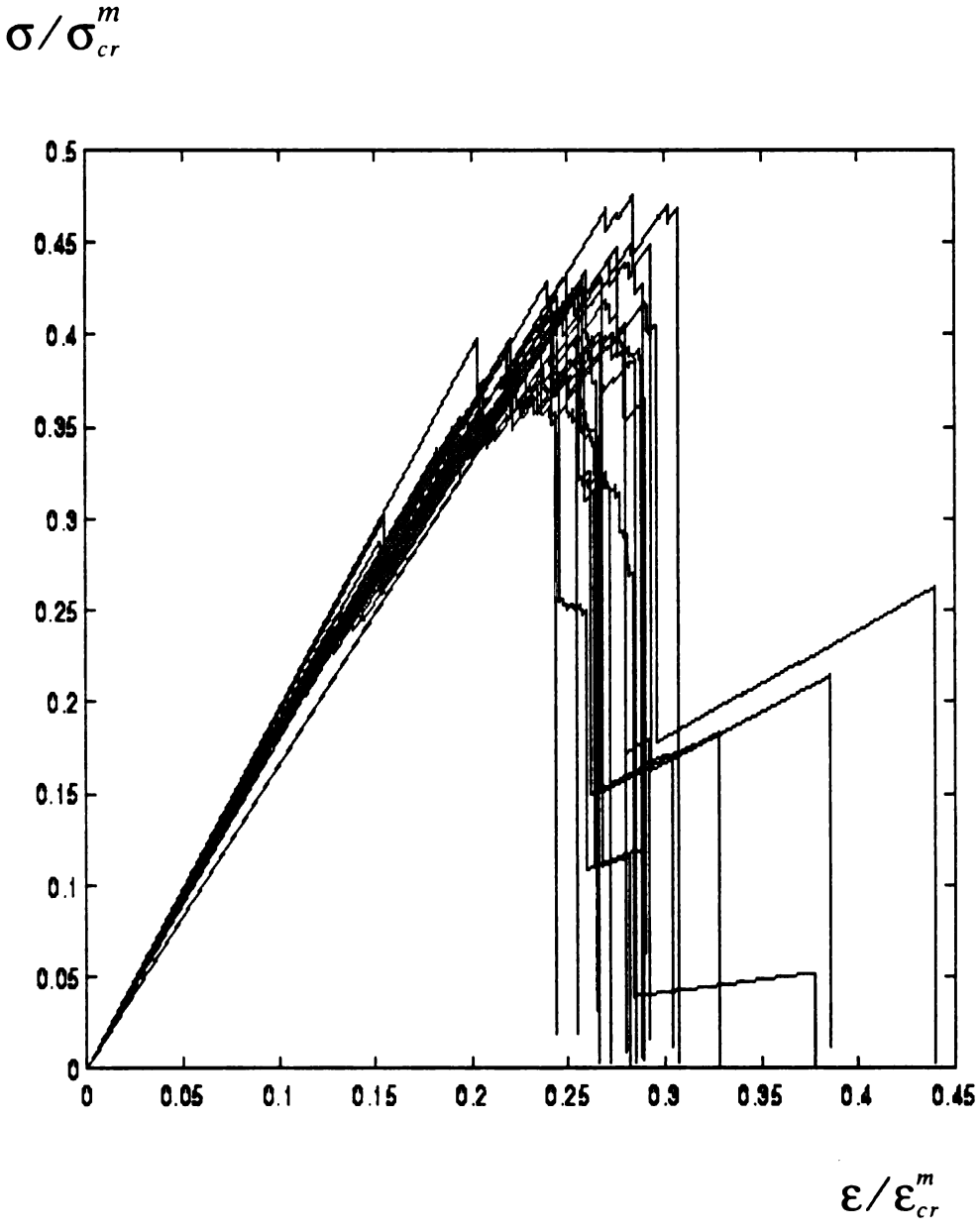

Fig.53 Effective constitutive curve, $\varepsilon^{i}/\varepsilon^{m} = 0.1$, $C^{i}/C^{m} = 10$ and 20 samples

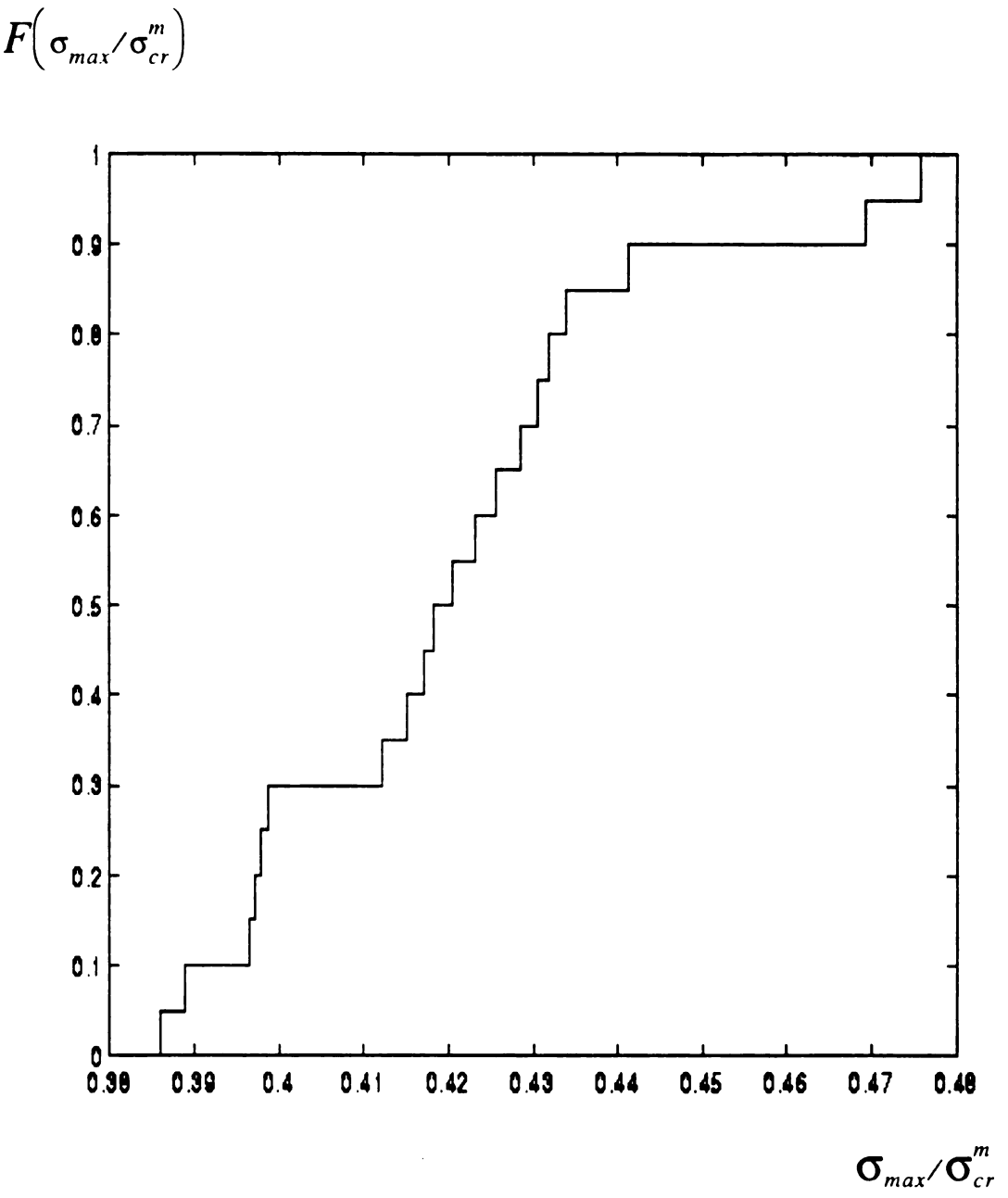

Fig. 54 Probability distribution function F (σ_{max}) for the case of

$\varepsilon^{i}/\varepsilon^{m} = 0.1, \quad C^{i}/C^{m} = 10$

$F\left(\varepsilon_{max}/\varepsilon_{cr}^{m}\right)$

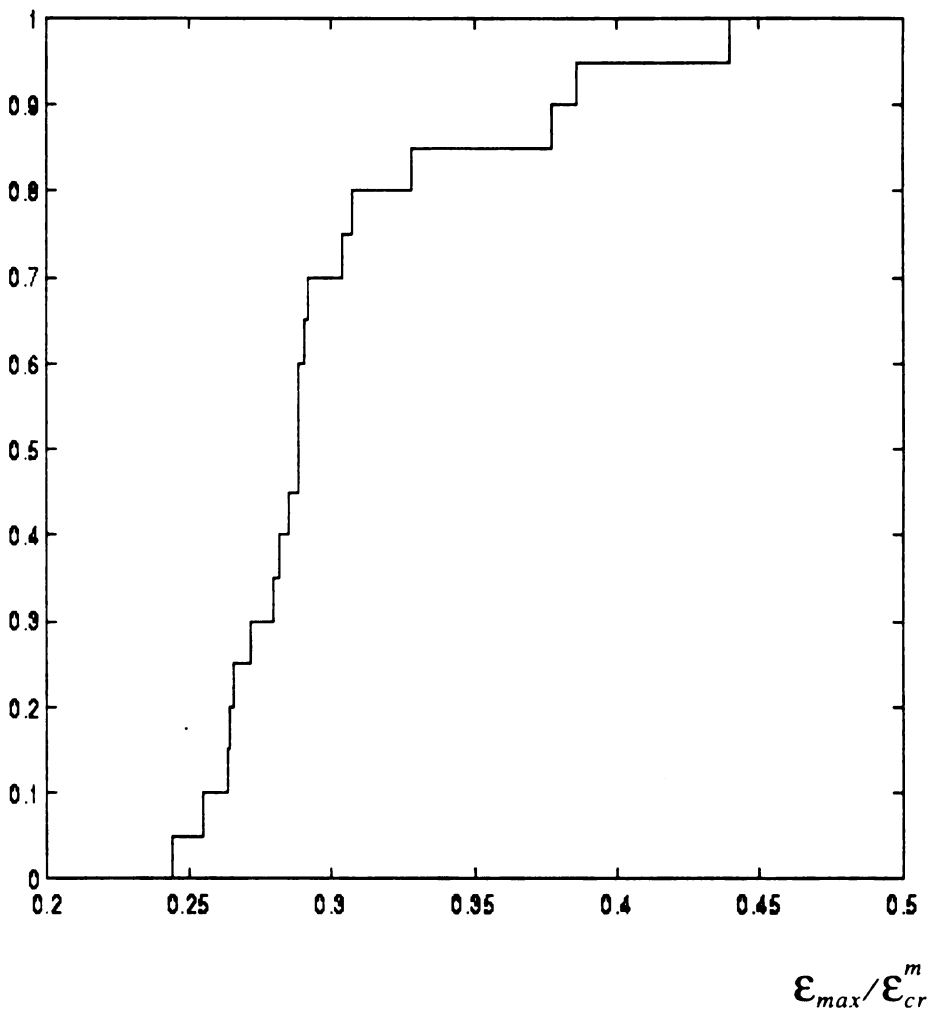

Fig. 55 Probability distribution function $F(\varepsilon_{max})$ for the case of

$\varepsilon^{i}/\varepsilon^{m} = 0.1, \quad C^{i}/C^{m} = 10$

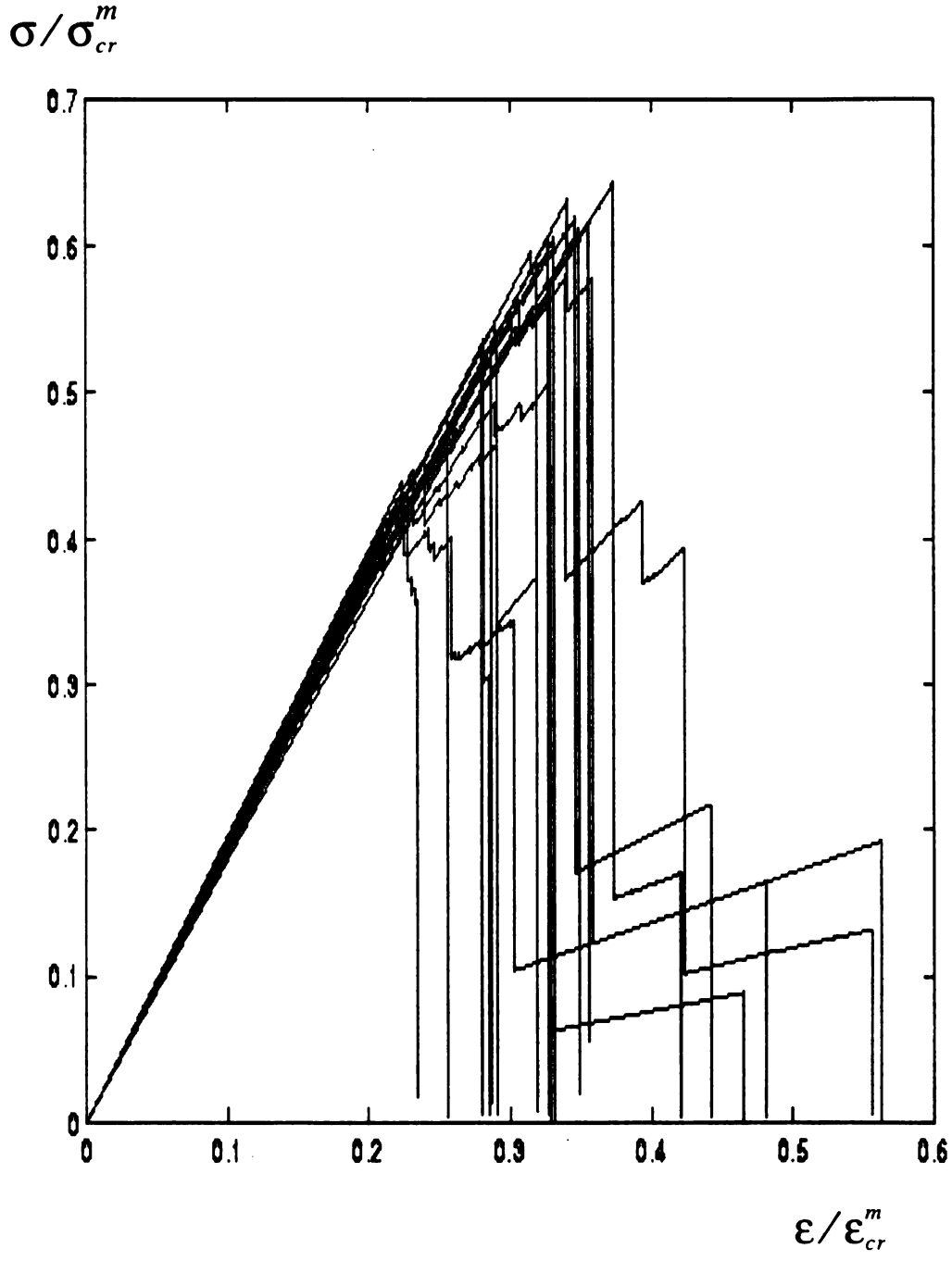

Fig. 56 Effective constitutive curve, $\varepsilon^{i}/\varepsilon^{m}= 10$, $C^{i}/C^{m} = 10$ and 20 samples

$F\left(\sigma_{max}/\sigma_{cr}^{m}\right)$

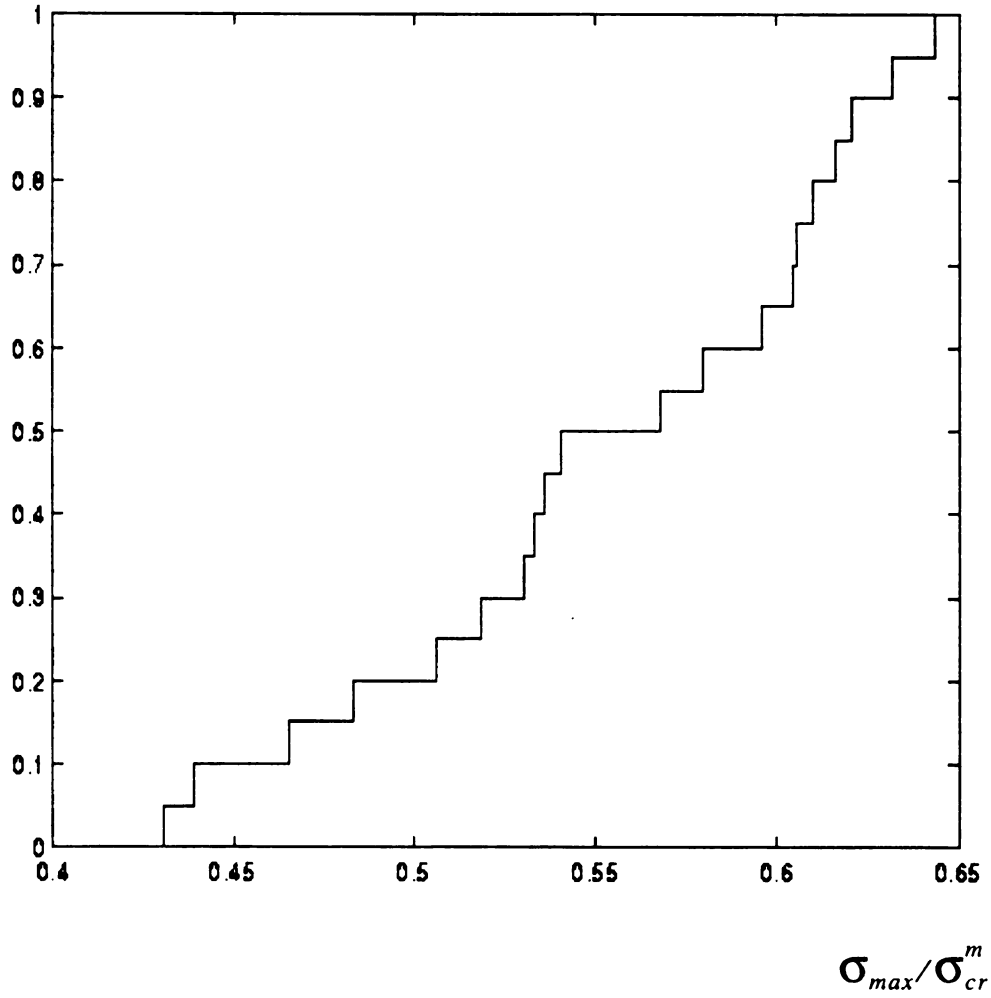

Fig. 57 Probability Distribution function $F(\sigma_{max})$ for the case of

$\varepsilon^{i}/\varepsilon^{m} = 10, \quad C^{i}/C^{m} = 10$

$F\left(\varepsilon_{max}/\varepsilon_{cr}^{m}\right)$

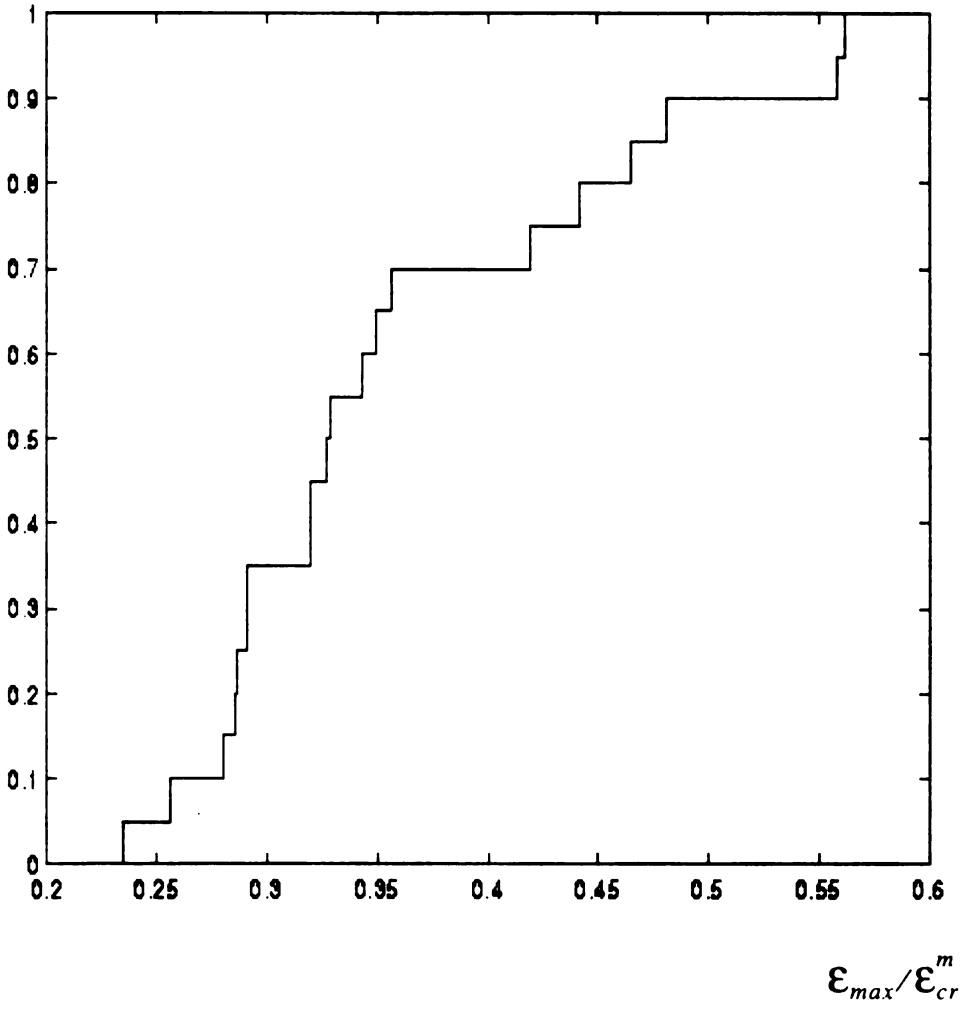

Fig. 58 Probability distribution function $F(\varepsilon_{max})$ for the case of

$\varepsilon^{i}/\varepsilon^{m} = 10, \quad C^{i}/C^{m} = 10$

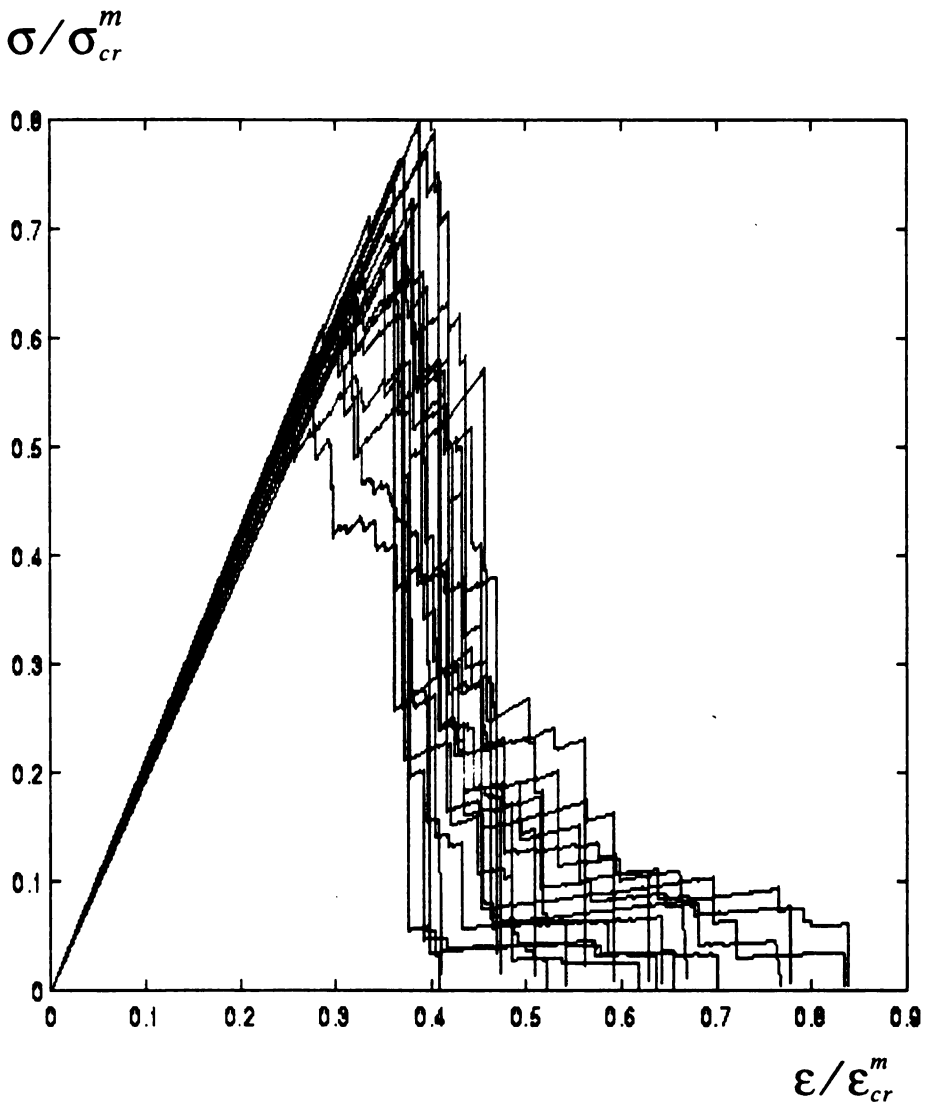

Fig. 59 Effective constitutive curve, $\varepsilon^{i}/\varepsilon^{m} = 1$, $C^{i}/C^{m} = 10$ and 20 samples

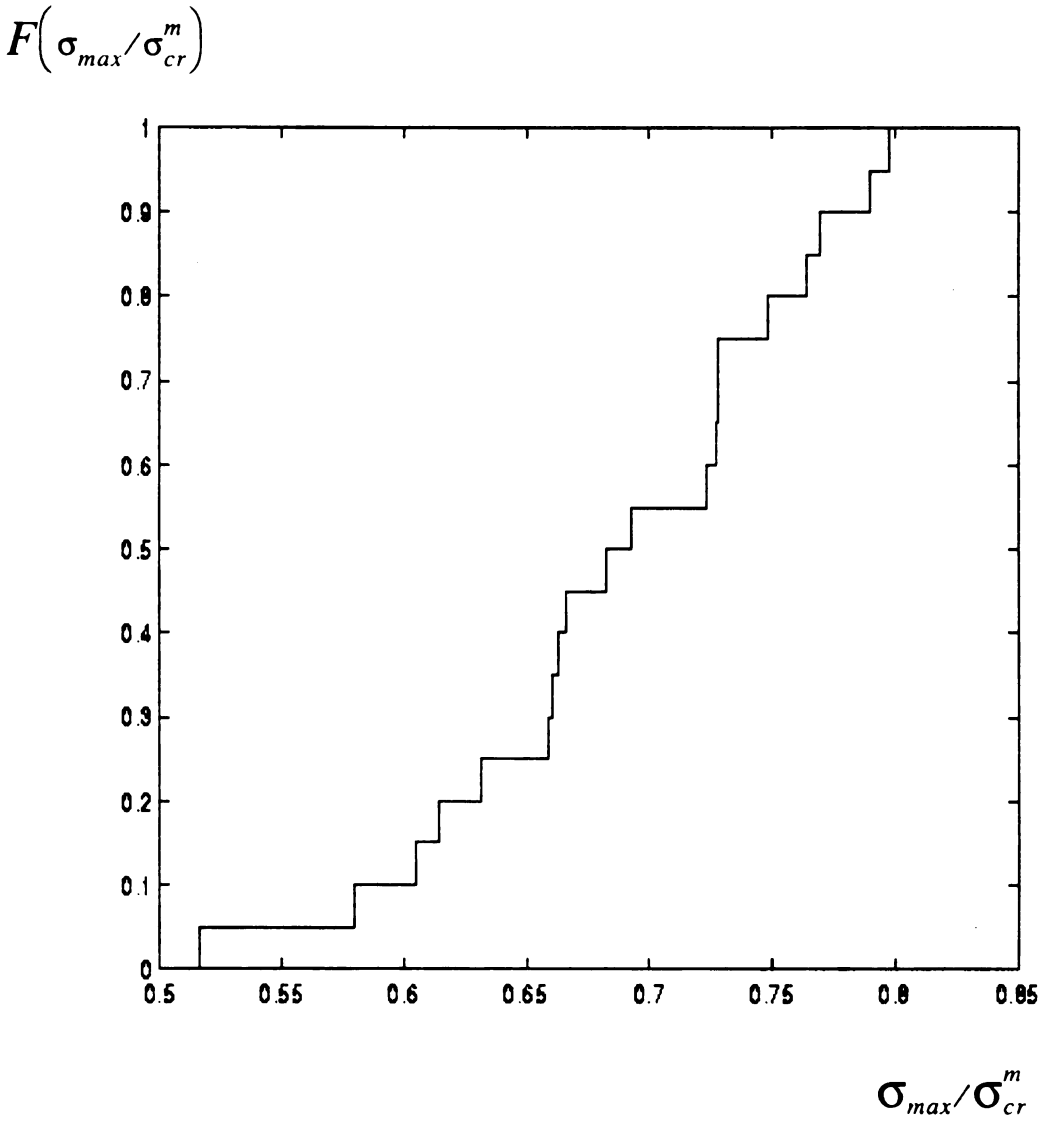

Fig. 60 Probability distribution function $F(\sigma_{max})$ for the case of

$\varepsilon^{i}/\varepsilon^{m} = 1, \quad C^{i}/C^{m} = 10$

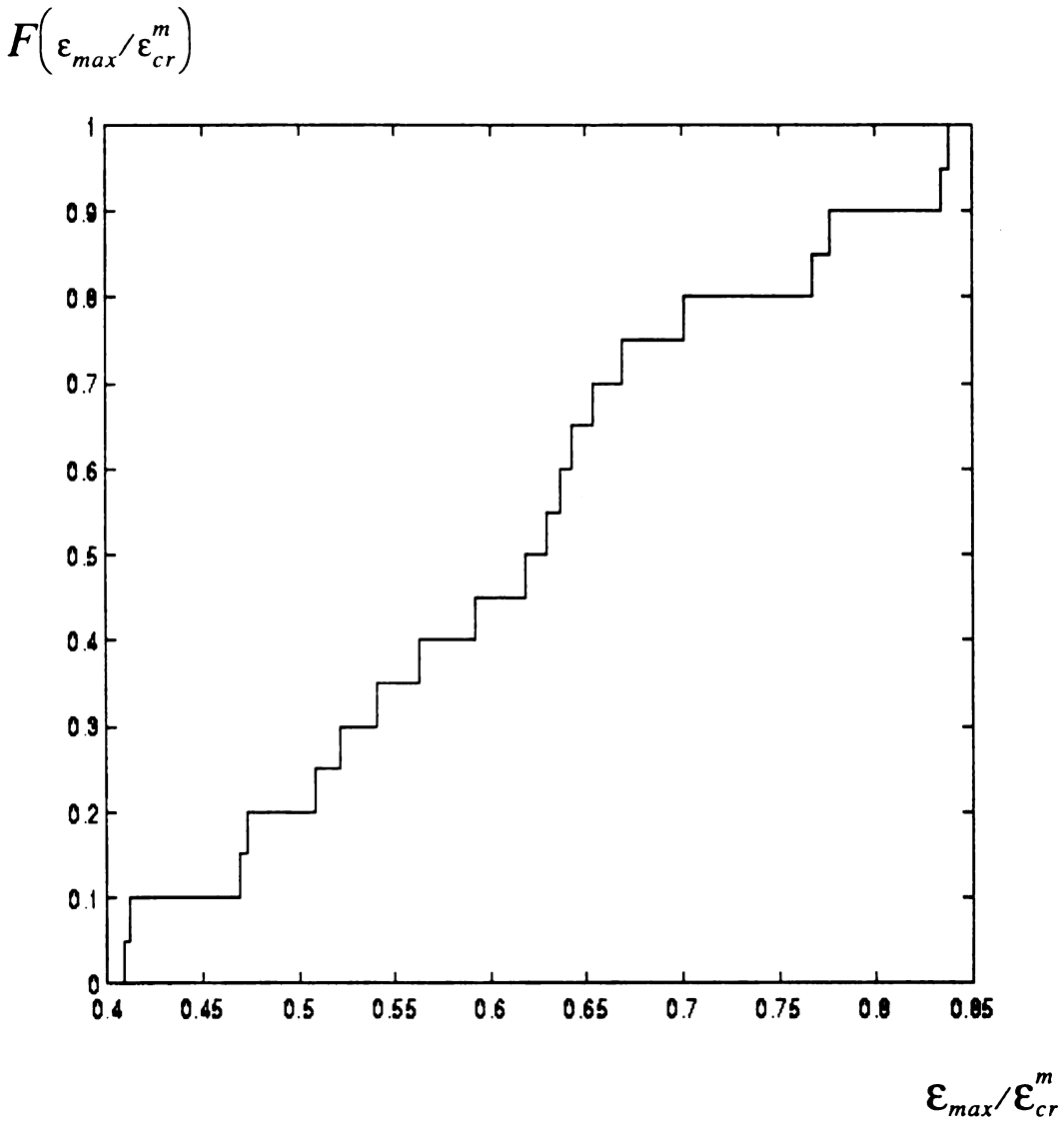

Fig. 61 Probability distribution function $F(\varepsilon_{max})$ for the case of

$\varepsilon^{i}/\varepsilon^{m} = 1, \quad C^{i}/C^{m} = 10$

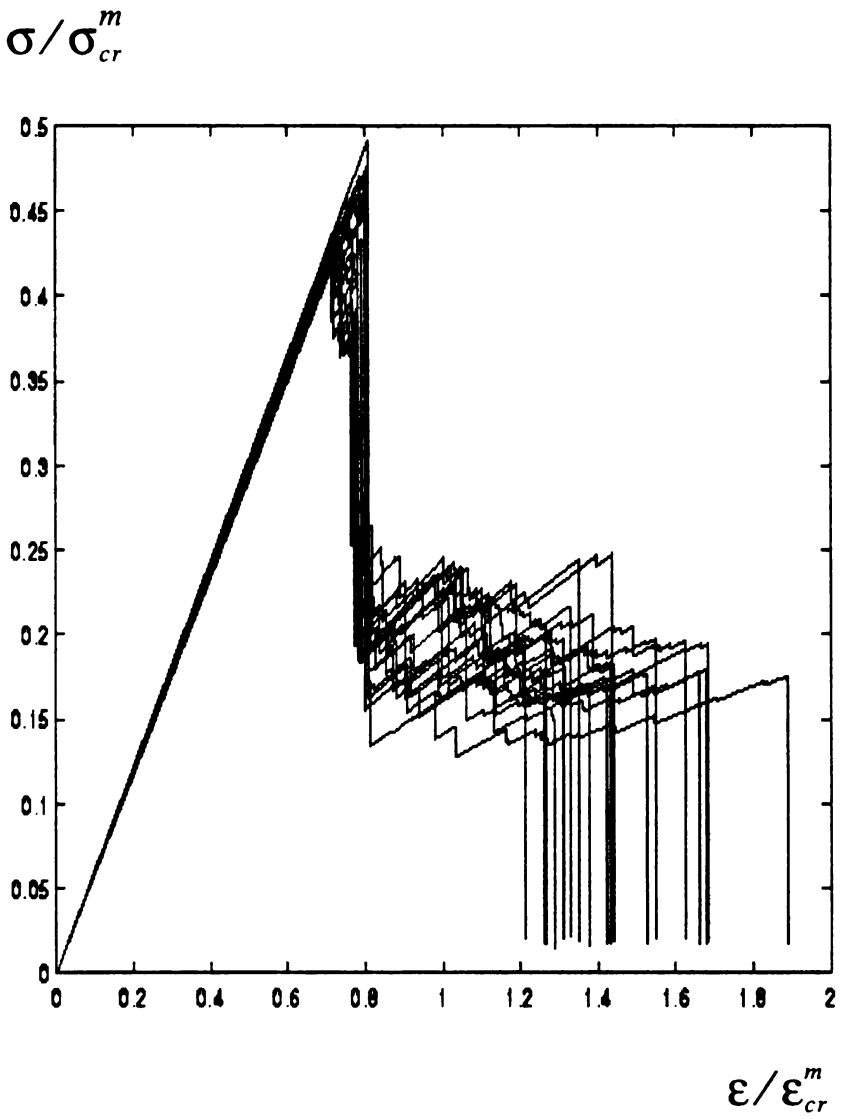

Fig.62 Effective constitutive curve, $\varepsilon^{i}/\varepsilon^{m}= 10$, $C^{i}/C^{m} = 0.1$ and 20 samples

$F\left(\sigma_{max}/\sigma_{cr}^{m}\right)$

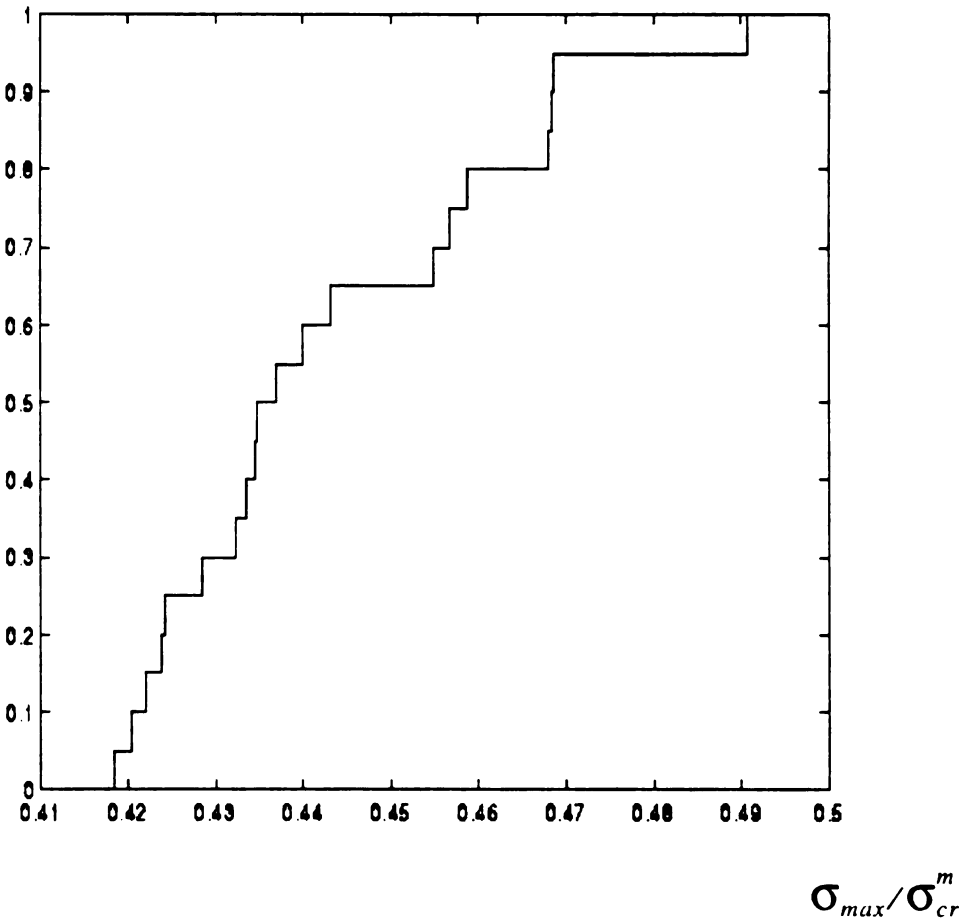

Fig. 63 Probability distribution function $F(\sigma_{max})$ for the case of

$\varepsilon^{i}/\varepsilon^{m} = 10, \quad C^{i}/C^{m} = 0.1$

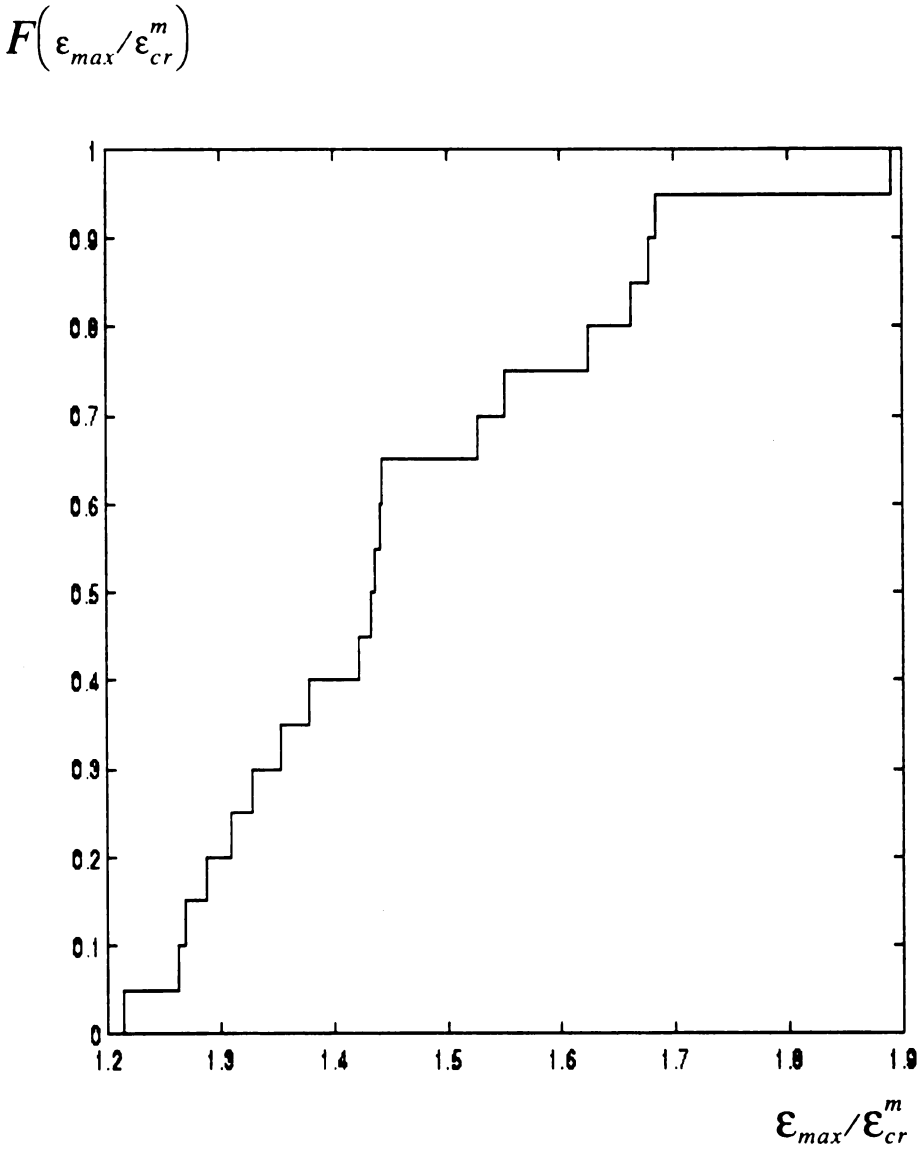

Fig. 64 Probability distribution function $F(\varepsilon_{max})$ for the case of

$\varepsilon^{i}/\varepsilon^{m} = 10, \quad C^{i}/C^{m} = 0.1$

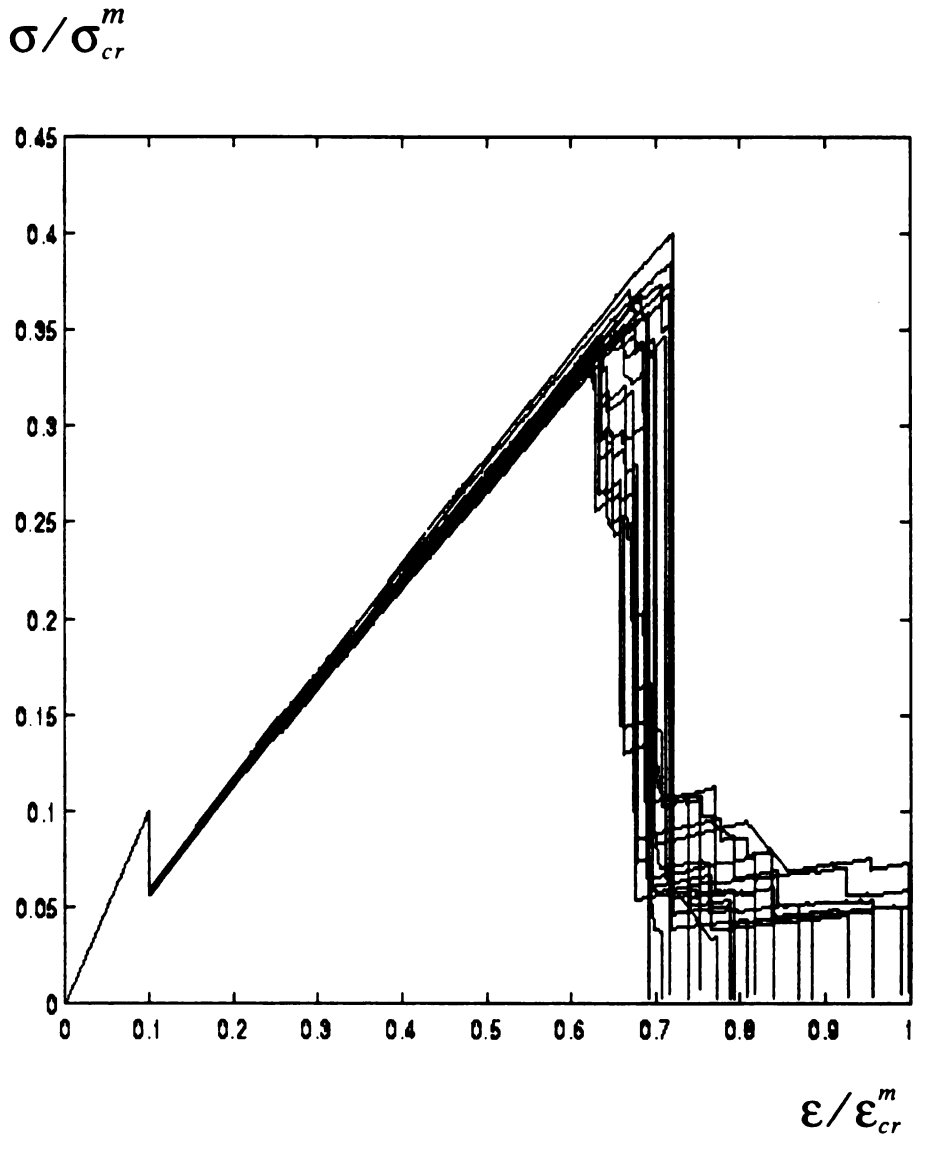

Fig. 65 Effective constitutive curve, $\varepsilon^i/\varepsilon^m = 0.1$, $C^i/C^m = 1$ and 20 samples

$F\left(\sigma_{max}/\sigma_{cr}^{m}\right)$

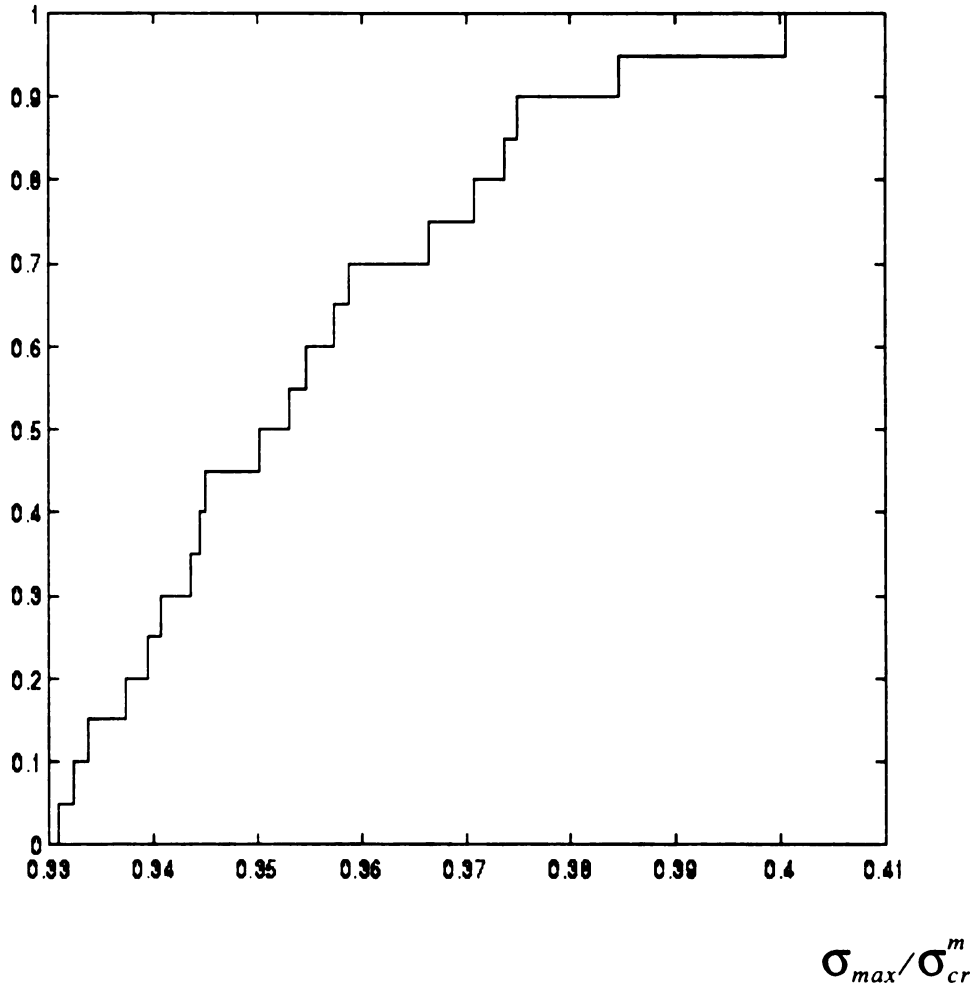

Fig. 66 Probability distribution function $F(\sigma_{max})$ for the case of

$\varepsilon^{i}/\varepsilon^{m} = 0.1, \quad C^{i}/C^{m} = 1$

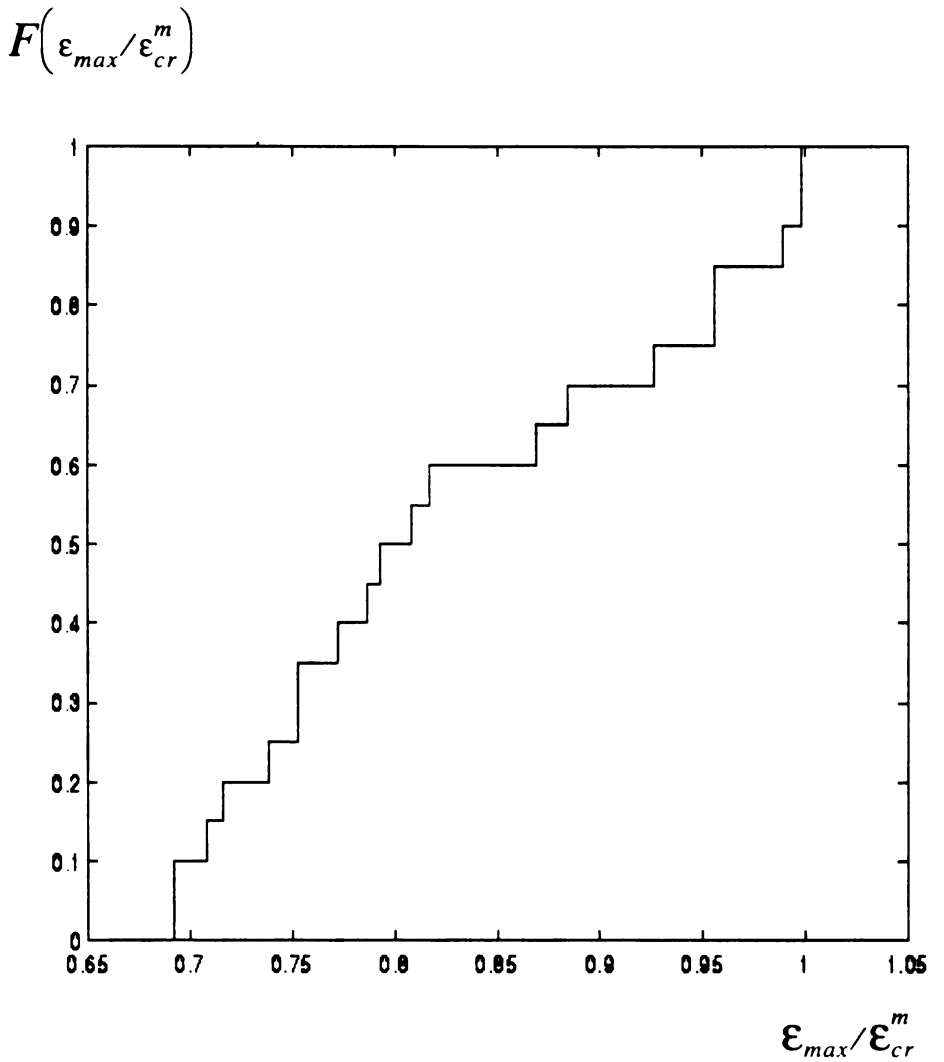

Fig. 67 Probability distribution function $F(\varepsilon_{max})$ for the case of

$\varepsilon^{i}/\varepsilon^{m} = 0.1, \quad C^{i}/C^{m} = 1$

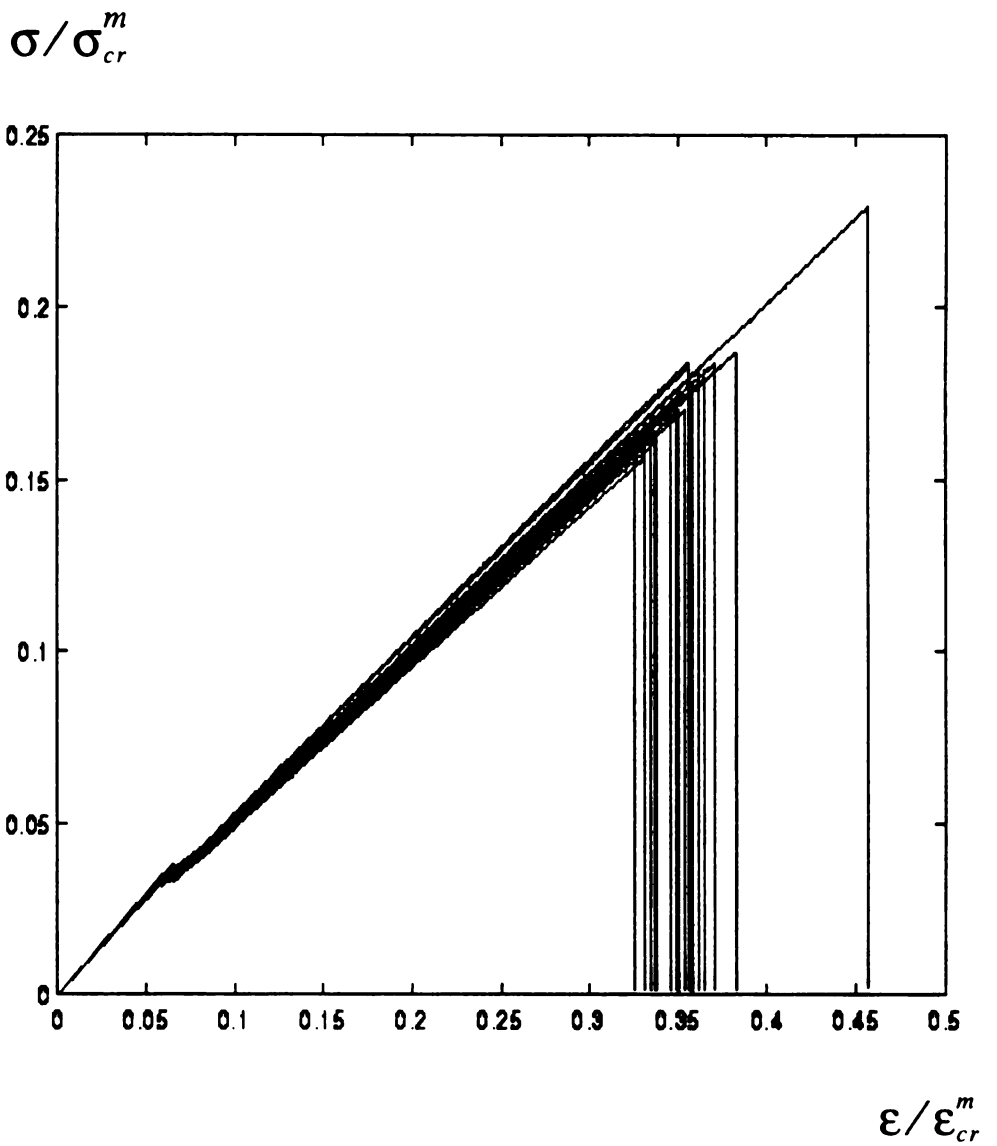

Fig. 68 Effective constitutive curve, $\varepsilon^i/\varepsilon^m = 0.1$, $C^i/C^m = 0.1$ and 20 samples

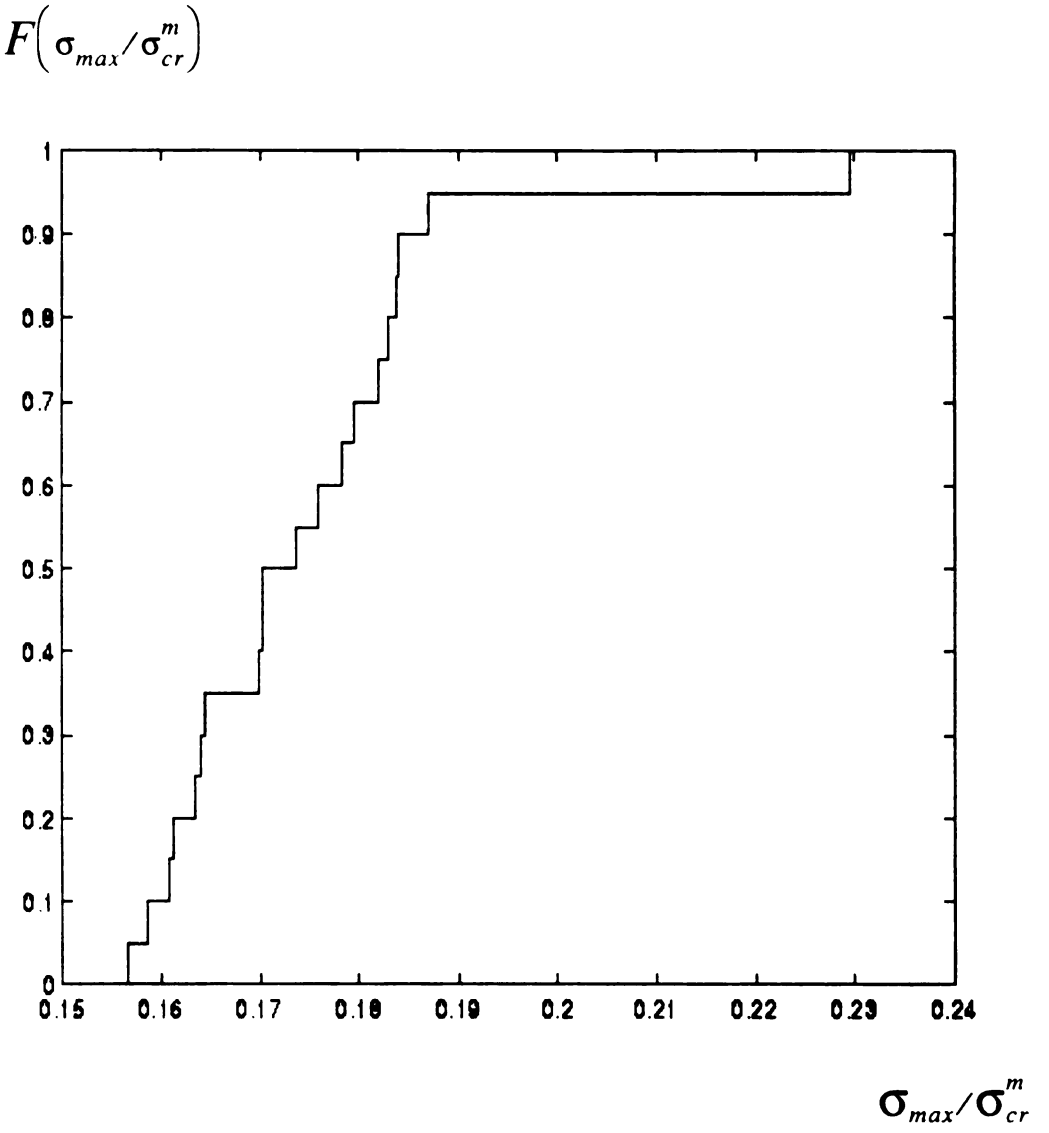

Fig. 69 Probability distribution function $F(\sigma_{max})$ for the case of

$\varepsilon^{i}/\varepsilon^{m} = 0.1, \quad C^{i}/C^{m} = 0.1$

$F\left(\varepsilon_{max}/\varepsilon_{cr}^{m}\right)$

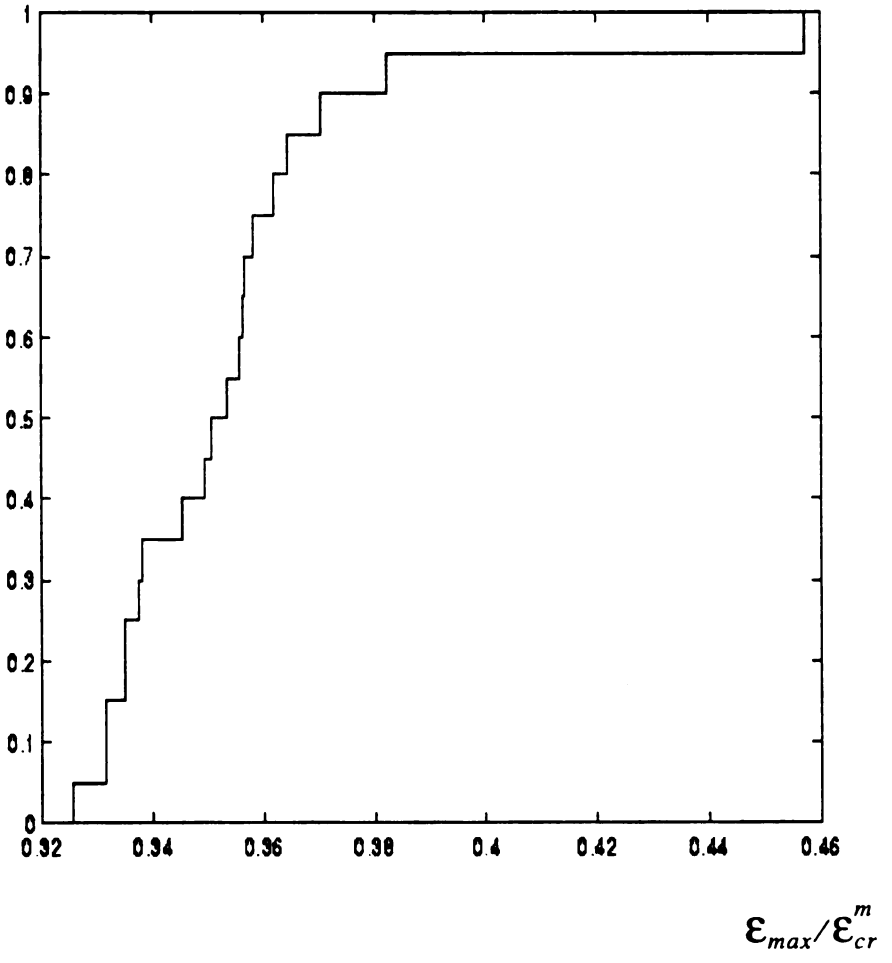

Fig. 70 Probability distribution function F(ε_{max}) for the case of

$\varepsilon^{i}/\varepsilon^{m} = 0.1, \quad C^{i}/C^{m} = 0.1$

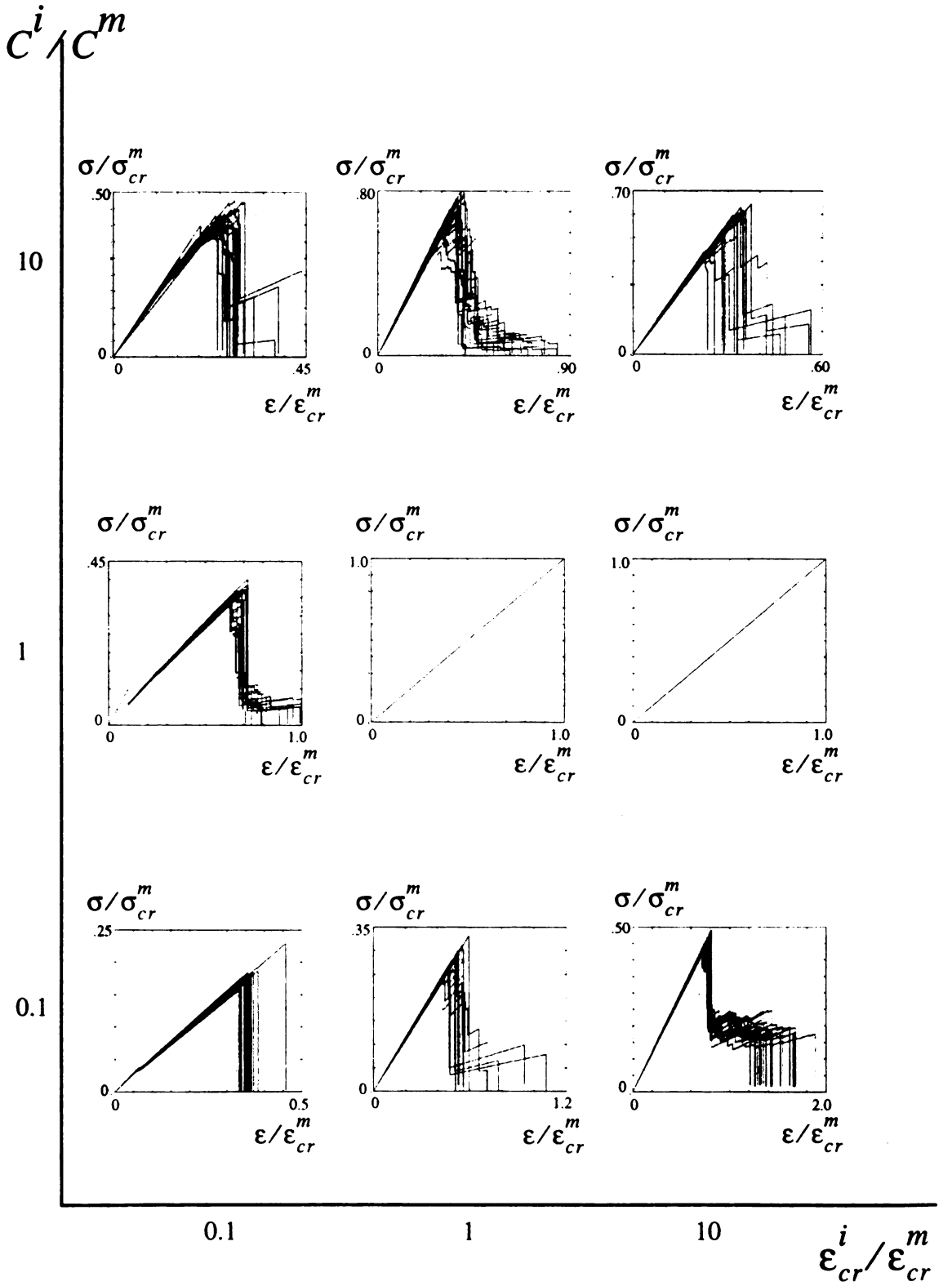

Fig. 71 Damage map, constitutive curves

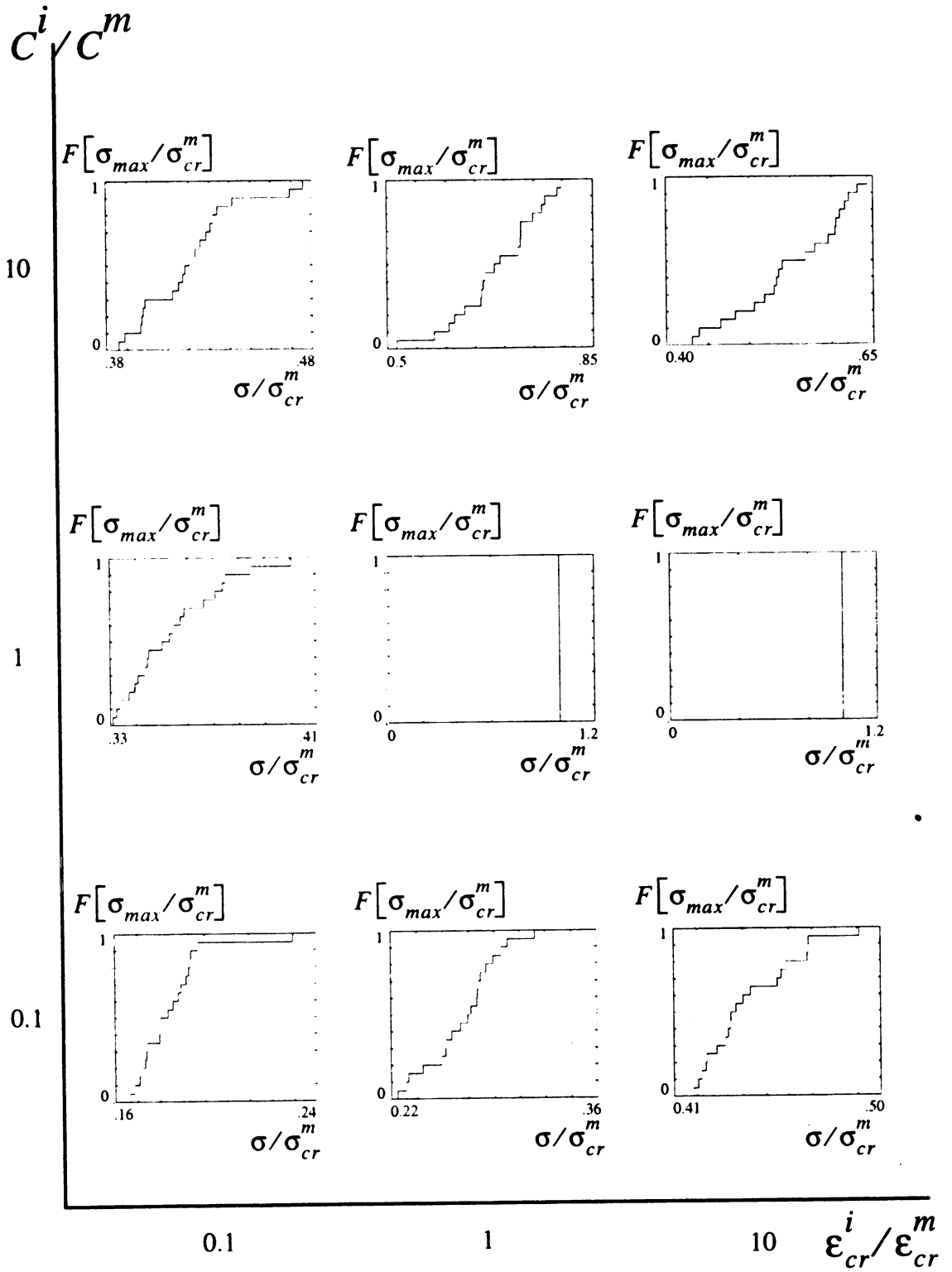

Fig.72 Damage map, distribution function $F(\sigma_{max})$

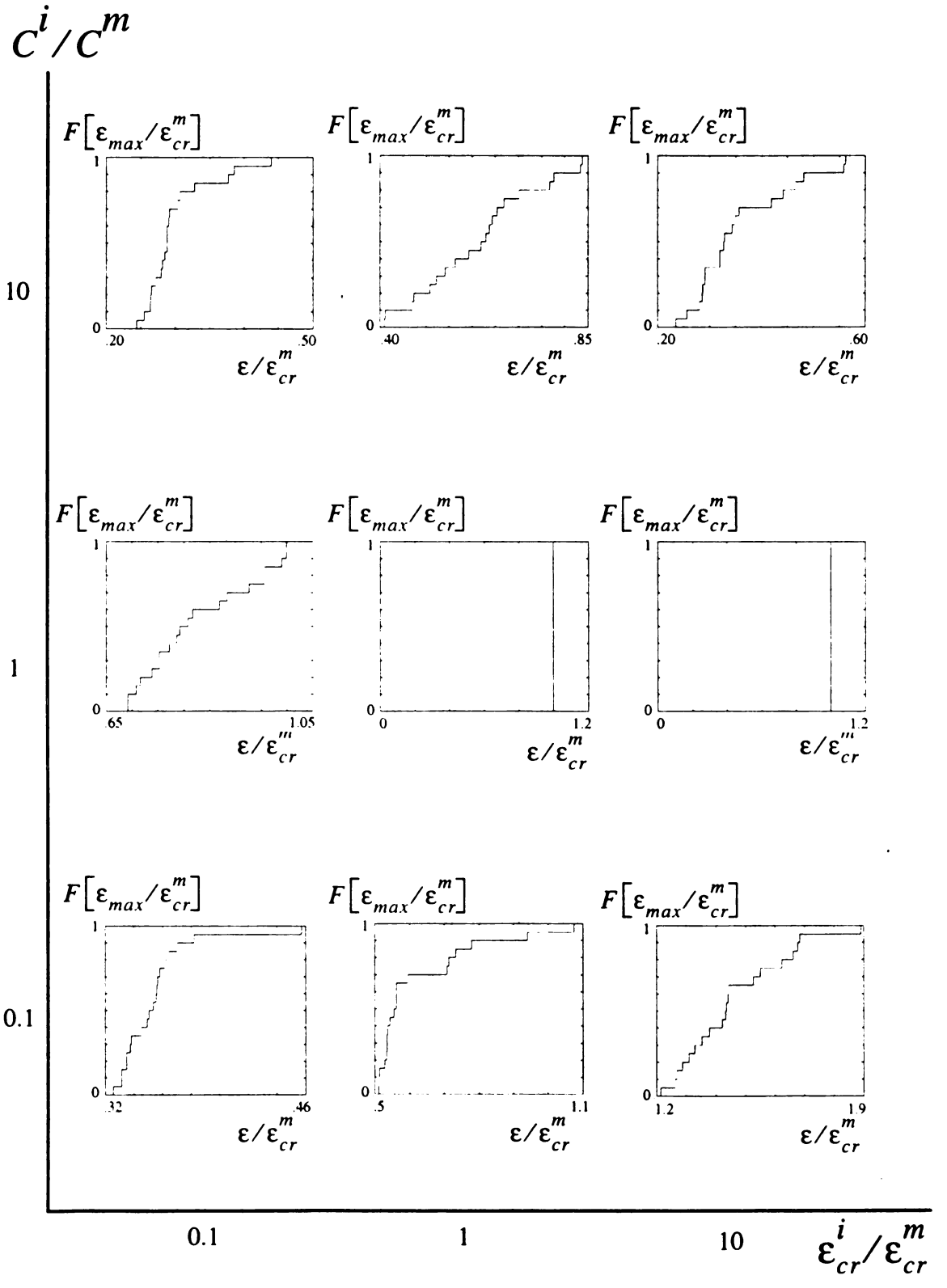

Fig. 73 Damage map, distribution function $F(\varepsilon_{max})$